

HAWKINS, MATTHEW D., PHD. Photophysical study of fused arene based dyes effective for Förster Resonance Energy Transfer. (2022)

Directed by Dr. Hemali Rathnayake and Dr. Joseph M. Starobin.

This dissertation work investigates the non-radiative energy transfer process in a blend of donor and acceptor of fused arene-based hybrid fluorophore materials. Aiming at understanding molecular interactions in a solvent-solute medium and in a solid-state, the goal is to create an efficient donor-acceptor hybrid system to use as a Foster Resonance Energy transfer (FRET) system for molecular-based optical communications. Broad application of fluorescent moieties is known to be hindered by self-quenching properties. Aggregation and restriction of intramolecular rotation play just as an important role in charge transfer efficiency and emission intensity as do external enhancement techniques. Herein, a significant attention was paid for the understanding of the interaction between 9-anthroic acid (a donor) and a silane branched perylene molecule (PTCBS) (an acceptor) as a FRET pair. This work highlights solvent and solute concentration dependencies on the efficiency of such non-radiative energy transfer mechanisms. We also present evidence, which conditions induce the rate limiting mechanisms that out-compete FRET. Preparation of an anthracene carboxylic acid-anchored PDMS was undertaken as a Donor fluorophore and evaluated for such an energy transfer use case, also. This effort was undertaken to prepare an easily curable fluorescent polymer enabling established thin-film formation protocols to be applicable to energy transfer device fabrication. The PDMS-donor functionalized system has concluded that a functionalized polymer retaining fluorescent activity, yet a synthetic preparation method could not be achieved for appropriate product purity and yield. A final sub-project regarding a siloxane nanoparticle synthesized for improved perylene fluorophore loading was studied. Thin-film formation effectiveness and synthesis parameters were improved to reduce overall nanoparticle diameter. This work showed that whilst decreasing particle diameter allowed for a theoretical maximum of over 97% particle volume to become accessible by a resonant donor, efficacy of monolayer thin-film formation significantly decreased when compared to the previously larger nanoparticles.

PHOTOPHYSICAL STUDY OF FUSED ARENE-BASED DYES EFFECTIVE FOR  
FÖRSTER RESONANT ENERGY TRANSFER

by

Matthew D. Hawkins

A Dissertation Submitted to  
the Faculty of The Graduate School at  
The University of North Carolina at Greensboro  
in Partial Fulfillment  
of the Requirements for the Degree  
Doctor of Philosophy

Greensboro  
2022

Approved by

Dr. Hemali Rathnayake

---

Committee Co-Chair

Dr. Joseph M. Starobin

---

Committee Co-Chair

APPROVAL PAGE

This dissertation written by Matthew D. Hawkins has been approved by the following committee of the Faculty of The Graduate School at The University of North Carolina at Greensboro.

Committee Co-Chair

---

Dr. Hemali Rathnayake

Committee Co-Chair

---

Dr. Joseph M. Starobin

Committee Members

---

Dr. Tetyana Ignatova

---

Dr. Jeffrey R. Alston

3/16/2022

Date of Acceptance by Committee

12/2/2021

Date of Final Oral Examination

## ACKNOWLEDGMENTS

I take this space to show appreciation to: my advisors; Dr. Hemali Rathnayake and Dr. Joseph Starobin, Professor Nathan Hammer and his student Austin Dorris; for their instrumentation and time, my committee members; Dr. Jeffrey Alston and Dr. Tetyana Ignatova, all staff in the Nanoscience department of the Joint School of Nanoscience and Nanoengineering, and the students of my research group and of the school.

## TABLE OF CONTENTS

LIST OF TABLES .....	vii
LIST OF FIGURES .....	ix
LIST OF SCHEMES.....	xx
CHAPTER I: INTRODUCTION .....	1
Overview.....	1
Aims of the Research .....	4
Overall Hypothesis.....	4
Dissertation Layout.....	8
CHAPTER II: BACKGROUND .....	9
Foundational Literature.....	9
Field Of Fret.....	9
Dyes And Derivatives.....	11
Methodology.....	13
Basics Of Förster Resonance Energy Transfer .....	13
Photophysics .....	18
Molecular Orbital Computations .....	20
Materials .....	21
CHAPTER III: EXPERIMENTAL METHODS .....	25
Photophysics .....	25
FRET Efficiency Measurement .....	25
Quantum Yield.....	28
Stern-Volmer.....	28
Molecular Orbital Computations .....	29
Stöber Process.....	30

Steglich Esterification.....	32
Film Formation .....	33
Spin-Coating .....	33
Langmuir Blodget.....	35
Spray-Coating .....	35
PDMS Thin-Film Limits.....	35
CHAPTER IV: SYNTHESIS PROCEDURES .....	37
PI-Anthracene .....	37
Polymer-Linker Synthesis and Work-up .....	37
Anthracene-Linker Synthesis and Work-up.....	38
Reaction Summary .....	41
PDMS-Anthracene .....	42
Synthesis and Work-up.....	42
PDI-Silane.....	49
Synthesis and Work-up.....	49
PDIB Nanoparticle.....	50
Synthesis and Work-up.....	51
Reaction Summary .....	58
Thin-Film Formation .....	58
CHAPTER V: ANTHRACENE DERIVATIVES.....	61
Donor Characterization and Performance.....	61
Polyimide Approach .....	61
PDMS Approach.....	72
CHAPTER VI: PERYLENE DERIVATIVES .....	88
Acceptor Characterization and Performance .....	88

PDI-Silane.....	88
PDIB-Siloxane Nanoparticles.....	92
Baseline Photophysical Characteristics .....	113
Thin-Film Formation .....	115
CHAPTER VII: FUSED ARENE PHOTOPHYSICS.....	121
Solvent Photophysics.....	121
Initial Functionality Confirmation .....	126
Concentration Guidance.....	135
Baseline Photophysics Of 9-Anthroic Acid In Solvents.....	136
Follow-Up Of Baseline Photophysics Of 9-Anthroic Acid In Solvents.....	142
Preliminary Solvent Dependence For Donor/Acceptor Blends .....	148
Quantum Yields .....	160
Trial Errors.....	163
THF Photophysical Behavior.....	170
Chlorobenzene Photophysical Behavior .....	178
Chloroform Photophysical Behavior .....	187
Time-Dependent Fluorescence .....	197
CHAPTER VIII: OUTLOOK.....	206
Donor .....	206
Acceptor .....	207
Photophysics .....	208
Outlook .....	210
REFERENCES .....	212
APPENDIX A: MOLECULAR ORBITAL SIMULATION.....	224

## LIST OF TABLES

Table 1 – Reaction summaries for anthracene linker syntheses .....	41
Table 2 – Table of experimental parameters for anthracene terminated PDMS.....	48
Table 3 – PDIB-siloxane nanoparticle reaction table for experiment MH104 .....	58
Table 4 – Particle diameter measurements for experiment MH104.1 .....	109
Table 5 – Particle diameter measurements for experiment MH104.2 .....	111
Table 6 – Particle diameter measurements for experiment MH104.3 .....	113
Table 7 – Table showing stock solution volumes used to create test solutions of PDIS, 9-AA, and a blended sample.....	127
Table 8 – Peak maxima for emission spectra of 9-AA test solution, PDIS test solution and both spectra with blended test solution.....	130
Table 9 – Loss and gain percentages resultant of FRET between 9-AA and PDIS. Transfer efficiency calculated via difference in CPS of both.....	130
Table 10 – Samples of average distance between molecules in 1 mL volume for 9-anthroic acid and PDI-silane.....	136
Table 11 – Solvent polarity table. The values were obtained from the CRC (87th edition), or Vogel's Practical Organic Chemistry (5th ed.) .....	136
Table 12 – Peak locations for absorption spectra .....	139
Table 13 – Peak locations for emission spectra .....	140
Table 14 – Preliminary CHCl <sub>3</sub> Relative FRET efficiency calculation results.....	149
Table 15 – Gaussian fit parameters for Figure 116.....	151
Table 16 – Growth of blended acceptor gaussian fits in comparison to reference acceptor peaks in chloroform.....	152
Table 17 – Preliminary THF Relative FRET efficiency calculation results.....	154

Table 18 – Gaussian fit parameters for Figure 118.....	155
Table 19 – Growth of blended acceptor gaussian fits in comparison to reference acceptor peaks in THF.....	155
Table 20 – Gaussian fit parameters for Figure 121.....	159
Table 21 – Growth of blended acceptor gaussian fits in comparison to reference acceptor peaks in acetonitrile.....	159
Table 22 – Molar concentration and attenuation values for PDMS-anthracene and PDI-silane.	160
Table 23 – Quantum yield calculation data table for 400-600 nm emission range .....	162
Table 24 – Quantum yield calculation data table for 400-480 nm emission range .....	163
Table 25 – Sample concentration guide of error analysis.....	164
Table 26 – Standard deviation of procedural error calculated for various PDI-silane concentrations blended with 50 $\mu$ M/mL 9-AA. ....	169
Table 27 – Sample preparation conditions for blended and reference samples.....	171
Table 28 – Relative FRET efficiency results for THF blend with error propagation.....	176
Table 29 – Sample concentration preparation guide.....	179
Table 30 – Sample concentration preparation guide.....	184
Table 31 – Sample concentration preparation guide.....	188
Table 32 – Sample concentration preparation guide.....	193
Table 33 – Fluorescent lifetime measurements for 5 mM and 50 $\mu$ M concentration solutions mixed in THF and chloroform. Where applicable, contribution percentage is indicated.....	200
Table 34 – Fluorescent lifetime counts for 5 mM and 50 $\mu$ M concentration solutions mixed in THF and chloroform.....	200
Table 35 – Ground state molecular orbitals after geometry optimization via DFT for 9-AA, PTCDA, and PDI-silan .....	227

## LIST OF FIGURES

Figure 1 – Jablonski diagram of FRET. Provided by: <a href="https://commons.wikimedia.org/wiki/File:FRET_Jablonski_diagram.svg">https://commons.wikimedia.org/wiki/File:FRET_Jablonski_diagram.svg</a> .....	14
Figure 2 – Diagram of FRET transition dipoles. Source: M. Kuscü and O. B. Akan, “A nanoscale communication channel with fluorescence resonance energy transfer (FRET),” 2011 IEEE Conf. Comput. Commun. Work. (INFOCOM WKSHPs), pp. 425–430, 2011. ....	15
Figure 3 – Dipole alignment energies for two dimer conformations. Source: Saikin, S. K.; Eisfeld, A.; Valleau, S.; Aspuru-Guzik, A. Photonics Meets Excitonics: Natural and Artificial Molecular Aggregates. <i>Nanophotonics</i> <b>2013</b> , 2 (1), 21–38. <a href="https://doi.org/10.1515/NANOPH-2012-0025">https://doi.org/10.1515/NANOPH-2012-0025</a> . 22	22
Figure 4 – General scheme for Stöber process. Source: By Smokefoot – Own work, CC BY-SA 3.0, <a href="https://commons.wikimedia.org/w/index.php?curid=25698603">https://commons.wikimedia.org/w/index.php?curid=25698603</a> .....	31
Figure 5 – Modified Stöber process scheme .....	32
Figure 6 – Steglich esterification reaction scheme. Source: B. Neises, W. Steglich, <i>Angew. Chem. Int. Ed.</i> , 1978, 17, 522-524. ....	32
Figure 7 – DMAP acceleration with Steglich Esterification. Source: <a href="https://www.organic-chemistry.org/namedreactions/steglich-esterification.shtm">https://www.organic-chemistry.org/namedreactions/steglich-esterification.shtm</a> .....	33
Figure 8 – Silica nanoparticle spin-coating protocol for monolayer formation. Source: T. Ogi, L. B. Modesto-Lopez, F. Iskandar, and K. Okuyama, “Fabrication of a large area monolayer of silica particles on a sapphire substrate by a spin coating method,” <i>Colloids Surfaces A Physicochem. Eng. Asp.</i> , vol. 297, no. 1–3, pp. 71–78, 2007.....	34
Figure 9 – FTIR spectrum for Polymer-Linker product from MH001 reaction .....	64
Figure 10 – Experimental <sup>1</sup> H NMR of linker/polymer reaction. Synthesis of 2-(4-(4-((6-hydroxyhexyl)amino)benzyl)phenyl)-1,3-dioxoisindoline-5-carbonyl chloride. DMSO-d <sub>6</sub> solvent. 400 MHz.....	65
Figure 11 – Experimental <sup>1</sup> H NMR of 9-anthroic acid. DMSO <sub>d</sub> solvent, 400 MHz. ....	66
Figure 12 – FTIR spectra comparing before and after methanol wash of sample MH003 .....	68

Figure 13 – Experimental proton NMR of 6-bromohexyl anthracene-9-carboxylate work-up (MH003). 400 MHz, DMSO-d <sub>6</sub> . .....	69
Figure 14 – FTIR spectrum of MH033 anthracene-linker work-up presenting precipitate from first gravity filter. ....	70
Figure 15 – FTIR spectrum of MH033 anthracene linker work-up presenting dried filtrate after hexanes wash. ....	71
Figure 16 – FTIR presenting all work-up stages of PDMS-anthracene synthesis MH047. ....	73
Figure 17 – Experimental proton NMR: PDMS-anthracene. DMSO-d <sub>6</sub> solvent. 400 MHz.....	74
Figure 18 – UV-vis: PDMS-anthracene in chloroform.....	75
Figure 19 – Fluorescence: PDMS-anthracene. In chloroform. Excited at 365 nm.....	75
Figure 20 – FTIR presenting PMDS-anthracene work-up filtrate after hexanes wash.....	76
Figure 21 – FTIR presenting PDMS-anthracene work-up filtrate after methanol wash.....	77
Figure 22 – FTIR presenting all work-up stages of PDMS-anthracene synthesis MH095. ....	78
Figure 23 – (left) UV-vis spectrum for final washed material. (right) Fluorescence taken with excitation values at 300 nm (black), 325 nm (red), and 350 nm (blue). Samples dissolved in chloroform.....	79
Figure 24 – FTIR presenting precipitate and filtrate from gravity filter after cooling MH108 post-reaction to -20°C. Comparison with 9-AA provided. ....	80
Figure 25 – Proton NMR taken of PDMS-NH <sub>2</sub> in DMSO-d <sub>6</sub> . 400 MHz.....	81
Figure 26 – Proton NMR taken of precipitate product from MH109 in CDCl <sub>3</sub> . 400 MHz.....	82
Figure 27 – Proton NMR taken of precipitate product from MH109 in CDCl <sub>3</sub> (rerun). 400 MHz .....	83
Figure 28 – (left) UV-vis for precipitate of MH109. (right) Fluorescence for precipitate of MH109. Excited at 375 nm. Solvated in chloroform. ....	84

Figure 29 – Thin-films were produced on 25x25 mm quartz slides via a spin-coating method. 100 $\mu$ L of solution was cast and processed at 1000 rpm for 30 seconds. ....	86
Figure 30 – Fluorescence for layered films of PDMS-anthracene and PDI-silane.....	87
Figure 31 – FTIR spectrum of PDI-silane after synthesis .....	89
Figure 32 – $^1\text{H}$ NMR of PDI-silane in $\text{CDCl}_3$ at 400 MHz. ....	90
Figure 33 – UV-vis spectrum data for PDI-silane .....	91
Figure 34 – Fluorescent spectrum data for PDI-silane. Excitation wavelength at 457 nm. ....	91
Figure 35 – Absorption and emission overlap for PDI-silane. Excitation wavelength set to 457 nm. ....	92
Figure 36 – Reaction summary table of PDIB-silane NPs .....	93
Figure 37 – SEM sample MH048: silica NPs.....	95
Figure 38 – SEM sample MH048: 24 hours into synthesis .....	95
Figure 39 – SEM sample MH048: 48 hours into synthesis .....	95
Figure 40 – SEM sample MH048: washed PDIB-silane NPs.....	95
Figure 41 – SEM sample MH048: supernatant.....	95
Figure 42 – SEM sample MH050: 0 hours into synthesis .....	96
Figure 43 – SEM sample MH050: 24 hours into reaction .....	96
Figure 44 – SEM sample MH050: 24 hours into reaction .....	96
Figure 45 – SEM sample MH050: washed final product .....	96
Figure 46 – SEM sample MH050: washed final product .....	96
Figure 47 – SEM sample MH050: supernatant.....	96
Figure 48 – SEM sample MH050: supernatant.....	96
Figure 49 – SEM sample MH052: 24 hours into reaction .....	97

Figure 50 – SEM sample MH052: washed PDIB-silane NPs.....	97
Figure 51 – SEM sample MH052: washed PDIB-silane NPs.....	97
Figure 52 – SEM sample MH056: PDIB-silane NPs, 1st supernatant .....	99
Figure 53 – SEM sample MH056: PDIB-silane NPs, 1st supernatant .....	99
Figure 54 – SEM sample MH056: PDIB-silane NPs, 1st supernatant .....	99
Figure 55 – SEM sample MH056: PDIB-silane NPs, 1st supernatant .....	99
Figure 56 – SEM sample MH056: Silica particles .....	99
Figure 57 – SEM sample MH056: Silica particles .....	99
Figure 58 – SEM sample MH057: PDIB-silane NPs, 1st supernatant .....	101
Figure 59 – SEM sample MH057: PDIB-silane NPs, 1st supernatant .....	101
Figure 60 – SEM sample MH057: PDIB-silane NPs 1st supernatant .....	101
Figure 61 – SEM sample MH057: PDIB-silane NPs, 1st supernatant .....	101
Figure 62 – SEM sample MH057: PDIB-silane NPs, 2nd supernatant .....	101
Figure 63 – SEM sample MH057: PDI-silane, 3rd supernatant .....	101
Figure 64 – SEM sample MH057: Final pellet.....	101
Figure 65 – SEM sample MH057: first supernatant after second centrifugation .....	102
Figure 66 – SEM sample MH057: first supernatant after second centrifugation .....	102
Figure 67 – Hitachi SEM sample MH058: silica nanoparticle formations.....	104
Figure 68 – Zeiss SEM sample MH058: dried silica plate .....	104
Figure 69 – Zeiss SEM sample MH058: silica particle clump .....	104
Figure 70 – Hitachi SEM sample MH048: 24-hour reaction sample .....	104
Figure 71 – Zeiss SEM sample MH058: 24-hour reaction sample.....	104
Figure 72 – Zeiss SEM sample MH058: 24-hour reaction sample.....	104

Figure 73 – Hitachi SEM sample MH058: 24-hour sample, PDIB-silane sheets.....	104
Figure 74 – Hitachi SEM sample MH058: 24-hour sample, PDIB-silane sheets.....	104
Figure 75 – Hitachi SEM sample MH058: 24-hour sample, PDIB-silane monolayer .....	104
Figure 76 – Hitachi SEM sample MH058: centrifuged sample, PDIB-silane nanoparticle layer.....	105
Figure 77 – Hitachi SEM sample MH058: centrifuged sample, PDIB-silane nanoparticle layer.....	105
Figure 78 – Zeiss SEM sample MH058: centrifuged sample, PDI-silane 'javelins'.....	105
Figure 79 – Zeiss SEM sample MH058: centrifuged sample, PDI-silane 'javelins'.....	105
Figure 80 – Zeiss SEM sample MH058: centrifuged sample, PDI-silane 'javelins'.....	105
Figure 81 – Zeiss SEM sample MH058: centrifuged sample, PDI-silane 'javelins'.....	105
Figure 82 – (left) UV-vis spectra of PDIB-NPs. (right) Fluorescent spectra of PDIB-NPs. Excitation wavelength set to 457 nm (right).....	106
Figure 83 – (left) PDIB-NPs imaged under SEM. 10kV accelerating voltage, x220k magnification. (right) PDIB-NPs imaged under TEM.....	107
Figure 84 – (top) SEM images of pellet from MH104.1 reaction. (bottom) SEM images of centrifuge solvent form reaction MH104.1.....	108
Figure 85 – (top) SEM images of pellet from MH104.2 reaction. (bottom) SEM images of centrifuge solvent form reaction MH104.2.....	110
Figure 86 – (top) SEM images of pellet from MH104.3 reaction. (bottom) SEM images of centrifuge solvent form reaction MH104.3.....	112
Figure 87 – UV-Vis absorbance of increasing concentration to solution saturation of PDIB nanoparticles in EtOH.....	114
Figure 88 – Fluorescence emission of PDIB-NPs via multiple excitation wavelengths .....	114
Figure 89 – SEM sample MH053.3: PDI-silane thin-film.....	116

Figure 90 – SEM sample MH053.3: PDI-silane thin-film.....	116
Figure 91 – SEM sample MH053.4: PDIB-silane NP thin-film.....	116
Figure 92 – SEM sample MH053.4: PDIB-silane NP thin-film.....	116
Figure 93 – SEM sample MH055.1: PDIB-silane NP thin-film (EtOH).....	118
Figure 94 – SEM sample MH055.1: PDIB-silane NP thin-film (EtOH).....	118
Figure 95 SEM sample MH055.2: PDIB-silane NP thin-film (EtOH).....	118
Figure 96 – SEM sample MH055.2: PDIB-silane NP thin-film (EtOH).....	118
Figure 97 – SEM sample MH055.3: PDIB-silane NP thin-film (C <sub>6</sub> H <sub>5</sub> Cl) .....	119
Figure 98 – SEM sample MH055.3: PDIB-silane NP thin-film (C <sub>6</sub> H <sub>5</sub> Cl) .....	119
Figure 99 – SEM sample MH055.4: PDIB-silane NP thin-film (C <sub>6</sub> H <sub>5</sub> Cl) .....	119
Figure 100 – SEM sample MH055.4: PDIB-silane NP thin-film (C <sub>6</sub> H <sub>5</sub> Cl) .....	119
Figure 101 – UV-vis absorbance of 9-AA, PDIS, and Blended test solutions. ....	128
Figure 102. Fluorescence spectra depicting 9-anthroic acid (black dots), PDI-silane (red dots), and an equal moiety blend of both (black line). All spectra were run in chloroform solvent solutions. ....	129
Figure 103 – Theoretical FRET efficiency curve dependent on distance between fluorophores. In this case, 9-AA and PDIS were used as the donor and acceptor, respectively. the quantum yield of the donor was set to 0.36 and the refractive index was 2.5. ....	131
Figure 104. Fluorescence spectra depicting summation of 9-anthroic acid reference and PDI-silane reference (black dash) overlaid with blend solution (black line).....	134
Figure 105 – Modeled average distance between monomeric 9-anthroic acid moieties in 1 mL volume.....	135
Figure 106 – Modeled average distance between monomeric PDI-silane moieties in 1 mL volume.....	135
Figure 107 – UV-vis absorption spectra of 9-anthroic acid in various solvents.....	137

Figure 108 – Fluorescent emission spectra of 9-anthroic acid in various solvents .....	138
Figure 109 – Normalized UV-vis absorption spectra of 9-anthroic acid in various solvents.....	139
Figure 110 – Normalized fluorescence spectra of 9-anthroic acid in various solvents. Excitation 365 nm. ....	140
Figure 111 – Absorption and fluorecence overlap for 9-anthroic acid in various solvents. Excitation 365 nm. ....	141
Figure 112 – Absorption and fluorecence overlap for 9-anthroic acid in various solvents. Excitation 365 nm. ....	143
Figure 113 – Absorption comparison between 0-hour and 2- hour measurement of 9-anthroic acid in various solvents.....	145
Figure 114 – Fluorescence comparison between 0-hour and 24-hour measurements of 9-anthroic acid in various solvents. ....	147
Figure 115 – (a and b) Fluorescence spectra for blend in CHCl <sub>3</sub> . Black dot represents 9-AA reference sample, red dot represents PDI-s reference sample, and black line represents blended sample. Excitation at 365 nm. (c) Blend vs. summation of 9-AA reference and PDI-silane reference.....	149
Figure 116 – Three gaussian spectral decomposition of THF solvated PDI-S reference solution and PDI-S blend component. (a) Reference PDI-S solution. (b) Blended PDI-S and 9AA solution.	151
Figure 117 – (a and b) Fluorescence spectra for blend in THF. Black dot represents 9-AA reference sample, red dot represents PDI-s reference sample, and black line represents blended sample. Excitation at 365 nm. (c) Blend vs. summation of 9-AA reference and PDI-silane reference...	153
Figure 118 – Two gaussian spectral decomposition of chloroform solvated PDI-S reference solution and PDI-S blend component. (a) Reference PDI-S solution. (b) Blended PDI-S and 9AA solution.....	154
Figure 119 – (a and b) Fluorescence spectra for blend in acetonitrile. Black dot represents 9-AA reference sample, red dot represents PDI-s reference sample, and black line represents blended	

sample. Excitation at 365 nm. (c) Blend vs. summation of 9-AA reference and PDI-silane reference..... 156

Figure 120 – Fluorescence spectra for blend in saturated acetonitrile. Black dot represents 9-AA reference sample, red dot represents PDI-s reference sample, and black line represents blended sample. Excitation at 365 nm. (c) Blend vs. summation of 9-AA reference and PDI-silane reference..... 157

Figure 121 – Three gaussian spectral decomposition of acetonitrile solvated PDI-S reference solution and PDI-S blend component. (a) Reference PDI-S solution. (b) Blended PDI-S and 9AA solution..... 158

Figure 122 – Stern-Volmer plot of blended concentration error trials showing 2<sup>nd</sup> order quadratic fit and one standard deviation from the mean..... 165

Figure 123 – Log base 10 scaled axes for Stern-Volmer plot of blended concentration error trials showing 2<sup>nd</sup> order quadratic fit and one standard deviation from the mean. .... 165

Figure 124 – Bar chart presenting the standard deviation in fluorescent emission CPS, and as a % of total CPS..... 166

Figure 125 – Normalized 9-AA emission Stern-Volmer plot of blended concentration error trials showing 2<sup>nd</sup> order quadratic fit and one standard deviation from the mean. .... 167

Figure 126 – Normalized 9-AA emission Log base 10 scaled axes for Stern-Volmer plot of blended concentration error trials showing 2<sup>nd</sup> order quadratic fit and one standard deviation from the mean..... 167

Figure 127 – Bar chart presenting the normalized 9-AA emission standard deviation in fluorescent emission CPS, and as a % of total CPS ..... 168

Figure 128 – (a) Fitting of standard deviation for reference spectra error. (b) Fitting of standard deviation for blended spectra error. .... 170

Figure 129 – Excitation spectra of reference solutions using 365 nm laser. .... 172

Figure 130 – Integration of each reference spectra from 350 – 800 nm..... 173

Figure 131 – excitation spectra blended solutions using 365 nm laser..... 174

Figure 132 – (a-e) Reference, summation, and blend fluorescence spectra for ratio samples 4:1, 2:1,1:1, 1:2, and 1:4, respectively. (f) Fluorescent spectrum for 9-AA excitation at 365 nm. Constant concentration of 50 $\mu\text{M}$ as donor for all trials. ....	175
Figure 133 – Relative FRET efficiency calculation results for THF blend.....	176
Figure 134 – Stern-Volmer plots for blended ratios in THF fitted with linear and quadratic curves. ....	177
Figure 135 – Fluorescent spectra of 9-AA and PDI-S in chlorobenzene. 9-AA was dissolved at high concentration of 360 $\mu\text{mol/mL}$ . PDI-S #1-4 were dissolved at a ratio of 250 $\mu\text{mol/mL}$ , 376 $\mu\text{mol/mL}$ , 501 $\mu\text{mol/mL}$ , and 626 $\mu\text{mol/mL}$ , respectively.....	181
Figure 136 – Integration of spectra produced from high concentration blends in chlorobenzene. Data labelled ‘Summation’ consists of two cumulated components: firstly, and consistently, the integration of the reference 9-AA emission; secondly, to its corresponding number, the PDI-S reference spectral integration. Data marked as ‘Reference’ consists of just the PDI-S integrated spectra associated with its number. Finally, data marked as ‘Blend’ is the integration of the blended sample spectra where both moieties present. ....	181
Figure 137 – Fluorescent spectra of 9-AA and PDI-S blended in chlorobenzene. 9-AA was dissolved at a high concentration of 360 $\mu\text{mol/mL}$ . Blends #1-4 contained 360 $\mu\text{mol/mL}$ of 9-AA and PDI-S at a molarity of 250 $\mu\text{mol/mL}$ , 376 $\mu\text{mol/mL}$ , 501 $\mu\text{mol/mL}$ , and 626 $\mu\text{mol/mL}$ , respectively. ....	182
Figure 138 – Stern-Volmer plot produced from the high concentration blend study in chlorobenzene. The Fluorophore was represented by 9-AA, and the Quencher was PDI-S. Data fitted in linear equation (left) and quadratic (right). ....	183
Figure 139 – Fluorescent spectra of 9-AA and PDI-S in chlorobenzene. 9-AA was dissolved at a concentration of 36 $\mu\text{mol/mL}$ . PDI-S #1-4 were dissolved at a ratio of 25 $\mu\text{mol/mL}$ , 38 $\mu\text{mol/mL}$ , 50 $\mu\text{mol/mL}$ , and 63 $\mu\text{mol/mL}$ , respectively. ....	184
Figure 140 – Fluorescent spectra of 9-AA and PDI-S blended in chlorobenzene. 9-AA was dissolved at a concentration of 36 $\mu\text{mol/mL}$ . Blends #1-4 contained 36 $\mu\text{mol/mL}$ of 9-AA and	

PDI-S at a molarity of 25 $\mu\text{mol/mL}$ , 38 $\mu\text{mol/mL}$ , 50 $\mu\text{mol/mL}$ , and 63 $\mu\text{mol/mL}$ , respectively. ....	185
Figure 141 – Stern-Volmer plot produced from the low concentration blend study in chlorobenzene. The Fluorophore was represented by 9-AA, and the Quencher was PDI-S. Data fitted with a linear equation. ....	186
Figure 142 – Fluorescent spectra overlay comparing 9-AA, PDI-S and blends in chlorobenzene. ....	187
Figure 143 – Fluorescent spectra of 9-AA and PDI-S in chloroform. 9-AA was dissolved at a concentration of 360 $\mu\text{mol/mL}$ . PDI-S #1-4 were dissolved at a ratio of 250 $\mu\text{mol/mL}$ , 376 $\mu\text{mol/mL}$ , 501 $\mu\text{mol/mL}$ , and 626 $\mu\text{mol/mL}$ , respectively. Excitation 365 nm. ....	189
Figure 144 – Fluorescent spectra of 9-AA and PDI-S blended in chlorobenzene. 9-AA was dissolved at a high concentration of 360 $\mu\text{mol/mL}$ . Blends #1-4 contained 360 $\mu\text{mol/mL}$ of 9-AA and PDI-S at a molarity of 250 $\mu\text{mol/mL}$ , 376 $\mu\text{mol/mL}$ , 501 $\mu\text{mol/mL}$ , and 626 $\mu\text{mol/mL}$ , respectively. Excitation 365 nm. ....	190
Figure 145 – Integration of spectra produced from high concentration blends in chloroform. Data labelled ‘Summation’ consists of two cumulated components: firstly and consistently, the integration of the reference 9-AA emission; secondly, to its corresponding number, the PDI-S reference spectral integration. Data marked as ‘Reference’ consists of just the PDI-S integrated spectra associated with its number. Finally, data marked as ‘Blend’ is the integration of the blended sample spectra where both moieties present. ....	191
Figure 146 – Stern-Volmer plot produced from the high concentration blend study in chloroform. The Fluorophore was represented by 9-AA, and the Quencher was PDI-S. Data fitted in linear equation (left) and quadratic (right). ....	192
Figure 147 – Fluorescent spectra of 9-AA and PDI-S in chloroform. 9-AA was dissolved at a concentration of 36 $\mu\text{mol/mL}$ . PDI-S #1-4 were dissolved at a ratio of 25 $\mu\text{mol/mL}$ , 38 $\mu\text{mol/mL}$ , 50 $\mu\text{mol/mL}$ , and 63 $\mu\text{mol/mL}$ , respectively. Excitation 365 nm. ....	194

Figure 148 – Fluorescent spectra of 9-AA and PDI-S blended in chloroform. 9-AA was dissolved at a concentration of 36 $\mu\text{mol/mL}$ . Blends #1-4 contained 36 $\mu\text{mol/mL}$ of 9-AA and PDI-S at a molarity of 25 $\mu\text{mol/mL}$ , 38 $\mu\text{mol/mL}$ , 50 $\mu\text{mol/mL}$ , and 63 $\mu\text{mol/mL}$ , respectively.....	195
Figure 149 – Stern-Volmer plot produced from the low concentration blend study in chloroform. The Fluorophore was represented by 9-AA, and the Quencher was PDI-S. Data fitted with a linear equation.....	196
Figure 150 – Fluorescent spectra overlay comparing 9-AA, PDI-S and molar blends in chloroform.....	197
Figure 151 – Fluorescence emission spectra of 5 mM concentration samples used for excited state lifetime measurements. ....	201
Figure 152 – Lifetime measurements of 5 mM concentrations THF and chloroform solvated samples of PDI-silane reference, 9-AA reference, and 1:1 blend.....	202
Figure 153 – Lifetime measurements of 50 $\mu\text{M}$ concentrations THF and chloroform solvated samples of PDI-silane reference, 9-AA reference, and 1:1 blend.....	203
Figure 154 – Ground state HOMO-LUMO after geometry optimization simulation via DFT for 9-AA, PTCDA, and PDI-silane.....	224
Figure 155 – Ground state molecular orbitals after geometry optimization via DFT for 9-AA, PTCDA, and PDI-silane.....	224
Figure 156 – Ground state HOMO-LUMO after geometry optimization simulation via DFT in chloroform for 9-AA, PTCDA, and PDI-silane.....	225
Figure 157 – Ground state molecular orbitals after geometry optimization via DFT in chloroform for 9-AA, PTCDA, and PDI-silane.....	225
Figure 158 – Ground state HOMO-LUMO after geometry optimization simulation via DFT in THF for 9-AA, PTCDA, and PDI-silane.....	226
Figure 159 – Ground state molecular orbitals after geometry optimization via DFT in THF for 9-AA, PTCDA, and PDI-silane.....	226

## LIST OF SCHEMES

Scheme 1 – Synthesis of poly(dimethylsiloxane)bis(3-aminopropyl) and 9-anthracenecarboxylic acid to form PDMS-anthracene .....	42
Scheme 2 – Synthesis of perylene-3,4,9,10-tetracarboxylic dianhydride and 3-aminopropyltriethoxysilane to form PDI-silane .....	49
Scheme 3 – Synthesis of PDI-silane and tetraethylorthosilicate to form PDI-B nanoparticles....	51

## CHAPTER I: INTRODUCTION

### OVERVIEW

The application-based literature regarding perylenetetracarboxylic dianhydride (PTCDA) and its derivatives tend to be split, at first, into the categories of thin-film or solution. Further narrowing of investigative topics considers analysis of quenching phenomenon. As a foundational tool for understanding photophysical behavior, quenching mechanisms can provide significant quantitative and qualitative information. The reemergence of recent interest in soluble PTCDA derivatives provide evidence for growing interest in application outside of the pigment industry <sup>1</sup>. Areas of research that can be accessed with an expanded solubility library are organic electronics, photoinduced processes and supramolecular organization <sup>2</sup>. PTCBS is a candidate for solvent-based quenching research and specifically, with a quenching mechanism known as Förster resonance energy transfer.

The calling for probes, diodes, and devices derived from photoluminescent materials has been growing larger within the first two decades of the twenty first century. Within these applications, Förster Resonance Energy Transfer (FRET) has been studied intensely due to its photophysical properties, and more uniquely, its intrinsic spatial determination. FRET follows an effective range law to the order of  $r^{-6}$ , resulting in a binary-like energy transfer response when two fluorophores interact within 10 nm of separation. This, for one reason, has been championing its presence in fields of biological study for a handful of decades. FRET's usefulness has been derived from its unique and paired interaction properties that result in a non-radiative energy transfer between two fluorophore dipoles. What makes FRET especially unique in this scenario is the near to guarantee of spatial resolution sub 10 nm. Beyond such distances, other quenching and radiative emission mechanisms will occur. The outcome of a binary system of fluorophores can then be characterized by a red shift in emitted light, post excitation.

By no coincidence, the early couple of decades in the twenty-first century also exhibited growth surrounding energy transfer. Through those years, the field of study was involved mostly in emission enhancement via various methods of resonance coupling <sup>3-7</sup>, plasmon enhancement <sup>8-10</sup> or direct pair interaction improvements <sup>11</sup>. These include confined nanoparticles <sup>4,9</sup>, metallic

surfaces <sup>12</sup>, nanoantenna waveguides <sup>7,8</sup>, and biased dipole alignment techniques <sup>13</sup>. However, application is still known to be hindered by self-quenching properties <sup>14</sup>. In 2009, aggregation-induced emission was studied and developed by a team interested in the effects of restriction of intramolecular rotation <sup>15</sup>. This work resulted in increased emission simultaneous to increased concentration. Quite an opposite outcome when compared to other intrinsically fluorescent molecules – such as perylene – which self-quenches at high concentrations because of  $\pi$ - $\pi$  stacking interactions <sup>16</sup>. Another remedy to self-quenching was to build fluorescent dyes into a rigid framework such as a silica nanoparticle <sup>17</sup> for metal-organic framework <sup>14</sup>.

The centerpiece of this work is a rylene dye known in shorthand to be PTCDA. Formally, perylenetetracarboxylic dianhydride. It is an organic semiconductor with nearly 9000 published scholar articles searchable through the Google Scholar engine, as of 2021. The scientific attraction to this molecule comes from its intense visible light absorption, thermal and chemical stability, electron accepting tendencies, and near unity quantum yield emission. It has made strong impressions in the organic solar cell disciplines <sup>18</sup> and is now used for sensing and probes <sup>19,20</sup>. A critique of PTCDA is its poor general solubility. Water, ethanol, chloroform, acetonitrile, and other similar solvents are not sufficient to effectively dissolve this dye molecule. Insolubility very quickly reduces the range of sensing application currently used in cheap and quick testing scenarios. In 1988, Demming et al. produced a functionalized PTCDA derivative intending to improve solubility and incurring improvements to fluorescence emission. This has been improved upon many years later by Türkmen et al. with four more soluble derivatives of PTCDA. Molecule 4 had been designed for aqueous environments where they could minimize electron transfer through the addition of acidic species. Concluding, a highly soluble, photoactive, electron transfer controllable, functionable molecule is a foundation for a research playground. In the same year (2009) as Türkmen, Wahab et al. produced and self-assembled thin-films from a perylenediimide-bridged silsesquioxane. This molecule is highly soluble in chloroform and can be used to build structure in two and three dimensions. This PTCBS (perylene-tetracarboxylic bridged siloxane) molecule could be produced within ‘green chemistry’ temperatures using a single step reaction. It does not retain as much chemical stability as the mother molecule PTCDA, but the framework capability expands application in other areas and substitutes if utilized correctly.

Aggregation of fluorescent dyes play a significant role in influencing electronic and photonic energy transfers. A dye being either induced to commit a non-radiative or radiative decay pathway depends heavily upon its environment of neighboring partners, be them of solvent or dye. With furthering efforts to produce more sensitive and complex optical probes and sensors, understanding energy transfer properties of fluorescent dyes is growing in importance. In a system where maximum intensity of sensing output is key, the direct solution of including more sensing dye comes with the typical drawbacks of aromatic aggregation. The  $\pi$ -conjugated backbones of high quantum yielding moieties that make them ideal for photonic sensing applications can also be their detriment due to strong tendency of  $\pi$ - $\pi$  stacking based aggregation, and a resultant self-quenching. There are of course ways in which this phenomenon can be used to take advantage of such aggregation, for example: it is a sure way to judge movements in solvent cage dynamics or appearance and interaction of system intruders. Nevertheless, understanding the limitations of environment and concentration in these sensing systems has great value to encourage new applications and methods. Derivatives of PTCDA known as “swallowtail” substituents <sup>21</sup> have been found effective at remaining soluble while simultaneously disrupting  $\pi$ - $\pi$  stacking interactions <sup>2</sup>. Other methods of disrupting stacking interactions included nanoparticle <sup>22</sup> and MOF <sup>14</sup> dye integration to sterically hinder orbital interaction.

This work intends to explore the parameters that induce quenching mechanism of a pair of fluorescent dyes; 9-anthroic acid and a silane derivative of PTCDA. In tandem, these fluorophores can exhibit multiple energy transfer mechanisms provided the environment of solvent and concentration as to do so. This work will also explore a potential method of engineering out certain transfer pathways via nanoparticle formation. Growth of application that fluorescent labels and sensors have shown in recent years is a great incentivizing factor of further experimentation for PDI-based nanoparticles inherently able to restrict undesired energy extinction pathways. It is also worth looking into ground state charge transfer proficiencies of both PDI-Silane, and PDIB-SQ nanoparticles.

A potential avenue to broaden the material catalogue is to experiment with known, and highly proficient organic fluorophores. One way to implement this is through synthesis of hybrid nanostructures. Such structures would be capable of producing or receiving a signal, and then enabling an action from that. These structures would contain signaling molecules that can

fluoresce/absorb light and move this energy around as the signal packet whilst be adapted with characteristics giving them ease of workability. Hybrid molecules have been previously developed using perylenediimide functionalized bridged siloxane <sup>22</sup>. When compared to other forms of molecular communication materials however, the siloxane particles are an order of magnitude larger. The phenomenon of Förster Resonance Energy Transfer (FRET) requires distances below 10 nm for any such possibility of signal transfer. Therefore, typically, single molecules are used for such practices. However, recent experimental work has shown that it is quite effective to use the FRET method for nanocommunication <sup>23</sup>. It has also been shown that halogenated phenylsilsesquioxanes can be implemented to provide structure and function in one measure <sup>24</sup>. This leaves a great many opportunities for integration of such materials with a FRET based device and exploration of that device's efficacy with nanocommunication. Given a combination material approach, it is vital to maintain and measure the continued usefulness of the fluorescent component. A hybrid material that improves workability at the sacrifice of FRET performance has not moved the field forward. The theme of this work presents ideas with which to avoid such trade-off.

## **AIMS OF THE RESEARCH**

The overall goal of this dissertation work is to investigate the FRET phenomena in fused arene-based donor and acceptor hybrid materials by understanding the photophysical properties in solution and thin films of novel derivatives of anthracene donor and perylenediimide acceptor. By exploring the solvent dependent adsorption and emission behavior of these two donor and acceptor systems could reveal the effect of solvent interactions on the FRET efficiency.

## **OVERALL HYPOTHESIS**

Structured, hybrid, workable fluorescent materials can still present manageable photophysical properties and perform Förster Resonant Energy Transfer in thin-film and solvent environments.

In order to understand the photophysical behavior of donor and acceptor systems of anthracene derivative and perylenediimide nanohybrids in solution and thin-film, the following three aims will be completed.

Aim 1: Synthesis, characterization, and performance measurements of anthracene-polymer derivative, PDMS-anthracene.

Under Aim1, the proposed research initiates with synthesis of an anthracene functionalized polymer derivative. The novelty of this attempt is to create a fluorescent polymer with controlled thin-film formation via spin-coating techniques.

### *Hypothesis*

Characteristic structural properties and workability of material will be maintained after integration with organic fluorophores and use of anthracene as an energy transfer donor is maintained.

### *Rational*

Polydimethylsiloxane (PDMS) is a widely used polymeric organosilicon compound mainly due to its rheological properties. It is used as a surfactant and defoamer, a viscous component in limited slip differentials, medicine, and cosmetics. Most relevant however, is its use in soft lithography. It is a highly controllable material for spin coating applications and mold forming via flow delivery. It is therefore an ideal material to use for device creation such as that presented here.

The functionalization of the PDMS provides the fluorescent component of the complete donor system known as PDMS-ANT. A derivative of anthracene – 9-anthracenecarboxylic acid – is the component to be added via esterification to PDMS. In this system, PDMS acts as a backbone, while maintaining the optical properties of anthracene moiety even in thin film stage.

Aim 2: Synthesis, characterization, and performance measurements, PDI-silane (monomer) and PDIB-NP (siloxane nanoparticle)

Under Aim 2, the proposed research initiates with preparation of Perylene-3,4,9, 10-Tetracarboxylic Dianhydride Bridged Silsesquioxane (PTCDBS) and nanoparticle PDI-functionalized bridged siloxanes (PDIB-NPs). The novelty of this aim focuses on reducing the diameter of the functionalized nanoparticles and evaluate their photophysical performance as a monolayer thin film.

### *Hypothesis*

Reduction of TetraEthyl OrthoSilicate (TEOS) in reaction procedure and appropriate counter measure in catalyzing base will result in PDIB-nanoparticle diameter reduction. Particles will retain similar interparticle interactions as those found with pure silica nanoparticles and will behave well for monolayer formation via spin-coating techniques.

### *Rational*

As an extension of work completed by Rathnayake et.al, succeeding those of Abdul Wahab, PDIB NPs are to be created with a smaller diameter than previously synthesized<sup>17,22</sup>. The ideal size for such particles lies in the realm of 10 nm. This feat will present progress for hybrid organotrialkoxysilane nanoparticles.

Two key details that encourage the use of PDIB-silane for the acceptor moiety in this research are the achievable size of such particles and the high concentration of organic content. It has been shown that approximately 70% load has been achieved into the siloxane core, which significantly reduces unfunctional space in the particle volume; a vital characteristic for FRET communication<sup>22</sup>. The integration of such high organic content vastly improves upon quantum efficiencies of a stand-alone polymer<sup>24</sup>.

The PDIB nanoparticles are prepared using a modified Stöber method following the previous published procedure. The typical method implemented for particle formation is the hydrolytic sol-gel route, this reaction can be a base- or acid-catalyzed hydrolysis and condensation. Monomeric alkoxy silane precursors are used in aqueous solvent for the final result<sup>24</sup>. In this case, the acceptors were synthesized using base-catalyzed hydrolysis and condensation. The PDI silane precursor is hydrolyzed and condensed in the presence of tetraethoxysilane and ammonium hydroxide in anhydrous ethanol. The diameter of the particles is reduced by adjusting the concentration of the base, TEOS, and organotrialkoxysilane components.

The PDI silane precursor and PDI nanoparticles will be evaluated for FRET. The PDI silane shows better film forming ability compared to nanoparticles. Such films are easily applicable to the device design proposed and simplify production for a first attempt at performing FRET between the donor and the acceptor.

Aim 3: Investigate photophysical properties, quenching pathways and Förster resonance energy transfer viability of anthracene (donor) and PDI-silane (acceptor).

Under Aim 3, isolated and blended photophysical properties of donor and acceptor will be explored under solvent and dry thin-film conditions.

#### *Hypothesis*

Photophysical properties will show solvent dependency in both blended and isolated cases. Solvent polarity will have an impact on emission efficiency due to competing energy transfer pathways when solvent increases aggregation.

#### *Rational*

An expanded understanding of the photophysical and molecular interaction between PDI-silane and 9-anthroic acid has great value when considering energy transfer quality with and without aggregation and complex formation. This aim explores the concentration limits of such a system to determine the threshold for good FRET performance; if it is at all possible to induce. It should be possible to observe energy transfer at concentrations that do not induce self-aggregation of PDI-silane and avoid complex formation characteristic of static quenching. at higher concentrations it is very likely to see the formation of complexes that take over the quenching pathway of energy transfer and possibly completely quenching the donor and acceptor system. with such a diverse possibility of outcomes available in a solvent-based system it is also valuable to assess solid state performance. A thin-film will be able to provide a non-variable environment for the donor and acceptor to remain stable in one configuration. The stable configuration would be determined by the preparation solvent and time in said solvent.

Aggregation of perylene derivatives is well observed under high concentration conditions. Such is induced by the near-field attraction that the  $\pi$ -conjugated ring structures have to one another. When blended with a donor fluorophore, the competition between donor-acceptor and acceptor-acceptor attraction has potential to shift from the dominant  $\pi$ - $\pi$  stacking attraction that interferes with resonant energy transfer.

## DISSERTATION LAYOUT

This dissertation is presented in the form of eight chapters. The first containing a brief overview introducing the field of nanocommunication, the applications in which it holds promise, and the challenges with which modern research faces. Chapter I also contains relevant state-of-the-art information to ground the work for future analysis. This chapter is finally concluded with a compact discussion regarding the goals of the conducted research. Chapter II presents a thorough review of foundational literature and experimental methodology regarding most topics brought into question during the successive chapters. It deliberates most major findings regarding FRET functionality, application, and manipulation. Furthermore, it discusses the outbreak of nanocommunication research shows claim to support FRET as a significant contribution to the field. Chapter III initiates with experimental methods of photophysical analysis with explicit instruction for approach. It follows with synthesis procedures schemes derived and repeated in this work. From there, procedures for film formation are discussed. Chapter IV presents in detail all synthetic procedures conducted throughout this work. It begins with donor synthesis for anthracene derived polymers and ends with the acceptor synthesis procedures based on the perylene molecule. Chapter V explores the experimentation to form anthracene functionalized polymer as donors. It provides experimental results and discussion of iterative design and outcome. Chapter VI explores the experimentation of diameter reduction for perylene derived siloxane nanoparticles. It also provides experimental results and discussion of iterative design and outcome. Chapter VII reports on solvent-based work analyzing 9-anthracene carboxylic acid and perylene-3,4,9,10-tetracarboxylic dianhydride bridged silsesquioxane as donor acceptor pairs for Förster resonant energy transfer. This chapter also explores further quenching pathways found to inhibit the desired process. Chapter VIII finally concludes the results of all sections and summarizes the efforts of this work to provide potential for future experiments followed with guidance and recommendations for future application.

## CHAPTER II: BACKGROUND

As a next generation form of communication, Förster Resonance Energy Transfer has incredible potential for spatially confined and unique interface applications. To appreciate the unique characteristics of FRET, a complete understanding of its derivation and properties is useful. Chapter 2 will introduce the fundamental understanding of FRET and the current state of the art science that is being conducted within its realm.

### FOUNDATIONAL LITERATURE

#### FIELD OF FRET

The FRET phenomenon is a quenching process that can be employed for short distance communication. It was experimentally observed in 1949 by Theodor Förster where an intermolecular energy transfer was observed between rhodamine B and tryptaflavin<sup>25</sup>. FRET involves the transfer of excited state energy – in the form of an exciton from an excited molecule (donor) – to a ground-state molecule (acceptor). This energy transfer happens as a non-radiative transfer of energy, i.e. without emission of a photon. These molecules, acting as fluorophores, must be within close proximity – typically no more than 10 nm<sup>26,27</sup> – for an effective transfer to take place. The excited state lifetime of these fluorophores is best currently modeled as a statistically random event, which ranges between 2 ns and 1  $\mu$ s depending upon emission type. The introduction of quenching pathways to a fluorophores emission, such as FRET, increases the relaxation rate. FRETs energy transfer rate is in the range of 1 ps to 1 ns, which allows for significantly higher communication rates compared to other molecular communication techniques<sup>27</sup>.

Since the discovery of this phenomenon, the desire to apply its photophysical characteristics to many sensing applications has accelerated. Biosensors have been the main driving force of research as this field is comfortably equipped for dealing with fluorescent detection; yet diversification is still underway<sup>28</sup>. Molecular tagging methods are generally accepted and have been used for protein folding confirmation<sup>29-31</sup>, and high resolution near- and far-field microscopy<sup>13,32</sup>. These areas still lacking the potential complexity that a nanocommunication can envision. Research that will allow great expansion of application comes from the side of

computational modelling and material/nanostructure engineering. Molecular information processing has become a growing field of interest as binary molecular switches have been realized and could be handled with an optical approach<sup>33</sup>. FRET capable systems work strongly dependently on probability and environmental conditions, so ensuring reliability of such systems is a very complex task.

It has been shown that engineered implementation of optical antennas can enhance and control the emission of quantum source much like those of FRET<sup>9</sup>. Such work is likely to enable an overall more reliable device for molecular communication and bolsters the argument for the use of FRET in such a task. There are however more passive methods to improving signaling when dealing with FRET communication. Orientation of the molecule dipoles plays a significant role in signal transfer strength and must be accounted for when considering a reliable network or when FRET is implemented for intensity analysis<sup>15</sup>.

Structure and properties of surrounding materials has also been a focus of study for physics-based research regarding FRET measurements and enhancement. It has been shown that physical field confinement of the FRET distance via nanoantennas have increased the FRET rates<sup>34</sup>. These nanoscale devices are designed to concentrate optical fields in the immediate vicinity of the FRET molecules. However, this is a device tailored for a single FRET pair and requires precise fabrication techniques. Larger FRET efficient structures have also been attempted to provide multiple donor-acceptor pairs within one system<sup>10</sup>. These systems still remain complex to fabricate as monolayers of quantum dots were required to be arranged into tri-layer structures. These systems and studies also revolve solely around metallic and inorganic materials<sup>35,36</sup>. Experimental and theoretical work has not been shown in the realm of FRET capable organic molecules with similar procedure.

For the advancement of current efforts with regards to FRET implementation for molecular communication, experimentation should be focused on addressing key components, which include: (1) device components must be of sufficiently small enough dimensions in order to reliably function; (2) the best reliability for a device will come from first polarizing the system, and by implementing all possible signal enhancement techniques appropriate; (3) an intelligent design of such device would have redundancy built in to recover from signal decay. Targeting to

improve these key concerns, this proposal research will focus on developing a novel donor-acceptor system and design an efficient FRET communication device with a support of theoretical analysis. Devices will be designed to enhance signal where possible and reduce probability of systematic signal loss. The aim is therefore to set a foundation for a real, sophisticated communication device capable of more complex and reliable data transfer. A valuable effort of research comes from targeting reliability of such materials used in energy transfer sensing applications. Currently, this can only be performed by testing such materials directly and in sequence.

Such materials used for FRET, or alternate pathways, are typically organic fluorescent dyes. Rhodamine is used often for its high quantum yield and tunable emission wavelengths through derivatives like Atto550 and Atto467N<sup>9</sup>. These derivatives have also been popularized for their ease of tagging DNA. Such methods have become a popular technique for maintaining and controlling separation of donor and acceptor as the DNA scaffold has also become a tool via DNA origami research. There is also a significant overlap with materials used for organic solar cells as the same photophysical properties are useful for FRET. Perylene is a valuable material to the solar cell field due to its chemical, thermal, and photochemical stability<sup>17,37,38</sup>. Those same properties make such a material competent for use in energy transfer sensing environments.

#### DYES AND DERIVATIVES

Interest in quenching dynamics of perylene dyes is periodic and has been spread over multiple decades. Early work aimed to identify single mechanisms under strict and controlled environments. These experiments showed strong efficacy of perylene dodecyldiimide as a strong quencher of various  $\pi$ -electron donors. Unusually high rates of static quenching were measured for the time and they were attributed to the Perrin model and singlet excited state electron transfer<sup>39</sup>. More modern applications of the perylenes strong quenching properties have been used for molecular sensing. A conjugated microporous polymer based on perylene tetraanhydride bisimide has been used to selectively sense for the presence of o-nitrophenol<sup>40</sup>. The mechanism utilized for such application was again electron transfer. The work determined that it was a combination of dynamic and static quenching that made quenching between acceptor and donor so dominant in the case of o-NP, over other quenching species.

There is a continuing effort to produce derivatives of perylene diimides in highly soluble forms. The methods for such typically called for substitutions to the imide with hydrocarbon chains and branches<sup>1,21</sup>. Such modifications allowed the previously very low solubility of PTCDA to become a material readily dissolved in common solvents such as hexane, chlorobenzene, chloroform and toluene<sup>41</sup>. Through creating such a versatile material some negative properties remained. Aggregated states for many organic dyes induce energy dissipation known as “aggregation caused quenching” (ACQ)<sup>42</sup>. What great photophysical properties PDIs once had were becoming less effective once concentrations induced aggregations to form. Efforts have been made to reduce aggregation with long -chain secondary alkyl groups which promote solubility and in turn deter aggregation<sup>21,43</sup>.

Aggregation is well understood to affect photophysical properties of materials and work is being done in both solid state and solution environments to understand its conflicts with energy transfer also. H- and J- aggregates have been studied in the solar cell environment to determine how tunable and to what affect these assemblies can have upon optical absorption, fluorescence, and excited state lifetime. It was found that j-type aggregates have a significantly superior photovoltaic performance over identical electronically structure h-aggregates<sup>44</sup>. It was determined that the improved photovoltaic properties were derivative of faster charge generation allowed by the more efficient exciton diffusion that j-aggregates have over h-aggregates.

A recent study analyzing the consequence of aggregation for BODIPIY-based fluorescent dyes explored the solvent and concentration dependence upon spectrum shape and intensity<sup>45</sup>. It was determined that concentration plays great significance in aggregation and could be used to tune fluorescence color, if so intended. BODIPY derivatives have been a focus for fluorescent chemosensors for some time as fifteen years prior to the aggregation study they were being analyzed for the solvent and pH dependent fluorescent properties<sup>46</sup>. The application for this work was to determine the viability of these derivatives for pH indication in acidic solutions.

Due to the modification of PTCDA for it to become highly soluble for a reasonable selection of solvents it is viable for use as a liquid phase sensor. This is on top of the advantageous weak intermolecular forces that PTCDA already is characterized to have<sup>47-49</sup>. These studies focused on 2-D structure and the resultant photophysical and optoelectrical properties associated with such

structures. Lesser attention has been paid towards nanoparticle derived PTCDA derivatives and the consequential photophysical behavior. A small section of research has considered nanoparticle, nanowire, and nanorod structures of PTCDA<sup>50</sup>, but this area is far from expansive. Current work typically concludes with observation as opposed to application advancements. This realm requires efforts in both categories. A leap towards practicality has yet to be taken. The efforts in this work attempt to resolve a small piece of this challenge and provide material research intent of resolving some practical limits of energy transfer for a PTCDA derivative.

## METHODOLOGY

### BASICS OF FÖRSTER RESONANCE ENERGY TRANSFER

Förster Resonance Energy Transfer can also go by the name of Fluorescent Resonance Energy Transfer. To understand FRET, it would be reasonable to break down each of its four words.

Fluorescence was first notably observed in 1560 by Bernardino de Sahagún. The phenomenon has a long history of aesthetic and scientific applications branching from terrestrial biofluorescence – a potential advantage for mating displays – to analytical spectroscopy: used for cell imaging<sup>51</sup>, compound identification<sup>52</sup> and targeted medicine<sup>53</sup>. As an approach to imaging, it is quite accurate and produces a relatively intense, easily detected emission. Advanced laser scanning fluorescent microscopes have axial resolution of 100 – 150 nm<sup>54</sup>. The resolution makes it quite a capable communication mechanism for 3-dimensional positioning.

For a fluorophore (fluorescent molecule) to fluoresce, the emitted energy is provided by an orbital electron in an excited singlet state relaxing to a ground state: this process produces a photon. An excitation can be presented with the following equation:



where  $S_0$  represent the ground state,  $h$  represents Plank's constant,  $\nu$  represents the frequency of light and  $S_1$  is the first excited singlet state. Using this same nomenclature, a fluorescence scheme can be written in the following way:

$$S_1 \rightarrow S_0 + h\nu_{em} + \text{heat} \quad (2)$$

The emitted photon ( $h\nu_{em}$ ) is typically of a lower energy than that of the excitation. This leads to a longer wavelength of that photon known as the Stokes shift.

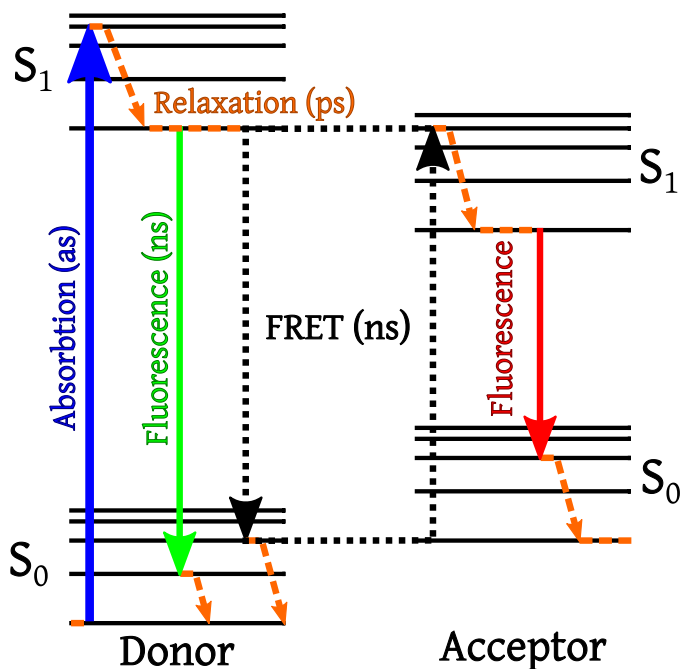


Figure 1 – Jablonski diagram of FRET. Provided by: [https://commons.wikimedia.org/wiki/File:FRET\\_Jablonski\\_diagram.svg](https://commons.wikimedia.org/wiki/File:FRET_Jablonski_diagram.svg)

However, this energy transfer gets much more interesting when the typical emission path is not taken. The initial excitation energy may have been provided by absorption of two photons; this would result in an emission wavelength shorter than the original radiation source. It is also possible to have a completely non-radiative energy transfer. This would be where the S<sub>1</sub> is transferred to another fluorophore entirely, and that is exactly what happens with FRET. As depicted in Figure 1.

When fluorescent resonant energy transfer is available, the excited state energy is transferred to a nearby, ground state fluorophore. This process happens non-radiatively and takes less than a nanosecond.

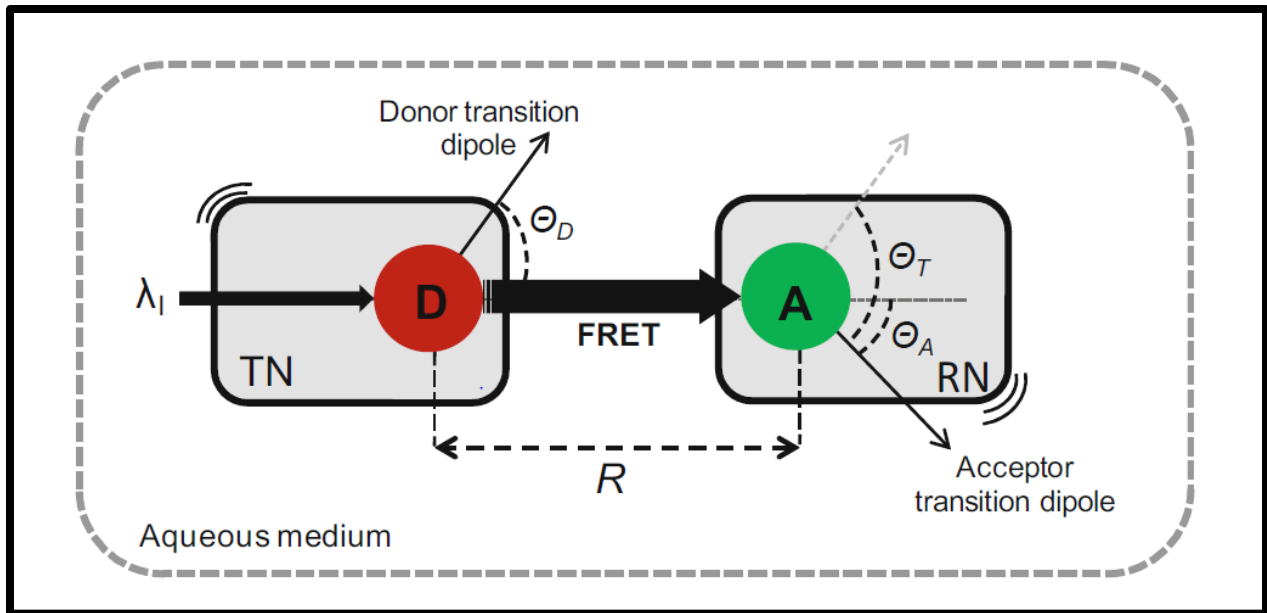


Figure 2 – Diagram of FRET transition dipoles. Source: M. Kuscü and O. B. Akan, “A nanoscale communication channel with fluorescence resonance energy transfer (FRET),” 2011 IEEE Conf. Comput. Commun. Work. (INFOCOM WKSHPs), pp. 425–430, 2011.

### Classical Electrodynamic Representation

As FRET is a non-radiative dipole-dipole coupling energy transfer there are many physical factors that affect its performance. There are in general three rules for effective FRET: 1) the distance between the optical centers of the donor and acceptor pair should be less than 10 nm, 2) there must be spectral overlap between the emission spectrum of the donor molecule and the absorption spectrum of the acceptor molecule, 3) optimal energy transfer depends upon relative orientation of the emission dipole moment for the donor and the absorption dipole moment for the acceptor.

Efficiency of FRET can be measured a couple of ways, but typically fluorescent lifetime measurements are made. Equipment is used to count the time a fluorophore remains in an excited state. In order to identify when FRET has occurred within a system a control is taken with a sample containing only donor molecules. A single peak should be produced resembling its emission. In a system containing donors and acceptors, there is an opportunity for FRET. It is not a guarantee however, so some donor molecules will still fluoresce, and some acceptor molecules will fluoresce. This will produce a double peak in the fluorescence lifetime measurement. The efficiency can be calculated from the ratio of peak heights relative to the isolated donor sample.

Resonance can be described with analogy as it appears in many typical scenarios of modern life. The simplest would be coupled pendula. The relative maximum amplitude for coupled pendula can only be met at resonant frequencies. For both radiative and non-radiative transfer of energy to occur the emission spectrum of the donor and the absorption spectrum of the acceptor must overlap. The key difference is the dependency upon distance between the two fluorophores ( $R$ ). FRET is a near field electromagnetic interaction; requiring models using a mixture of real and virtual photons<sup>55</sup>. As a result, the inverse square law for the rate of radiative transfer cannot apply. The non-radiative transfer rate is proportional to the inverse of  $R$  to the sixth power.

The efficiency of FRET is defined by the fraction of energy that is passed on to the acceptor, having previously been absorbed by the donor. This energy is typically measured by photon count and the expression for efficiency can be represented in by the following:

$$efficiency = E = \frac{R_0^6}{R_0^6 + R^6} \quad (3)$$

Where  $R_0$  is the Förster distance, and  $R$  is the distance between the centers of the fluorophore dipole moments. The Förster distance is defined as the distance were the energy transfer efficiency is at 50%<sup>56</sup>.

The Förster distance can be calculated using an overlap integral of the donor emission spectrum and the acceptor absorption spectrum. This combined with the mutual molecular orientation is used to create the following equation:

$$R_0^6 = \frac{2.07}{128\pi^5 N_A} \frac{\kappa^2 Q_D}{n^4} \int F_D(\lambda) \epsilon_A(\lambda) \lambda^4 d\lambda \quad (4)$$

here,  $N_A$  represents Avogadro's constant,  $\kappa^2$  represents the dipole orientation factor,  $Q_D$  represents the quantum yield of the donor fluorescence,  $n$  represents the medias refractive index<sup>57</sup>.

The dipole orientation factor needs further expansion; it can be given by:

$$\kappa = \hat{\mu}_A \cdot \hat{\mu}_D - 3(\hat{\mu}_D \cdot \hat{R})(\hat{\mu}_A \cdot \hat{R}) \quad (5)$$

here,  $\hat{\mu}$  represents the normalized transition dipole moment and  $\hat{R}$  represents the normalized inter-fluorophore displacement. In standard cases, it is fair to assume that  $\kappa^2$  is equal to  $2/3$ . This can happen when both the donor and acceptor are freely rotating, and isotropic assumption can be made. It is also important to add that the greater contributing variable to  $\kappa$  is  $R$ <sup>58</sup>.

Dipole alignment is a key piece of the proposed work and can be manipulated in an accessible way for a thin-film device. The standard electric dipole moment can be easily calculated via the following:

$$p = qd \quad (6)$$

Where,  $q$  represents the charge of the pole and  $d$  represents the distance between the dipoles<sup>59</sup>.

To vary the electric dipole moment, an object can be subject to torque. This torque is provided by an external electric field. If the  $E$  field is strong enough, it will align the dipole with the direction of the field<sup>60</sup>. For a uniform electric field, the torque can be calculated via the following:

$$\boldsymbol{\tau} = \mathbf{p} \times \mathbf{E} \quad (7)$$

For application however, care is only really given to make sure the electric field is strong enough to provide high dipole moment alignment.

Fluorescent measurements can also be used to identify FRET efficiency and computed using the following:

$$E = 1 - \frac{F_{DA}}{F_D} \quad (8)$$

Where  $F_{DA}$  represents the fluorescence intensity of the donor in the presence of the acceptor, and  $F_D$  represents the fluorescence intensity of the donor in the absence of the acceptor.

## PHOTOPHYSICS

### Dynamic quenching

Dynamic quenching occurs in the excited state of a molecule. The environment has strong effect on the rate in which quenching occurs. An increase in ambient temperature will cause an increase in the rate of dynamic quenching. Dynamic quenching is active in solution hence, when more energy is provided to the motion of molecules, the chance of collision increases. The result of this seen through a spectrofluorometer, is a decrease in fluorescence intensity as temperature increases. observations to the excited-state lifetime and absorption spectrum are important to note. The excited state lifetime of a molecule can be changed through dynamic quenching whereas the shape and magnitude of the absorption spectra will remain a constant.

### Static Quenching

Static quenching begins in the ground state of a molecule. It is introduced to a system when non-excited molecules form complexes that have strong coupling due to orbital interactions. Environment plays a significant role again as it did with dynamic quenching. Temperature will decrease the rate of static quenching as complexes will be less likely to form. The solvent used will also have a significant effect on complex formation as most dyes are induced into aggregation through hydrophobic interaction. Qualitative measurements of such characteristics can be made with UV-vis spectroscopy. Complex formation can be observed through distortion and peak shifting of the absorption spectrum. Not surprisingly, excited state lifetime measurements are of no use in this case as photonic emission does not occur with complexed molecules and the free molecules have no change to their excited state lifetime.

### Energy Transfer

A short yet comprehensive description of energy transfer mechanisms can be taken from the book: *Structure and Dynamics of Macromolecules* by J. Albani<sup>61</sup>.

$D + h\nu_0$	$\rightarrow$	$D^*$	Absorption
$D^*$	$\rightarrow$	$D + h\nu_1$	Fluorescence
$D^*$	$\rightarrow$	$D$	Non-radiative deexcitation
$D^* + A$	$\rightarrow$	$D + A^*$	Energy transfer
$A^*$	$\rightarrow$	$A$	Non-radiative deexcitation
$A^*$	$\rightarrow$	$A + h\nu_2$	Induced fluorescence

These mechanisms form the foundation of quenching fluorescence. They can be applied to simple, single-moiety systems or complex, multi-moiety systems with energy transfer interactions across many species. Energy transfer is a subset of dynamic quenching. The other two processes which generally complete the category of dynamic quenching are electron transfer and electron exchange. Coulombic energy transfer does not rely upon the transfer of an electron as the packet of energy. In the case for Förster resonance energy transfer, the packet of energy is said to be a virtual photon. the energy is transferred through resonance coupling, also known as dipole-dipole coupling. This transfer between the donor and the acceptor needs two simultaneous transitions. these transitions are the non-radiative deexcitation of the donor and the non-radiative excitation of the acceptor. the rate that this energy transfer can occur is dependent upon the oscillator strength of the radiative transitions. FRET only occurs in the singlet-singlet state whereas mechanisms that exchange electrons can occur in singlet-singlet or triplet-triplet. The name Dexter energy transfer is given to such mechanism of electron exchange.

#### FRET lifetime

The excited state lifetime is a very literal title and describes the period of time before deexcitation of an excited molecule. It is not generally experimentally convenient to obtain single molecule lifetime measurements, so the numerical evaluation of lifetime is a mean time during which observed molecules are in an excited state. Fluorescence lifetime is equal to<sup>61</sup>:

$$\tau_f = \frac{1}{k} = \frac{1}{(k_r + k_{isc} + k_i)} \quad (9)$$

were  $k_r$  is the radiative rate constant,  $k_{isc}$  is the intersystem crossing rate constant, and  $k_i$  is the internal conversion rate constant.

The excited state lifetime of a donor and acceptor pair is a very telling characterization technique for identifying FRET. In the ideal case, a delay to the fluorescence emission of the acceptor will be observed due to the extra steps needed for the initial energy source to excite the acceptor. this delay may be only a few nanoseconds but, when compared to the directly excited acceptor, it is significant.

Figure 1 presents the Jablonski diagram for resonant energy transfer. It is important to note that fluorescence and FRET take place within similar time frames. Both processes can occur within nanoseconds. The energy transfer occurs from the lowest energy excited state; just as the fluorescence occurs for the non-quenched donor.

#### MOLECULAR ORBITAL COMPUTATIONS

Molecular orbital calculations are a strong tool for subsidizing and interpreting experimental results. Open source and proprietary software exist for making approximate calculations for multiple characteristics of molecules. This work uses Density Functional Theory (DFT) to minimize the energy of an input file built from Cartesian coordinates dictating the position of every atom in the given molecule. The calculation goes through an iterative process to minimize the structural energy, cycling until self-consistency. This method of calculation will provide the total energy of the molecule, the molecular orbitals, and the orbital energies. This work uses Gaussian to find HOMO and LUMO energy levels of the donor, 9-anthroic acid, and the acceptor, PDI-silane.

There are known failures of DFT computations and one of those is its competency with extended  $\pi$  conjugation. There is likely significant underestimation of molecular HOMO-LUMO band gaps resulting in such molecules being treated metal-like<sup>62</sup>. It appears that the current best practice for obtaining results closer to experimental values is to artificially increase the gap<sup>63,64</sup>. These

downfalls are addresses using Time Dependent-Density Functional Theory (TD-DFT)<sup>65</sup>. TDFT is very capable of predicting low-energy excitation transitions.

## MATERIALS

### Aggregation

Aggregation is the attraction and formation of assemblies of molecules in suspension of a liquid. these assemblies can form homoaggregates – caused via aggregation of like molecules – and heteroaggregation – caused via aggregation of dissimilar molecules. the rate of aggregation can be determined in homo and hetero systems and is typically denoted with a ‘*k*’. How molecules in the aggregate pack to one another can determine properties of the resultant structure. two types of aggregates that express variable photophysical properties to their monomer counterparts are J- and H-aggregates.

J-aggregates are driven by hydrophobic and  $\pi$ -stacking interactions. A predominantly head-to-tail arrangement of monomers cause j-type aggregation, and it results in the relative alignment of the transition dipole moments for the adjacent molecules. These interactions induce changes in the electron distribution for each constituent molecule resulting in a shift to the light absorption spectrum. When compared to the monomer absorption spectrum, a j-aggregate will produce a red-shifted absorption peak. Driving forces for such structures are typically high concentration environments. j-aggregates retain the fluorescent properties of the monomer molecule.

H-aggregates are built upon similar principles as those of J-aggregates. The crucial difference between these types is the dominance of face-to-face stacking found in h-type aggregates. this stacking pattern forms a non-fluorescent complex and results in an absorption spectrum shifted blue.

The shifts in absorption spectra are dependent upon the gap between the highest occupied molecular orbital (HOMO) and lowest unoccupied molecular orbital (LUMO). a blue shift would mean that this gap has expanded, and a red shift would mean the gap has shrunk. The variation in orbital energies is derived form the relative orientations of the molecule transition dipole which in turn varies the frequency of electronic excitations. When two monomers come together a

superposition must be created for the eigen states that describe the resultant dimer. With equal transition frequencies and parallel dipole moments only one of these superposition states is allowed. Figure 3 presents these superpositions states for (A) a blue shifted dimer configuration and (B) a red shifted dimer configuration. These states relate to H- and J-aggregates, respectively.

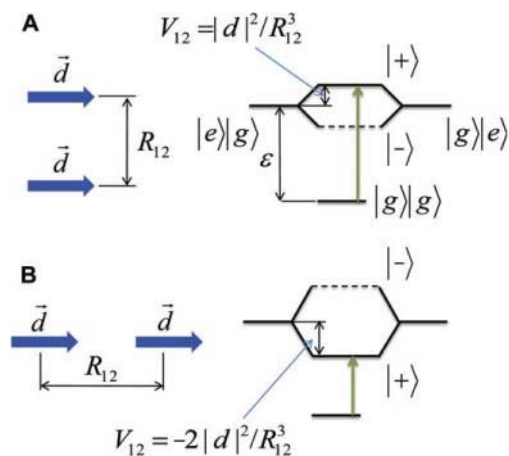


Figure 3 – Dipole alignment energies for two dimer conformations. Source: Saikin, S. K.; Eisfeld, A.; Valleau, S.; Aspuru-Guzik, A. *Photonics Meets Excitonics: Natural and Artificial Molecular Aggregates*. *Nanophotonics* **2013**, 2 (1), 21–38. <https://doi.org/10.1515/NANOPH-2012-0025>.

## Particles and siloxanes

Dye-loaded nanoparticles designed to retain energy transfer mechanisms do exist in current literature. Motivation for such work is found with the stability and workability of such products whilst retaining the majority of preferential photophysical properties. There does not appear to be a comprehensive literature base for dye loaded particles regarding FRET. Similar research experiments have observed quantum dots tagged with dye terminated peptides have been used to understand energy transfer mechanisms of hetero- and homo-FRET for monomer and dimer acceptors<sup>66</sup>. Although similar in many ways, equating a dye loaded siloxane nanoparticle to a quantum dot for energy transfer studies ignores crucial surface chemistry properties and quenching pathways. Organic fluorescent dyes integrated into a particle framework still retain potential  $\pi$ -bonding properties and conjugation variations under environmental stress. They are potentially a more variable system and require a separate experiment effort.

Particles also compete with traditional thin-films as they can form into monolayers. The differences between the two come when comparing surface area and uniform smoothness. Particle monolayers have holes between each sphere and maintain a varying surface contour. This can produce a surface that is more difficult to interact with or make a surface have a greater number of interaction sites.

### Thin-films and polymers

The term 'thin-film' presents itself in a vast variety of application and experimental topics as the diversity of materials and conformation branch the complexity tremendously. From modified and patterned PDMS intent of creating hydrophilic surfaces<sup>67</sup>, to plasmon coupled nanoparticle monolayers capable of plasmon coupling to resonant energy transfer pathways<sup>10</sup>, there are many reasons for the term to be found in literature. The popularity of use could be attributed to the variety of methods available for production and the practical dimensionality. Thin-films have potential to mimic both one- and three-dimensional properties, dependent upon orientation. Two derivatives of thin-films were used for this work; one being an organic spin-coating and the other being metallic films formed via physical vapor deposition (PVD).

Spin-coating is a widely used technique as it is capable of forming quick and uniform films. In principle it consists of a spinning substrate to which material is applied to, and then centripetal forces and surface tension distribute and thin-out the material over the substrate. It is a very reliable technique that can be dialed to produce thin-films of consistent thickness time and time again. Different spin speeds and material viscosity are variables used to control thickness. A faster angular speed will thin the film more and so will a lower viscosity material. When using a liquid film material, solvent can be added to reduce viscosity. In the case of solids, the concentration of the solvent-solid solution can be varied. The higher the solution concentration typically the more material deposited on the substrate. This technique is highly sensitive to the substrate cleanliness. Physical debris and foreign chemicals on the surface will cause imperfections as the film-forming material passes over them. As a technique used in the silicon chip manufacturing process, there has been valuable development of surface cleaning procedure. Silicon wafers are a common substrate and use a method of cleaning known as RCA clean. This process strips the surface of metal ions and leaves an oxide layer of protection. In combination with deionized water washes

and ozone or plasma cleaning, a very clean surface can be achieved. Modifications to the RCA clean procedure can be made for other substrate materials that may need less aggressive chemical treatment. When done correctly, spin-coating is capable of producing pristine films inches in diameter and only nanometers thick.

Physical vapor deposition is another method of film creation that can boast such disparities between dimensions also. This process is more suited to metallic films, as it uses a plasma arch to evaporate raw metals and guide them to an electrically charged target. The process is done in vacuum and uniformity of the film is dependent upon the quality of the vacuum. This technique can also be used to cover 3-dimensional objects using a rotating stage as long as there is direct line of sight between the source and the target's surface. PVD is capable of layering sub-nanometer films with a slow enough evaporation rate and an ultra-high vacuum.

## CHAPTER III: EXPERIMENTAL METHODS

### PHOTOPHYSICS

#### FRET EFFICIENCY MEASUREMENT

There are four well accepted methods of experimental FRET efficiency measurement; each one has their own complexity and limitations. The most accurate, yet least practical, is through measurement of quantum yield of the Donor and then the Donor/Acceptor blend. The efficiency is expressed using the following equation:

$$E = 1 - \frac{QY_{DA}}{QY_D} \quad (10)$$

where  $QY_{DA}$  represents the quantum yield of the donor and acceptor blended specimen and  $QY_D$  represents the quantum yield of the donor specimen alone. Quantum yield measurements are difficult to perform as they require low absorption values that exists preferably between 0.02 and 0.07. For dynamically interacting samples in solution, this can be difficult to acquire when a typical cuvette cell length of 10 mm and concentrations of 10-1000  $\mu\text{M}$  are required.

Fluorescence lifetime can be used to characterize FRET efficiency in a very similar manner. Lifetime is typically independent of concentration. This makes the approach resistant to experimental preparation errors. The equation for efficiency is as follows:

$$E = 1 - \frac{\tau_{DA}}{\tau_D} \quad (11)$$

where  $\tau_{DA}$  represents the lifetime if the donor and acceptor blended specimen and  $\tau_D$  represents the lifetime of the donor specimen alone. This technique can also avoid the strict low concentration limit set for the quantum yield method.

Thirdly, measurement of energy transfer efficiency can be made from the acceptor emission. This method is the most convoluted of the four as two instruments and five spectra are needed for its completion. The equation for efficiency is as follows:

$$E = 1 - \frac{I_{AD}A_{AA} - I_{AA}A_{AD}}{I_{AA}A_{DD}} \quad (12)$$

where  $I_{AD}$  is the intensity of the acceptor using direct donor excitation,  $A_{AA}$  is acceptor absorption at the acceptor excitation wavelength,  $I_{AA}$  is acceptor intensity using direct acceptor excitation,  $A_{AD}$  is acceptor absorption at donor excitation wavelength and  $A_{DD}$  is donor absorption at the donor excitation wavelength. As presented in this form, this method is the most labor intensive and impractical if excitation of the acceptor cannot be done outside of the donor's absorption band.

The final method of FRET efficiency measurement can be described as a ratiometric efficiency. This is a qualitative measurement as it relies upon donor and acceptor intensities alone. It is also a measurement technique that requires the most additional corrective factors. Its appeal is the simplicity of initial instrument use and broad requirements for sample preparation parameters. The equation for this technique is as follows:

$$E_{rel.} = \frac{I_A}{I_D + I_A} \quad (13)$$

where  $I_A$  is the total acceptor intensity and  $I_D$  is the total donor intensity. Both values are taken after donor excitation. In this state, donor and acceptor spectra are assumed not to overlap. If overlap is present, then decomposition of the spectra is needed to correctly attribute intensity to the correct components.

This final method can be used to calculate a true efficiency with some minor modifications. Firstly, one must consider the direct excitation of acceptor by the donor's excitation wavelength. This is measured using a reference acceptor sample of identical concentration. Secondly, the ratio of quantum yield between in donor and the acceptor is needed to appropriately adjust the intensity spectra for each.

#### Relative Efficiency Via Spectral Decomposition

For this work a modified version of method four is used to compute relative FRET efficiency along with the further quantum yield corrections to determine a true efficiency value, where applicable.

From this point on, specimens that contain both acceptor and donor fluorophores will be referred to as blend. References to donor and acceptor samples indicate single moiety specimens.

The initial equation form for the relative FRET calculations is as follows:

$$E_{rel.} = \frac{I_B}{(I_D + I_B)} \quad (14)$$

where  $I_B$  is the total intensity of the blended sample and  $I_D$  is the total intensity of the donor sample. This equation works only when in reality the donor is completely quenched in the blend sample. Experimentally, this has been rarely the case, so the following equation is modified to account for radiative excitation.

$$E_{rel.} = \frac{(I_B - I_A)}{((I_B - I_A) + I_D)} \quad (15)$$

where  $I_A$  is the total intensity of the acceptor sample. This modification accounts for excitation and radiative emission left over from the donor moiety and direct excitation of the acceptor moiety causing radiative emission.

The final modification needed to complete accuracy of this measurement technique is to address the emission overlap between the donor and acceptor. Because of the nature of fluorescent spectroscopy measurements distinction of overlapping spectra is sometimes obscured. The method applied in this case results in a calculation that most biased towards eliminating all radiative emission from the donor artificially increasing the acceptors emission intensity at each overlapping wavelength. The following equation presents that modification:

$$E_{rel.} = \frac{(I_B^{\lambda_h} - I_A^{\lambda_l})}{((I_B^{\lambda_h} - I_A^{\lambda_l}) + I_D)} \quad (16)$$

where  $\lambda_l$  and  $\lambda_h$  represent the low and high integration bounds of the associated spectrum. These bounds are determined by the end wavelength of the acceptor absorption and the end wavelength of the absorption emission.

## QUANTUM YIELD

Quantum yield (QY) is a valuable tool used to determine the effective number of molecules that produce fluorescent light when compared to the number of molecules that were initially excited. Quantum yield is a complex relationship of multiple rate constants that are often never measured individually. The general expression for QY ( $\varphi_F$ ) is as follows:

$$\varphi_F = \frac{k_F}{k_F + k_{IC} + k_{EC} + k_{ISC} + k_C} \quad (17)$$

where  $k_F$  is the rate constant for Fluorescence,  $k_{IC}$  is the rate constant for Internal Conversion,  $k_{EC}$  is the rate constant for External Conversion,  $k_{ISC}$  is the rate constant for InterSystem Crossing and  $k_C$  is the rate constant for any other Competing processes.

## STERN-VOLMER

Although in this work dynamic quenching process is desired to be observed and understood, it is very likely that static quenching will play a significant role and appear in cases where a high concentration of fluorophores are used. Static quenching is common when complexes or aggregates are formed. When this process takes place at the ground state, non-fluorescent complexes are formed that outcompete dynamic quenching entirely<sup>61</sup>. The set of equations that describe the physics of static quenching are as follows:



where  $F$  denotes the fluorophore,  $Q$  denotes the quencher, and  $FQ$  denotes the complexed form of both. It is of course possible that the complex be comprised of only one type of molecule.

The next equation derives a constant that can be determined from a ratio relationship between these three components. In a closed system, the ratio of the concentration of the complex to the combined concentration of the fluorophore and quencher should be constant.

$$K_a = \frac{[FQ]}{[F]_1[Q]_1} \quad (19)$$

Here, the brackets denote concentration of the value enclosed and the subscript of '1' denotes free/available moiety. One can also describe the total fluorophore concentration in the following way:

$$[F]_0 = [F]_1 + [FQ] \quad (20)$$

where the subscript of '0' denotes a total count of all reference components in the system. Equation (9) and (20) can then be combined to form equation (21).

$$\frac{[F]_0}{[F]_1} = 1 + K_a[Q]_1 \quad (21)$$

Two final modifications can be made to equation (21) for practical use. Firstly, concentration of the fluorophore is proportional to the intensity of fluorescence when considered as a ratio between total and free components. Secondly, it can be possible to assume that the number of quencher molecules involved in the complex is proportionally very small to this free in the system. Applying these two modifications results in the final equation below.

$$\frac{I_0}{I} = 1 + K_a[Q] \quad (22)$$

A trial of a few different concentration blends with fluorophore and quencher can quickly lead to a plot capable of providing the association constant  $K_a$  when the slope of the linear fit is found of the data.

## MOLECULAR ORBITAL COMPUTATIONS

Geometry optimization calculations were performed with Gaussian in order to optimize geometry of input molecules. Geometry optimization was calculated for no solvent, THF and chloroform. molecules computed were 9-anthracic acid and PTCDA. PDI-silane was attempted but failed to pass self-consistency iterations. The model chemistry used for these calculations was a ground state DFT calculation using the functional B3LYP. The calculations were run with the larger than minimum basis set 6-31G. No polarization was added nor a diffuse function in order to save on computational expense. The molecules were assumed to have neutral charge and spin multiplicity

was singlet. Once an optimized geometry was found, TD-DFT was performed for single point energy optimization. Parameters of the basis set were reused from the geometry optimization calculations for consistency.

## **STÖBER PROCESS**

In this work, the Stöber process is used to form PDI-silane integrated SiO<sub>2</sub> nanoparticles. This process was originally reported in 1968 and is renowned for its controllable and monodispersed attributes<sup>68</sup>. This sol-gel reaction involves a single-step between the precursor of tetraethyl orthosilicate (TEOS) (Figure 4), and if so desired, another compatible derivative (Figure 5). In this case, PDI-silane is used to load the nanoparticle and provide photophysical attributes<sup>22</sup>. these precursors are hydrolyzed in ethanol and catalyzed by ammonia. precisely controlling quantity of catalyst and time of the reaction provides for particles sizes that range 30 to 2000 nm.

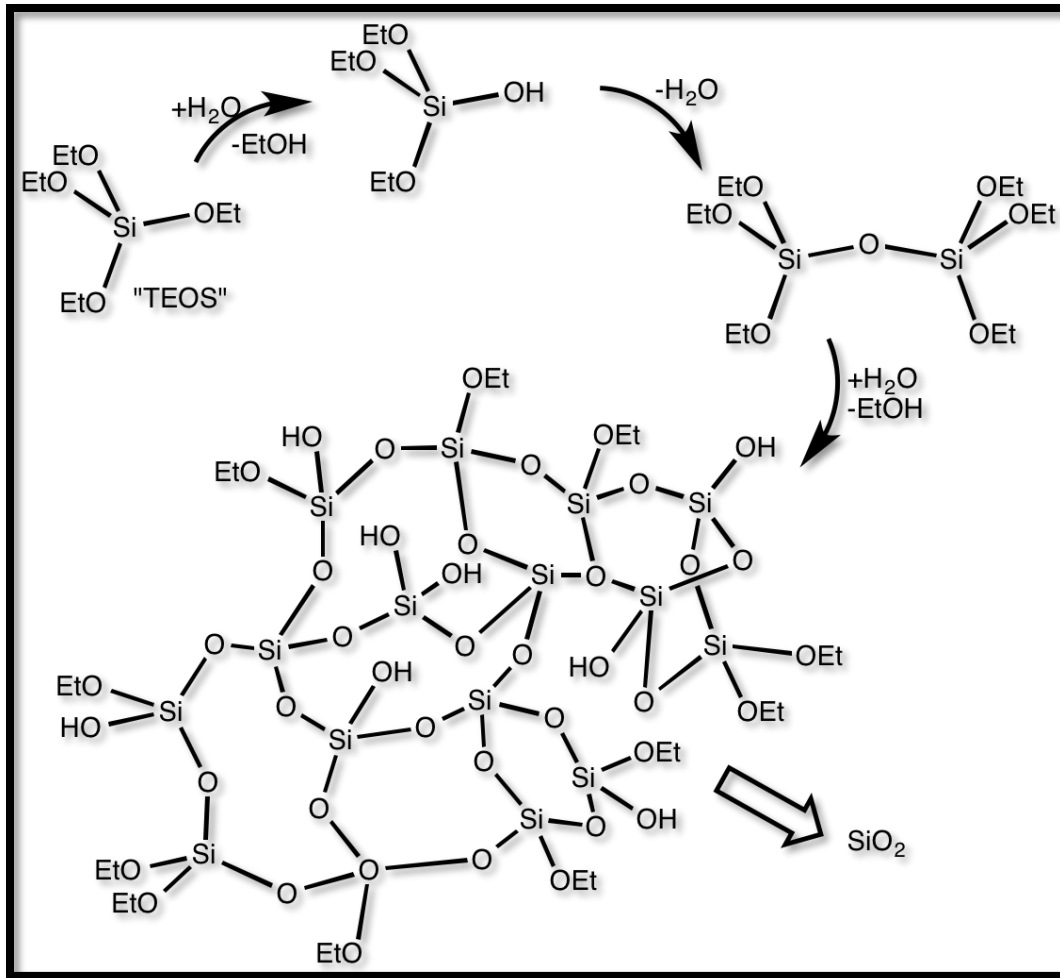


Figure 4 – General scheme for Stober process. Source: By Smokefoot – Own work, CC BY-SA 3.0, <https://commons.wikimedia.org/w/index.php?curid=25698603>

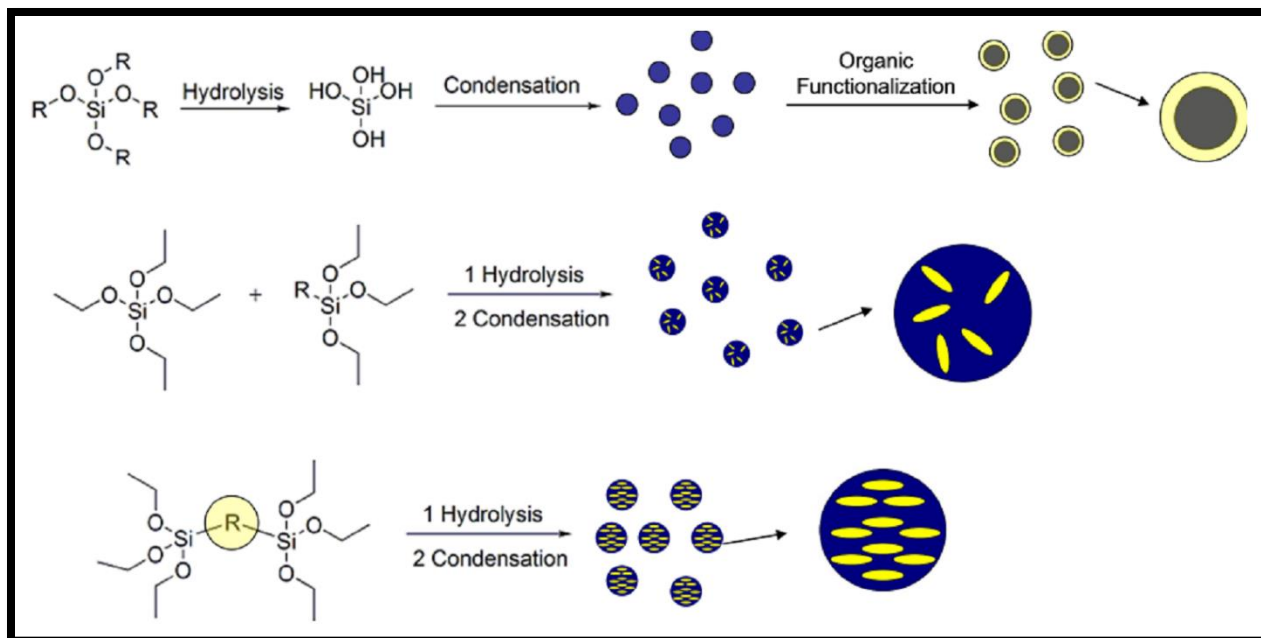


Figure 5 – Modified Stober process scheme

### STEGLICH ESTERIFICATION

Steglich esterification is an evolution from Fischer esterification. It is a mild reaction that can remove the water byproduct that results from the Fischer method. The carboxylic acid precursor and DCC mediator form O-acylisourea as an intermediate. This intermediate is then able to react with the alcohol precursor species to form the ester and stable dicyclohexylurea<sup>69</sup>. The reaction scheme is simplified here in and Figure 6.

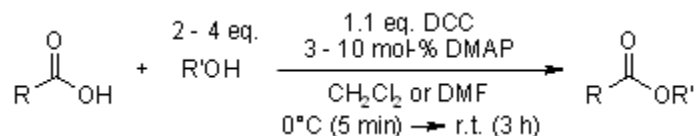


Figure 6 – Steglich esterification reaction scheme. Source: B. Neises, W. Steglich, *Angew. Chem. Int. Ed.*, 1978, 17, 522-524.

The application of this reaction to successfully form esters is significantly helped through the use of DMAP as an accelerator due to being a stronger nucleophile than the alcohol species in the intermediate stage.

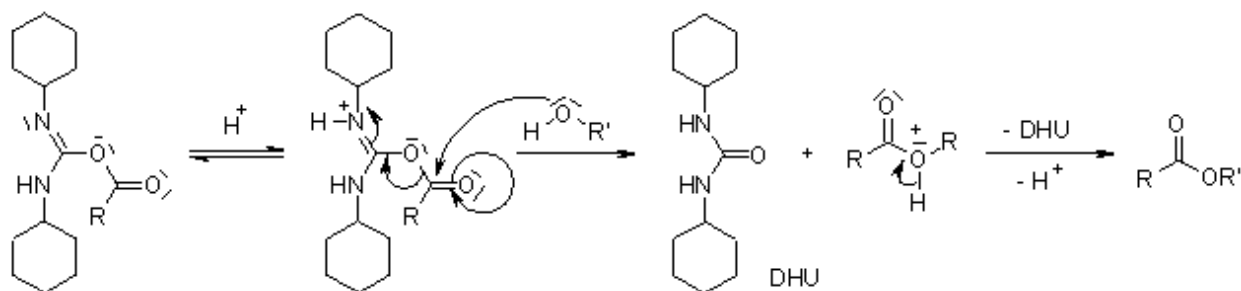


Figure 7 – DMAP acceleration with Steglich Esterification. Source: <https://www.organic-chemistry.org/namedreactions/steglich-esterification.shtm>

The action of DMAP in the Steglich esterification is pictorially represented in Figure 7. here, DMAP is an acyl transfer agent in this role. it then reacts with the alcohol created from the DCC intermediary and finally allows the ester to form.

## FILM FORMATION

There are many acceptable methods for assembling thin-films of nanoparticles. Most use convective assembling techniques which include dip-coating<sup>12,70-72</sup>. these methods are controlled by the rate of lifting of the substrate out of the solvent. These techniques are therefore very reliant upon the quality of the machine doing the lifting. A precise and steady rate of lift provides the best quality film. another technique for thin-film formation is Langmuir-Blodgett (LB). This method also uses very precise equipment to provide controlled surface tension with which the film is formed<sup>73-75</sup>.

## SPIN-COATING

Some of the best monodispersed silica nanoparticle layers that have been provided in literature have been produced through a two-step process<sup>76</sup>. the success of such process is mildly associated with particle diameter but significantly dependent upon centrifugal and capillary forces associated with the particles and solvent. The first step of spin coating is designed to balance the forces of centrifugal and capillary with the intention of forming a wet monolayer. the second stage acts as a cleaning and drying process. material that is not needed to complete the monolayer area coverage is thrown off the substrate. the high rpm also rapidly dries the substrate which further encourages the particles in the monolayer to compact together. These steps are presented in Figure 8.

A significant step in the process not discussed in the published work of monolayer spin-coating is the initial deposition of the material on the substrate. the question being, is the material deposited on a still substrate or is it cast while the substrate is spinning. respectively, these two options are labeled static and dynamic casting.

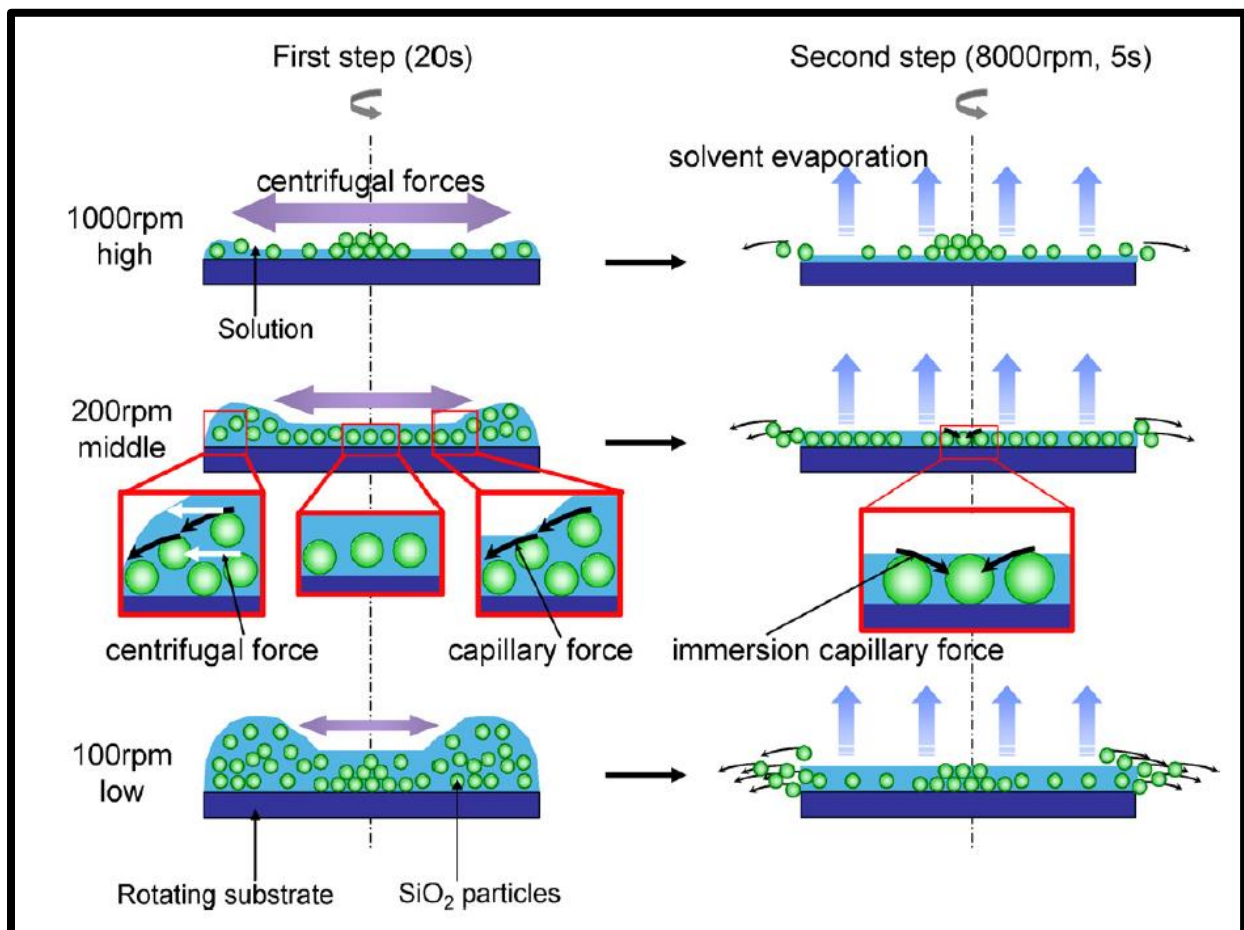


Figure 8 – Silica nanoparticle spin-coating protocol for monolayer formation. Source: T. Ogi, L. B. Modesto-Lopez, F. Iskandar, and K. Okuyama, “Fabrication of a large area monolayer of silica particles on a sapphire substrate by a spin coating method,” *Colloids Surfaces A Physicochem. Eng. Asp.*, vol. 297, no. 1–3, pp. 71–78, 2007.

### Dynamic Drop-casting

Dynamic drop casting is a method of material deposition used for spin-coating where the substrate is spun up to the first step operating speed before material is placed on the substrate. the rate of deposition is also important in this process as a forceful, therefore fast, stream of material can

improve substrate coverage. too forceful of a deposition on the other hand can eject too much material from the substrate before particles have time to form into a hydrated monolayer.

### Static Drop-casting

Static drop-casting has very similar complications to its process as compared to the dynamic equivalent. Static drop casting takes place prior to rotational acceleration of the substrate. the benefit of this method is that the substrate can be confirmed to be completely wetted before spinning begins. on the other hand, very volatile solvents can begin to dry before the first step of spinning can effectively distribute the particles. another variable with this method is the rate of acceleration of the substrate. Jerk of the spinning motion can disrupt uniform material distribution, so a variable acceleration of the substrate is required to achieve optimal results.

### LANGMUIR BLODGET

The Langmuir-Blodgett technique comes from a long line of experimental observations from Benjamin Franklin and Agnes Pockels. the name of the method describes the contraction used to mediate to surface tension and film distribution. this method typically using the interaction of polar molecules and water to form monolayer films on the surface of the water. once the material is monodispersed, a substrate can be lifted through the layer to collect upon its surface the ordered material. an interesting additional value that this method brings is the fact that both side of a thin enough substrate can be coating at once produced identical and mirrored coatings.

### SPRAY-COATING

Spray coating is a method of film-deposition the is commercially used for painting and similar colloidal or soliton film dispersion. It is very good for large area coatings but does lack the precise control of film thickness that other film deposition methods retain. in this method compresses air is used to produce a directed aerosol from a solvated material. the air gun's nozzle can be adjusted to increase concentration of the spray and distance from substrate can be varied to control the velocity of the material hitting the substrate.

### PDMS THIN-FILM LIMITS

Film thickness is crucial factor when establishing an energy transfer signal visible with standard photospectroscopy equipment. With FRET having a maximum effective range of 10 nm, a film

thickness of 100 nm may contribute to a 90% radiative emission signal obscuring relevant energy transfer emission. The best published work providing PDMS thin-film procedure achieves  $3.8 \pm 0.8$  nm, with a controllable process up to  $27 \pm 1.1$  nm<sup>67</sup>. This range was achieved through a thinning agent such as toluene or THF. Such is proof of potential to create an ideal donor thin-film but does not provide evidence that PDMS functionalization will allow for the same results.

## CHAPTER IV: SYNTHESIS PROCEDURES

### PI-ANTHRACENE

#### POLYMER-LINKER SYNTHESIS AND WORK-UP

##### MH001

To a 100 mL three-neck round-bottom flask, add 0.5 g of 6-bromo-1-hexanol and 1.2 equivalent weight of potassium hydroxide (0.19 g). Add 0.5 g of Poly[trimellitic anhydride chloride-co-4, 4'-methylenedianiline] to the solution. Add 40 mL of DMSO: in doing so, rinse the walls of the flask to wash all polymer into the solution. Seal all three necks of the flask and run the reaction overnight ( $\approx$ 20 Hours) at room temperature with a stir bar.

After the reaction has run for approximately 20 hours, use a rotary evaporator to evaporate the DMSO. Add acetonitrile to the solution and filter to remove the 6-bromo-1-hexanol. Leave to dry before storage. FTIR was performed for characterization.

##### MH002

To a 100 mL three-neck round-bottom flask, 6-bromo-1-hexanol (0.5 g, 2.76 mmol), 1.2 equivalent weight of potassium hydroxide (0.19 g, 3.39 mmol), and Poly[trimellitic anhydride chloride-co-4, 4'-methylenedianiline] (1.0 g) were added. Followed by addition of DMSO (40 mL), the flask walls were rinsed well into the reaction solution. The reaction was sealed using a silicone septum and left to stir at room temperature over 30 hrs.

The reaction was stopped after 30 hours of stirring and concentrated in the rotovap. The resultant dark orange solution was precipitated in acetonitrile by adding  $\approx$ 25 mL acetonitrile. The orange-yellowish solid was collected by gravity filtration and dried in air in the hood to yield 1.27 g of the final product. The product was characterized by proton-NMR and confirmed the successful functionalization. FTIR was performed for further characterization.

## ANTHRACENE-LINKER SYNTHESIS AND WORK-UP

### MH003

To a 100 mL round-bottom flask add: 0.5 g (2.25 mmol) of 9-anthracene carboxylic acid, 1.2 equivalent weight of DCC (0.56 g, 2.71 mmol), 1.2 equivalent weight of 6-bromo-1-hexanol (0.49 g, 2.71 mmol), 4-5 crystals of DMAP ( $\approx 20$  mg), and 40 mL of DCM. Seal the neck of the flask and run the reaction overnight ( $\approx 20$  Hours) at room temperature with a stir bar. Wrap flask with aluminum foil as reaction is light sensitive.

Once the reaction has run for  $\approx 20$  hours, using a gravity filter, pass the entire solution through to remove waste product. This should leave clear yellowish liquid in flask. Use a rotating evaporator to evaporate DCM at 30 °C. Wash the remaining product with hexane and filter once more. Leave product in filter paper to dry before storage. The product yield was 0.47 g. Further purification was needed for this batch, so it was washed with methanol and ran through a gravity filter once more. This removed any leftover DCC and DMAP and left a yield of 0.187 g.

### MH004

To a 100 mL round-bottom flask add: 1.0 g (5.50 mmol) of 9-anthracene carboxylic acid, 1.2 equivalent weight of DCC (1.12 g, 5.42 mmol), 1.2 equivalent weight of 6-bromo-1-hexanol (0.98 g, 5.42 mmol), 8-10 crystals of DMAP ( $\approx 40$  mg), and 60 mL of DCM. Run the reaction under nitrogen or Argon. Wrap flask with aluminum foil as reaction is light sensitive. Leave the reaction overnight ( $\approx 20$  Hours) at room temperature with a stir bar.

Once the reaction has run for  $\approx 20$  hours, using a gravity filter, pass the entire solution through to remove waste product. This should leave clear yellowish liquid in flask. Use a rotating evaporator to evaporate DCM at 30 °C. Wash the remaining product with hexane and filter once more. After drying, washed with methanol and run through a gravity filter once more.

### MH027

To a 100-mL round-bottom flask: 1.0 g (5.50 mmol) of 9-anthracene carboxylic acid, 1.2 equivalent weight of DCC (1.12 g, 5.42 mmol), 1.2 equivalent weight of 6-bromo-1-hexanol (0.98 g, 5.42 mmol), 8-10 crystals of DMAP ( $\approx$ 40 mg), and 60 mL of DCM was added. The reaction was run under nitrogen atmosphere. The flask was wrapped completely with aluminum foil due to the light sensitive nature of the reaction. The reaction was then left overnight ( $\approx$ 20 Hours) at room temperature mixing with a stir bar. Once the reaction had ran for approximately 20 hours, using a gravity filter, the waste product was removed, and the filtrate was collected. The filtrate was a clear, yellowish liquid. Using a rotating evaporator at 30 °C, the remaining DCM was removed from the product. The remaining syrupy liquid was then mixed with hexane and fed through another gravity filter.

The initial filtered waste from this reaction weighed over 800 mg. It was believed at the time to not contain any product. This reaction was therefore concluded as a poor synthesis and was changed later. Recently, the filtered waste has been analyzed from other reactions to suggest that good product is present in the precipitant.

### MH033

The reaction parameters for this synthesis changed by increasing the mass of DMAP added and decreasing the volume of DCC for the reaction to take place. A thoroughly washed 100 mL round bottom flask was dried in 80 °C oven before use. To the 100-mL round-bottom flask: 1.0 g (5.50 mmol) of 9-anthracene carboxylic acid, 1.2 equivalent weight of DCC (1.12 g, 5.42 mmol), 1.2 equivalent weight of 6-bromo-1-hexanol (0.98 g, 5.42 mmol), 60 mg of DMAP, and 40 mL of DCM was added. The reaction was run under a nitrogen atmosphere. The flask was wrapped completely with aluminum foil due to the light sensitive nature of the reaction. The reaction was then left for two days ( $\approx$ 48 Hours) at room temperature mixing with a stir bar. Once the reaction had ran for approximately 48 hours, using a gravity filter, the waste product was removed, and the filtrate was collected. The filtrate was a clear, yellowish liquid. Using a rotating evaporator at 30 °C, the remaining DCM was removed from the product. The remaining syrupy liquid was then mixed with hexane and fed through another gravity filter. Characterization revealed that the product was not clean and therefore another wash cycle was implemented. A methanol wash was

used followed by filtration to remove DCC and DMAP that could be identified from an FTIR spectrum of the sample.

This procedure was modified from MH027 due to low yield. The DCM solvent was reduced to increase concentration in reaction and DMAP weight was increased to aid yield potential. To relinquish one possible cause for poor product yield, samples from each step of the work-up were taken and observed using FTIR whilst still in solution. This figure demonstrated that the use of a silica gel column would be a possible necessary work-up method for this reaction.

#### MH034

This new reaction was initiated at half the scale of previous. It used a relatively large volume of DCM and similar ratio weight for DMAP. A round-bottom, 100 mL flask was used and to it: 0.5 g (2.25 mmol) of 9-anthracene carboxylic acid, 1.2 equivalent weight of DCC (0.56 g, 2.71 mmol), 1.2 equivalent weight of 6-bromo-1-hexanol (0.49 g, 2.71 mmol), 4-5 crystals of DMAP ( $\approx 20$  mg), and 40 mL of DCM was added. The flask neck was sealed, and a nitrogen atmosphere filled the reaction vessel. The reaction was run overnight ( $\approx 20$  Hours) at room temperature with foil covering the flask and a stir bar.

As a response to problematic work-up results. A silica gel column was used to provide a more precise method of collecting this product. After running the dry samples through FTIR, the results from the column were promising and showed that the column could be used to isolate the pure product. The synthesis however still did not provide ideal product mass.

## REACTION SUMMARY

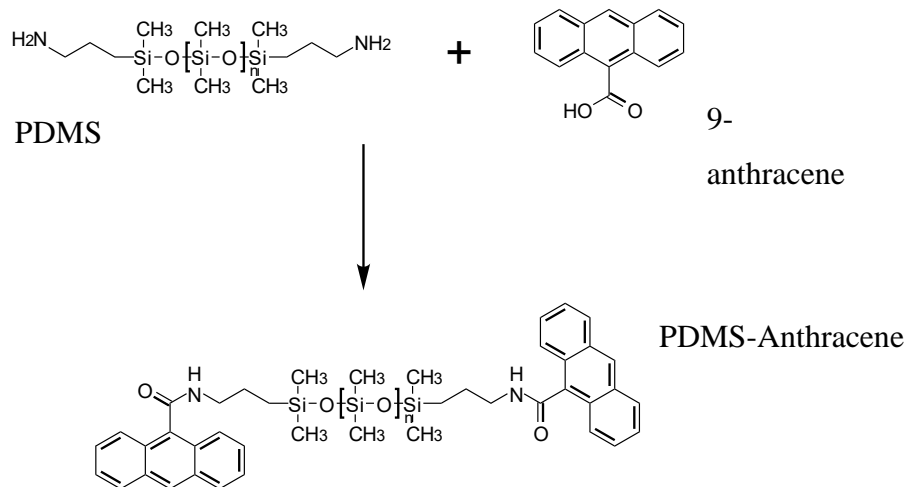
<i>Experiment</i>	<i>9-anthroic acid</i>	<i>6-bromo-1-hexanol</i>	<i>DCC</i>	<i>DMAP</i>	<i>Solvent</i>
<i>MH004</i>	500 mg	484 mg (1.2 eq.)	560 mg (1.2 eq.)	39.9 mg	DCM 40 mL
<i>MH004</i>	1.00 g	981 mg (1.2 eq.)	1.160 g (1.2 eq.)	39.9 mg	DCM 50 mL
<i>MH027</i>	1.00 g	990 mg (1.2 eq.)	1.12 g (1.2eq.)	40 mg	DCM 60 mL
<i>MH033</i>	1.00 g	990 mg (1.2 eq.)	1.12 g (1.2 eq.)	60 mg	DCM 40 mL
<i>MH034</i>	500 mg	490 mg (1.2 eq.)	560 mg (1.2 eq.)	20 mg	DCM 40 mL

Table 1 – Reaction summaries for anthracene linker syntheses

## PDMS-ANTHRACENE

### SYNTHESIS AND WORK-UP

This procedure using Steglich esterification to synthesize a functional PDMS molecule with anthracene capped termination points.



Scheme 1 – Synthesis of poly(dimethylsiloxane)bis(3-aminopropyl) and 9-anthracenecarboxylic acid to form PDMS-anthracene

### Hydroxy Terminated PDMS

#### *MH047*

Setup for this experiment required a thorough wash of a 100-mL round bottom flask which was then dried at 80 °C in an oven, the flask was then allowed to cool to room temperature. To the flask, add 0.444 g of 9-anthracene carboxylic acid, 0.408 g of DCC, and 20 mg of DMAP. To the flask, now add 40 mL of DCM along with a stir bar and begin stirring. Finally, add 1.0 g of PDMS-OH terminated. Cap the flask and cover with aluminium foil. Leave reaction to run for 48 hours.

After 48 hours, filter the reaction mixture using a gravity filter. The filtrate is then concentrated in the rotovap which removed the DCM. A yellow wet solid remained. This solid was washed with hexane and filtered once more. Solid from filter was collected and washed with water followed by ethanol. A purification step was then required so the product was dissolved in 20 – 30 mL of chloroform in a beaker. This solution was then filtered, and the filtrate was collected and rotovapped. The solid was allowed to dry before storage

#### *MH059*

Setup for this experiment required a thorough wash of a 100-mL round bottom flask which was then dried at 80 °C in an oven, the flask was then allowed to cool to room temperature. To the flask, add 0.444 g of 9-anthracene carboxylic acid, 0.408 g of DCC, and 20 mg of DMAP. To the flask, now add 40 mL of DCM along with a stir bar and begin stirring. Finally, add 1.0 g of PDMS-OH terminated. Cap the flask and cover with aluminium foil. Leave reaction to run for 48 hours.

After 48 hours, filter the reaction mixture using a gravity filter. The filtrate is then concentrated in the rotovap which removed the DCM. A yellow wet solid remained. This solid was washed with hexane and filtered once more. Solid from filter was collected and washed with water followed by ethanol. A purification step was then required so the product was dissolved in 20 – 30 mL of chloroform in a beaker. This solution was then filtered, and the filtrate was collected and rotovapped. The solid was allowed to dry before storage.

#### *MH078*

Setup for this experiment required a thorough wash of a 100-mL round bottom flask which was then dried at 80 °C in an oven, the flask was then allowed to cool to room temperature. To the flask, add 0.444 g of 9-anthracene carboxylic acid, 0.408 g of DCC, and 20 mg of DMAP. To the flask, now add 40 mL of DCM along with a stir bar and begin stirring. The flask is then cooled in ice-water for five minutes to bring the temperature down to 0°C. Finally, add 1.0 g of PDMS-OH terminated and bring the flask of the ice bath to allow it to come to RT. Cap the flask and cover with aluminum foil. Leave reaction to run for 48 hours.

Product was gravity filtered and solvent was removed with rotovap. product was suspended then in hexanes and gravity filtered once more. cake was suspended in ethanol and solution was passed through gravity filter. both filtrate and precipitate were characterized after drying.

#### *MH094*

The reaction was weighted with respect to 1 g of PDMS-OH (0.4 mmol) as it was added to a 100 mL round bottom flask. 186 mg (2.1 eq, 0.837 mmol) of 9-anthracene carboxylic acid, 173 mg (2.1 eq, 0.838 mmol) of DCC and 20 mg (0.164 mmol) of DMAP was prepared together before adding to the flask. The flask was then topped with 30 mL of acetonitrile, a stir bar was set to 600 rpm, and the reaction flask was covered for 48 hours.

Upon uncovering the reaction flask after 48 hours, the solution appeared to be clear and mildly tinted yellow; with an additional yellow, tacky substance present. This product was dirtier in color to the solution and precursor of anthracene. There were no particulates present in the reaction vessel so the first approach to workup of this reaction was rotary evaporation to remove acetonitrile. This left a mostly dry yellow powder coating the flask. The flask was then flushed with hexanes and scraped down to remove all material. Following a gravity filter, the filtrate was tinted a similar dirty yellow and a yellow powder remained as the precipitate. The filtrate was saved and stored in a glass vial for later analysis. The precipitate was further washed with methanol and another gravity filter. The complete mass of yellow powder was dissolved into the methanol and passed through the filter. A cleaner, yellow filtrate remained along with no discernable precipitate. Both the hexane filtrate and methanol filtrate were dried with rotary evaporation to leave testable material. After drying of the hexane filtrate, a thick, yellowish liquid remained (similar consistency to PDMS-NH<sub>2</sub>) which contained yellow particulates. This liquid was analyzed using FTIR and NMR (d-DMSO). The methanol filtrate was given the same drying treatment and produced a dry yellow solid. This solid was analyzed using FTIR and NMR (d-DMSO).

### *MH135*

Setup for this experiment required a thorough wash of a 100-mL round bottom flask which was then dried at 80 °C in an oven, the flask was then allowed to cool to room temperature. To the flask, now add 40 mL of DMF along with a stir bar and begin stirring. Bring flask to sub-zero Celsius using ice or LN<sub>2</sub>. To the flask, add 0.444 g of 9-anthracene carboxylic acid, 0.408 g of DCC, and 20 mg of DMAP. Begin stirring on stir plate. Finally, add 1.0 g of PDMS-OH terminated. Cap the flask and cover with aluminum foil. Leave reaction to run for 48 hours.

With no suspension present, remove DMF with rotary evaporation. Flush dried material with hexane(s) and gravity filter. Take dry cake and dissolve into ethanol then filter. Dry filtrate and precipitate.

## -NH<sub>2</sub> Terminated PDMS

### *MH095*

The reaction was weighted with respect to 1 g of PDMS-NH<sub>2</sub> (0.4 mmol) as it was added to a 100 mL round bottom flask. 186 mg (2.1 eq, 0.837 mmol) of 9-anthracene carboxylic acid, 173 mg (2.1 eq, 0.838 mmol) of DCC and 20 mg (0.164 mmol) of DMAP was prepared together before adding to the flask. The flask was then topped with 30 mL of DCM, a stir bar was set to 600 rpm, and the reaction flask was covered for 48 hours.

Upon uncovering the reaction flask after 48 hours, the solution appeared to be a suspension of particulates contained in a bright yellow solution. The solution was gravity filtered to yield a clean, yellow solution. The precipitate caught the filter appeared to be a white powder. The filtrate was dried using rotary evaporation, removing DCM and leaving crystal like formations along with bright yellow clumps of material. The dry filtrate was then washed with hexanes and gravity filtered once more. Yellow powder remained as a precipitate in the filter as a yellow filtrate solution was collected in the flask.

### *MH105*

The reaction was weighted with respect to 1 g of PDMS-NH<sub>2</sub> (0.4 mmol) as it was added to a 100 mL round bottom flask. 186 mg (2.1 eq, 0.837 mmol) of 9-anthracene carboxylic acid, 173 mg (2.1 eq, 0.838 mmol) of DCC and 20 mg (0.164 mmol) of DMAP was prepared together before adding to the flask. The flask was then topped with 30 mL of DCM, a stir bar was set to 600 rpm, and the reaction flask was covered for 48 hours.

Upon uncovering the reaction flask after 48 hours, the solution appeared to be a suspension of particulates contained in a bright yellow solution. The solution was gravity filtered to yield a clean, yellow solution. The precipitate caught the filter appeared to be a white/clear crystal powder. The filtrate was dried using rotary evaporation, removing DCM and leaving crystal like formations along with bright yellow clumps of material. The filtrate was then washed with hexanes and gravity filtered once more. Yellow wax remained as a precipitate in the filter as a yellow filtrate solution was collected in the flask. NMR was completed in CDCl<sub>3</sub>.

### *MH107*

The reaction was weighted with respect to 1 g of PDMS-NH<sub>2</sub> (0.4 mmol) as it was added to a 100 mL round bottom flask. 186 mg (2.1 eq, 0.837 mmol) of 9-anthracene carboxylic acid, 173 mg (2.1 eq, 0.838 mmol) of DCC was prepared together before adding to the flask. The flask was then topped with 30 mL of DCM, a stir bar was set to 600 rpm, and the reaction flask was capped and blacked-out for 48 hours.

Reaction was stopped after 48 hours. Bright yellow liquid resided in flask particulates floated throughout. Reaction flask was placed in -20°C freezer for 1 hour. Funnel and filter was frozen for 1 hour also. Solution was gravity filtered leaving white powder (presumably dicyclohexylurea) and a hint of yellow (unreacted anthracene or possibly lost product). The precipitate was dried via roto evaporation. Clear, oil-like substance remained with yellow particulates embedded. Appearance indicates reaction did not form product intended.

### *MH108*

The reaction was weighted with respect to 1 g of PDMS-NH<sub>2</sub> (0.4 mmol) as it was added to a 100 mL round bottom flask. 186 mg (2.1 eq, 0.837 mmol) of 9-anthracene carboxylic acid, 173 mg (2.1 eq, 0.838 mmol) of DCC was prepared together before adding to the flask. The flask was then topped with 30 mL of DCM, a stir bar was set to 300 rpm, and the reaction flask was capped and blacked-out for 48 hours. Nitrogen was flushed through for the remainder of the reaction.

Reaction was stopped after 96 hours. Bright yellow liquid resided in flask particulates floated throughout. Reaction flask was placed in -20°C freezer for 1 hour. Funnel and filter was frozen for 1 hour also. Solution was gravity filtered leaving white powder (presumably dicyclohexylurea) and a hint of yellow (unreacted anthracene or possibly lost product). The precipitate was dried via roto evaporation. Clear, yellow, oil-like substance remained. Appearance is promising.

### *MH109*

The reaction was weighted with respect to 1 g of PDMS-NH<sub>2</sub> (0.4 mmol) as it was added to a 100 mL round bottom flask. 186 mg (2.1 eq, 0.837 mmol) of 9-anthracene carboxylic acid, 173 mg (2.1 eq, 0.838 mmol) of DCC was prepared together before adding to the flask. DCM was dried with 100 mg of magnesium sulfate and gravity filtered. The flask was then topped with 30 mL of DCM, a stir bar was set to 300 rpm, and the reaction flask was capped and blacked-out for 24

hours. A couple of Drierite rocks was added to the reaction as a capture of water produced by the reaction.

After 24 hours the reaction was placed in a freezer to cool to -20 °C. Solution was then gravity filtered. This process was extremely slow and a small amount of clear yellow liquid precipitated through.

#### *MH110*

The reaction was weighted with respect to 1 g of PDMS-NH<sub>2</sub> (0.4 mmol) as it was added to a 100 mL round bottom flask. 186 mg (2.1 eq, 0.837 mmol) of 9-anthracene carboxylic acid, 173 mg (2.1 eq, 0.838 mmol) of DCC was prepared together before adding to the flask. DCM was dried with 100 mg of magnesium sulfate and gravity filtered. The flask was then topped with 30 mL of DCM, a stir bar was set to 300 rpm, and the reaction flask was capped and blacked-out for 24 hours. A couple of Drierite rocks was added to the reaction as a capture of water produced by the reaction.

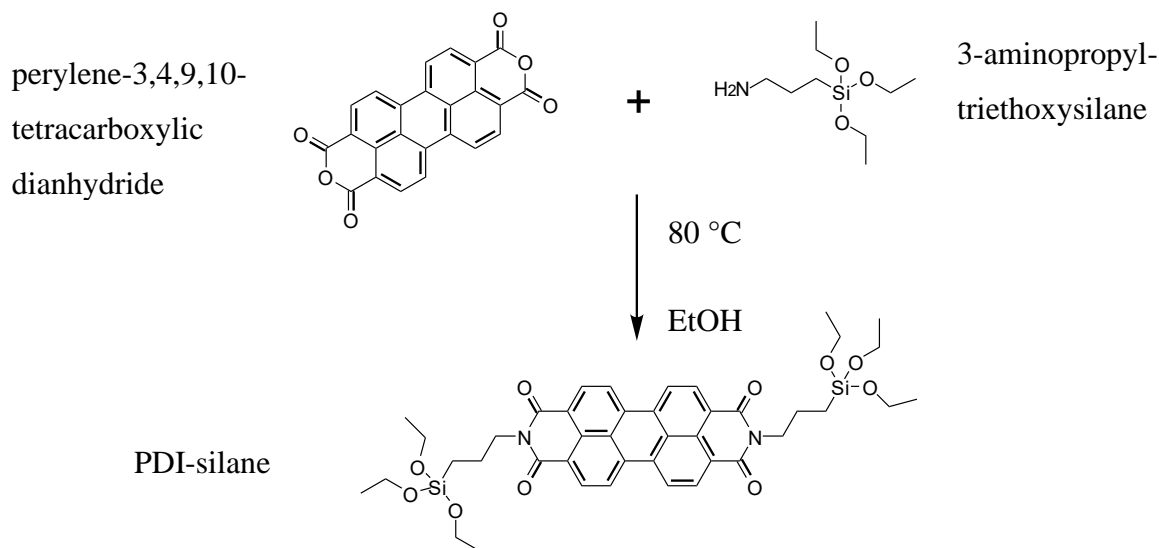
## Reaction Summary

Table 2 – Table of experimental parameters for anthracene terminated PDMS

<i>Experiment</i>	<i>9-anthroic acid</i>	<i>PDMS Termination</i>	<i>DMAP</i>	<i>DCC</i>	<i>Solvent</i>
<i>MH047</i>	0.444 g	1.0 g (OH)	20 mg	0.408g	40 mL (DCM)
<i>MH049</i>	0.444 g	1.0 g (OH)	20 mg	0.408g	40 mL (DCM)
<i>MH059</i>	0.444 g	1.0 g (OH)	20 mg	0.408g	40 mL (DCM)
<i>MH078</i>	0.444 g	1.0 g (OH)	20 mg	0.408g	40 mL (DCM)
<i>MH094</i>		1.0 g (OH)	20 mg		40 mL (acetonitrile)
	0.186 g (2.1 eq.)			0.173 g (2.1 eq.)	
<i>MH095</i>		1.0 g (OH)	20 mg		30 mL (acetonitrile)
	0.186 g (2.1 eq.)			0.173 g (2.1 eq.)	
<i>MH105</i>		1.0 g (NH <sub>2</sub> )	N/A		30 mL (DCM)
	0.186 g (2.1 eq.)			0.173 g (2.1 eq.)	
<i>MH107</i>		1.0 g (NH <sub>2</sub> )	N/A		30 mL (DCM)
	0.186 g (2.1 eq.)			0.173 g (2.1 eq.)	
<i>MH108</i>		1.0 g (NH <sub>2</sub> )	N/A		30 mL (DCM)
	0.186 g (2.1 eq.)			0.173 g (2.1 eq.)	
<i>MH109</i>		1.0 g (NH <sub>2</sub> )	N/A		30 mL (DCM)
	0.186 g (2.1 eq.)			0.173 g (2.1 eq.)	
<i>MH110</i>		1.0 g (NH <sub>2</sub> )	N/A		30 mL (DCM)
	0.186 g (2.1 eq.)			0.173 g (2.1 eq.)	
<i>MH134</i>	0.444 g	1.0 g (OH)	20 mg	0.408g	40 mL (DCM)
<i>MH135</i>	0.444 g	1.0 g (OH)	20 mg	0.408g	40 mL (DMF)

## PDI-SILANE

Scheme 2 shows the synthesis diagram for the single-step replacement reaction that forms PDI-silane. Beginning with perylene-3,4,9,10-tetracarboxylic dianhydride and 3-aminopropyltriethoxysilane a reflux reaction was initiated in 200 proof ethanol over 48 hours.



Scheme 2 – Synthesis of perylene-3,4,9,10-tetracarboxylic dianhydride and 3-aminopropyltriethoxysilane to form PDI-silane

### SYNTHESIS AND WORK-UP

All glassware was dried prior to use. ~1000 mg of Perylene-3,4,9,10-tetracarboxylic dianhydride was added to a two-necked round-bottom flask. 10 mL of (3-aminopropyl) triethoxysilane was added to the flask. The flask was then fitted to the reflux column, purged and filled with a nitrogen atmosphere. 50 mL of anhydrous EtOH was added to the flask via syringe through a plugged neck. The flask was then lowered into the oil bath to begin equilibrating temperature. The oil bath was stabilized to  $\approx 80$  °C for the reflux reaction. The reaction was left for 36 hours.

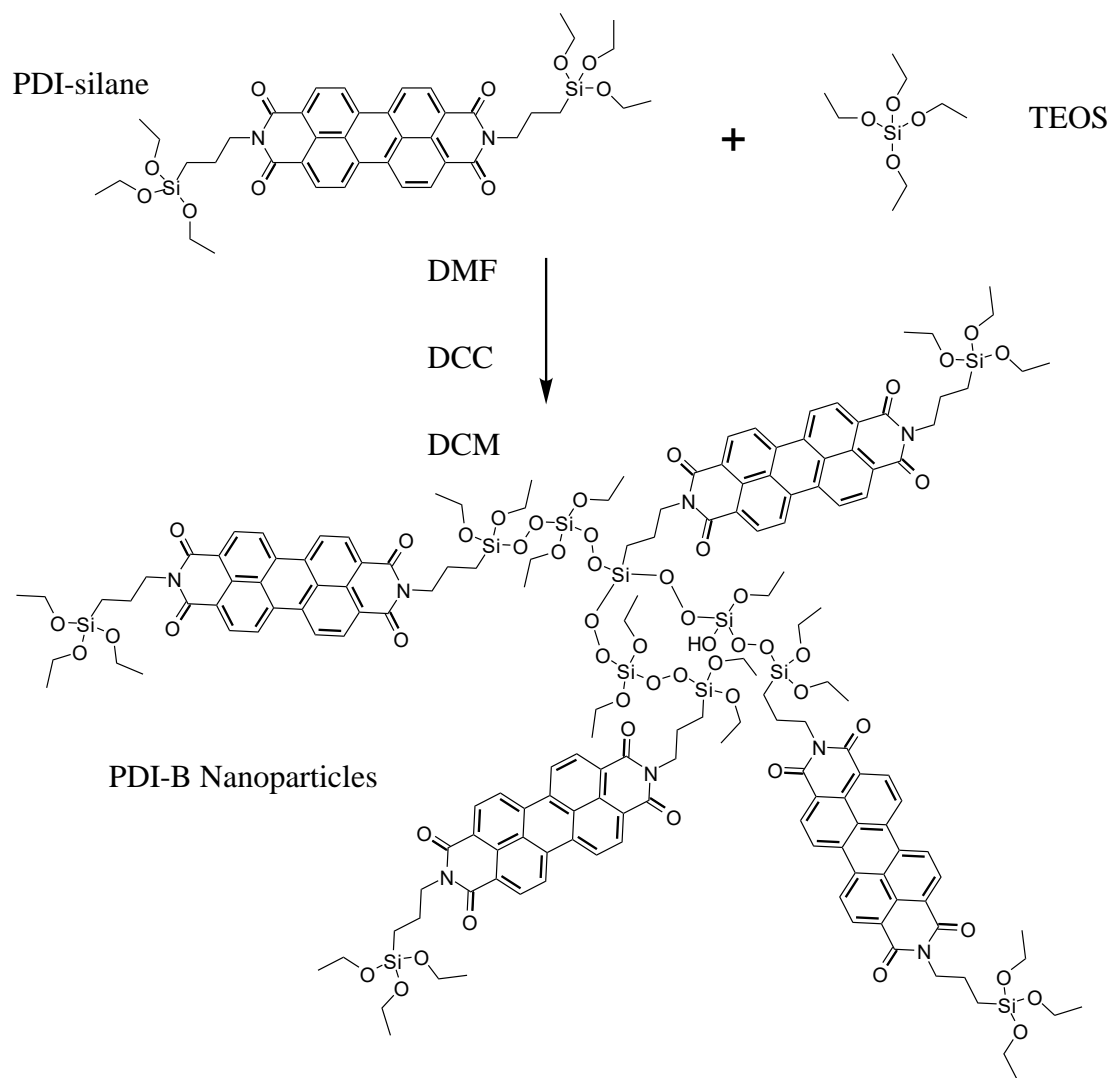
When performing reaction in solvent, excessive 3-APT is required. 10 mL of 3-APT to 1 g of PTCD seems to be a reliable place to start. This coincidentally provides 10 3-APT molecules per reaction site. Volume of EtOH could potentially be reduced 20%. Untidy stirring is helpful to

prevent solid buildup on sides on flask. Don't aim for a specific temperature, aim to reach just past boiling and make sure condensation is working.

After time, remove the round bottom flask from the oil bath and allow it to cool to room temperature. Add hexane to the flask to force the product out of solution. Pour the suspension through a gravity filter, this will remove the ethanol and left over reactants (one-sided PDI-silane). Remaining in the filter paper should be perylene and product. Wash the filter and suspend solid with chloroform. Wash through second ashless gravity filter and collect product in filtrate solution. Rotary evaporation is then used to remove chloroform and product solution is left to dry. Allow to dry overnight in desiccator or glovebox, protect from oxygen atmosphere and direct light. Once product is dry, scrape thoroughly product from sides of flask and collect in vial. To store, fill vial with nitrogen atmosphere and seal.

### **PDIB NANOPARTICLE**

A typical procedure begins with a dry, 100 mL round bottom flask to which 40 mL of anhydrous ethanol and 5 mL of ammonium hydroxide is added. A stir bar is added to thoroughly mix the two liquids before precursors are added. 100 mg of PDI-silane is dissolved into 10 mL of chloroform and sonicated to ensure complete dispersion. 1 mL of TEOS simultaneously with the PDI-silane solution is added to the round bottom flask. The reaction is then capped and left for 24 hours. Upon completion, the reaction volume is distributed into 50 mL centrifuge tubes and particles are forced out of solution at 10000 rpm. Depending upon particle diameter, desired product resides in either the pellet or reaction solvent. In the case where particles remain in suspension, they are dried as quickly as possible to prevent further reaction due to the catalyst presence of ammonium hydroxide. Particles that reside in the pellet after the first centrifugation are twice washed with chloroform to remove unreacted PDI-silane and centrifuged. They are then washed with ethanol to remove excess ammonium hydroxide. SEM samples are prepared from dry samples and UV-vis and Fluorescence is studied in ethanol solution.



Scheme 3 – Synthesis of PDI-silane and tetraethylorthosilicate to form PDI-B nanoparticles

#### SYNTHESIS AND WORK-UP

#### MH048

Setup for this experiment required a thorough wash of a 100-mL round bottom flask which was then dried at 80 °C in an oven, the flask was then allowed to cool to room temperature. To the flask, 40 mL of anhydrous ethanol was added. Following this, 7.5 mL of ammonium hydroxide was added and the mixture was left to stir for 15 minutes. Once sufficiently mixed, 0.5 mL of

TEOS was added to the flask and the reaction was capped and allowed to run for 15 minutes further. This mixture did not turn cloudy after the 15-minute mark had passed. During this time, a solution of PDI-silane was prepared by adding 100 mg of PDI-silane to 10 mL purified chloroform. Once the TEOS had been running for 15 minutes, the PDI-silane solution was added to the flask through a 0.45  $\mu\text{m}$  filter.

Before adding the PDI-silane solution, a sample was taken of the silicas NP growth after 15 minutes of reaction time. After 24 hours under reaction conditions a sample was taken and prepared on a silica wafer shard. After 48 hours, this sample was dried on a silica wafer shard for imaging under SEM. The product was separated into two 50 mL falcon tubes before centrifugation at 8000 rpm for 30 minutes. The supernatant was then decanted, and 10 mL of anhydrous ethanol was added to the tubes. A sample of the supernatant was dried on a silica wafer shard for imaging under SEM. The pellet was dispersed via agitation. The sample was then centrifuged once more at 8000 rpm for 30 minutes. The supernatant was then decanted, and 10 mL of chloroform was added to the tubes. The pellet was dispersed via agitation. The sample was then centrifuged once more at 8000 rpm for 30 minutes. The supernatant was decanted, and 10 mL of chloroform was added to the tube. The pellet was dispersed via agitation. The sample was once more centrifuged at 8000 rpm for 30 minutes. The chloroform was decanted, and a small sample of the pellet was taken and suspended in ethanol. This small sample was then used to form a SEM sample when dropped and dried on a silica wafer shard. The product was dried and stored.

#### MH050

Setup for this experiment required a thorough wash of a 100-mL round bottom flask which was then dried at 80  $^{\circ}\text{C}$  in an oven, the flask was then allowed to cool to room temperature. To the flask, 40 mL of anhydrous ethanol was added. Following this, 7.5 mL of ammonium hydroxide was added and the mixture was left to stir for 30 minutes. During this stirring period, 100 mg of PDI-silane powder was dissolved into 10 mL of anhydrous chloroform. This solution was then vortexed and sonicated to aid solution formation. The PDI-silane was then passed through a 0.45  $\mu\text{m}$  filter. The filtered PDI-silane solution, along with 0.5 mL of TEOS, was then added to the

round bottom flask and the reaction was capped. The reaction was let to run for 24 hours stirring at moderate intensity.

Just after adding the PDI-silane, a sample was taken from the reaction and prepared on a silica wafer shard for SEM imaging. After 24 hours under reaction conditions a sample was taken and prepared on a silica wafer shard. The product was separated into two 50 mL falcon tubes before centrifugation at 8000 rpm for 30 minutes. The supernatant was then decanted, and 10 mL of anhydrous ethanol was added to the tubes. A sample of the supernatant was dried on a silica wafer shard for imaging under SEM. The pellet was dispersed via agitation. The sample was then centrifuged once more at 8000 rpm for 30 minutes. The supernatant was then decanted, and 10 mL of chloroform was added to the tubes. The pellet was dispersed via agitation. The sample was then centrifuged once more at 8000 rpm for 30 minutes. The supernatant was decanted, and 10 mL of chloroform was added to the tube. The pellet was dispersed via agitation. The sample was once more centrifuged at 8000 rpm for 30 minutes. The chloroform was decanted, and a small sample of the pellet was taken and suspended in ethanol. This small sample was then used to form a SEM sample when dropped and dried on a silica wafer shard. The product was dried and stored.

## MH052

Setup for this experiment required a thorough wash of a 100-mL round bottom flask which was then dried at 80 °C in an oven, the flask was then allowed to cool to room temperature. To the flask, 40 mL of anhydrous ethanol was added. Following this, 10 mL of ammonium hydroxide was added and the mixture was left to stir for 30 minutes. After time, 1 mL of TEOS was added to the flask and left to stir for 15 minutes. During this stirring period, 100 mg of PDI-silane powder was dissolved into 10 mL of anhydrous chloroform. This solution was then vortexed and sonicated to aid dissolving. The PDI-silane was then passed through a 0.45 µm filter. The filtered PDI-silane solution was then added to the round bottom flask once the TEOS had been present for 15 minutes and the reaction was capped. The reaction was let to run for 24 hours stirring at moderate intensity.

After 24 hours under reaction conditions a sample was taken and prepared on a silica wafer shard. After 48 hours, this sample was dried on a silica wafer shard for imaging under SEM. The product

was separated into two 50 mL falcon tubes before centrifugation at 8000 rpm for 30 minutes. The supernatant was then decanted, and 10 mL of anhydrous ethanol was added to the tubes. A sample of the supernatant was dried on a silica wafer shard for imaging under SEM. The pellet was dispersed via agitation. The sample was then centrifuged once more at 8000 rpm for 30 minutes. The supernatant was then decanted, and 10 mL of chloroform was added to the tubes. The pellet was dispersed via agitation. The sample was then centrifuged once more at 8000 rpm for 30 minutes. The supernatant was decanted, and 10 mL of chloroform was added to the tube. The pellet was dispersed via agitation. The sample was once more centrifuged at 8000 rpm for 30 minutes. The chloroform was decanted, and a small sample of the pellet was taken and suspended in ethanol. This small sample was then used to form a SEM sample when dropped and dried on a silica wafer shard. The product was dried and stored.

#### MH056

Setup for this experiment required a thorough wash of a 100-mL round bottom flask which was then dried at 80 °C in an oven, the flask was then allowed to cool to room temperature. To the flask, 40 mL of anhydrous ethanol was added. Following this, 0.1 mL of ammonium hydroxide was added, and the mixture was left to stir for 30 minutes. After time, 1 mL of TEOS was added to the flask and left to stir for 15 minutes. During this stirring period, 100 mg of PDI-silane powder was dissolved into 10 mL of anhydrous chloroform. This solution was then vortexed and sonicated to aid dissolving. The PDI-silane was then passed through a 0.45 µm filter. The filtered PDI-silane solution was then added to the round bottom flask once the TEOS had been present for 15 minutes. Immediately following this addition, 0.9 mL of ammonium hydroxide was added to the flask to further aid particle formation. The reaction was let to run for 24 hours stirring at moderate intensity.

After 24 hours under reaction conditions the volume was separated into two 50 mL falcon tubes before centrifugation at 8000 rpm for 30 minutes. The supernatant was then decanted, and 10 mL of anhydrous ethanol was added to the tubes. A sample of the supernatant was dried on a silica wafer shard for imaging under SEM. The pellet was dispersed via agitation. The sample was then centrifuged once more at 8000 rpm for 30 minutes. The supernatant was then decanted, and 10 mL

of chloroform was added to the tubes. A sample of the supernatant was dried on a silica wafer shard for imaging under SEM. The pellet was dispersed via agitation. The sample was then centrifuged once more at 8000 rpm for 30 minutes. The supernatant was decanted, and 10 mL of chloroform was added to the tube. A sample of the supernatant was dried on a silica wafer shard for imaging under SEM. The pellet was dispersed via agitation. The sample was once more centrifuged at 8000 rpm for 30 minutes. The chloroform was decanted, and a small sample of the pellet was taken and suspended in ethanol. This small sample was then used to form a SEM sample when dropped and dried on a silica wafer shard. The product was dried and stored.

#### MH057

Setup for this experiment required a thorough wash of a 100-mL round bottom flask which was then dried at 80 °C in an oven, the flask was then allowed to cool to room temperature. To the flask, 40 mL of anhydrous ethanol was added. Following this, 1 mL of ammonium hydroxide was added and the mixture was left to stir for 30 minutes. After time, 0.5 mL of TEOS was added to the flask and left to stir for 15 minutes. During this stirring period, 100 mg of PDI-silane powder was dissolved into 8 mL of anhydrous chloroform. This solution was then vortexed and sonicated to aid dissolving. The PDI-silane was then passed through a 0.45 µm filter. The filtered PDI-silane solution was then added to the round bottom flask and the reaction was capped. The reaction was let to run for 24 hours stirring at moderate intensity.

After 24 hours under reaction conditions the volume was separated into two 50 mL falcon tubes before centrifugation at 10000 rpm for 60 minutes. The supernatant was then decanted, and 10 mL of anhydrous ethanol was added to the tubes. A sample of the supernatant was dried on a silica wafer shard for imaging under SEM. The pellet was dispersed via agitation. The sample was then centrifuged once more at 10000 rpm for 60 minutes. The supernatant was then decanted, and 10 mL of chloroform was added to the tubes. A sample of the supernatant was dried on a silica wafer shard for imaging under SEM. The pellet was dispersed via agitation. The sample was then centrifuged once more at 10000 rpm for 60 minutes. The supernatant was decanted, and 10 mL of chloroform was added to the tube. A sample of the supernatant was dried on a silica wafer shard

for imaging under SEM. The pellet was dispersed via agitation. The sample was once more centrifuged at 10000 rpm for 60 minutes. The chloroform was decanted, and a small sample of the pellet was taken and suspended in ethanol. This small sample was then used to form a SEM sample when dropped and dried on a silica wafer shard. The product was dried and stored.

#### MH058

Setup for this experiment required a thorough wash of a 100-mL round bottom flask which was then dried at 80 °C in an oven, the flask was then allowed to cool to room temperature. To the flask, 40 mL of anhydrous ethanol was added. Following this, 1 mL of ammonium hydroxide was added and the mixture was left to stir for 30 minutes. During this stirring period, 100 mg of PDI-silane powder was dissolved into 5 mL of anhydrous chloroform. This solution was then vortexed and sonicated to aid dissolving. The PDI-silane was then passed through a 0.45 µm filter. The filtered PDI-silane solution, along with 0.5 mL of TEOS, was then added to the round bottom flask and the reaction was capped. The reaction was let to run for 24 hours stirring at moderate intensity.

The PDI-silane was more difficult to dissolve in chloroform compared with previous experiments where more chloroform was used. Filtration was also more difficult (more filters used due to blockage) indicating that a good solution was not formed. It is very likely that this experiment had lower quantities of PDI-silane than previous procedures.

After 15 minutes of TEOS reaction, a sample was taken from the flask for later SEM analysis of the silica particle formation. After 24 hours under reaction, a sample was taken from the solution and prepared by drop casting onto a silicon wafer shard. The batch was then treated to a rotary evaporator with the water bath at 60 °C to remove chloroform and ammonium hydroxide. With the reaction now containing only water and ethanol, the volume was moved to a centrifuge tube for spinning at 8000 rpm for 1 hour. The supernatant was then taken from the tube and stored in a glass vial. Particles remain in ethanol suspension.

MH104

Setup for this experiment required a thorough wash of a 100-mL round bottom flask which was then dried at 80 °C in an oven, the flask was then allowed to cool to room temperature. To the flask, 40 mL of anhydrous ethanol was added. Following this, 1 mL of ammonium hydroxide was added, and the mixture was left to stir for 30 minutes. During this stirring period, 100 mg of PDI-silane powder was dissolved into anhydrous chloroform. This solution was then vortexed and sonicated to aid dissolving. The PDI-silane was then passed through a 0.45 µm filter. The filtered PDI-silane solution, along with 0.5 mL of TEOS, was then added to the round bottom flask and the reaction was capped. The reaction was let to run for 24 hours stirring at moderate intensity.

## REACTION SUMMARY

EXPERIMENT NO.	MH104.1	MH104.2	MH104.3
ETOH (ML)	40	40	40
NH <sub>4</sub> OH (ML)	1	1	1
TEOS (μL)	500	500	500
PDI-SILANE (MG)	100	100	100
CHCL <sub>3</sub> (ML)	2.5	5	7.5

Table 3 – PDIB-siloxane nanoparticle reaction table for experiment MH104

After 24 hours the solutions were transferred to 50 mL Falcon centrifuge tubes for work-up at 3500 rpm for 4 hours. A luminous orange solution remained separate from a dark red pellet. Solution was separated, and pellet was allowing to dry. SEM samples were prepared of both pellet and solution.

## THIN-FILM FORMATION

### MH053

The two ITO substrates were prepared using a modified RCA cleaning method. First, a soapy-brush wash was used to remove macro debris and form a hydrophobic surface. The substrates were then placed in a base-bath formed from 20 mL of ammonium hydroxide, 20 mL of hydrogen peroxide, and 60 mL of deionized water. This solution was heated to 80 °C and the substrates were submerged for 15 minutes. The substrates were then given a 20-minute sonication in deionized water. The substrates were then dried with the nitrogen gun and stored in a clean petri dish. Before spin coating, the substrates were placed under a high-powered UV lamp for cleaning in an ozone atmosphere. This treatment was carried out for 20 minutes to form a hydrophilic surface. The solution used for MH053.3 was a PDI-silane/chlorobenzene mix at 15 mL/mg concentration. The solution used for MH053.4 was a PDIB-silane/anhydrous ethanol mix at 15 mL/mg concentration.

These two solutions were sonicated upon first compilation for 20 minutes and left overnight. Before depositing onto the ITO substrate, the solutions were sonicated for another 20 minutes. MH053.3 was dropped onto the ITO substrate through a 0.45  $\mu\text{m}$  filter and spread over the entire substrate. The heat lamp was lit over the spin-coating stage and the substrate was accelerated to 300 rpm for 30 seconds followed by further acceleration to 3300 rpm for 30 seconds. MH053.4 was dropped onto the ITO substrate and spread over the entire substrate. The substrate was accelerated to 300 rpm for 30 seconds followed by further acceleration to 3300 rpm for 30 seconds.

#### MH055

The four ITO substrates were prepared using a modified RCA cleaning method. First, a soapy-brush wash was used to remove macro debris and form a hydrophobic surface. The substrates were then placed in a base-bath formed from 20 mL of ammonium hydroxide, 20 mL of hydrogen peroxide, and 60 mL of deionized water. This solution was heated to 80 °C and the substrates were submerged for 15 minutes. The substrates were then given a 20-minute sonication in deionized water. The substrates were then dried with the nitrogen gun and stored in a clean petri dish. Before spin coating, the substrates were placed under a high-powered UV lamp for cleaning in an ozone atmosphere. This treatment was carried out for 20 minutes to form a hydrophilic surface. The solution used for MH055.1 was a PDIB-silane/anhydrous ethanol mix at 15 mL/mg concentration. The solution used for MH055.2 was a PDIB-silane/anhydrous ethanol mix at 30 mL/mg concentration. The solution used for MH055.3 was a PDIB-silane/chlorobenzene mix at 15 mL/mg concentration. The solution used for MH055.4 was a PDIB-silane/chlorobenzene mix at 30 mL/mg concentration. These four solutions were sonicated upon first compilation for 20 minutes and left overnight. Before depositing onto the ITO substrate, the solutions were sonicated for another 20 minutes.

The solution for MH055.1 was dropped onto the ITO substrate and spread over the entire substrate. The substrate was accelerated to 200 rpm for 30 seconds followed by further acceleration to 6000 rpm for 5 seconds. The solution for MH055.2 was dropped onto the ITO substrate and spread over the entire substrate. The substrate was accelerated to 200 rpm for 30 seconds followed by further

acceleration to 6000 rpm for 5 seconds. The solution for MH055.3 was dropped onto the ITO substrate through a 0.45  $\mu\text{m}$  filter and spread over the entire substrate. The heat lamp was lit over the spin-coating stage and the substrate was accelerated to 200 rpm for 30 seconds followed by further acceleration to 6000 rpm for 5 seconds. The solution for MH055.4 was dropped onto the ITO substrate through a 0.45  $\mu\text{m}$  filter and spread over the entire substrate. The heat lamp was lit over the spin-coating stage and the substrate was accelerated to 200 rpm for 30 seconds followed by further acceleration to 6000 rpm for 5 seconds.

## CHAPTER V: ANTHRACENE DERIVATIVES

### DONOR CHARACTERIZATION AND PERFORMANCE

#### POLYIMIDE APPROACH

##### *Discussion*

With the intent of creating a donor component that was easily formed and cured into a resilient thin film whilst having fluorescent caps sterically available for energy transfer, there were inevitably a few modifications to the design approach and chemical synthesis. Beginning with the original synthesis process, the molecule was comprised of three pieces. The polymer base was chosen to be poly[trimellitic anhydrous chloride-co-4, 4', methylenedianiline] due to its high temperature stability. A linker, 6-bromo-1-hexanol, was then to be attached within the chain that provided easier functionalization of the polyimide. The linker also allowed more room for the fluorescent anthracene molecule to attach to the polymer chains. The anthracene molecule took the form of 9-anthracene carboxylic acid.

Through the trials of creating this molecule, four synthesis procedures were undertaken; two providing the polyimide with the additional linker, and two providing the linker attached to the anthracene molecule. These procedures showed success initially but as discussed later, they were not ideally repeatable due to a trade-off between high yield and high purity. The anthracene linker synthesis was revisited to improve the yield and purity. From a 0.5 g scale reaction (MH003), 0.47 g of product was produced before washing. It was expected that a wash would not impact this value too much. However, once washed, 60 % of this mass was lost indicating unreacted 9-anthracene carboxylic acid was prominent in this reaction. When scaling this reaction to 1.0 g (MH027) to reduce wasted reactants a similar story was told. A close to doubling of the product mass was achieved at 0.8090 g but washing again caused drastic reduction of the final products weight. To confirm that the reaction procedure was sound, a different work-up was attempted. The direction taken following these trials was to improve yield from the reactions and develop an improved work-up procedure leading to a cleaner product.

## Characterization

### *Polymer-Linker reaction*

Poly[trimellitic anhydrous chloride-co-4, 4', methylenedianiline]

The polymer used in the phase 1 set of reactions was Poly[trimellitic anhydrous chloride-co-4, 4', methylenedianiline]. In order to estimate  $^1\text{H}$  NMR, the monomer form was used terminated by a chlorine and amine. This should be an effective tool as the only variable pieces of the molecule through reaction are located at termination ends of the polymer. The  $n$  groups that exist in-between are effectively irrelevant. The best indicator of reaction efficacy would be the integrated value of the peak associated with the amine. Within the polymer, and at the functionalized linker end, it should integrate to  $n \times 1$  or 1, respectively. But with unreacted polymer there should be a peak integration of 2. This is all with the assumption that all three peaks are distinguished and resolved from each other. This monomer prediction provided: 3.83 (2H, s), 3.9 (2H, s), 6.34 (2H, d), 6.80 (2H, d), 7.10 (2H, d), 7.30 (2H, d), 7.99 (1H, d), 8.27 (1H, s), 8.54 (1H, d). All peak positions were predicted with high confidence except for the amine termination group.

### 6-bromo-1-hexanol

The inker used for the phase 1 set of reactions was a brominated hexanol molecule. Its intended purpose was to improve reactivity between the polymer and fluorophore by reducing steric hinderances. Simulating its  $^1\text{H}$  NMR allowed some confirmation that the hydroxy hydrogen was the least shielded hydrogen in the molecule. The prediction in total gave: 1.24 (1H, t), 1.33 (2H, q), 1.47 (2H, q), 1.58 (2H, q), 1.82 (2H, q), 3.52 (2H, t), 3.62 (2H, q). Upon successful reactions shifts to the tail end hydrogens are expected.

### Predictive $^1\text{H}$ NMR

To predict the expected reaction outcome proton NMR, the same methods were as in previous predictions. Attention is paid towards the peak shift from the amine associated hydrogen and the reduced shielding of the hydrogens in the hexanol chain. These shifts, in combination, should be enough to confirm reaction outcome without integration for a qualitative conclusion. Again, it is important to note the low confidence in the amine hydrogen peak position after prediction. The

predicted proton NMR calculates  $\{\delta, \text{ppm}\}$ : 1.24 (1H, t), 1.29 (2H, q), 1.47 (2H, q), 1.58 (4H, q), 3.11 (2H, t), 3.62 (2H, q), 3.83 (2H, s), 3.6 (1H t), 6.51 (2H, d), 6.90 (2H, d), 7.10 (2H, d), 7.30 (2H, d), 7.99 (1H, d), 8.27 (1H, s), 8.54 (1H, d). It is important to indicate that most dramatic changes to shielding are centered around the amine reaction site. The spectral peak for this one hydrogen is now a triplet due to its increased neighbors. the 1 and 2 carbons on the hexanol chain have also made significant changes. The '2' carbon has had significant shifting lower and is now symmetrical with carbon 5. Carbon 1 also has sifted relative to its component position when shielded by the bromine chain-end.

MH001

After complete work-up, FTIR from this reaction shows broad O-H stretching from the hydroxy group tailing the linker. The presence of tertiary amines in this spectrum are not identified due to their weak intensity and probably location in a 'busy' area ( $1250\text{-}1020\text{ cm}^{-1}$ ). This is due to the lack of polarity in the C-N bond. The secondary amine N-H stretching typically appears with medium strength between  $3350\text{-}3310\text{ cm}^{-1}$ , indicated via red lines in Figure 9. There does not appear to present any peaks within this region given good indication that mostly tertiary amines are present. NMR is needed to further analyze this reaction success.

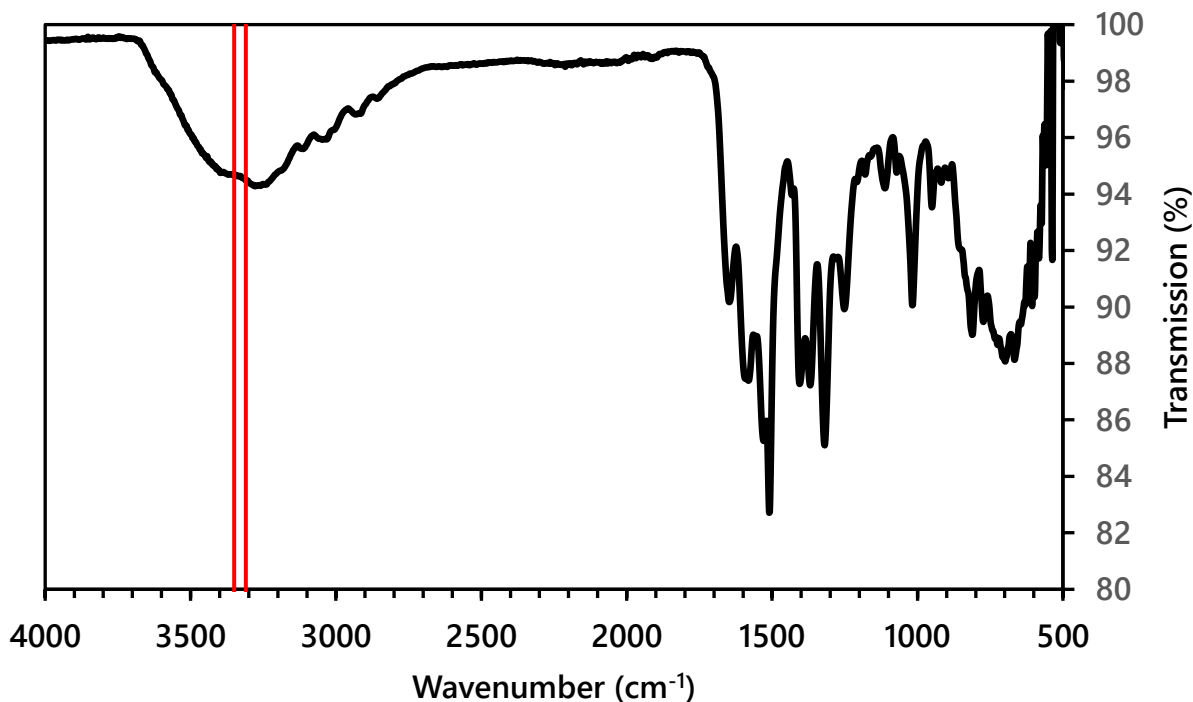


Figure 9 – FTIR spectrum for Polymer-Linker product from MH001 reaction

#### MH002

The previous reaction (MH001) was repeated and scaled-up to 1 g. After complete work-up, NMR was performed in DMSO-d<sub>6</sub>. Peaks presenting at 3.897 ppm and 3.986 ppm appear from the two methylene hydrogens fixed between the ring structures in the polyimide. Comparing the integration of these peaks to that from 3.346 ppm indicates a large discrepancy as integration of this single peak appears 4x greater than integration including both peaks from the methylene. This peak has likely a large contribution from the C '6' (shielded by the OH group) of the linker. There is indication here then that there is overwhelming presence of unreacted linker at workup and a complexity in identifying a successful synthesis for this scheme. This problem encourages the attempt to react the linker with 9-anthracic acid first to then attempt this mating as the secondary step.

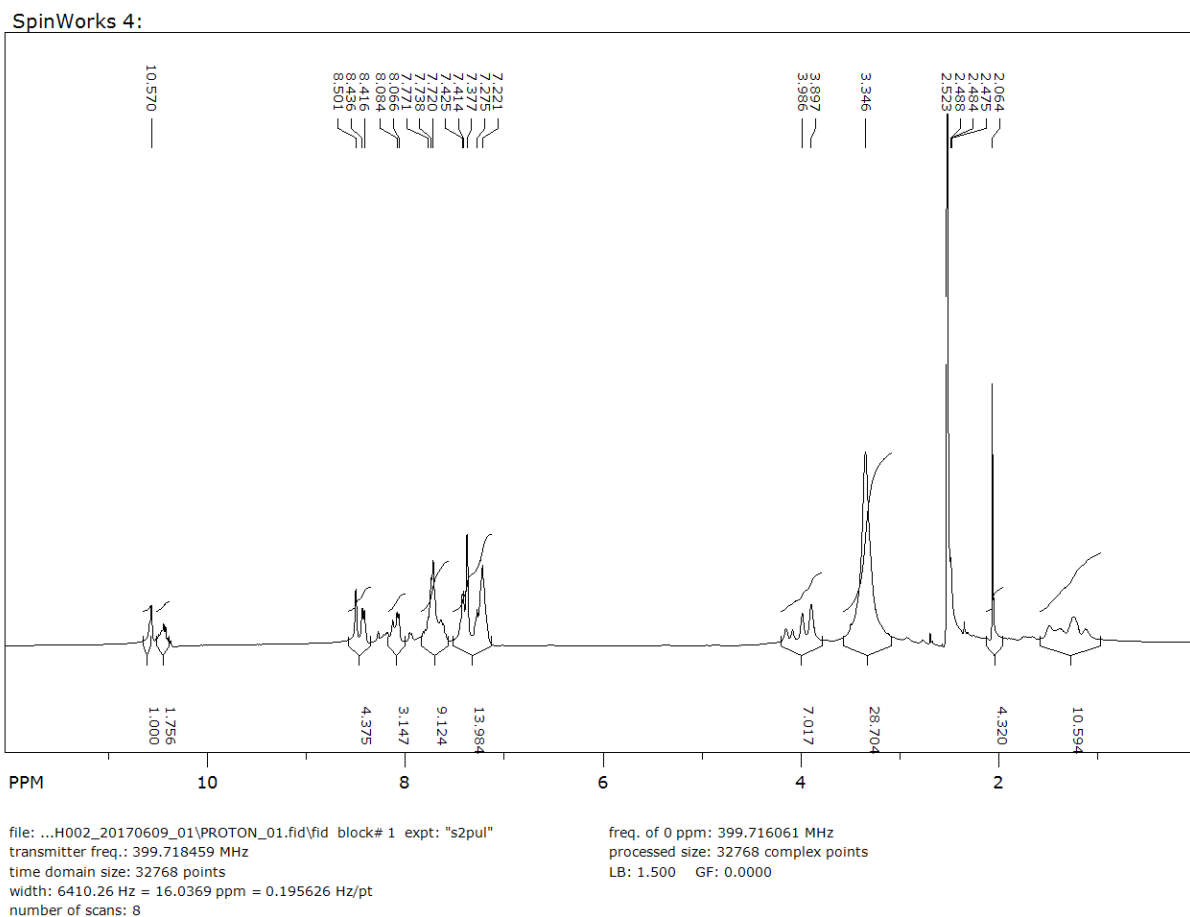


Figure 10 – Experimental  $^1\text{H}$  NMR of linker/polymer reaction. Synthesis of 2-(4-(4-((6-hydroxyhexyl)amino)benzyl)phenyl)-1,3-dioxoisindoline-5-carbonyl chloride. DMSO- $d_6$  solvent. 400 MHz.

### *Linker-Fluorophore reaction*

#### 9-anthroic acid

Initial understanding of precursor materials was gained through experimental and computational methods. To set a baseline, proton NMR predictions were made using the built-in computation of ChemDraw 17. Proton NMR for 9-anthroic acid was computed to reveal general peak position in order to analyze experimental data faster. The general reaction schemes using 9-AA involved esterification and the carboxylic acid functional group. Knowing the relative position of the hydroxy hydrogen in the NMR spectrum made understanding reaction products quick. Estimated

$^1\text{H}$  NMR position for this reaction indicator to be around 12 ppm. The anthroic hydrogens were predicted to exist around 8.78 (1H, s), 8.16 (2H, d), 8.01 (2H, d), 7.59 (2H, t), 7.55 (2H, t). For further practical reasons and to improve accuracy of the rough calculations, solvent proton NMR was used to analyze 9-anthroic acid. Figure 11 shows the results of such analysis and reveals that the hydroxy group exists a little higher on the shielding axis.  $^1\text{H}$ -NMR in  $\text{DMSO-d}_6$   $\{\delta, \text{ppm}\}$ : 13.85 (1H, s), 8.71 (1H, s), 8.13 (2H, d), 8.02 (2H, d), 7.61 (2H, t), 7.55 (2H, t). Peaks found at 3.30 (2H, d) and 2.47 (6H, t) indicate the DMSO solvent used and its non-anhydrous nature.

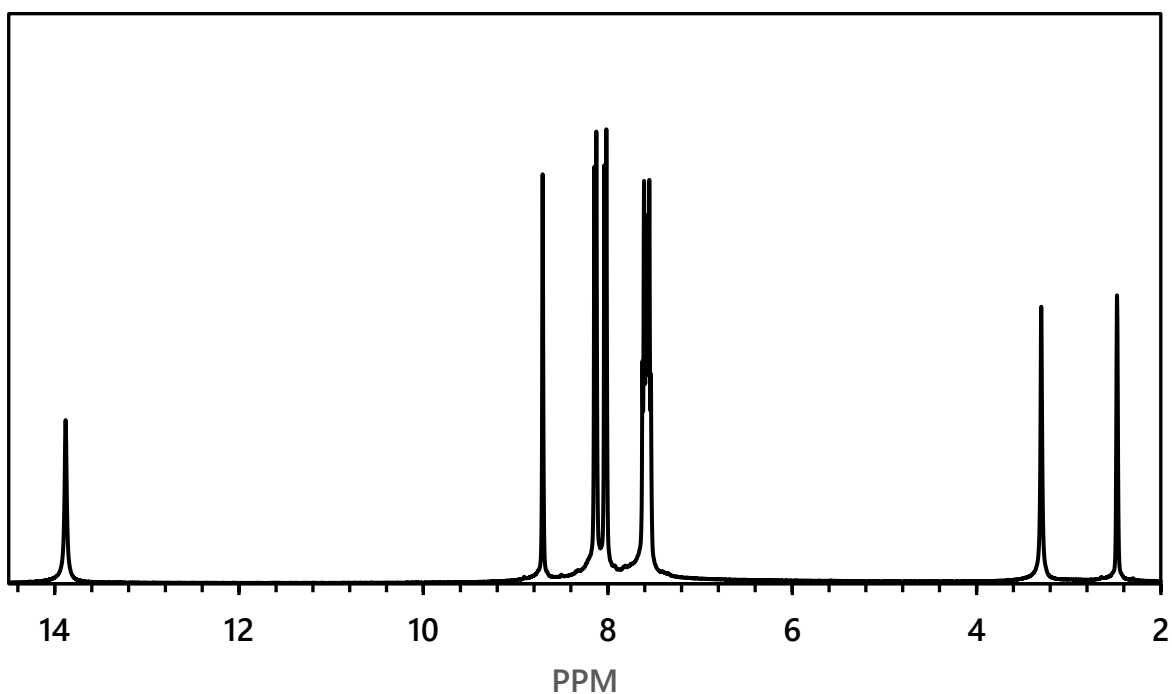


Figure 11 – Experimental  $^1\text{H}$  NMR of 9-anthroic acid.  $\text{DMSO-d}_6$  solvent, 400 MHz.

MH003

After work-up was complete this reaction provided 187 mg of material. this reaction was setup to provide a potential maximum yield around 900 mg. The yield of this reactions is not sufficient for production of a PI-anthracene derivative. FTIR spectra reveal the standard work-up to not removed unreacted 9-anthroic acid. this is shown with the broad O-H stretching from  $3500\text{-}3000\text{ cm}^{-1}$ . The methanol wash provides a yield that has removed 9-AA but shows that DHU still remains with

large peaks at  $2929\text{ cm}^{-1}$  and  $2852\text{ cm}^{-1}$ . The methanol wash did remove DCC from the standard work-up signified by the disappearance of N=C=N stretching not present at  $2115\text{ cm}^{-1}$  in the following spectra.

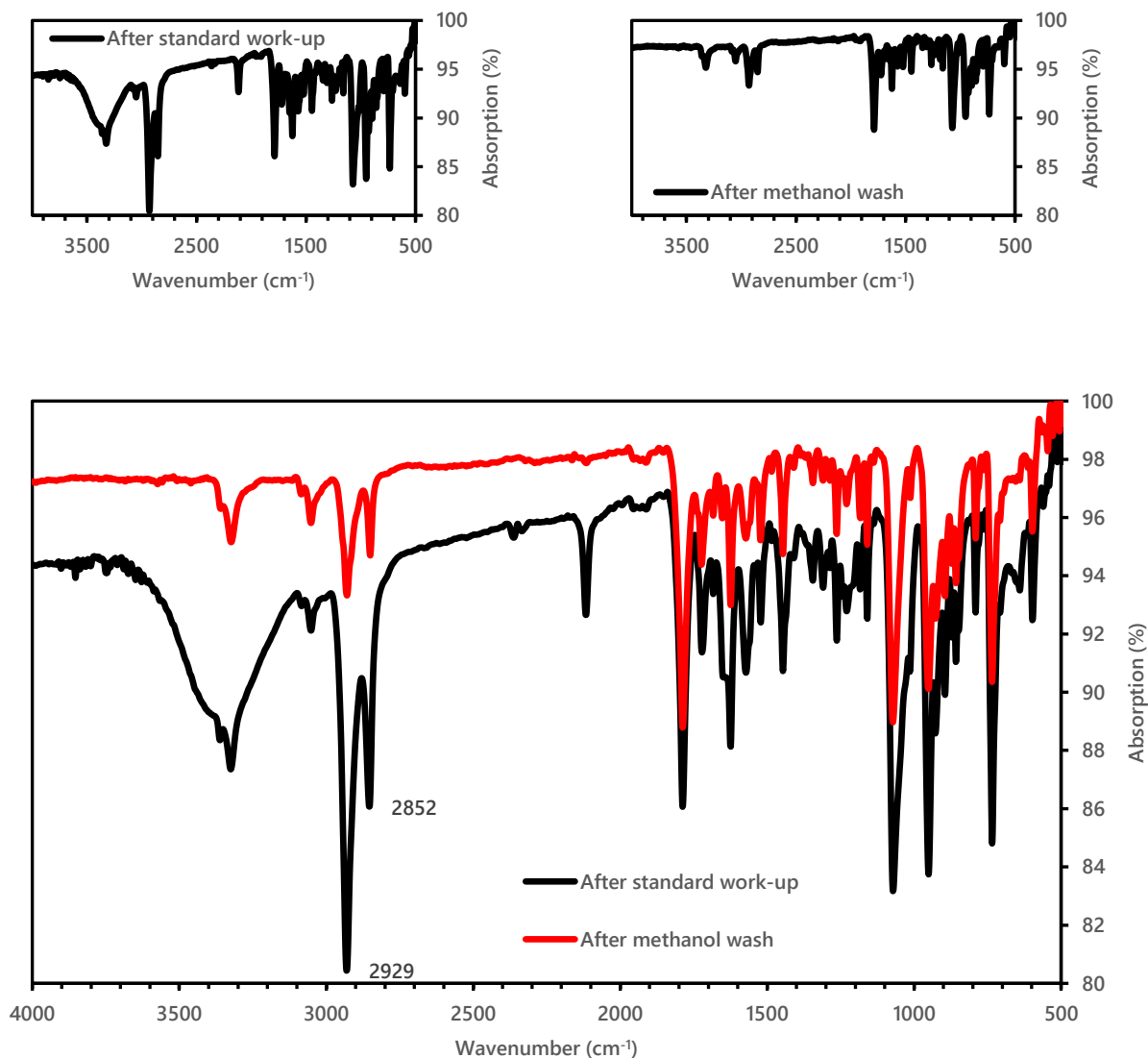


Figure 12 – FTIR spectra comparing before and after methanol wash of sample MH003

Proton NMR reveals no presence of the hydrogen belonging to 9-AA signifying that unreacted 9-AA was removed with the full work-up procedure. The anthracene rings are represented by signal counts around 7-8 ppm. Previous NMR predictions indicated that the associated hydrogens of the 1 and 6 carbons along the hexyl chain should appear at 4.33 ppm and 3.52 ppm, respectively. These peaks are not present in appropriate magnitude with comparison to their neighboring and associated protons. This indicates a failure to mate 6-bromo-1-hexanol with 9-anthracic acid.

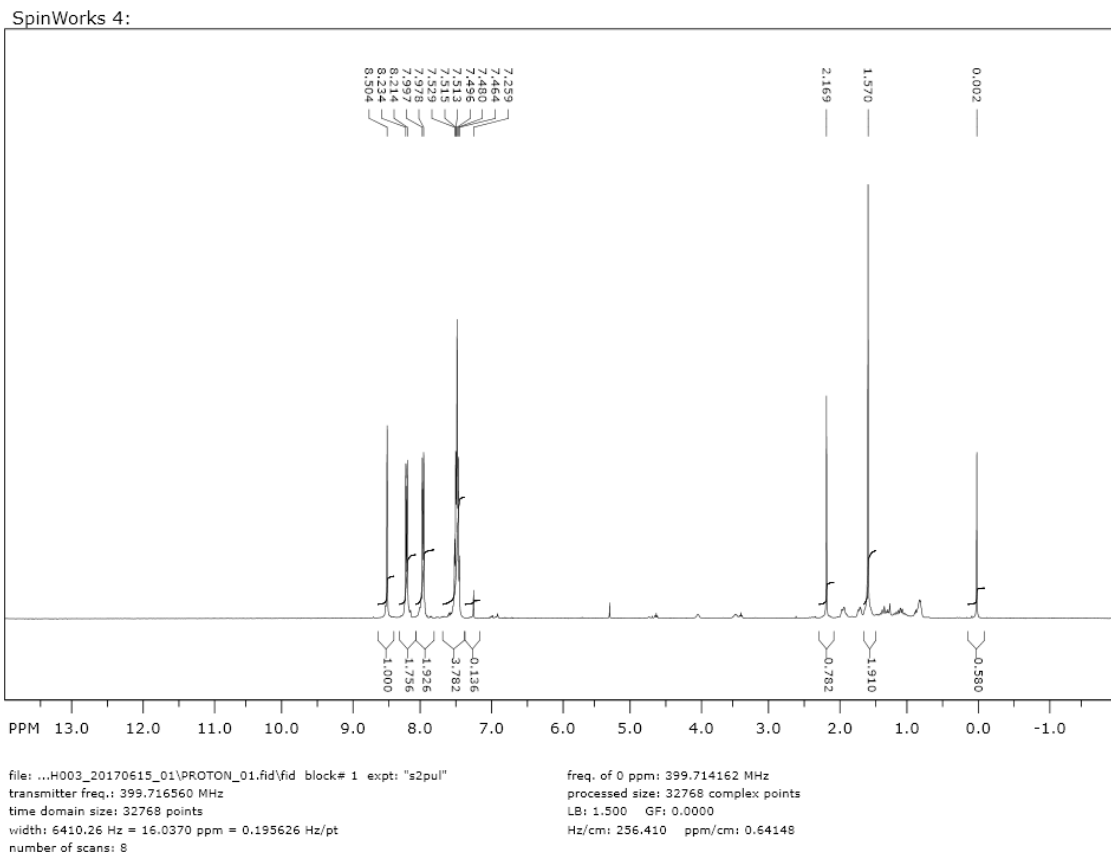


Figure 13 – Experimental proton NMR of 6-bromohexyl anthracene-9-carboxylate work-up (MH003). 400 MHz, DMSO-d<sub>6</sub>.

#### MH004

This scaled-up reaction of MH004 provided no better success with functionalization or a significant yield improvement.

#### MH033

Gravity filter precipitate FTIR results (Figure 14) provide secondary amine peak at 3322 cm<sup>-1</sup> indicating the transition of DCC to the intermediate, O-acylisourea, and finally, onto the stable dicyclohexylurea (DHU) identified by this peak. This is further supported by 1624-1568 cm<sup>-1</sup> indicating C=C cyclic alkene presence and 2927-2850 cm<sup>-1</sup> presenting C-H alkanes. This implies that an esterification process has taken place and that the first filtrate contains unwanted material.

The minor peak appearing at  $2116\text{ cm}^{-1}$  suggests a small amount of DCC remains in this work-up step. The portion of the work-up that remained in DCM solution was dried via rotary evaporation and washed over with hexanes through a gravity filter.

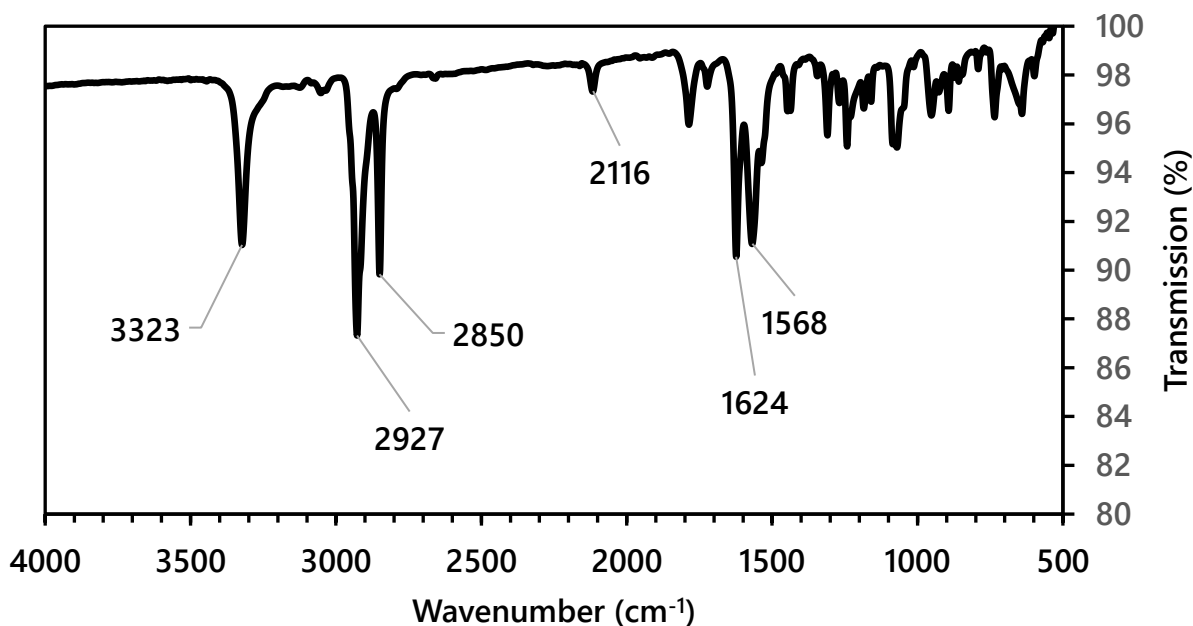


Figure 14 – FTIR spectrum of MH033 anthracene-linker work-up presenting precipitate from first gravity filter.

FTIR spectrum of the considered product showed broad peak formation from  $3300\text{-}2500\text{ cm}^{-1}$  indicating O-H stretching from carboxylic acid.  $2800\text{-}2500\text{ cm}^{-1}$  present the overtone and combination bands of O-H, further suggesting remanence of carboxylic acid. C-H stretching from alkanes in the hydrocarbon linker could also be located in this region, but obscured (medium peak  $3000\text{-}2840\text{ cm}^{-1}$ ). The strong peaks present at  $1786\text{ cm}^{-1}$  and  $1724\text{ cm}^{-1}$  are attributed to C=O stretching.  $1624\text{ cm}^{-1}$  appears still, indicating a possible presence of DHU, but much weaker than found in previous sample.

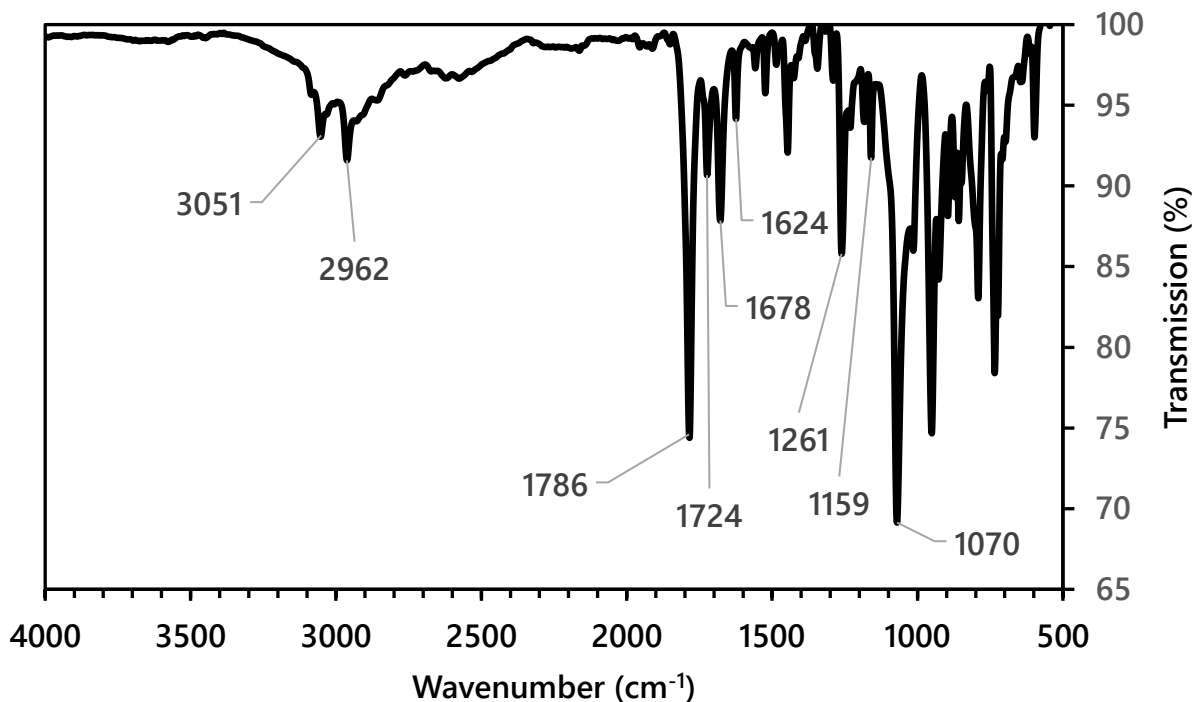


Figure 15 – FTIR spectrum of MH033 anthracene linker work-up presenting dried filtrate after hexanes wash.

The presence of DHU in the reaction work-up suggested that an esterification process had taken place. The counterpoint to this being the remanence of carboxylic acid O-H groups indicating that the precursor 9-anthroic acid remain in high volume. the current work-up was insufficient to isolate the 6-bromohexyl anthracenecarboxylate product in order to certify its formation.

#### Concluding Remarks

This design method did not present a clear pathway forward for reliable and scalable synthesis for a functionalized polymer-based fluorescent dye. synthesis yields were too low in volume for what was required for device manufacturing. Purity was another concern as multiple washing methods were needed to obtain usable material yet complete removal of DCC and DHU remained unachievable. Because the synthesis for the anthracene linker and PI-anthracene derivative had proven insufficient thus encouraging the experimentation with functionalizing PDMS with the

same fluorescent molecule as an alternative. The advantage of this process is that it is a one-step synthesis to add the fluorescent molecule into the polymeric network. PDMS has as long history as a material used in thin-film and patterning applications, ideal for the current device strategy.

## PDMS APPROACH

### Discussion

In an effort to simplify synthesis and still produce a workable polymer-based fluorescent dye product, the material backbone was changed to PDMS. Termination ends of -OH and -NH<sub>2</sub> were selected for esterification and condensation single step reactions, respectively. Both reactions were tested for yield and reliability.

### Characterization (-OH terminated PDMS)

#### *MH047*

Multiple wash cycles were performed for the work-up of PDMS-anthracene synthesis. With the product residing in the first filtrate after gravity filtering and dried via rotary evaporation (Figure 16 black). Following a wash with water and ethanol (Figure 16 red) the product remained in the precipitate signified by the strong C=O stretching at 1786 cm<sup>-1</sup>. DCC is seen in the filtrate from three peaks of 3325 cm<sup>-1</sup>, 2927 cm<sup>-1</sup>, and 2850 cm<sup>-1</sup>. DCC also appears at 1626 cm<sup>-1</sup> and 1574 cm<sup>-1</sup>. DCU appears to remain in the precipitate based on peak positions at 3321 cm<sup>-1</sup> (Figure 16 black) and 3319 cm<sup>-1</sup> (Figure 16 red). After a final wash with chloroform, it appears that reaction catalysts and byproducts have been removed from the product. A weak peak remains (Figure 16 yellow) at 3049 cm<sup>-1</sup> indicating possible O-H stretching from alcohol terminated PDMS. This indicates that not all precursor material was used-up in the reaction. This is supported by the primary alcohol C-O stretching present at 1070 cm<sup>-1</sup> in the same spectrum. It is possible that 1568 cm<sup>-1</sup> is an obscured aromatic C=C indicating the presence of anthracene and being inseparable from DCC post reaction.

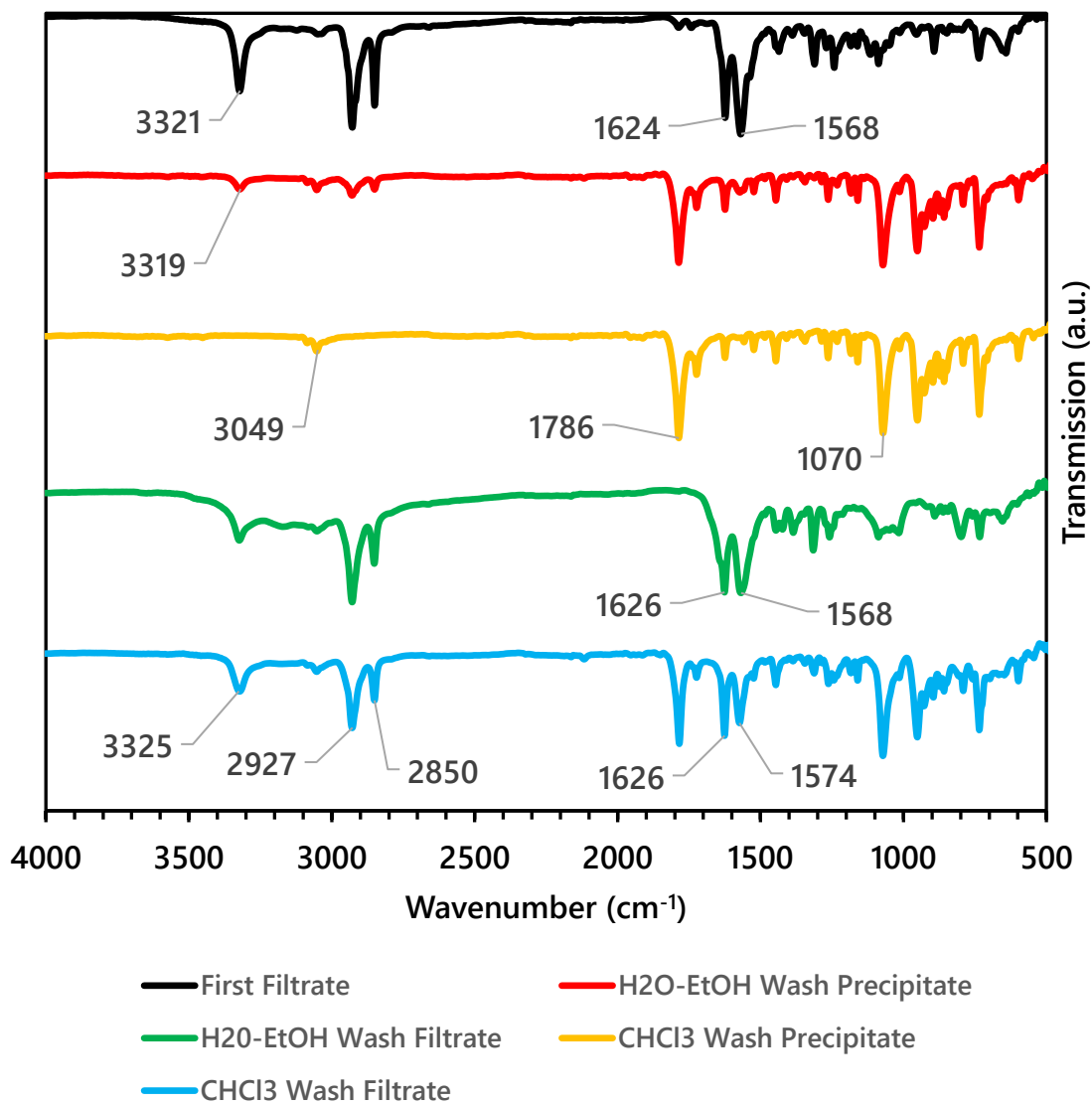


Figure 16 – FTIR presenting all work-up stages of PDMS-anthracene synthesis MH047.

Proton NMR shows the presence of both PDMS and anthracene. The -OH signaling peak defining 9-AA is not present around 13.85 ppm indicating again that there is no precursor 9-AA material in this sample. 1.949 ppm indicates the presence of -OH termination from the PDMS revealing that work-up has not sufficiently removed unreacted PDMS. This may not be too much of a problem as long as fluorescence performance remains. 0.077 ppm presents the PDMS backbone of CH<sub>3</sub>. Taking the average molecular weight of the PDMS material to be around 550 g/mol, the integration

of this peak should be 21x more. This is due to the average chain length being 7 units long and containing 6 hydrogens per unit compared to the 2 hydrogens capping the ends of the polymer. From Figure 17 the integration of proton signal from the PMDS backbone does not satisfy the relation to the chain ends. A much greater emphasis is placed upon signal from the alcoholic chain ends.

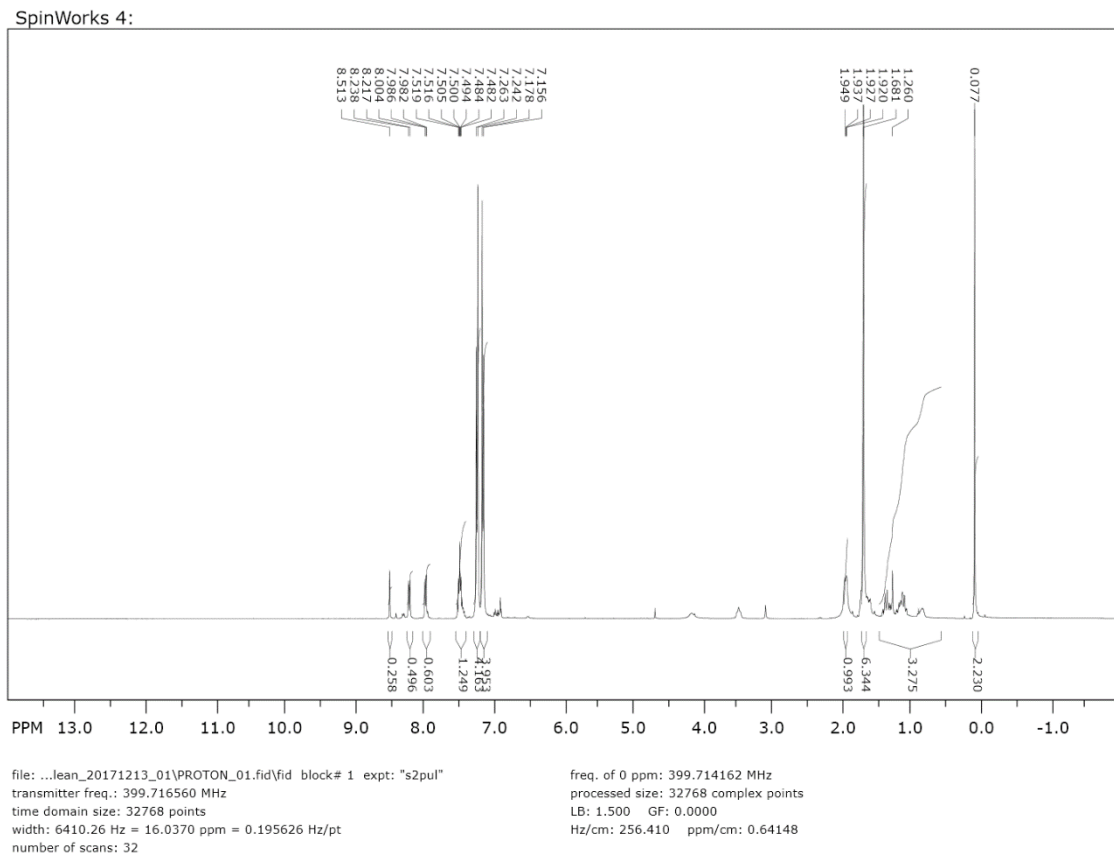


Figure 17 – Experimental proton NMR: PDMS-anthracene. DMSO-d<sub>6</sub> solvent. 400 MHz.

Following synthesis, confirmation of fluorescence was studied through UV-vis and Fluorescence. UV-vis spectral analysis (Figure 18) revealed characteristic peaks of anthracene with most intensity around 365 nm. Fluorescence spectrum (Figure 19) showed broad emission with a poorly

resolved peak intensity maximum at 475 nm. Comparing these spectra to 9-anthracene carboxylic acid confirmation can be made that fluorescent functionalization was successful.

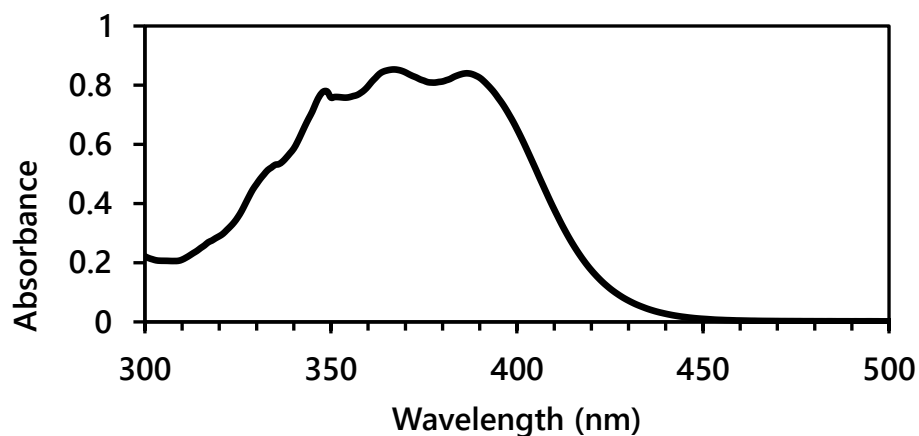


Figure 18 – UV-vis: PDMS-anthracene in chloroform

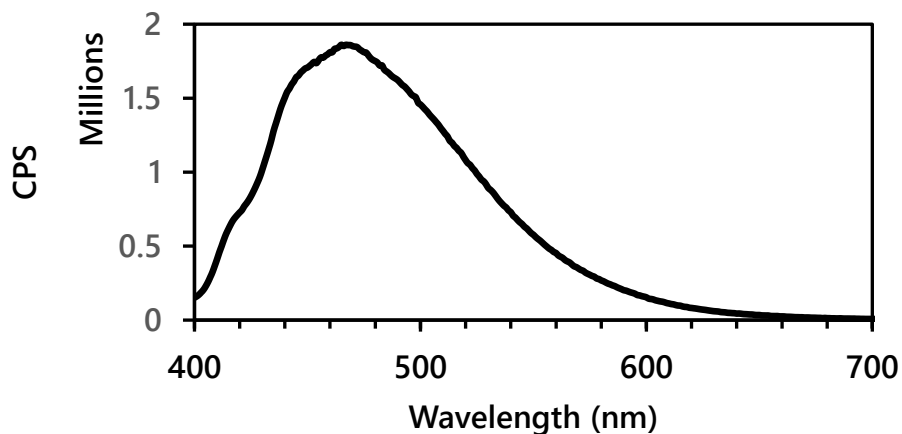


Figure 19 – Fluorescence: PDMS-anthracene. In chloroform. Excited at 365 nm.

*MH094*

Figure 20 presents FTIR spectrum of the filtrate after hexanes wash. Peaks from DCC are present at  $2961\text{ cm}^{-1}$ ,  $2931\text{ cm}^{-1}$  and  $2120\text{ cm}^{-1}$ . Indication of aromatic C=C is present with a weak and broad peak centered around  $1567\text{ cm}^{-1}$ . This argument can be further bolstered the description of appears in the work-up notes presenting the dried appearance of this material as yellow. The PDMS

backbone is also present with Si-CH<sub>3</sub> stretching at 1257 cm<sup>-1</sup> and 789 cm<sup>-1</sup>, and Si-O-Si stretching at 1011 cm<sup>-1</sup>. With no indication of -OH groups between 3500-2800 cm<sup>-1</sup>, there is a good chance that a functional product remains in this filtrate.

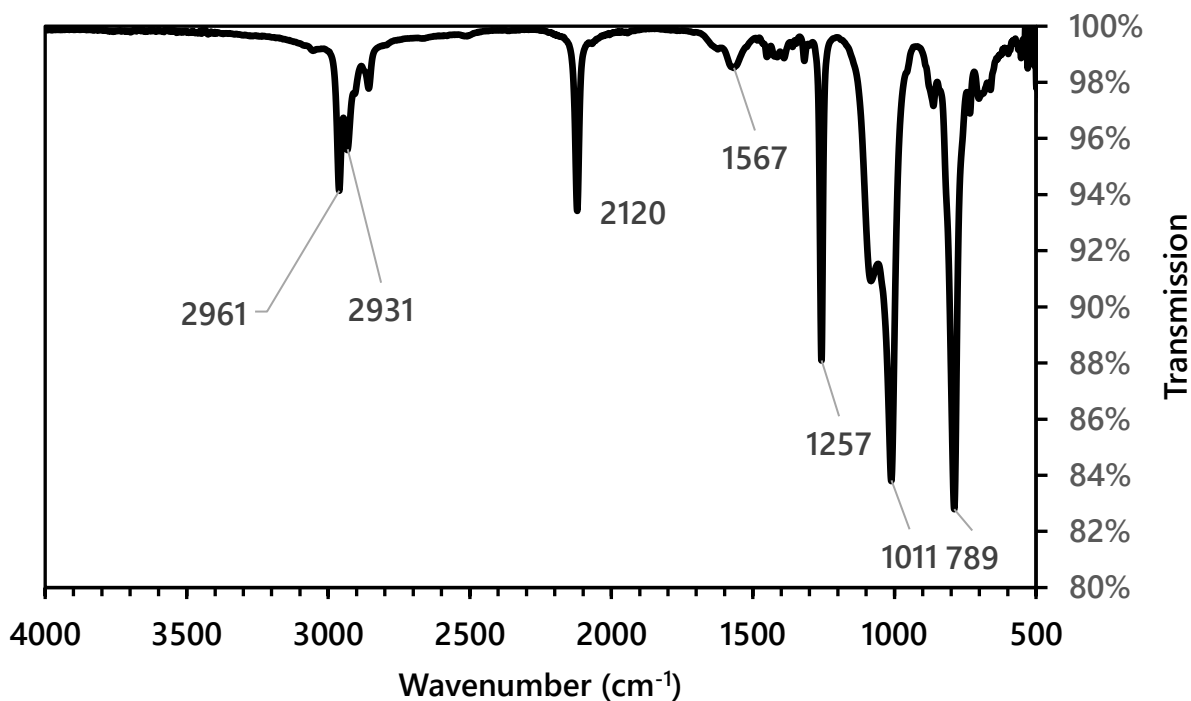


Figure 20 – FTIR presenting PMDS-anthracene work-up filtrate after hexanes wash.

The post methanol wash (Figure 21) filtrate shows strong indication of DCU from peak at 3320 cm<sup>-1</sup>, 2926 cm<sup>-1</sup>, 2850 cm<sup>-1</sup>, 1625 cm<sup>-1</sup>, and 1572 cm<sup>-1</sup>. PDMS indicators are still present at 1258 cm<sup>-1</sup>, 1014 cm<sup>-1</sup>, and 795 cm<sup>-1</sup>. Strong presence of convincing stretching from aromatic C=C is unconfirmed.

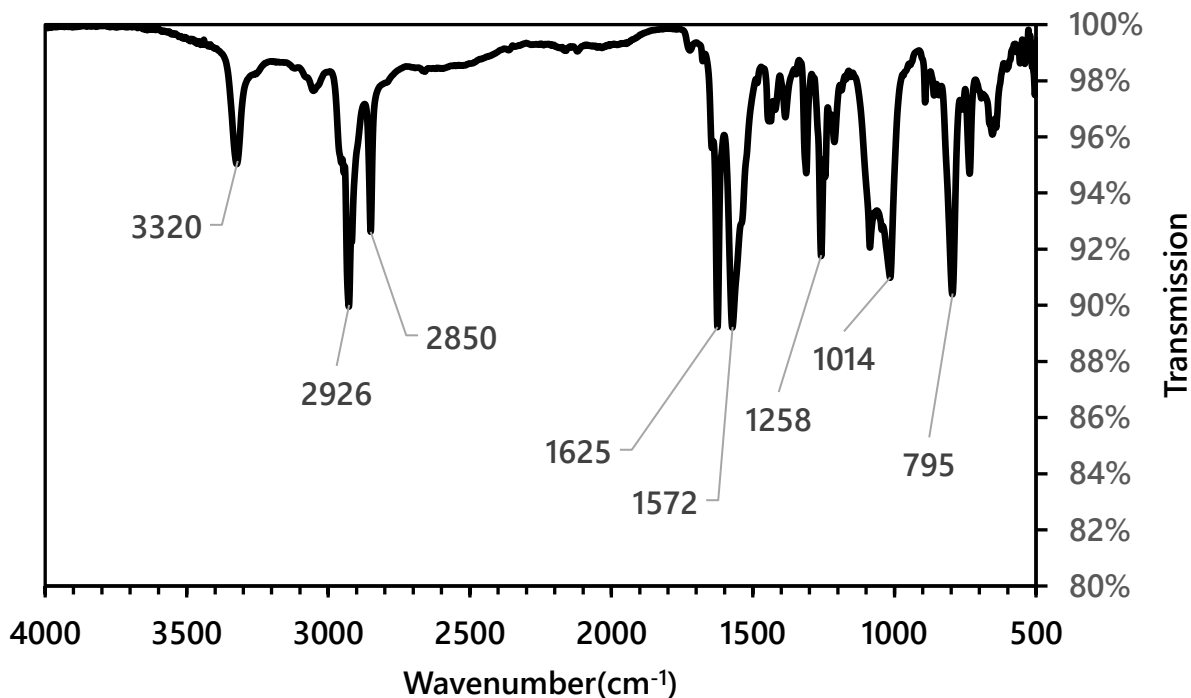


Figure 21 – FTIR presenting PDMS-anthracene work-up filtrate after methanol wash.

#### Summary (-OH terminated PDMS)

Multiple experiments were run for this synthesis sporadically over many months. A consistent problem remained poor yield and an inability to separate a clean product from DCC or non-functionalized PDMS. Three different polar aprotic solvents were tested to add variation to solubility of involved materials. Non resulted in clear front-runner for high yield. The problem regarding DCC and DCU are their similar properties to the desired compound. It would seem at this point a different esterification protocol should be considered.

#### Characterization (-NH<sub>2</sub> terminated PDMS)

##### *MH095*

Pre-wash precipitate from work-up presented as a near-white powder. FTIR analysis of material signifies significant presence of DCU (Figure 22) in this part of the work-up. After Hexane wash,

presence of DCU was reduced greatly in filtrate yet remained in small part in precipitate. Hexane filtrate showed presence of DCC. The appearance was yellow and waxy. This appearance is a strong indicator of anthracene and significant presence of PDMS. PDMS indicators are still present at  $1257\text{ cm}^{-1}$ ,  $1017\text{ cm}^{-1}$ , and  $790\text{ cm}^{-1}$  in both precipitate and filtrate. The yellow color both filtrate and precipitate after hexane wash is supported by the FTIR with the presence of C=C aromatics.

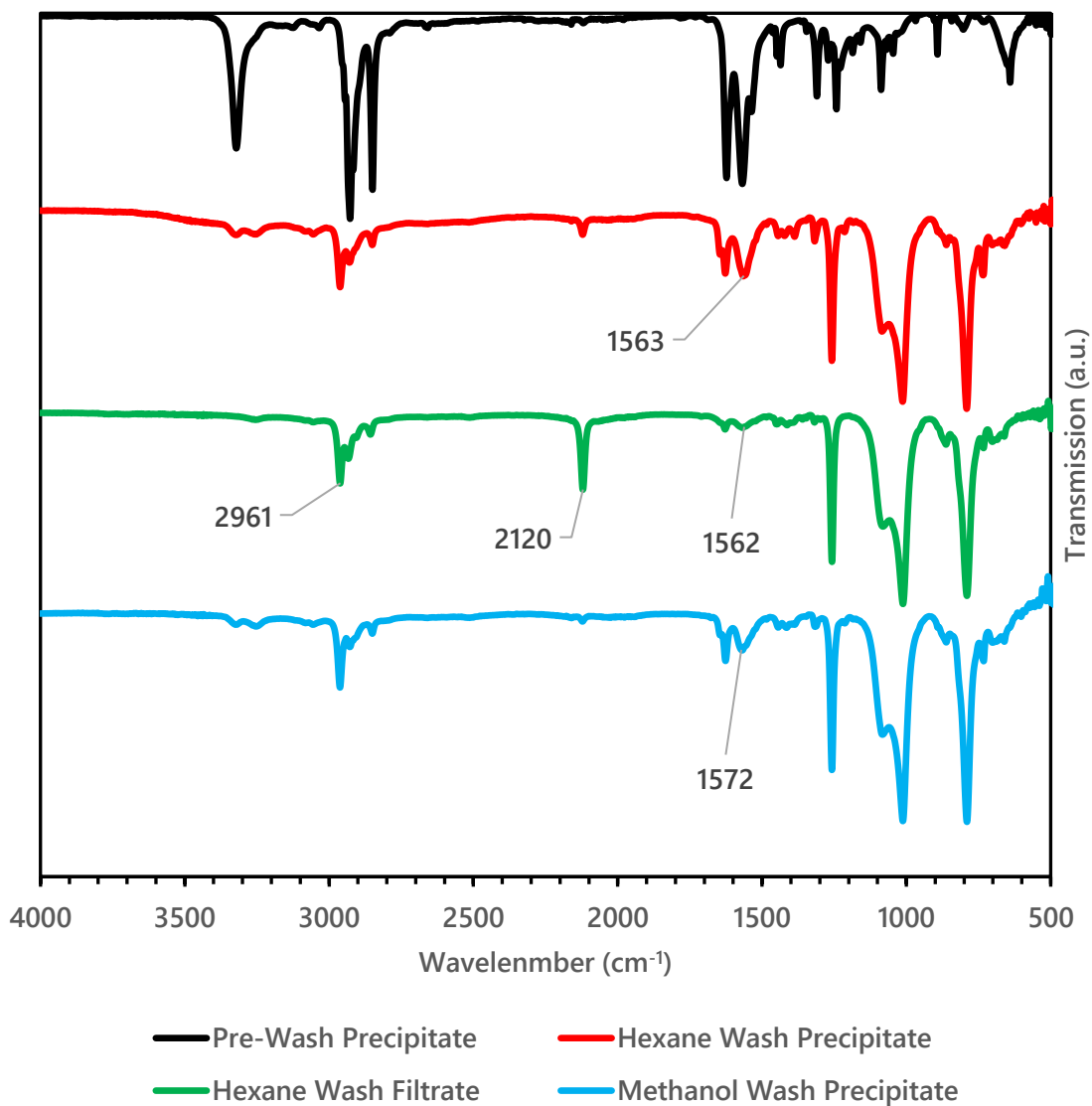


Figure 22 – FTIR presenting all work-up stages of PDMS-anthracene synthesis MH095.

Enough material was present from this reaction scheme to make solutions in chloroform and perform spectroscopic analysis. Figure 23 presents a UV-vis spectrum showing strong vibronic resolution present from the PDMS-anthracene. Fluorescence performance also holds with strong emission from excitation at 350 nm. The peak resolution is close to holding a mirror image. Solvent broadening of the right shoulder of the spectrum is present.

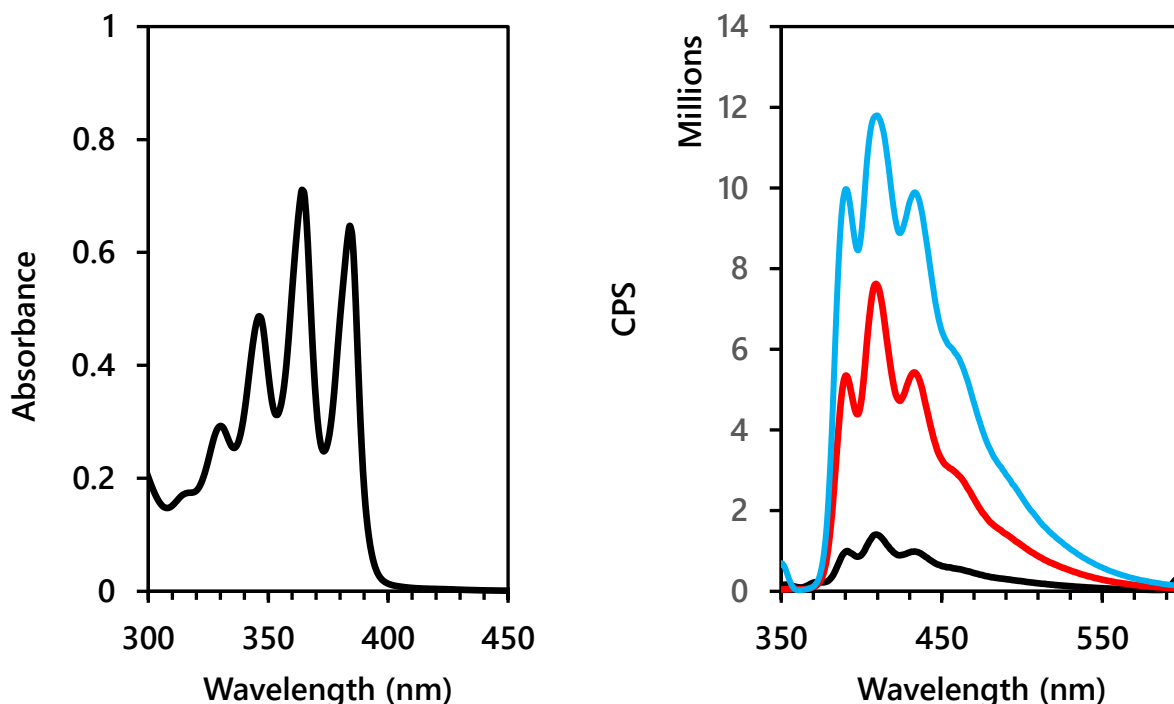


Figure 23 – (left) UV-vis spectrum for final washed material. (right) Fluorescence taken with excitation values at 300 nm (black), 325 nm (red), and 350 nm (blue). Samples dissolved in chloroform.

### *MH108*

Taking further measures in the work-up procedure to remove DCC and DCU from product a cooling stage was introduced. Post reaction, the flask was placed into  $-20^{\circ}\text{C}$  as DCC's solubility is greatly reduced in cold DCM. Filtrate shows clear presence of DCU and precipitate presents clearly with DCC. The precipitate is also the component that retains peaks for PDMS and aromatic groups of anthracene.

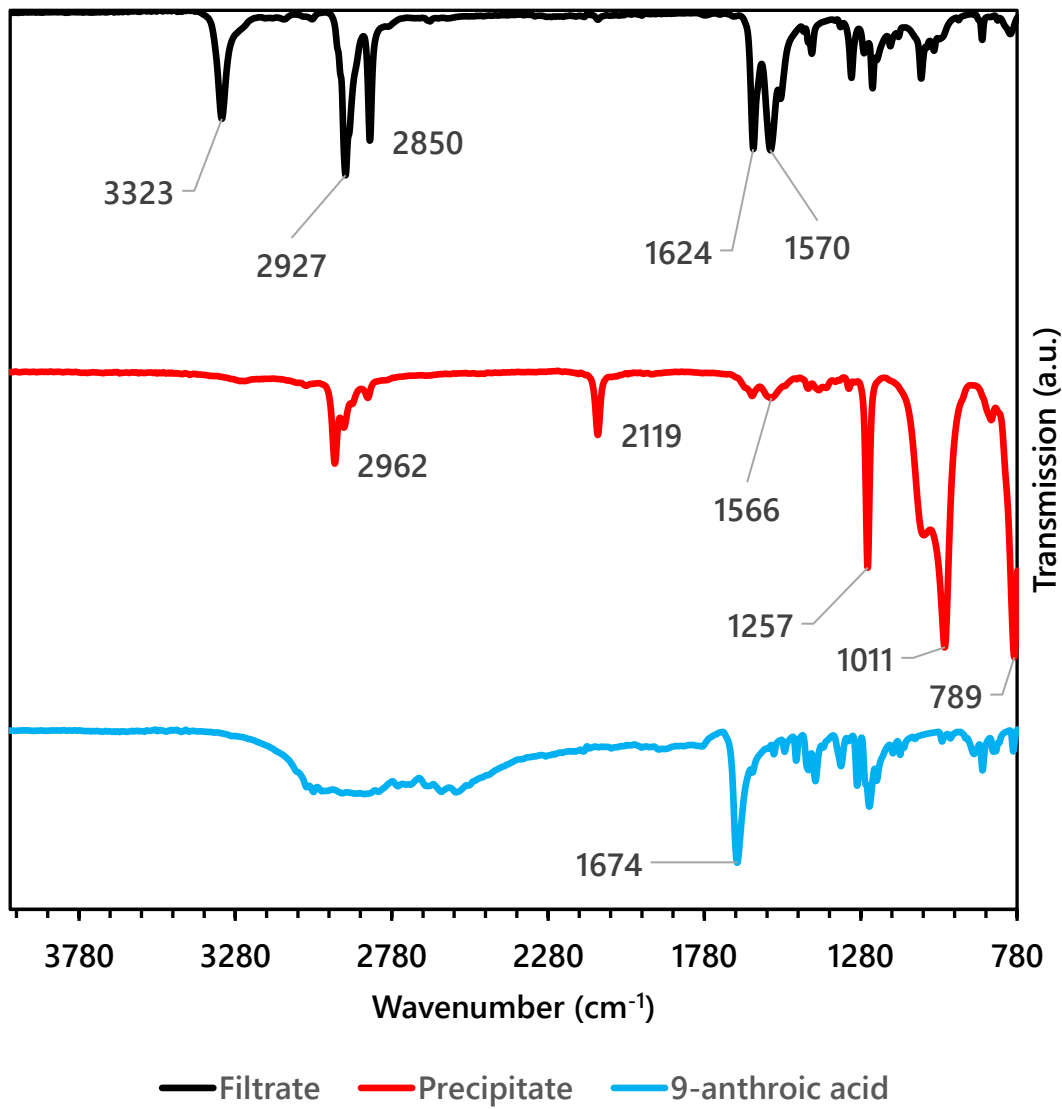


Figure 24 – FTIR presenting precipitate and filtrate from gravity filter after cooling MH108 post-reaction to  $-20^{\circ}\text{C}$ . Comparison with 9-AA provided.

### *MH109*

Matching the synthesis and work-up of MH108, more product was synthesized for NMR comparison to PDMS-NH<sub>2</sub> precursor. Integration calibration was set at peaks around 1.3 ppm as this appears as a stable location for precursor and product measurement. Integration of the polymer backbone around 0.02 ppm shows a ratio of 1:23. Translating this ratio over to Figure 26 presenting NMR data for the precipitate from the work-up of sample MH109 and using the same peak position

for integration calibration it is shown that the ratio drops to half at 1:12. Experimentally, the 1.3 ppm reference appears in a busy part of the spectrum as the work-up procedures are not perfect for purifying product. Figure 27 presents a rerun of this sample and isolates the 3.4 ppm and 2.3 ppm. Predictive NMR calculated that these two values should be associated with the same protons. Under functionalization of PDMS by 9-AA, greater shielding is provided to the final CH<sub>2</sub> before the secondary amine shifting the proton signal higher. The presence of both peaks indicates a partial functionalization of the PDMS in this sample. The ratio of these signal is determined to be very near 1:1.

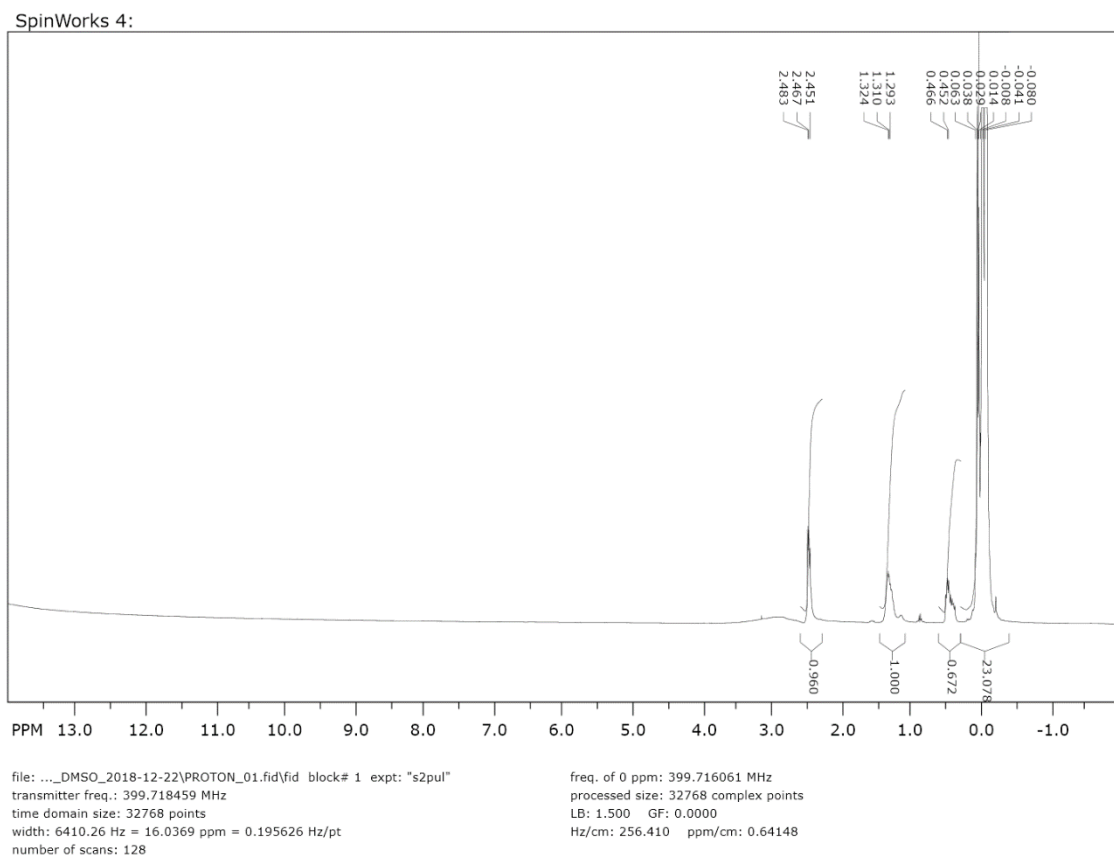


Figure 25 – Proton NMR taken of PDMS-NH<sub>2</sub> in DMSO-d<sub>6</sub>. 400 MHz.

SpinWorks 4:

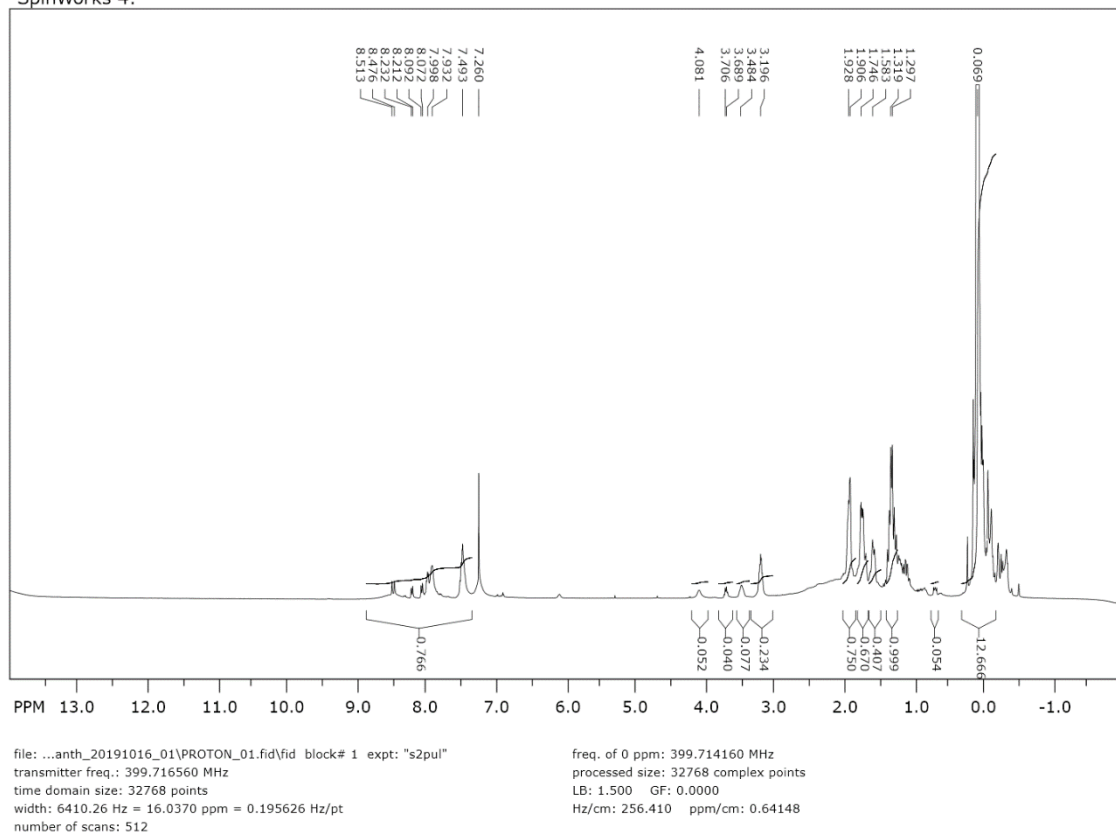


Figure 26 – Proton NMR taken of precipitate product from MH109 in  $\text{CDCl}_3$ . 400 MHz.

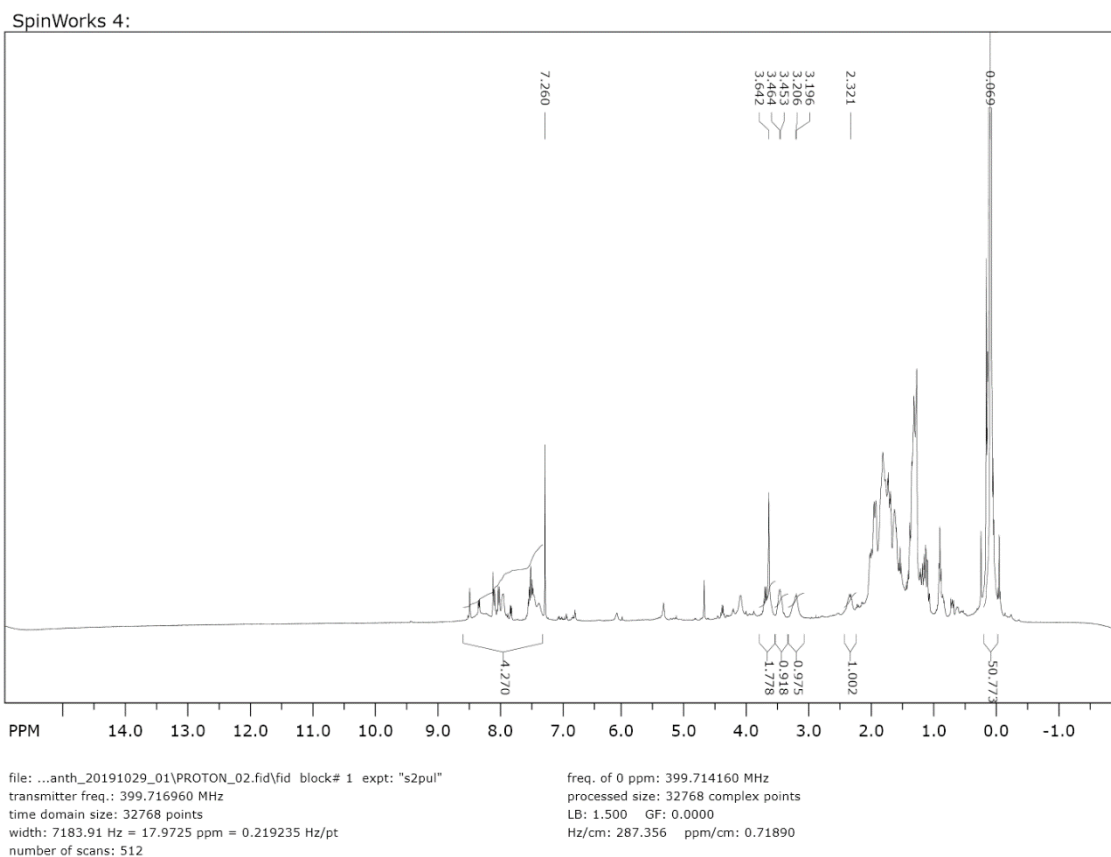


Figure 27 – Proton NMR taken of precipitate product from MH109 in  $\text{CDCl}_3$  (rerun). 400 MHz

The work-up had enough material to again test absorption and fluorescence performance. Samples were less concentrated than those run from MH095. Concentrations of 25  $\mu\text{g/mL}$  were used for both UV-vis and photoluminescence. Vibronic resolution was present for absorbance spectrum but there was a significant yield loss in fluorescence. It is possible that sample had photobleached over the period of work-up and analysis.

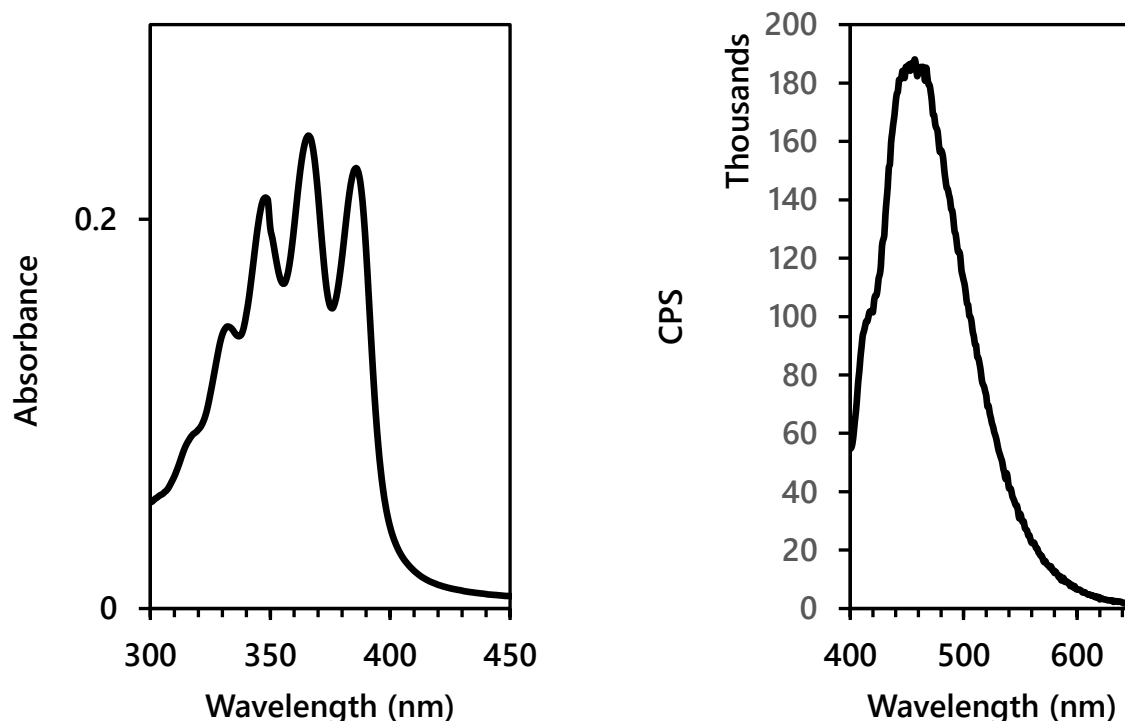


Figure 28 – (left) UV-vis for precipitate of MH109. (right) Fluorescence for precipitate of MH109. Excited at 375 nm. Solvated in chloroform.

#### Summary (-NH<sub>2</sub> terminated PDMS)

With the minor modification to synthetic scheme consistency of some yield from this reaction type was improved. The amine group proves to be a strong nucleophile and does not require DMAP as previously needed to accelerate the kinetics of the alcohol-based functionalization reaction. There are still persistent difficulties with DCC remaining within the product isolate after wash procedures and ‘freezing’ to encourage a crash out of solution from DCM. Given the crude purity of this product and low yield, further experimentation with thin-film fabrication is set to a minimum. Presented here is still a potential of viability for this product as there is proof of PDMS-anthracene functionalization across FTIR, NMR, and photo-spectrometry analysis. Some material was confirmed functional and in quantity large enough to test with photospectroscopy. Overall, reactions were not reliably repeatable, and yields were typically too low for device fabrication

trials. Reactions MH105 and MH108 appeared to provide the best relative result from yield, appearance and analytics.

### Thin-Film Results

Thin-film measurements of PDMS-anthracene were produced using quartz substrates. Material from MH109 was used for the PDMS-anthracene and MH106 (sample from generic synthesis not explicitly analyzed in this work) for PDI-silane. They were compared to PDI-silane thin films and an attempt to blend both solutions together is presented (Figure 30). Concentrations of stock solution were increased to saturation to provide the most fluorescent signal possible. Concentrations were around 25 mg/mL, but not accurately measured due to filtration of a small amount of insoluble material. Spectra taken present raw data (Figure 29). The quality of such measurements was hindered by material availability creating difficulty with preparation as non-ideal concentrations were used for spin-coating. Furthermore, substrate alignment with detector is key to viable results and with no fine tuning available with the current apparatus, consistency for measurement is not present. Via the same casting techniques used in the isolated study (Figure 29), the layered thin films present a significant decrease in fluorescence intensity for both moieties. To many factors exist to conclude a reason for such results as measurement alignment, layer wash-off, and surface modification for the second coating all vary outcome.

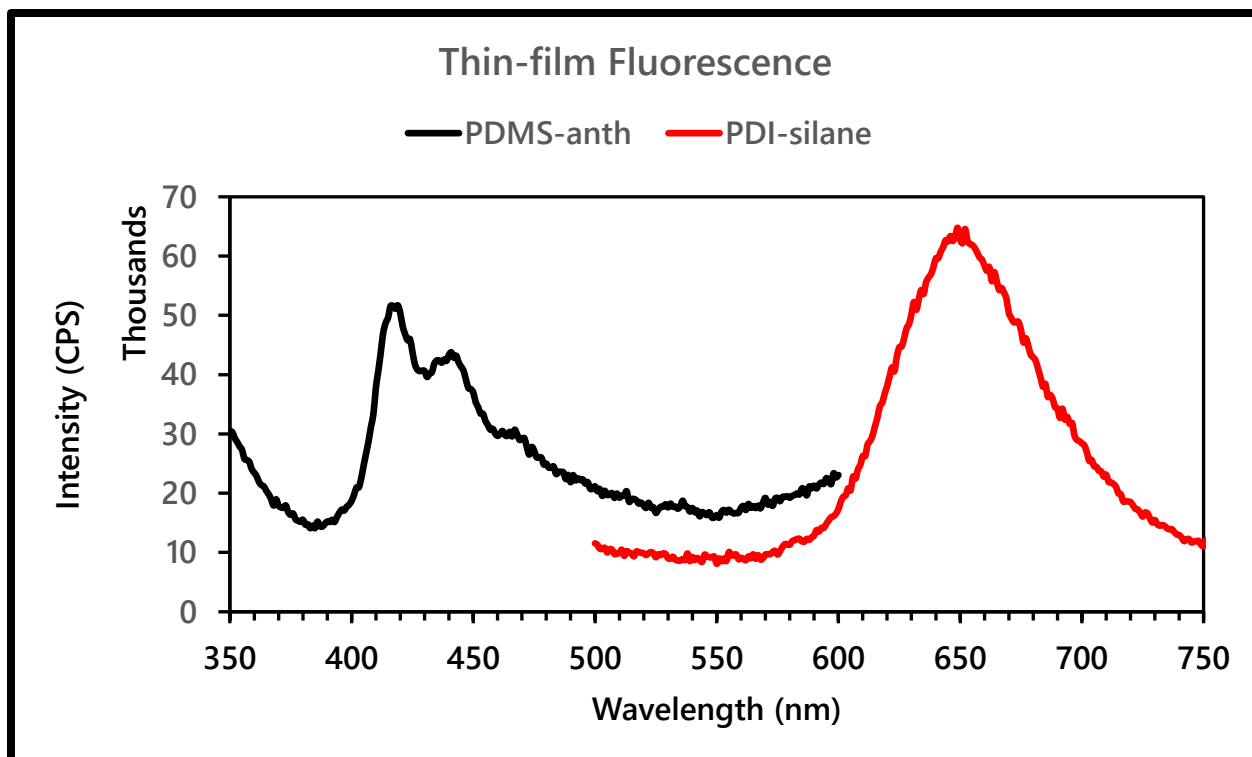


Figure 29 – Thin-films were produced on 25x25 mm quartz slides via a spin-coating method. 100  $\mu$ L of solution was cast and processed at 1000 rpm for 30 seconds.

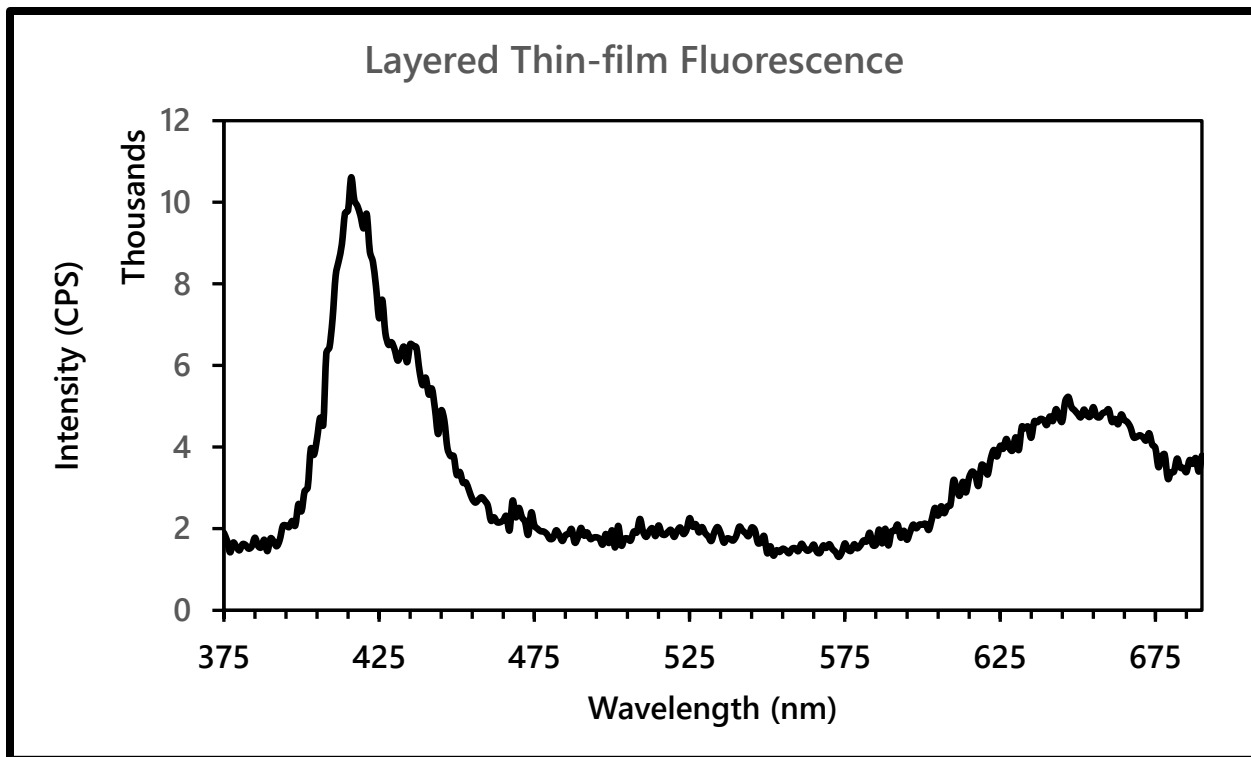


Figure 30 – Fluorescence for layered films of PDMS-anthracene and PDI-silane

## CHAPTER VI: PERYLENE DERIVATIVES

### ACCEPTOR CHARACTERIZATION AND PERFORMANCE

This section focuses on the synthesis and workability of the accepting component of the energy transfer system. It discusses the process of creating the PTCDA derivative known as PDI-silane, and the subsequent nanoparticle evolution PDIB-siloxane. To repeat, the creation of these materials is not novel to this work. Some modifications have been made to synthesis procedures that have not been published and could be considered incremental improvements and new. Furthermore, nanoparticle diameter was reduced using from prior literature limits using synthesis modifications, which again, could be considered as a new incremental improvement.

#### PDI-SILANE

##### Discussion

This section will discuss synthesis of PDI-silane and PDI-BS nanoparticles, and thin film formation of both materials.

##### Characterization

The purified product was characterized via FTIR and NMR to reveal structural confirmation of a successful synthesis. Infrared spectrum presents C-H at 2973-2883  $\text{cm}^{-1}$ , C-O at 1693  $\text{cm}^{-1}$ , Si-C at 1344  $\text{cm}^{-1}$ , and Si-O at 1072  $\text{cm}^{-1}$ .

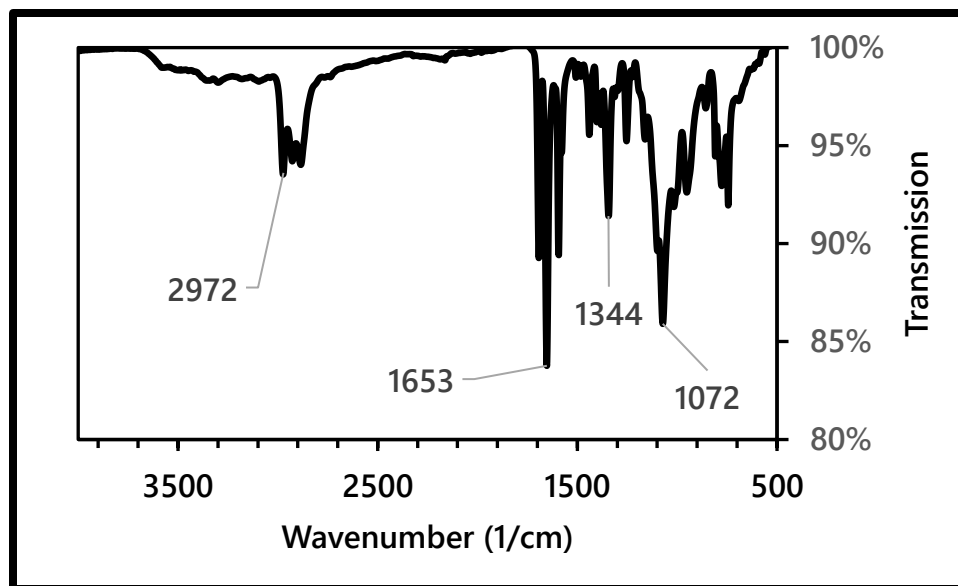


Figure 31 – FTIR spectrum of PDI-silane after synthesis

Previous literature synthesizing PDI-silane does not provide  $^1\text{H}$  NMR for reference<sup>17</sup>, only solid state carbon and silicon references exist. To aid in characterization, Chemdraw was used to simulate proton NMR results. The simulated reads,  $^1\text{H}$ -NMR in  $\text{CDCl}_3$   $\{\delta, \text{ppm}\}$ : 0.56 (2H, d), 1.39 (6H, d), 1.55 (2H, t), 3.72 (2H, d), 3.83 (6H, d), 7.85 (4H, d), 8.15 (4H, d). Experimental NMR provides fair agreement positionally with recorded peaks. The ratio of silane to perylene structure is marginally imbalanced implying unreacted 3-APTEOS remains in sample.



does not seem to affect fluorescence however, as the emission spectrum does not reflect this band in Figure 7. For FRET, acceptor absorption spectrum retains the majority of function information. Specifically, the spread of light absorption. From Figure 33 the spread of PDI-silane's absorption starts near ultra-violet and drops rapidly after 550 nm. It should be noted that PDI-silane can be excited and fluoresce via any one of these wavelengths of light.

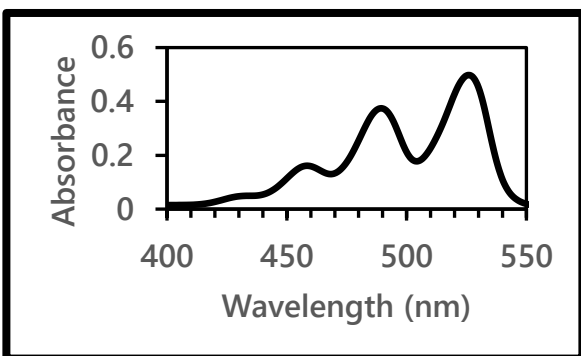


Figure 33 – UV-vis spectrum data for PDI-silane

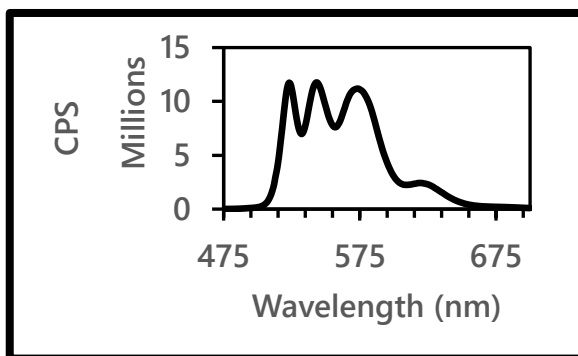


Figure 34 – Fluorescent spectrum data for PDI-silane. Excitation wavelength at 457 nm.

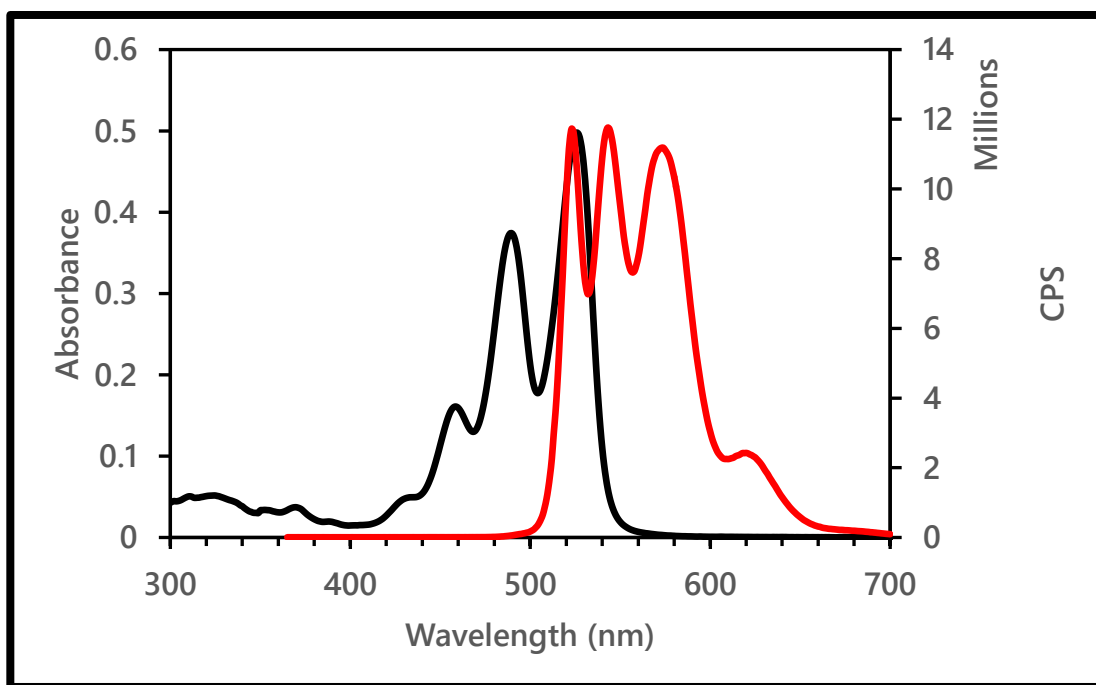


Figure 35 – Absorption and emission overlap for PDI-silane. Excitation wavelength set to 457 nm.

#### Concluding remarks

Synthesis of PDI-silane was successful in volume appropriate for experimentation. photophysical characteristics are good for the intended use for FRET. Absorption band is prominent from 400-550 nm. The emission band exists between 500-675 nm. Overlap of absorption and emission may contribute to complexity of analysis during blend sample analysis when a donor is present.

#### PDIB-SILOXANE NANOPARTICLES

##### Discussion

Expanding upon the run of experiments regarding the synthesis of acceptor nanoparticles, three more experiments were performed. These experiments were initiated to test particle diameter reduction, procedure technique and repeatability of a past procedure. The new experiments are designated MH048, MH050 and MH052.

Experiment MH048 was designed with the reduction in TEOS weight to stunt the maximum growth diameter of the silica particles. Experiment MH050 involved a change to the procedure order with regards to timing of the addition of PDI-silane to the reaction. Instead of waiting 15 minutes after the TEOS has been added to the reaction, the PDI-silane was added immediately after the TEOS. Experiment MH052 was simply completed for the purpose of making material for later thin-film trials. A known procedure was used in order to produce the particles. Coincidentally this was an opportunity for a repeatability test regarding this procedure. I believe it may have been the same batch of PDI-silane for experiment MH042 and MH052, so constant results would show stability of the PDI-silane using our current storage method.

	MH039	MH042	MH043	MH044	MH046	MH048	MH050	MH052	MH056	MH057
<b>ETOH (ANHYDROUS)</b>	40 mL	40 mL	60 mL	60 mL	40 mL	40 mL	40 mL	40 mL	40 mL	40 mL
<b>NH<sub>4</sub>OH</b>	5 mL	10 mL	5 + 5 mL	5 + 2.5 mL	7.5 mL	7.5 mL	7.5 mL	10 mL	0.1 + 0.9 mL	1 mL
<b>TEOS</b>	1 mL	1 mL	1 mL	1 mL	1 mL	0.5 mL	0.5 mL	1 mL	1 mL	0.5 mL
<b>PDI-SILANE</b>	100 mg	100 mg	100 mg	100 mg	100 mg	100 mg	100 mg	100 mg	100 mg	100 mg
<b>CHCL<sub>3</sub></b>	10 mL	10 mL	10 mL	10 mL	10 mL	10 mL	10 mL	10 mL	10 mL	8 mL
<b>SYNTHESIS NOTES</b>	15- minute silica NP synthesis	15-minute silica NP synthesis	Second batch of NH <sub>4</sub> OH was added just after PDI- silane solution. 15- minute silica NP synthesis	Second batch of NH <sub>4</sub> OH was added just after PDI- silane solution. 15- minute silica NP synthesis	15-minute silica NP synthesis	15-minute silica NP synthesis	TEOS and PDI-silane added at the same time; no seeding period for silica NPs	15-minute silica NP synthesis	Second batch of NH <sub>4</sub> OH was added just after PDI- silane solution. 15- minute silica NP synthesis	15-minute silica NP synthesis
<b>PARTICLE DIAMETER</b>	100 – 150 nm PDIB	~250 nm PDIB	~70 nm (silica)  No PDIB NPs	~ 150 nm (silica)  No PDIB NPs	170 nm (silica)  No PDIB NPs	200 – 250 nm (silica)  ~190 nm PDIB	>500 nm  PDIB	240 nm PDIB	~35 nm	~25 nm

Figure 36 – Reaction summary table of PDIB-silane NPs

### *MH048*

This procedure did not produce smooth particles. Growths of PDI-silane or silica can be found on the surface of the particles. Seed silica particles ranged from 200 -250 nm in diameter. The PDIB-silane NPs were below 200 nm in diameter. The 24-hour reaction sample showed very similar results to the 48-hour reaction sample. This suggests that the 48-hour reaction time is not necessary. Five samples of experiment MH048 were imaged under SEM. The silica NP sample showed clean, consistent particle formation with diameters around the 230-nm mark (Figure 37). The 24-hour synthesis sample showed particles with good shape and an apparent reduced diameter. The typical PDI-silane ‘ribbons’ existed intertwined in the sample. The sample was also covered in ‘crumbs’ of PDIB-silane or silica particles. These ‘crumbs’ were mainly found on the PDI-silane ‘ribbons’ (Figure 38). The 48\_hour synthesis sample showed an almost identical scene to that of the 24-hour sample (Figure 39). The sample bearing the washed product shows particle size below 200 nm. The ‘crumb’ particulates remain in the sample, and it appears that they are fused to the larger spherical particles (Figure 40). The supernatant sample showed no sign of particles, only PDI-silane (Figure 41).

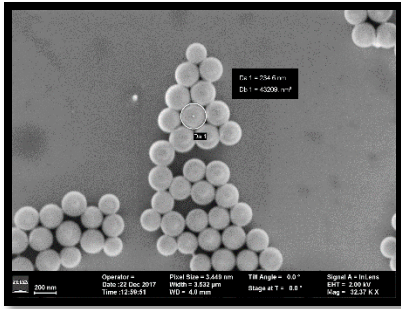


Figure 37 – SEM sample MH048: silica NPs

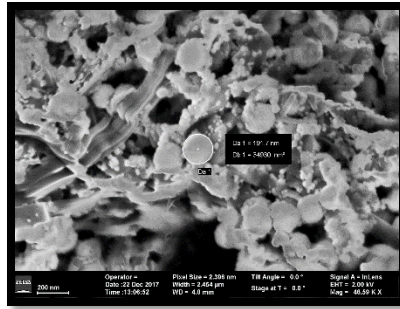


Figure 38 – SEM sample MH048: 24 hours into synthesis

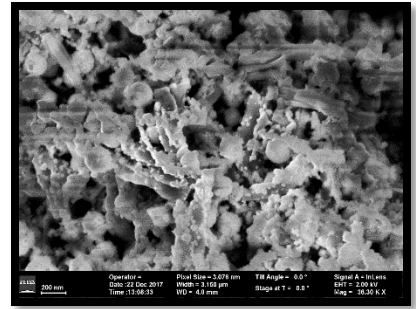


Figure 39 – SEM sample MH048: 48 hours into synthesis

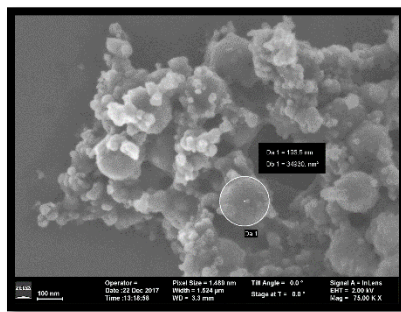


Figure 40 – SEM sample MH048: washed PDIB-silane NPs

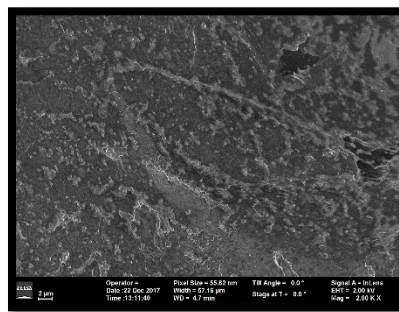


Figure 41 – SEM sample MH048: supernatant

### MH050

This sample had signs, in early stages of the reaction, of smooth particle formation. Throughout the 24-hour reaction, the isolated particles disappeared and bulky clumps of ill-shaped particles were left over. The 0-hour sample showed interesting initial particle shapes. They were not smooth spheres as previously observed. Clumping had occurred in some cases of pre-developed; other locations of the sample showed larger formations of bulky material (Figure 42). The 24-hour synthesis sample shows better particle formation. Smooth particles are present, but diameter distribution is large. Bulky structures still exist on the sample also. Three populations of structure exist in this sample: smooth particles, large bulk structures, and small clumping of pre-developed particles (Figure 43 and Figure 44). The final washed product showed no instances of individual





catalyst and a reduction in TEOS. Both of these factors should lead to reduced particle size but still allowing for integration of the PDI-silane.

#### *MH056*

This experiment should be considered a great success, certainly compared to past results. Particles were generated in abundance and in diameters of 35 nm and a little below. Interestingly, silica particle formation was unrepresentative of the final particle size. Silica particles were large and ill-defined. The samples that were prepared from the first supernatant are most interesting from this procedure. The particles produce a not provoked out of solution with 8000 rpm centrifugation over 30 minutes. This is likely due to their small size. Dried particles formations were present on the sample in huge volumes (Figure 52 and Figure 53). All particles were very uniform and had ideal packing for surface coating (Figure 54 and Figure 55). The volume of particle produce was quite impressive and the formation of canyon like sheets indicates that thin film formation should be achievable. The sample prepared to show silica particle synthesis shows quite different results however. Particles present in this sample are large, over 150 nm, and not well defined. They are smooth yet connected to one another in a melted fashion (Figure 56 and Figure 57).

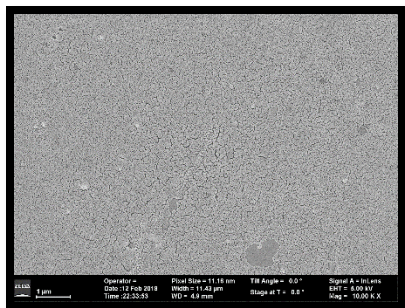


Figure 52 – SEM sample MH056: PDIB-silane NPs, 1st supernatant

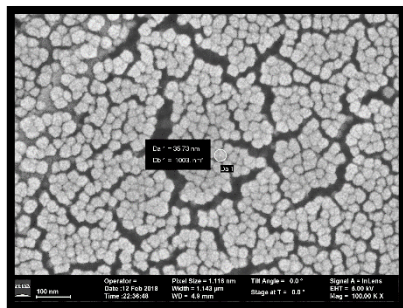


Figure 53 – SEM sample MH056: PDIB-silane NPs, 1st supernatant

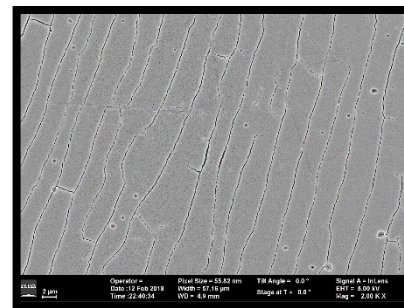


Figure 54 – SEM sample MH056: PDIB-silane NPs, 1st supernatant

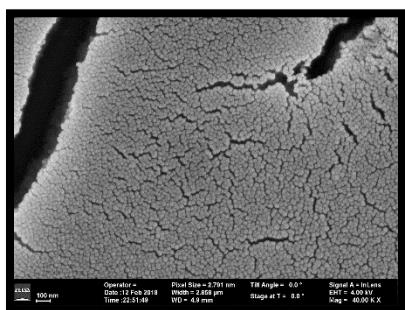


Figure 55 – SEM sample MH056: PDIB-silane NPs, 1st supernatant

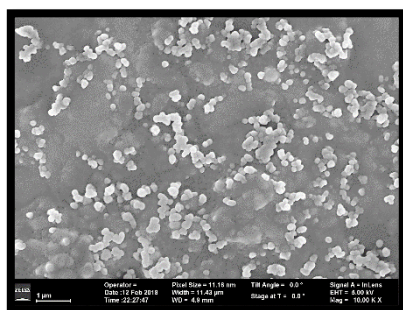


Figure 56 – SEM sample MH056: Silica particles

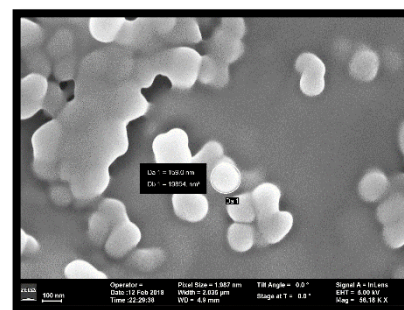


Figure 57 – SEM sample MH056: Silica particles

### MH057

This sample essentially confirms procedure capability of producing particles around the 30-nm mark. It also informs upon the location of these particles being in the 1<sup>st</sup> and 2<sup>nd</sup> supernatant washes. This should decrease work-up time and generally make this procedure more efficient. A step that still needs to take place however is the removal of any unused PDI-silane. There is also interesting growth that difference from previous observations. PDI-silane forms prominent ribbons that end-up covered in particles. These samples need to be reimaged in order to be quantitatively compared to other results due to lack of metadata. Under unfortunate circumstances regarding user interface for the SEM, images for this set of data do could not provide any analytical data. Therefore, as a disclaimer, unknown parameters are as follows: working distance, magnification, line/diameter measurements. Based on experience with the previous sample, MH056, I can

confidently say that these particles are at least similar in radius (Figure 58 and Figure 59). This statement is based upon ease of imaging and limit of sharp focus. Once again, the most abundant particles are found in the first supernatant. These particles are uniform in size and shape, and resemble a raspberry in figure. The first supernatant also contains 'highways' of presumably PDI-silane sheets that are completely coated with smaller particles (Figure 60 and Figure 61). As the sample washes progress, the abundance of particles drops, yet still contains many (Figure 62). With the chloroform washes, supernatant samples just contain PDI-silane formations (Figure 63). The final washed pellet shows clumped particles that are significantly larger than those in the supernatants (Figure 64). The particles are also ill-formed and predominantly found forming around sheets/rods of a different structure.

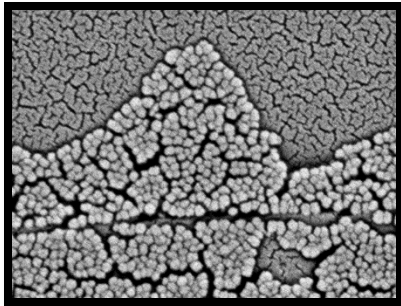


Figure 58 – SEM sample MH057: PDIB-silane NPs, 1st supernatant

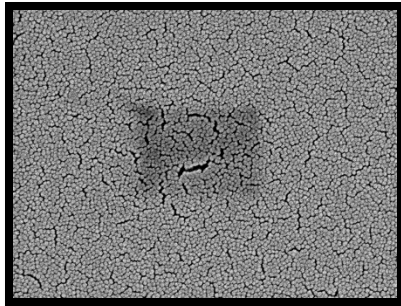


Figure 59 – SEM sample MH057: PDIB-silane NPs, 1st supernatant

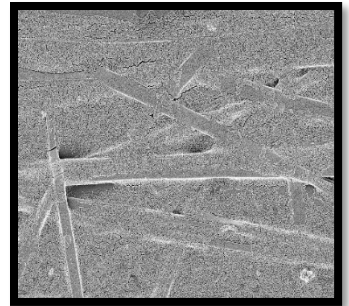


Figure 60 – SEM sample MH057: PDIB-silane NPs 1st supernatant

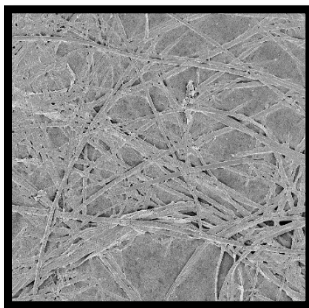


Figure 61 – SEM sample MH057: PDIB-silane NPs, 1st supernatant

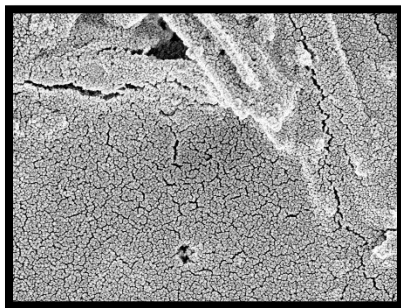


Figure 62 – SEM sample MH057: PDIB-silane NPs, 2nd supernatant

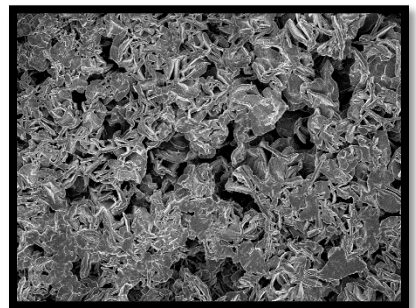


Figure 63 – SEM sample MH057: PDI-silane, 3rd supernatant

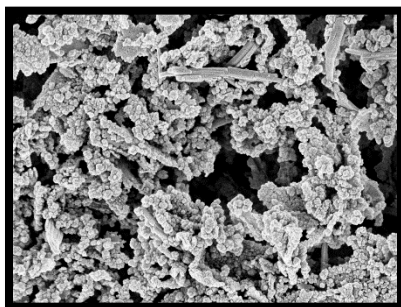


Figure 64 – SEM sample MH057: Final pellet

As seen previously, synthesized particles from reaction MH057 act as a colloid in the ethanol solvent in which the reaction took place. These particles remain colloidal after centrifugation at 8000 rpm from 1 hour. SEM imaging of a sample prepared from the supernatant show particles

around 30 nm in diameter (Figure 65). This sample also contains sheets of PDI-silane that did not crash out under centrifugation (Figure 66). Because the first supernatant is likely to contain chloroform, water, ethanol and ammonium hydroxide, the vial containing this mixture was left open in the hood for a couple of days to allow for evaporation of chloroform and ammonium hydroxide. After the second day, a visible red cloud was present at the top of the vial. This sample was once again placed in the centrifuge for 1 hour at 8000 rpm to make removal of the clean PDIB-silane particles from the PDI-silane cloud easier.

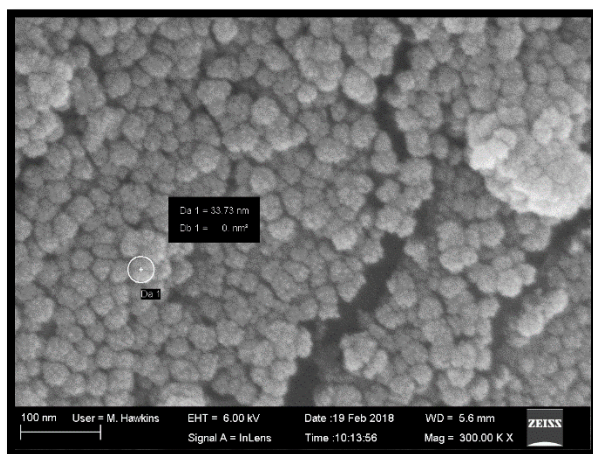


Figure 65 – SEM sample MH057: first supernatant after second centrifugation

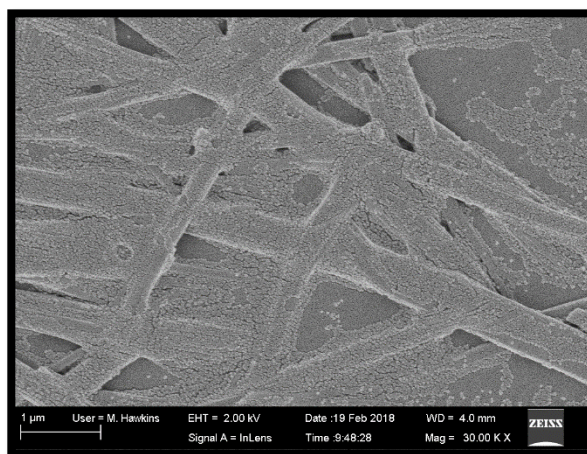


Figure 66 – SEM sample MH057: first supernatant after second centrifugation

### *MH058*

Observation of the sample intending to contain silica nanoparticles, taken from the reaction after 15 minutes, revealed very little in terms of well-defined spheres. The closest structures resembling spheres found on the sample were clearly made from aggregates of smaller particles (Figure 67). A cause is possibly the mechanism for smooth particle formation has been hindered due to general insufficient access to the ammonium hydroxide. The same sample imaged under the Zeiss microscope solidifies the argument that isolated particles are not significantly present on this sample (Figure 68 and Figure 69). Moving to the sample taken from the 24-hour reaction volume, the representative concoction of components is observed. A large mass of PDI-silane sheets are present and typically covered in particle averaging 30 nm in diameter (Figure 70, Figure 71 and

Figure 72). In regions where PDI-silane sheets are not prevalent, the nanoparticles take on two forms. Firstly, they are found in large, thick, cracked, sheets resembling a dried salt bed (Figure 73 and Figure 74). Secondly, they can appear in a monolayer form with two packing structures: groups of closely packed particles make up the larger structure of the monolayer (Figure 75). After centrifugation, the monolayer formations still exist (Figure 76 and Figure 77). Remaining PDI-silane takes on a javelin shape and tends to group into star-like formations (Figure 78). These structures do have particle on their surface but with lower density (Figure 79). The centrifugation brings a new form of particle aggregation also, particle can be found in large bulk concentrations with random structure (Figure 80 and Figure 81).

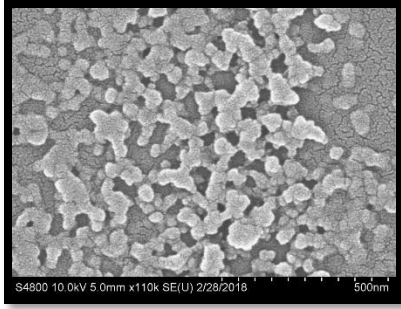


Figure 67 – Hitachi SEM sample MH058: silica nanoparticle formations

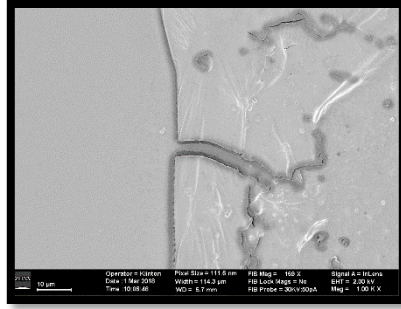


Figure 68 – Zeiss SEM sample MH058: dried silica plate

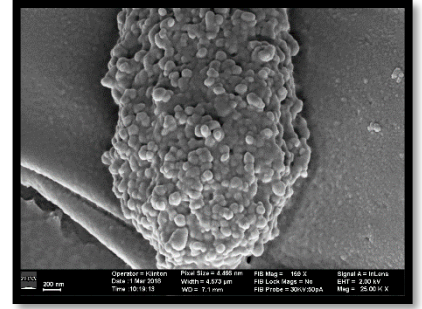


Figure 69 – Zeiss SEM sample MH058: silica particle clump

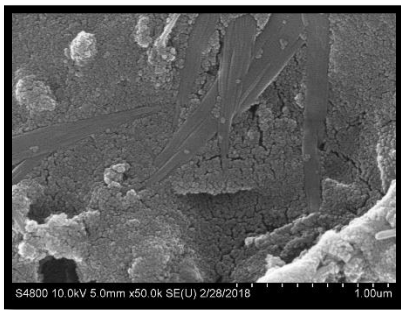


Figure 70 – Hitachi SEM sample MH048: 24-hour reaction sample

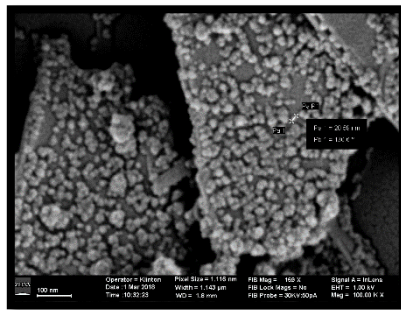


Figure 71 – Zeiss SEM sample MH058: 24-hour reaction sample

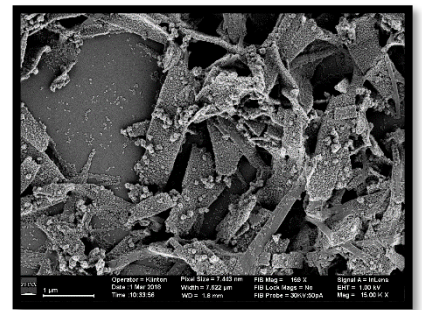


Figure 72 – Zeiss SEM sample MH058: 24-hour reaction sample

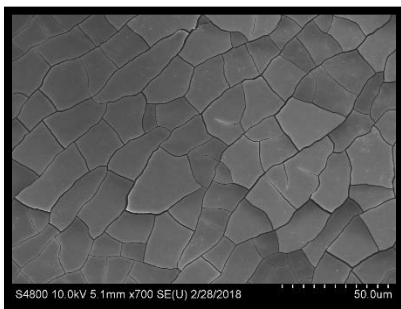


Figure 73 – Hitachi SEM sample MH058: 24-hour sample, PDIB-silane sheets

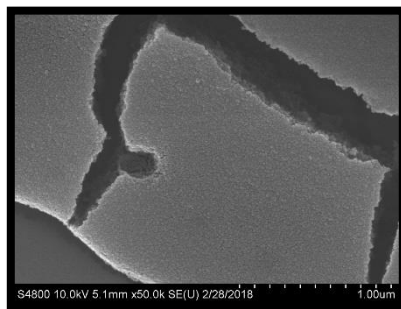


Figure 74 – Hitachi SEM sample MH058: 24-hour sample, PDIB-silane sheets

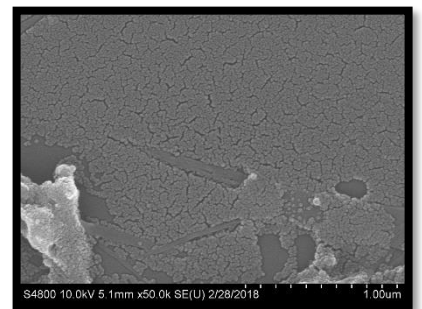


Figure 75 – Hitachi SEM sample MH058: 24-hour sample, PDIB-silane monolayer

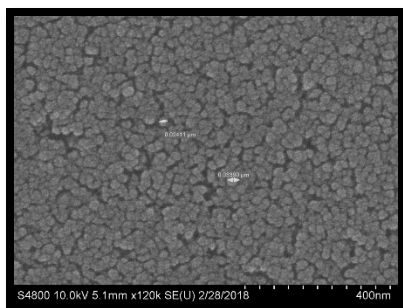


Figure 76 – Hitachi SEM sample MH058: centrifuged sample, PDI-silane nanoparticle layer

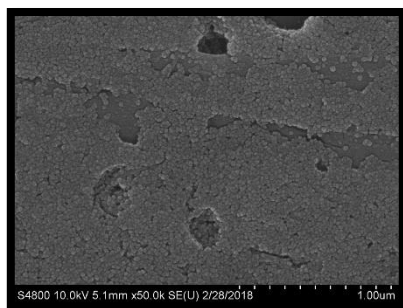


Figure 77 – Hitachi SEM sample MH058: centrifuged sample, PDI-silane nanoparticle layer

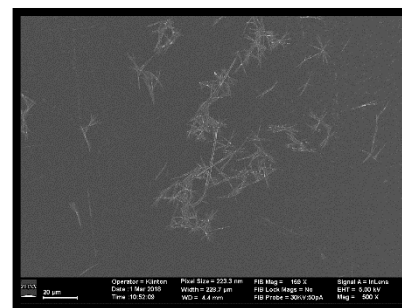


Figure 78 – Zeiss SEM sample MH058: centrifuged sample, PDI-silane 'javelins'

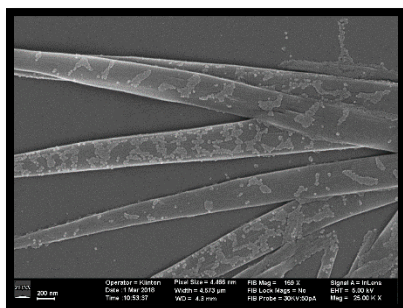


Figure 79 – Zeiss SEM sample MH058: centrifuged sample, PDI-silane 'javelins'

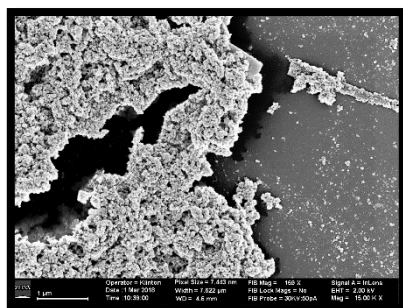


Figure 80 – Zeiss SEM sample MH058: centrifuged sample, PDI-silane 'javelins'

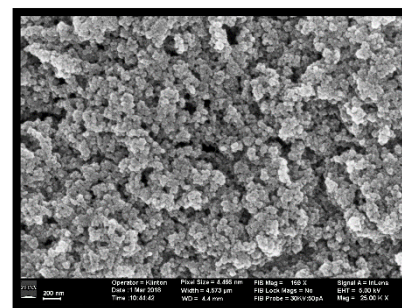


Figure 81 – Zeiss SEM sample MH058: centrifuged sample, PDI-silane 'javelins'

## Characterization

A fascinating observation regarding the fluorescent emission (Figure 82 right) of the PDI-B NPs is the disappearance of the distinct peaks that are present for the PDI-silane monomers. An explanation for the formation of a single peak emission is best understood through resonant strain. The siloxane network formation from PDI-silane has the benefit of loading more fluorescent molecule per particle radius than any surface functionalization. Yet simultaneously, those molecules are resonantly constrained. The distinct peaks from perylene-3,4,9,10-tetracarboxylic dianhydride can be resolved only when the molecule is not under mechanical strain. The nanoparticle system presented here offers a very strenuous environment for the fluorescent

molecule. This data presents strong indication that the siloxane particles formed are indeed fully integrated with PDI and not just surface functionalized.

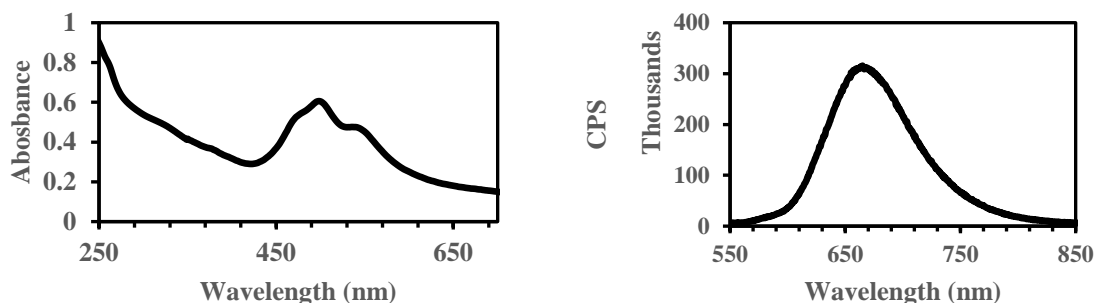


Figure 82 – (left) UV-vis spectra of PDIB-NPs. (right) Fluorescent spectra of PDIB-NPs. Excitation wavelength set to 457 nm (right)

PDI-B nanoparticles produced from this reaction have minimum diameter of 20 nm and a maximum around 30 nm. SEM imaging (Figure 83 left) has confirmed a smooth and typically spherical particle morphology. As previously realized from fluorescent spectra, the PDI-B nanoparticles have PDI molecules loaded throughout the particle. This can also be observed via TEM imaging (Figure 83 right) as dense nodes are present in the core of each particle. These dense nodes resemble tightly packed PDI-silane molecules interspersed in the siloxane network.

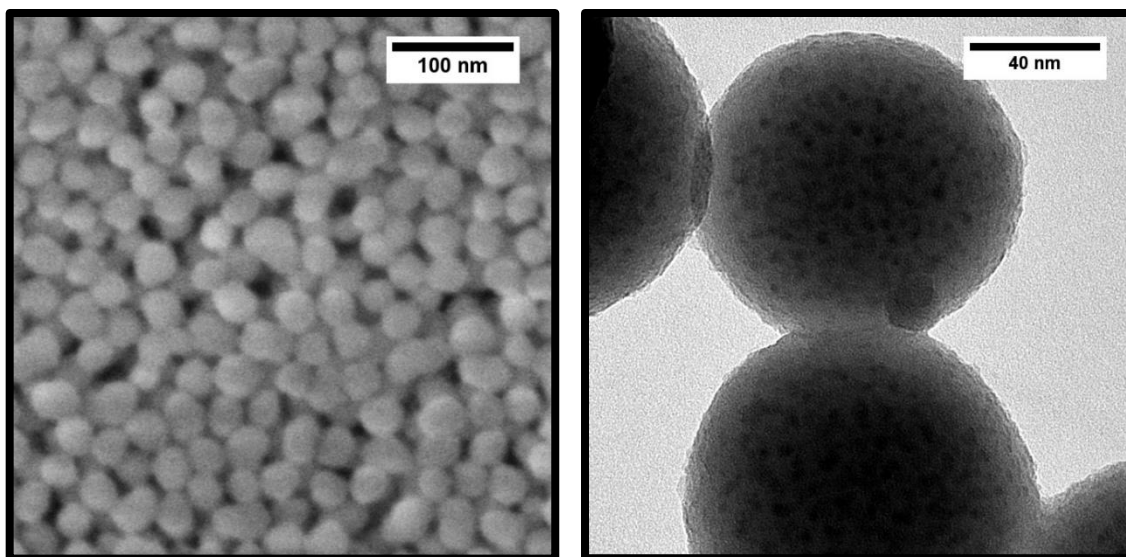


Figure 83 – (left) PDIB-NPs imaged under SEM. 10kV accelerating voltage, x220k magnification. (right) PDIB-NPs imaged under TEM.

#### Further Trials

##### *MH104.1*

Pellet showed no definable particles (Figure 84 top). Material present was conglomerated bulk. Solution showed particle formations as expected from slow centrifugation speed (Figure 84 bottom). Particles seemed a little clumped, but borders were clear. Average measured diameter was just under 25 nm (Table 4). This is a good reproduction of past experiments.

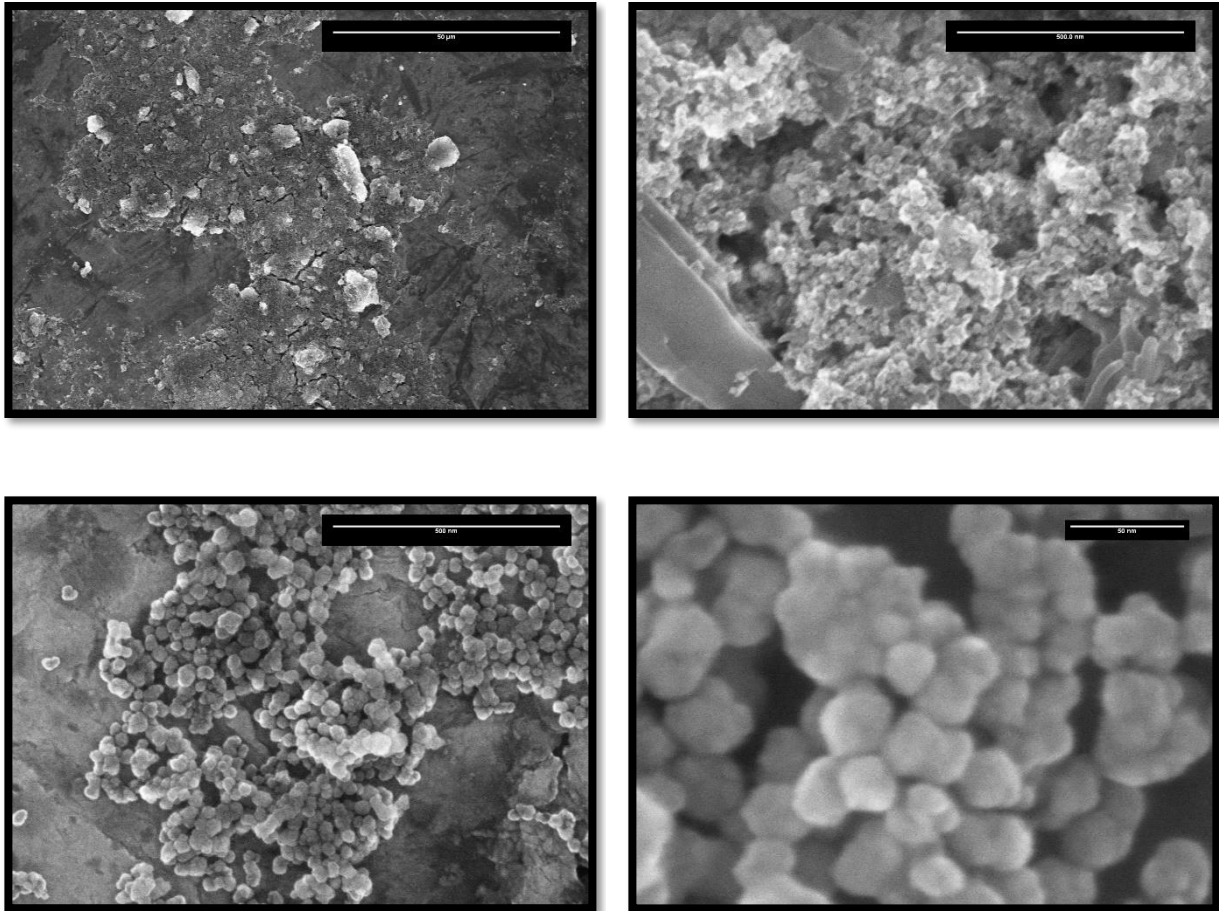


Figure 84 – (top) SEM images of pellet from MH104.1 reaction. (bottom) SEM images of centrifuge solvent form reaction MH104.1

<b>MEASUREMENT</b>	<b>AREA</b>	<b>MEAN</b>	<b>MIN</b>	<b>MAX</b>	<b>ANGLE</b>	<b>LENGTH (NM)</b>
<b>1</b>	0.961	179.206	116	214.336	2.578	23.635
<b>2</b>	0.953	167.47	136	195.529	3.426	23.057
<b>3</b>	1.305	162.121	102.862	215.584	4.22	31.036
<b>4</b>	0.961	175.414	125	206.238	0.466	24.207
<b>5</b>	1.156	147.635	81	193.886	-178.197	28.784
<b>6</b>	0.93	117.05	77	144.255	-11.623	16.61
<b>MEAN</b>	1.044	158.149	106.31	194.971	-29.855	24.555
<b>SD</b>	0.152	22.995	23.817	26.459	72.908	5.024
<b>MIN</b>	0.93	117.05	77	144.255	-178.197	16.61
<b>MAX</b>	1.305	179.206	136	215.584	4.22	31.036

Table 4 – Particle diameter measurements for experiment MH104.1

*MH104.2*

Pellet showed similar features when compared with those of MH104.1. It also included ~5 nm particle formations likely to be silica nanoparticles (Figure 85 top). Resolution of particles is very poor but recognizable. Solution showed well defined particle formation (Figure 85 bottom). Average measurement was around 55 nm (Table 5).

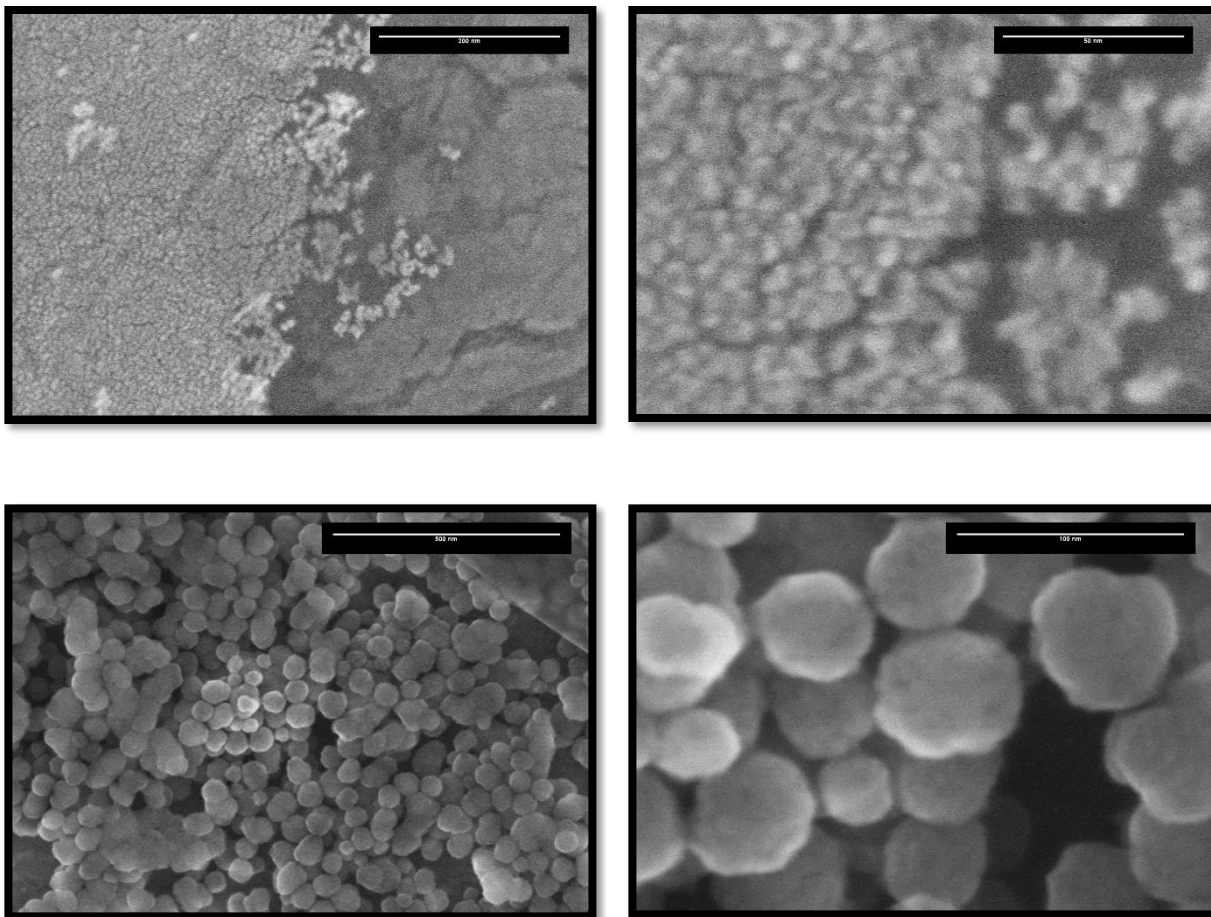


Figure 85 – (top) SEM images of pellet from MH104.2 reaction. (bottom) SEM images of centrifuge solvent form reaction MH104.2

<b>MEASUREMENT</b>	<b>AREA</b>	<b>MEAN</b>	<b>MIN</b>	<b>MAX</b>	<b>ANGLE</b>	<b>LENGTH (NM)</b>
<b>1</b>	1.953	124.388	98	180	0	49.405
<b>2</b>	1.976	124.15	94	153	180	50
<b>3</b>	2.406	112.282	87	162	180	60.913
<b>4</b>	2.508	122.449	88	147	180	63.492
<b>5</b>	2	117.414	84	187	180	50.595
<b>MEAN</b>	2.169	120.137	90.2	165.8	144	54.881
<b>SD</b>	0.266	5.211	5.675	17.196	80.498	6.759
<b>MIN</b>	1.953	112.282	84	147	0	49.405
<b>MAX</b>	2.508	124.388	98	187	180	63.492

Table 5 – Particle diameter measurements for experiment MH104.2

*MH104.3*

Pellet revealed typical bulky formations excluding resemblance of defined particles (Figure 86 top). Solution again produced well-defined particles (Figure 86 bottom). A binomial distribution is in this sample with the smaller set measuring an average of 36 nm in diameter (Table 6).

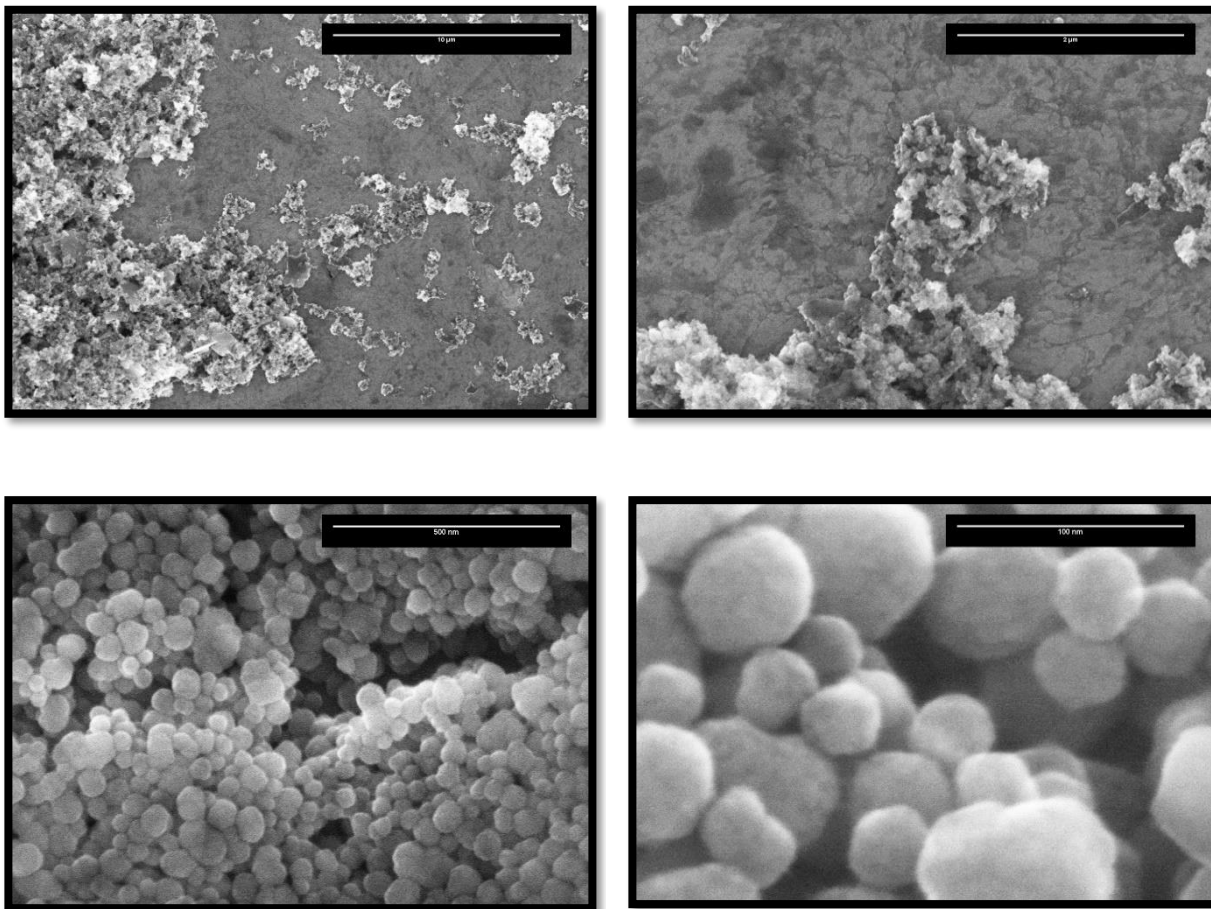


Figure 86 – (top) SEM images of pellet from MH104.3 reaction. (bottom) SEM images of centrifuge solvent form reaction MH104.3

MEASUREMENT	AREA	MEAN	MIN	MAX	ANGLE	LENGTH (NM)
<b>1</b>	1.391	161.91	95	226	0	35.119
<b>2</b>	1.375	146.653	115	186	0	34.722
<b>3</b>	1.617	140.034	93	164	0	40.873
<b>4</b>	1.555	182.095	146	248	180	39.286
<b>5</b>	1.195	158.654	112	187	180	30.159
<b>MEAN</b>	1.426	157.869	112.2	202.2	72	36.032
<b>SD</b>	0.166	16.184	21.3	33.974	98.59	4.215
<b>MIN</b>	1.195	140.034	93	164	0	30.159
<b>MAX</b>	1.617	182.095	146	248	180	40.873

Table 6 – Particle diameter measurements for experiment MH104.3

#### BASELINE PHOTOPHYSICAL CHARACTERISTICS

Preliminary absorbance and fluorescence spectra were obtained for the PDIB-NPs synthesized. initial sample concentration is unknown as samples were maintained in solution and never dried. S5 absorbance from Figure 87 presents the concentration taken directly from the work-up flask. Descending concentrations from this point were measured in 0.5x increments of dilution.

In these absorption spectra, there remains some resolution of the vibronic peaks characteristic of PDI-silane fluorophore imbedded in the siloxane network. Peaks appear at 481 nm, 497 nm, and 549 nm. This final peak, in comparison to the PDI-silane precursor, is red-shifted from the 530 nm it resided in previous analysis (Figure 33).

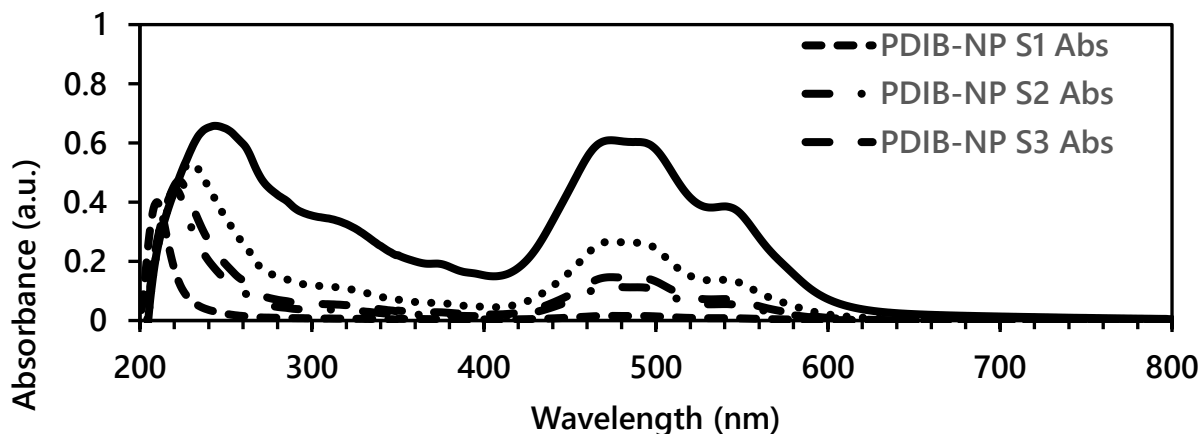


Figure 87 – UV-Vis absorbance of increasing concentration to solution saturation of PDIB nanoparticles in EtOH

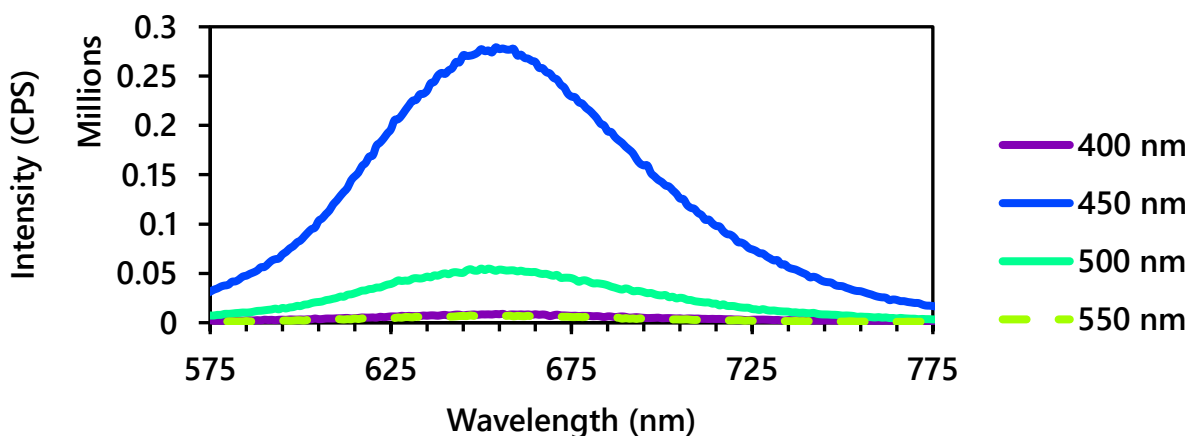


Figure 88 – Fluorescence emission of PDIB-NPs via multiple excitation wavelengths

PDIB-NPs show variable fluorescent emission intensity when excited with different frequency of light sources. Minimal return of fluorescence was found when approaching 400 nm excitation and 550 nm excitation. The greatest strength emission is located around 450 nm and appears to diminish quickly when excited by either more ‘red’ or more ‘blue’ light. Peak maxima is shifted

considerable when compared to PDI-silane precursor. Peak maximum is found here around 655 nm whereas PDI-silane produces vibronic peaks reaching maxima between 525-575 nm.

### Concluding Remarks

As a continuation of original work synthesizing perylene loaded silica nanoparticles diameter was reduced to  $25\pm 5$  nm, down from  $37\pm 7$  nm<sup>22</sup>. This work shows a 32% reduction in particle diameter is possible with only adjustments to synthesis procedure. Ideal synthesis procedure for lowest diameter particles was to introduce minimal base catalyst into the reaction vessel. This did appear to reduce particle surface smoothness and made aggregation more prevalent in samples imaged.

### THIN-FILM FORMATION

#### Discussion

Silica nanoparticles have been proven to provide uniform layered thin-films via spin-coating techniques<sup>76</sup>. The same approach to silica particle monolayers was applied for PDIB-silane nanoparticles.

#### Characterization

##### *MH053*

Both samples were imaged under SEM on the ITO substrate. MH053.3 showed good coverage of the PDI-silane with very few defects (Figure 89 and Figure 90). This sample was later used for capacitance measurements. Sample MH053.4 showed uniform coverage of PDIB-silane nanoparticles however, particles were aggregated into 'islands' with open areas of uncoated ITO. These particles have high affinity to each other. Particle integrity was not affected however (Figure 91 and Figure 92).

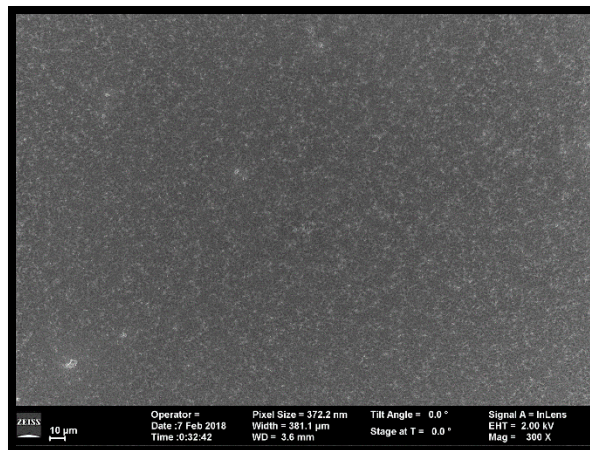
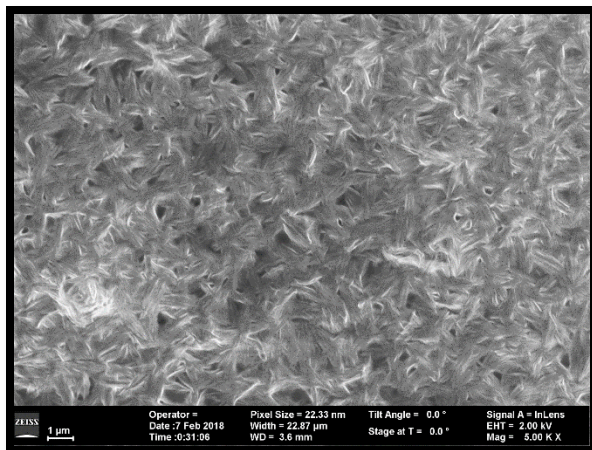


Figure 89 – SEM sample MH053.3: PDI-silane thin-film

Figure 90 – SEM sample MH053.3: PDI-silane thin-film

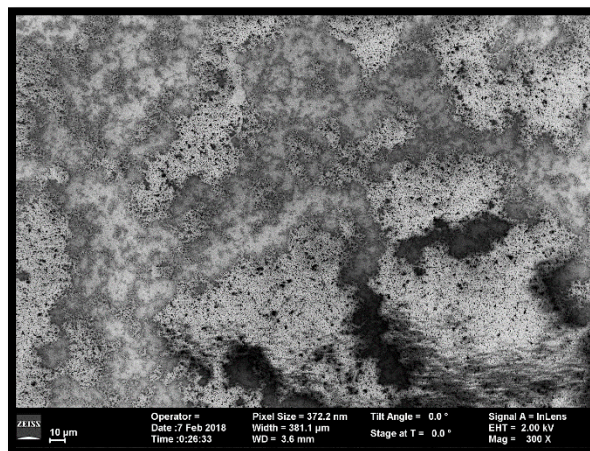
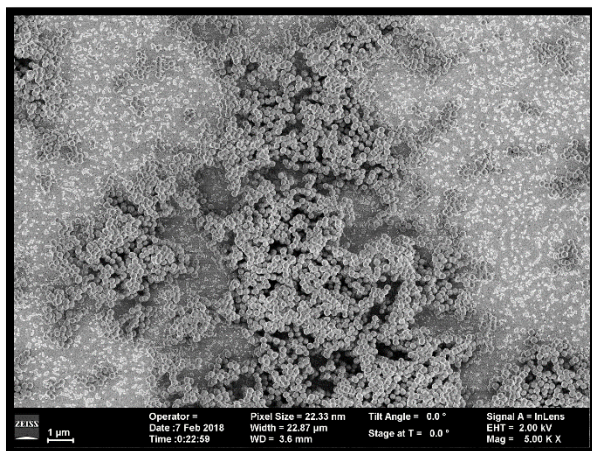


Figure 91 – SEM sample MH053.4: PDIB-silane NP thin-film

Figure 92 – SEM sample MH053.4: PDIB-silane NP thin-film

### MH055

This set of experiments shows a comparison between anhydrous ethanol and chlorobenzene as spin-coating solvents for PDIB-silane nanoparticles. Toluene is a possible future solvent to add to these results. All four samples were imaged under SEM on the ITO substrate. Sample MH055.1 showed a better coverage when compared to sample MH053.4. This was likely due to the revised

spin parameters. Initial spin speed reduced from 300 rpm to 200 rpm and drying speed increased from 3300 rpm to 6000 rpm resulted in a thinner spread of material of the substrate. The island formation was still present however leaving a lot of ITO uncovered. The islands were small, many in number and close together (Figure 93 and Figure 94). Sample MH055.2, with a higher concentration of PDIB-silane NPs, gave better coverage still, but still not complete. Surface features of particle islands were significantly larger resulting in a very non-smooth surface (Figure 95 and Figure 96). Sample MH055.3 showed thinner coverage when compared to MH055.1. Island structures were again present but larger in diameter than MH055.1 (Figure 97 and Figure 98). Sample MH055.4 showed smaller island structure than MH055.3 but, clearly worse ITO coverage. It is likely that spin parameters are not ideal for chlorobenzene solution (Figure 99 and Figure 100). Particles remain more attracted to aggregation over layer formation.

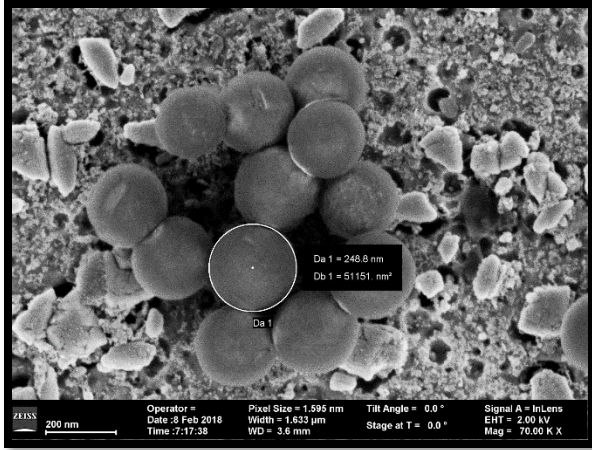


Figure 93 – SEM sample MH055.1: PDIB-silane NP thin-film (EtOH)

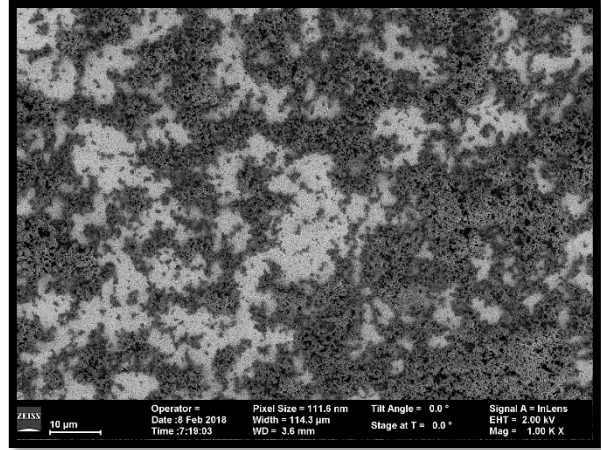


Figure 94 – SEM sample MH055.1: PDIB-silane NP thin-film (EtOH)

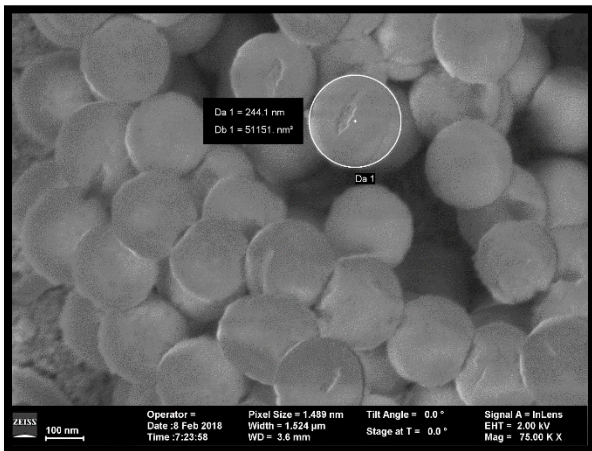


Figure 95 SEM sample MH055.2: PDIB-silane NP thin-film (EtOH)

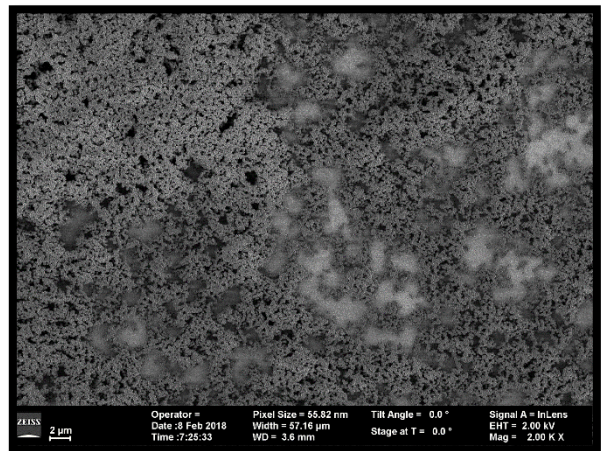


Figure 96 – SEM sample MH055.2: PDIB-silane NP thin-film (EtOH)

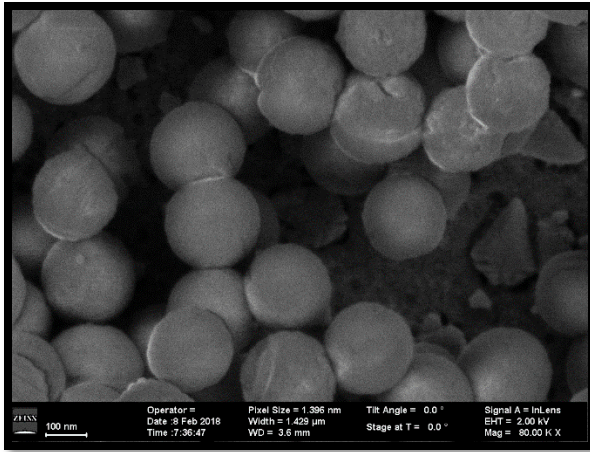


Figure 97 – SEM sample MH055.3: PDIB-silane NP thin-film (C<sub>6</sub>H<sub>5</sub>Cl)

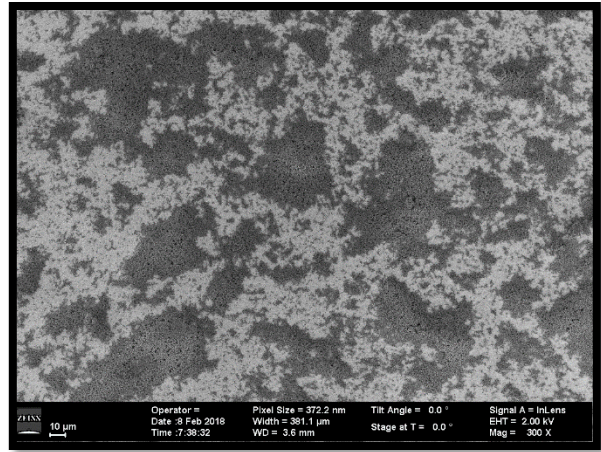


Figure 98 – SEM sample MH055.3: PDIB-silane NP thin-film (C<sub>6</sub>H<sub>5</sub>Cl)

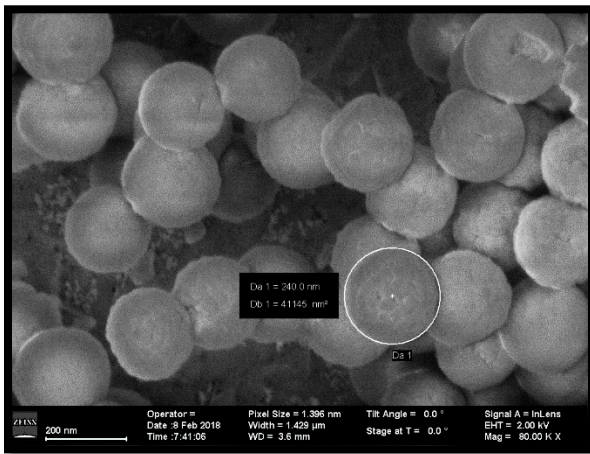


Figure 99 – SEM sample MH055.4: PDIB-silane NP thin-film (C<sub>6</sub>H<sub>5</sub>Cl)

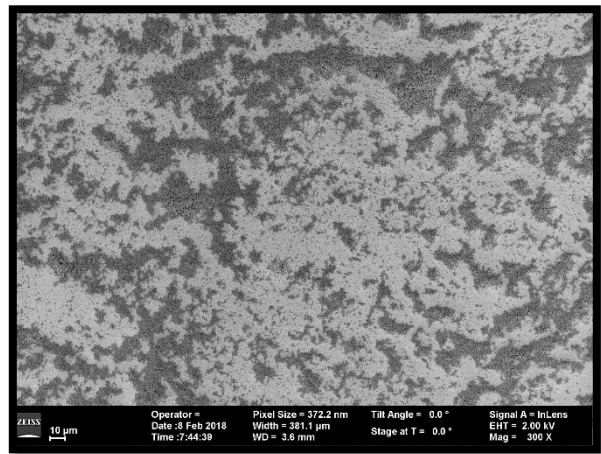


Figure 100 – SEM sample MH055.4: PDIB-silane NP thin-film (C<sub>6</sub>H<sub>5</sub>Cl)

### Concluding Remarks

When compared to the pure silica nanoparticle counterparts, the PDIB-silane nanoparticles appear to have a greater affinity to one another when performing the spin-coat method. Even dry, the nanoparticles remain in island structures as though bonded to one another. It does not appear that centripetal forces are great enough to break the PDIB-silane nanoparticles apart in such a way that

they can fall into place as the solvent dries through the high rpm phase. In order to form monolayer thin films with such material there must first be a certainty that particles are separated from one another. There is currently no reference data that can be used to determine if these particles aggregate in solution or during the drying process through spinning. Characteristic TEM imaging (Figure 83) has shown these particles existing in isolation under dry conditions. For sample preparation of such analysis, the product is diluted to a point unfit for the parameters recommended for spin-coating. There should exist an ideal case of correct concentration and minimal particle attraction, but that case was not found through these experimental parameters.

## CHAPTER VII: FUSED ARENE PHOTOPHYSICS

### SOLVENT PHOTOPHYSICS

Organic fluorophores remain as an area of interest for FRET applications due to the well-described pairs and established signal amplification techniques. Competition for application has grown due to the availability of quantum dots (QDs) after great improvements to synthesis procedures, however many properties of organic dyes have remained superior. Their size is comfortably sub-nanometer, meaning spatial interference with resonant energy transfer is rarely problematic. QDs have sizes ranging from a couple of nanometers to tens of nanometers dependent upon their hydrodynamic diameter if a colloid is needed. Organic dyes often present near unity quantum yields, can be photostable, thermostable, and chemically stable. Solubility and functionality can be controlled via well-established protocols. The optical properties of organic dyes are determined by electronic transitions set discretely on a per-molecule basis. The energy gap between the quantized ground and excited states determines the energy of photon it can absorb and emit. When excited in number, a characteristic spectrum is produced providing a definable cumulative state of all the excitable dyes at once. When created from dyes in solution, the shape of this spectra is determined by the energies associated with the molecules Frank-Condon state. Solvent interaction plays a significant role in the cycle of excitation and relaxation of a fluorescent capable dye molecule. The first state is the equilibrium ground state. The molecule has no excess energy absorbed and the solvent cage around it remains at an energetic minimum. Upon absorption of a photon of sufficient energy, the molecule transitions to an excited state faster than the equilibrium of its solvent cage can shift. This represents the nonequilibrium excited state, and the second state in the cycle. The solvent cage then must change shape in some manner to accommodate the higher energy electrostatic environment defined by the excited molecule. This produces an equilibrium excited state defined as the third phase in the cycle. The final phase in the cycle, before the return to an equilibrated ground state, is via a relaxation process. If this process of relaxation happens via fluorescence – the emission of light from the excited fluorophore – the molecule will exist in a nonequilibrium ground state where the solvent cage remains in an electrostatic stabilization as

though dye molecule has higher energy. The solvent cage eventually catches upon with its organization for the equilibrium ground state to be established.

The quantifiable change in energy as each of these phases progress defines how absorption and emission spectra present after measurement. Shifts left or right to a spectrum's peak position provides insight into the strength of interaction that a solvent can have with the dye. Generally, the greater the solvent interaction, the greater the blue-shift to the absorption spectrum because a nonequilibrium excited state molecule will force strongly interacting solvents to increase in polarity. The energy differential between ground and excited states is then forced to grow, relative to weaker interacting solvents that feel polarity increase to a lesser extent. A similar sequence of events must occur for deexcitation of a molecule. For a dye potentially fluorescing, two events occur. Firstly, the solvent cage equilibrates with the newer electrostatic state of the excited molecule. This is a very fast dynamic on the time scale of vibrational relaxation and the energy of the system is reduced. Simultaneously, the excited electronics of the dye molecule are going through non-radiative intramolecular transitions until they reach the lowest energy excited singlet state. From this point the molecule can emit a photon to return to its ground state. However, just as with the excitation, the solvent cage exists in the state equilibrated with the excited molecule. This means that the energy differential between the equilibrium excited state and this non-equilibrium ground state is significantly smaller than that occurred for excitation. This process will cause fluorescence spectra to typically be of longer wavelength than absorption. Once the dye molecule is in its ground state, the solvent cage can relax once more to equilibrate back into the state at which this cycle started.

Fluorescence is not the only pathway for deexcitation of an organic dye molecule. With multiple neighboring molecules in a solvated system, excited state energy transfer can occur between like molecules. Resonant energy transfer occurs as an exchange of excited vibrational energy from one molecule to a nearby neighbor. This neighbor can then fluoresce at a longer wavelength to deexcite or potentially again pass along the energy to another molecule which absorbs and excites at even longer wavelengths. When exchange of resonant energy happens in the near-field, it can be treated as a electronic dipole-dipole interaction. Such interaction is known as Förster Resonance Energy Transfer. At distances between 0.5 nm and 10 nm between the accepting ground state molecule

and the excited donor molecule coulombic perturbation may allow for a nonradiative transfer of energy.

Below 5 Å, there is a much greater probability of a different form of energy transfer coined by Dexter<sup>77</sup>. At such close distances intermolecular and intramolecular exchange of electrons can take place. the short-range energy transfer can happen from singlet-singlet exchange or triple-triplet. instead of the excited electron releasing energy to assume the molecules ground state, it will swap the electron directly with another in a ground state. The accepting molecule will have an excited state electron.

Förster and Dexter energy transfer processes are both part of a quenching pathway possible to the donor molecule. They may be deemed as collisional quenching mechanisms as the excited donating fluorophore is assisted with the non-radiative transition to ground state via ‘collision’ interaction with the quenching acceptor. in higher concentration solutions there is the other possibility of static quenching. Static quenching derives from complexes of fluorophores forming at the ground state. For dye molecules, a driving force of complex formation is hydrophobic interaction with the solvent environment. The packing of such is similar to the solvent cage formed around isolated molecules but these complexes become nonfluorescent and shift their absorption spectra to shorter wavelengths.

All of these mechanisms have been used in some form or another to create photonic probes, passive event detection, signal relays, and drug or toxic species detection. None of such applications are viable without a complete understanding of the material behaviors present in the system. To gain a complete picture of how solvents and fluorophores behave in potential application environments many analytical techniques can be applied. For detection and measurements of FRET, steady state and lifetime fluorescent measurements are a valuable tool. this can be coupled with UV-vis absorption spectra for quantum yield values and a complete understanding of a donor acceptor system can be made. The same methods can be used for observation of Dexter energy transfer with the careful consideration they both share undetectable non-radiative mechanisms; measurements are only made of the result, post transfer. detection of complex formation and static quenching can be confirmed with the use of fluorescent spectra and application of the Stern-Volmer equation. this

equation can allow for the determination of the rate of quenching. If only one mechanism is present the rate will present linear as concentrations of the quenching material change. If the fit to the equation appears quadratic, there are extra quenching mechanisms present increasing the rate. This method is a fine tool for identifying the existence of multiple quenching pathways after the assumption for the existence of only one.

Introductory work regarding energy transfer was produced in 1967 by Birks et al. with a study of anthracene and perylene<sup>78</sup>. Using concentration depended fluorescent lifetime measurements they were able to determine transfer rates via Stern-Volmer kinetics consistent with Förster resonance energy transfer. This study was limited in scope at the time in part by the limits of spectroscopic equipment but also by the solubility of perylene. Benzene was the only solvent used in this study so solvent influence was understudied. Since then, recent literature has presented an array of applications for perylene derivatives as sensing probes. Geng et al. has used a derivative for 0-nitrophenol sensing. This is a poisonous material and is a known contaminant of soil near former explosives, fabric factories and military plants<sup>79</sup>. Cheng et al. have developed silver ion sensors derived from perylene that have the ability to switch transfer mechanism upon interaction<sup>80</sup>. Silver ions are known to be toxic by inactivating specific enzymes in an organism and accumulate in the body.

These works have strongly relied upon the electronic properties of a perylene dye known in shorthand as PTCDA. Formally, perylenetetracarboxylic dianhydride. It is an organic semiconductor with nearly 900 published scholarly articles searchable through the Google Scholar search engine. The scientific attraction to this molecule comes from its intense visible light absorption, thermal and chemical stability, electron accepting tendencies, and near unity quantum yield emission. A particular disadvantage that PTCDA has regarding application is that there are few non-toxic solvents that sufficiently induce high solvation. Expansive work with the perylene core has, in some cases, relied upon dendrimer formations that still require harsh solvents such as DCM and toluene. Common and safer solvents such as water, ethanol, chloroform, and acetonitrile are not sufficient to dissolve effectively this base molecule. Insolubility in common solvents very quickly reduces the range of sensing applications as most environments of application do not exist in toxic solvents. In 1988, Demmig et al. produced a functionalized PTCDA derivative with the intention

of improving solubility without incurring detrimental characteristics that reduce fluorescence emission <sup>81</sup>. In fact, improving the solubility could only improve the fluorescence yield. The variety of PTCDA derivatives was improved upon in 2009 by Türkmen et al. with four more soluble forms. In particular some were designed for aqueous environments where they could minimize electron transfer through the addition of acidic species.

In the same year as Türkmen (2009), Wahab et al. Produced and self-assembled thin-films from a perylenediimide-bridged silsesquioxane <sup>17</sup>. This molecule is highly soluble in chloroform and can be used to build in the and three dimensions. Issued the acronym PTCBS, this molecule could be produced at fairly low temperatures using a single-step reaction. although this form does not retain as great chemical stability as the mother-molecule, PTCDA, it gains a superior framework capability.

This chapter aims to reintroduce the fundamental energy transfer studies to highly soluble PTCBS now that the diversity of solvents capable for studies have increased. A focus on energy transfer dependence upon concentration and solvent properties is key to this study as experiments are set to understand the mechanisms that precede and follow Förster resonance energy transfer over such variable parameters. Even with leaps in computational efficiency over the 80 years since the introduction of the theory of FRET, it remains more practical to explore energy transfer experimentally as the multibody systems are extremely computationally expensive and designed outcome bias is a difficult programming consequence to avoid.

To fulfill the prerequisites of such work firstly, it was important to find a donor material that would provide good spectral overlap with the absorption spectrum of PDI-silane and be compatible with the appropriate solvent selection. It was suitable to consider a similar organic fluorophore as opposed to a metallic derivative due to easier solvent compatibility. Most metallic and semiconducting QDs require lipid coatings for solvation whereas organic dyes typically come solvent friendly. Anthracene was found to have high quantum yield and a considerable emission overlap with PDI-silane absorption spectrum. the derivative, 9-anthroic acid, was selected for all work due to its high solvent compatibility and access to further synthesis schemes via sue of the reactive carboxylic functional group.

## INITIAL FUNCTIONALITY CONFIRMATION

Prior to this study, the standard approach of stock solution creation had been to target unity absorbance via changing the concentration of two separate stock solutions of PDI-silane (PDIS) and 9-anthroic acid (9-AA). The solutions were blended in different manners (constant volume blend or variable volume blend) to create a mixture intended to induce a measurable quantity of FRET. The poor performance of these mixtures prompted a high concentration blend. The stocks solutions in this case were created to saturate the solvent disregarding unity absorbance. In relation to quantum yield experiments where the solution concentrations were on the order of  $\mu\text{g/mL}$ , these stock concentrations were produced at concentrations of  $\text{mg/mL}$ . The stock solution for 9-AA was created at a concentration of  $2.2 \text{ mg/mL}$  ( $10 \text{ mM}$ ) and PDIS stock solution was created at a concentration of  $8 \text{ mg/mL}$  ( $10 \text{ mM}$ ). Both solutions were made in chloroform. These relatively high concentrations are still expected to fully dissolve yet, PDI-silane did not. There were still small, barely visible flakes remaining in the solution after 30 minutes of sonication. To remedy this, the stock solution was filtered through a  $0.45 \mu\text{m}$  filter. This would of course reduce the concentration of the solution, but the matter left in the filter did not appear to contribute to much significant weight after drying. A worst-case estimate would state a 10% loss of material providing the PDIS stock solution with  $9 \text{ mM}$ .

The test solutions were then created from these stock quantities to check individual fluorophore performance and blended system performance. For each test solution, the volume was held constant to maintain fluorophore density in solution. After this dilution, the solution concentrations contained  $500 \mu\text{M}$  of fluorophore in  $1 \text{ mL}$  of solvent for the reference solutions. The blended solution had  $500 \mu\text{M/mL}$  each for donor and acceptor.

	9-anthroic acid	PDI-silane	Solvent
PDI-S test solution	$0 \mu\text{M}/\mu\text{L}$	$10 \mu\text{M}/\mu\text{L}$	$950 \mu\text{L}$
9-AA test solution	$10 \mu\text{M}/\mu\text{L}$	$0 \mu\text{M}/\mu\text{L}$	$950 \mu\text{L}$
Blended test solution	$10 \mu\text{M}/\mu\text{L}$	$10 \mu\text{M}/\mu\text{L}$	$900 \mu\text{L}$

Table 7 – Table showing stock solution volumes used to create test solutions of PDIS, 9-AA, and a blended sample.

## Absorbance

The first measure taken for this experiment was the collection of absorbance for all three test solutions. This was performed with only single beam collection resulting in a distinct plateau feature to the peaks maxima. This can be remedied with a double slit setup and should allow for even greater absorbances to be measured accurately. Nonetheless, important information can be gained from this current plot. Firstly, the absorbance values for all three test samples are more than three times the prior stock solution experiment setups. Secondly, the absorbance maxima for PDIS and 9-AA are roughly at the same value ( $\approx 3.5$ ). Finally, these maximum peak heights are maintained in the blended test solution; this means that fluorophore density has been maintained. We can also take note of the peak maxima locations. 9-AA has absorption peaks located at 348 nm, 365 nm, and 381 nm. PDIS has absorption peaks located at 361 nm, 390 nm, and 526 nm.

Ideally for FRET measurement, the acceptor fluorophore has no absorbance overlap with the excitation wavelength; this give a clear indication of when the acceptors fluorescence is achieved via energy transfer. In the case for PDIS, there seems to be a low level of absorbance continually occurring from 300nm to 400 nm. The local minimum of this absorbance is located very near to 400 nm. This is still within the absorbance of 9-AA, so the first test will excite these fluorophores at 400 nm.

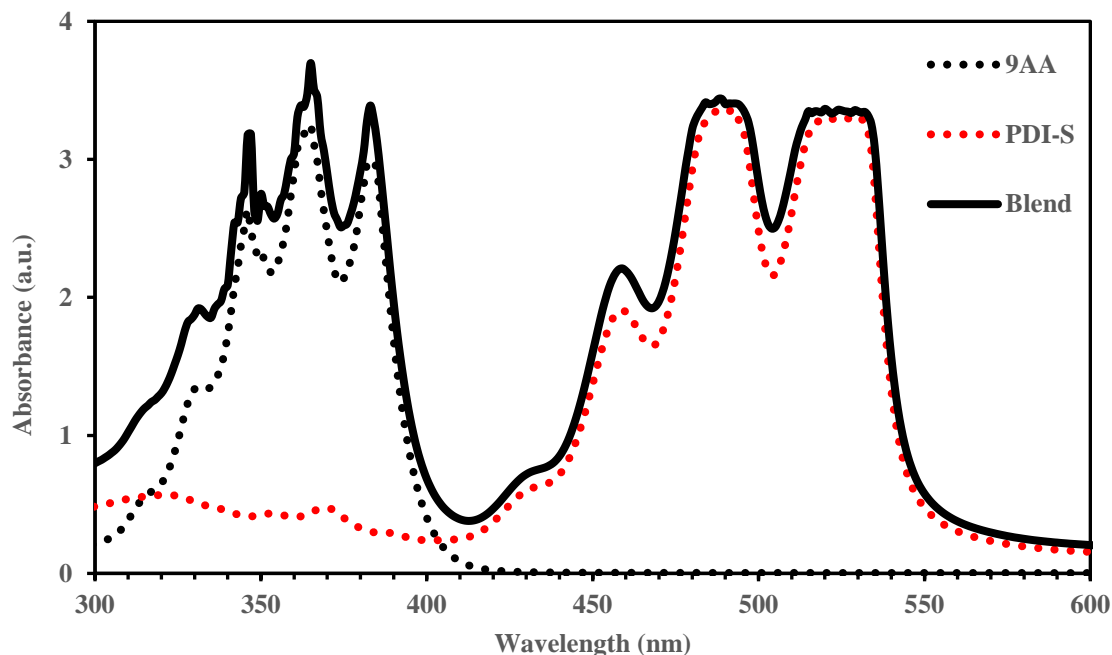


Figure 101 – UV-vis absorbance of 9-AA, PDIS, and Blended test solutions.

### Emission

Fluorescent spectra of for the 9-AA and PDIS test solutions both perform with strong fluorescence when excited at 400 nm. Both solutions were tested to provide a baseline for the Blended solution to be compared against. The performance of the blended solution gives us great insight into the interaction of these fluorophores in solution. There is a strong quenching of the 9-AA; the mechanism – of which is indicated by the increase of fluorescence for PDIS – being FRET. The broad width of the 9-AA emission peak is reduce significantly; a likely reason for this is revealed when the emission of 9-AA and absorption of PDIS is compared directly. The vast majority of PDIS absorbance exists beyond 450 nm, this blue-sifts the blended 9-AA’s emission peak maxima.

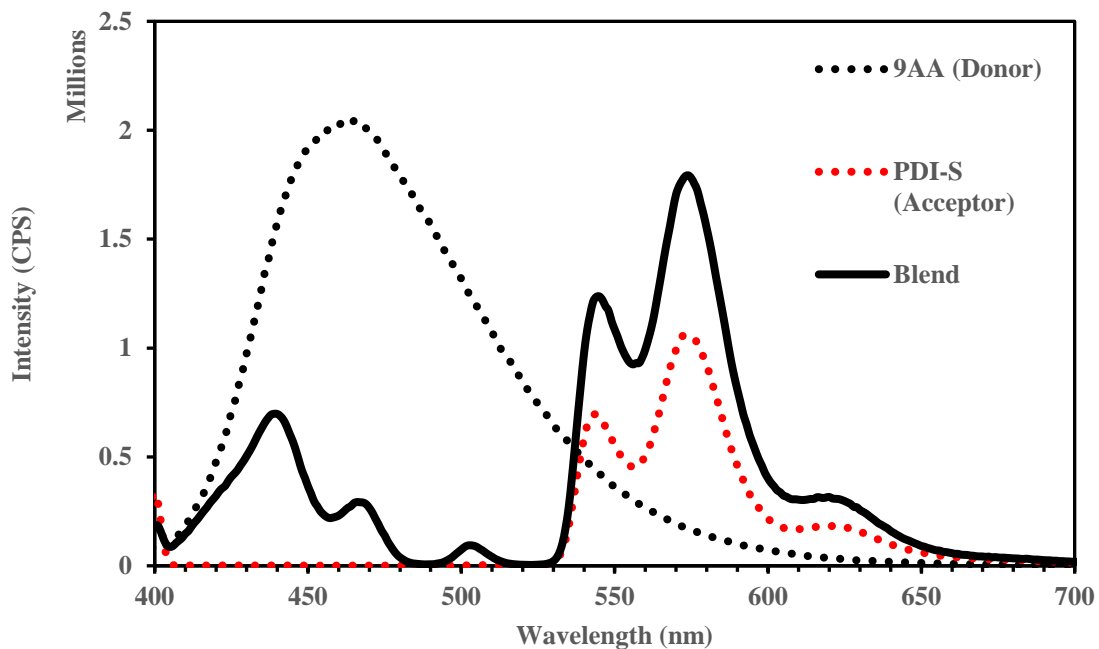


Figure 102. Fluorescence spectra depicting 9-anthroic acid (black dots), PDI-silane (red dots), and an equal moiety blend of both (black line). All spectra were run in chloroform solvent solutions.

The maximum emission peak values were obtained for 9-AA, PDIS and their corresponding in the blend. These values were then used to calculate the losses and gains for 9-AA and PDIS emission, respectively.

<i>9-AA maximum emission</i>	<i>PDIS maximum emission</i>	<i>Blended 9-AA maximum emission</i>	<i>Blended PDIS maximum emission</i>
$2.04 \times 10^6$ CPS	$1.06 \times 10^6$ CPS	$6.98 \times 10^5$ CPS	$1.79 \times 10^5$ CPS

Table 8 – Peak maxima for emission spectra of 9-AA test solution, PDIS test solution and both spectra with blended test solution

It is noted that 66% of 9-AA’s original emission strength is lost in the blend solution. PDIS gains 169% of its of its original emission in the blend solution. A transfer efficiency can be calculated solely from the change in peak maxima. We find that 54% of 9-AA’s lost emission counts get transferred to PDIS’s blended emission. It must be emphasized that this is not a FRET efficiency calculation, as it does not consider quantum yield of either fluorophore. The FRET efficiency is calculated via the following equation,

$$E = 1 - \frac{FD'}{FD} \quad (23)$$

Here, FD’ represents fluorescent intensity of the donor in the presence of the acceptor and FD represents fluorescent intensity of the donor in the absence of the acceptor. In this case the FRET efficiency (*E*) is calculated to be 66%. This is a very good donor/acceptor system that has been developed at these high concentrations. It could be assumed that the fluorophores are in very close proximity to each other, but there is another method to confirm this.

	<i>CPS</i>	<i>Percent</i>
<i>9-AA blend loss</i>	$-1.34 \times 10^6$	66%
<i>PDIS blend gain</i>	$7.33 \times 10^5$	169%
<i>Transfer efficiency (via CPS exchange)</i>	$-6.12 \times 10^5$	54%

Table 9 – Loss and gain percentages resultant of FRET between 9-AA and PDIS. Transfer efficiency calculated via difference in CPS of both.

Provided with the FRET efficiency from equation 1, an estimation of the average distance between fluorophores can be made using the following two equations:

$$E = \frac{1}{1 + (r/R_0)^6} \quad (24)$$

$$R_0^6 = \frac{2.07}{128\pi^5 N_A} \frac{\kappa^2 Q_D}{n^4} \int F_D(\lambda) \epsilon_A(\lambda) \lambda^4 d\lambda \quad (25)$$

FRET efficiency can be reimagined by knowing the Förster distance ( $R_0$ ) and the average distance between fluorophores ( $r$ ). the Förster distance I obtained by calculating the spectral overlap ( $J$ ) of the donor emission and acceptor absorption. In equation 3,  $N_A$  represents Avogadro's constant,  $\kappa^2$  represents the dipole orientation factor,  $Q_D$  represents the quantum yield of the donor fluorescence,  $n$  represents the medias refractive index. The resulting plot shown in the figure below reveals the theoretical average distance between each fluorophore. The resulting number is 1.41 nm.

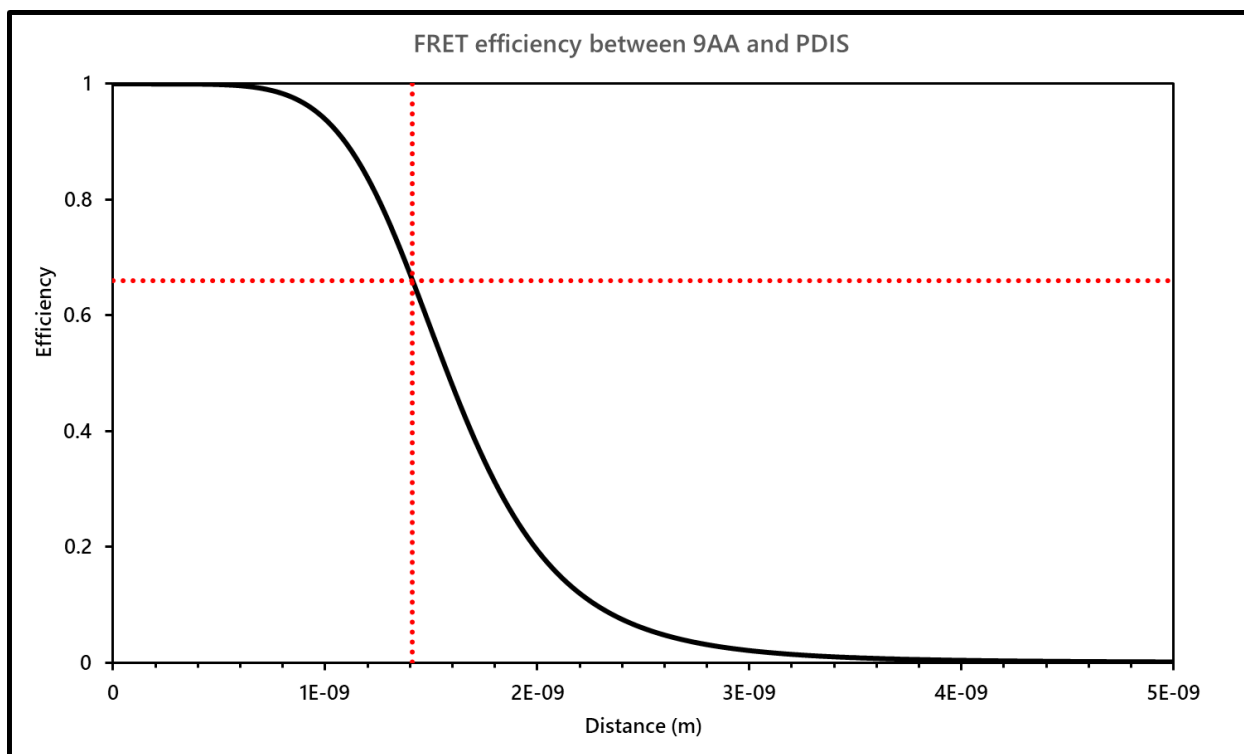


Figure 103 – Theoretical FRET efficiency curve dependent on distance between fluorophores. In this case, 9-AA and PDIS were used as the donor and acceptor, respectively. the quantum yield of the donor was set to 0.36 and the refractive index was 2.5.

## FRET Efficiency

FRET efficiency ( $E$ ) can be derived in a few different ways depending upon initial information obtain from experimentation. The truest computation of efficiency is derived from the quantum yield of the energy-transfer transition. That is the probability of an energy transfer occurring per donor excitation:

$$E = \frac{k_{ET}}{k_f + k_{ET} + \sum k_i} \quad (26)$$

where  $k_{ET}$  is the rate of energy transfer,  $k_f$  is the radiative decay rate of the donor, and  $k_i$  is/are the rates of any other de-excitation pathways excluding energy transfers to other acceptors.

A more computationally and analytically focused method of computing  $E$  is with regards to donor-acceptor separation distance.

$$E = \frac{1}{1 + (r/R_0)^6} \quad (27)$$

$$R_0^6 = \frac{2.07}{128\pi^5 N_A} \frac{\kappa^2 Q_D}{n^4} \int F_D(\lambda) \epsilon_A(\lambda) \lambda^4 d\lambda \quad (28)$$

here,  $N_A$  represents Avogadro's constant,  $\kappa^2$  represents the dipole orientation factor,  $Q_D$  represents the quantum yield of the donor fluorescence,  $n$  represents the medias refractive index. Spectral overlap can be calculated with the following.

$$J = \frac{\int f_D(\lambda) \epsilon_A(\lambda) \lambda^4 d\lambda}{\int f_D(\lambda) d\lambda} = \int \bar{f}_D(\lambda) \epsilon_A(\lambda) \lambda^4 d\lambda \quad (29)$$

## Radiative or Non-radiative assistance

The first experimental confirmation for fluorophore compatibility is shown in Figure 102. Fluorescent spectra of 9-AA and PDI-S were collected as reference for comparison to their blended

counterpart. This blend was made of a 1:1 moiety count. The purpose for the reference data is to show unequivocally that peak amplitude for the acceptor moiety has risen due to the presence of donor. This method of energy transfer confirmation has a small shortcoming, however. As is clearly presented here, there is an overlap with the 9-AA and the PDI-S emission spectra. Knowing that the PDI-S absorption spectra presents itself at higher energies, it is quite possible to suggest that high wavelength emission from the donor is not completely absorbed by the acceptor. The blend peak amplitude in the acceptor region could then be artificially increased from hidden detector counts courtesy of radiative emission from the donor. This idea is supported by looking at the same plot in the region between 400-500 nm, where a significant drop in donor emission is observed but not zero. This region is not optimal for acceptor absorption and therefore is not eliminated from the possibility of radiative emission.

To remedy the possibility that acceptor radiative emission increase is actually just a combined effort of radiative emission from donor and acceptor in the same bandwidth, a simple summation can be calculated. Addition of the 9-AA and PDI-S reference spectra are compared to that of the blend in Figure 104. This plot shows a substantial increase in the area under the curve between 530-700 nm indicating that some of this acceptor emission had energy contribution via non-radiative energy transfer from the donor moiety.

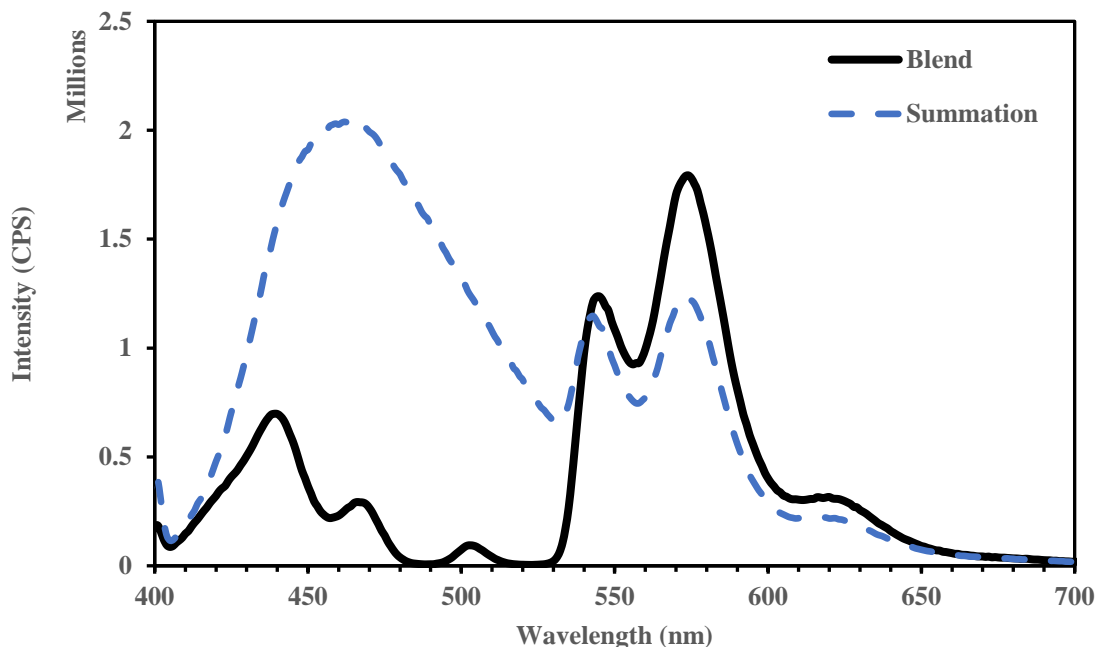


Figure 104. Fluorescence spectra depicting summation of 9-anthroic acid reference and PDI-silane reference (black dash) overlaid with blend solution (black line)

#### Concluding Remarks

This initial trial satisfactorily provides evidence of increased acceptor emission upon introduction of donor to the solvated system. It provides experimental confirmation that spectral overlap of the donor emission and acceptor absorption is sufficient for energy transfer to take place and contribute to the acceptor emission yield. It also confirms that a 1:1 molar ratio of donor to acceptor may provide an efficient environment for resonant energy transfer. To further understand the process in place, concentrations higher and lower from this reference should be explored as well as ratios of imbalance favoring either side. This expansion of experimentation would be done to provide a measure of ideal efficiency within the bounds of this system. Further experiments of such design may discover a limit of energy transfer for a minimum and a maximum concentration; formerly, where collisions reduce to immeasurably small probability and latterly, high concentration induced aggregation quenching overcomes resonance energy transfer pathways.

## CONCENTRATION GUIDANCE

Before trials, conceptual guidance of appropriate sample concentrations was found using a simple density model. Assuming each particle was homogeneously distributed in solution, the average distance between each particle was calculated for a range of concentrations from  $1\mu\text{g/mL}$  to  $1\text{ mg/mL}$ . For an energy transfer process that is dependent upon dynamic collisional interaction it seemed valuable to gauge the ideal-case system.

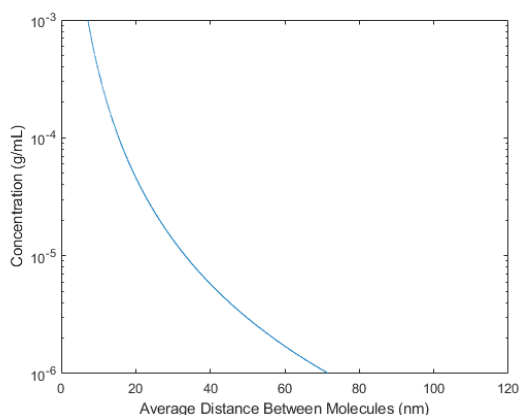


Figure 105 – Modeled average distance between monomeric 9-anthroic acid moieties in 1 mL volume.

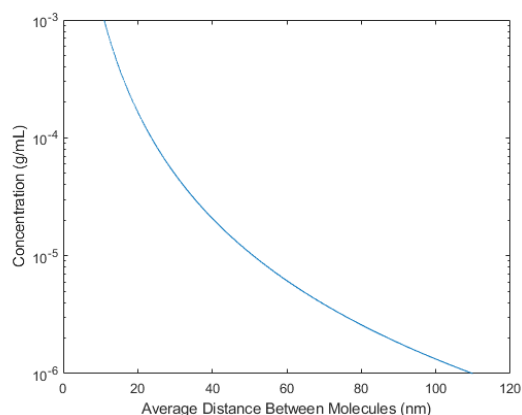


Figure 106 – Modeled average distance between monomeric PDI-silane moieties in 1 mL volume.

Table 10 shows extracted points from these calculations to provide an average distance between molecules for each magnitude of concentration between  $1\mu\text{g/mL}$  and  $1\text{ mg/mL}$ . These values suggest that an initial starting point for concentration blends aiming at producing a high number of dynamic collisional energy transfer would be around the  $1\text{ mg/mL}$  mark. This produces an average distance between molecules on the order of  $10\text{ nm}$ ; right at the limit for FRET. There are clear limitations to this model as it ignores solvent interaction and resultant aggregation effects that would create a non-homogeneous distribution of molecules in solution. These effects must be studied experimentally.

Concentration	$1E-3\text{ g/mL}$	$1E-4\text{ g/mL}$	$1E-5\text{ g/mL}$	$1E-6\text{ g/mL}$
---------------	--------------------	--------------------	--------------------	--------------------

<i>9-anthroic acid distance between molecules</i>	7.17 nm	15.45 nm	33.29 nm	71.73 nm
<i>PDI-silane distance between molecules</i>	10.99 nm	23.67 nm	51.00 nm	109.89 nm

Table 10 – Samples of average distance between molecules in 1 mL volume for 9-anthroic acid and PDI-silane.

#### BASELINE PHOTOPHYSICS OF 9-ANTHROIC ACID IN SOLVENTS

##### Preliminary

This experiment was set-up to understand the solvent effects on 9-anthroic acid. Concentrations of 125  $\mu$ M in five different solvents were made. All excitation was done at 365 nm. These baselines are needed to determine complex and aggregation type after formation. Concentration aggregation shift spectra red or blue depending on the relationship of ground and excited state energies.

<i>Solvent</i>	<i>Acetonitrile (Polar aprotic)</i>	<i>Chlorobenzene (Non-polar aprotic)</i>	<i>Chloroform (Non-polar aprotic)</i>	<i>Ethanol (Polar protic)</i>	<i>Tetrahydrofuran (Non-polar aprotic)</i>
<i>Solvent Polarity (Index)</i>	0.460 (5.8)	0.188 (2.7)	0.259 (4.1)	0.654	0.207 (4.0)
<i>Solvent Dipole Moment</i>	3.44	1.54	1.15	1.66	1.75
<i>Solvent Dielectric Constant</i>	36.64	5.69	4.81	24.6	7.52

Table 11 – Solvent polarity table. The values were obtained from the CRC (87th edition), or Vogel's Practical Organic Chemistry (5th ed.)

Table 11 shows polarity of the five solvents involved in this study. A general rule for solvent polarity is that as polarity increases, absorption spectra shift red. A more accurate description is with relation to solvent interaction; a solvent that does the most to bring the gap between excited state and ground state closer will cause the most red-shift.

## Results and Discussion

Qualitative observation of absorption (Figure 107) and emission (Figure 108) provide some initial insight into solvent interaction. Four of five solvents provide clean and distinguished vibronic peak absorption spectra. The chloroform is the outlier in this case as vibronic peaks from the anthracene spectrum are less well defined. The cause of this is typically due to solvent broadening and solvation changes over time. There could also be competition between dimer and monomer being shown as low vibronic peak resolution. This is a trait seen of 9-AA because of the carboxylic acid hydrogen bonding.

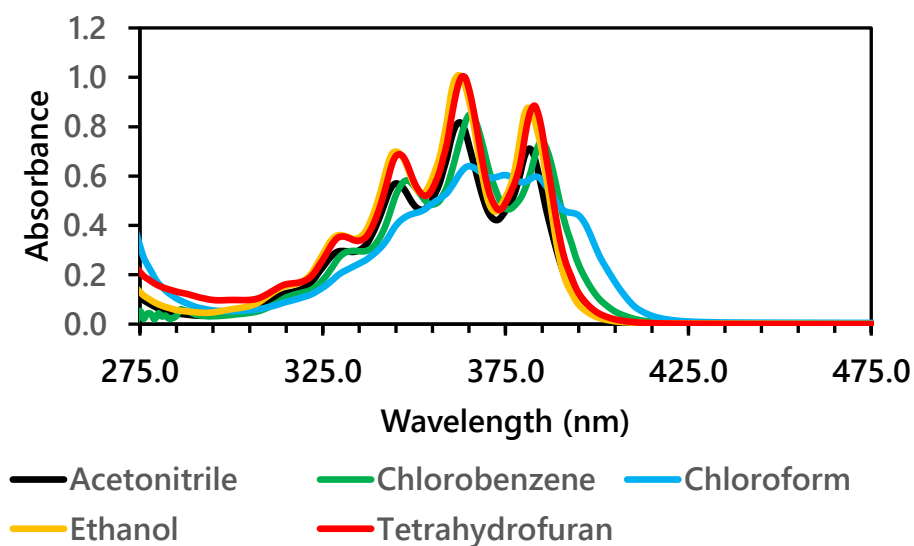


Figure 107 – UV-vis absorption spectra of 9-anthric acid in various solvents.

Further qualitative analysis of fluorescence in Figure 108 show the yield performance varies significantly with solvent choice. Chlorobenzene and tetrahydrofuran perform with the highest

intensity fluorescent emission. This may be attributed to the fact that that these two solvents share similar ring structure and relatively strong electron donor properties.

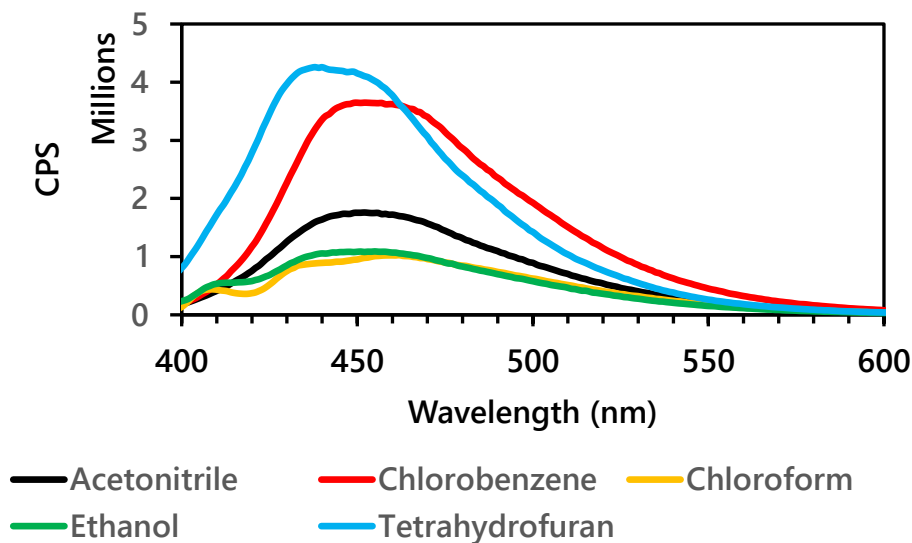


Figure 108 – Fluorescent emission spectra of 9-anthroic acid in various solvents

Quantitative comparison of peak position can be seen in Table 12 and Table 13; this data is taken from Figure 109 and Figure 110. The highest polarity solvents used both share the shortest wavelength maximum absorption peak position. This information alone would imply that acetonitrile and ethanol are the most strongly interacting solvents with the 9-anthroic acid system. Second, with a peak at 363 nm, is THF. This solvent is capable of hydrogen bonding as either an acceptor or donor. The shift to a slightly higher wavelength informs that this solvent is acting more of a hydrogen bonding donor when compared to acetonitrile and ethanol. The two chlorinated solvents – chlorobenzene and chloroform – are the least polar solvents in this study. This characteristic is shown with the lesser interaction by having the longest wavelength measured of the five. Although they share similar UV-vis peak positions, the fluorescent performance between the two is vastly different. It may be true that the electron availability influences fluorescent emission far more than absorption spectra can infer.

Figure 110 and Table 13 show a slightly different story to solvent performance over absorption. Here, THF shows the strongest blue-shift to the spectrum. Preliminary expectations would imply

similar order of shift to those found in absorbance. Acetonitrile, chlorobenzene and ethanol appear very close in peak maxima location. Finally, chloroform appears with its peak quite late around 462 nm. The chloroform spectrum also shows much more vibronic definition and favors intensity towards the red-most local maxima. Vibronic definition can also be seen ethanol.

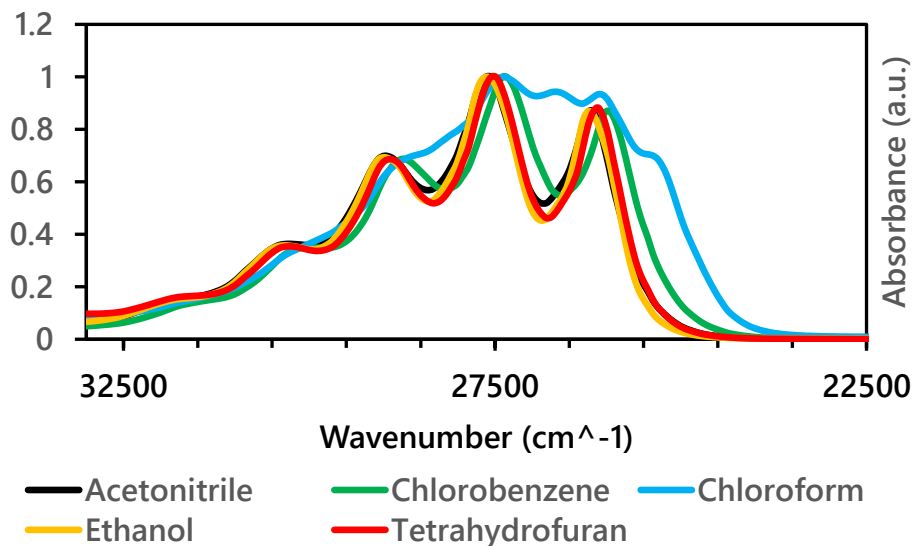


Figure 109 – Normalized UV-vis absorption spectra of 9-anthroic acid in various solvents

<i>Solvent</i>	<i>Acetonitrile</i>	<i>Chlorobenzene</i>	<i>Chloroform</i>	<i>Ethanol</i>	<i>Tetrahydrofuran</i>
<i>Maximum Peak Position</i>	362 nm	365 nm	365 nm	362 nm	363 nm

Table 12 – Peak locations for absorption spectra

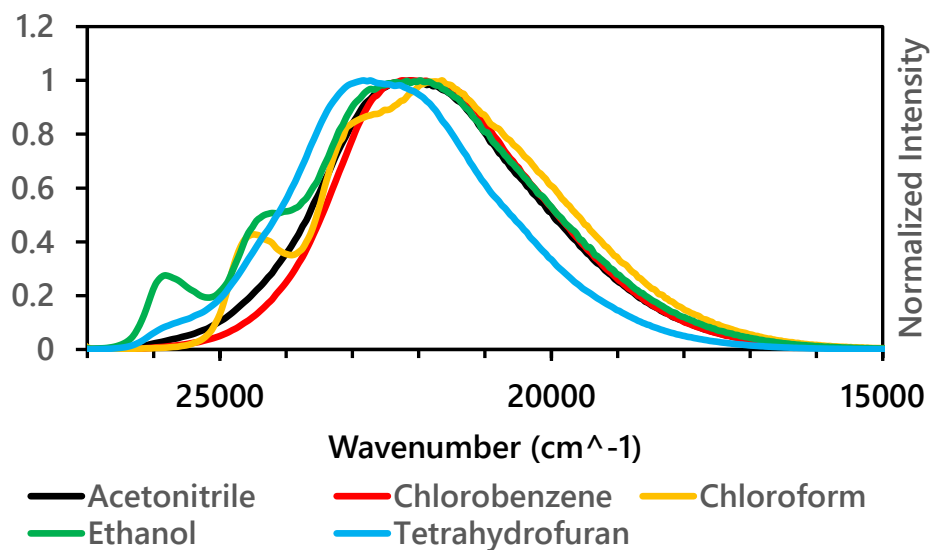


Figure 110 – Normalized fluorescence spectra of 9-anthroic acid in various solvents. Excitation 365 nm.

<i>Solvent</i>	<i>Acetonitrile</i>	<i>Chlorobenzene</i>	<i>Chloroform</i>	<i>Ethanol</i>	<i>Tetrahydrofuran</i>
<i>Maximum Peak Position</i>	452 nm	452 nm	462 nm	455 nm	438 nm

Table 13 – Peak locations for emission spectra

Figure 111 shows all five solvents with absorption and fluorescence layering. Here we can see a very slight overlap between absorption and emission spectra for chloroform, ethanol, and THF. These are the spectra that exhibit the most vibronic shape. Acetonitrile and chlorobenzene exhibit the least overlap and retain the fewest shapely features in the emission spectra.

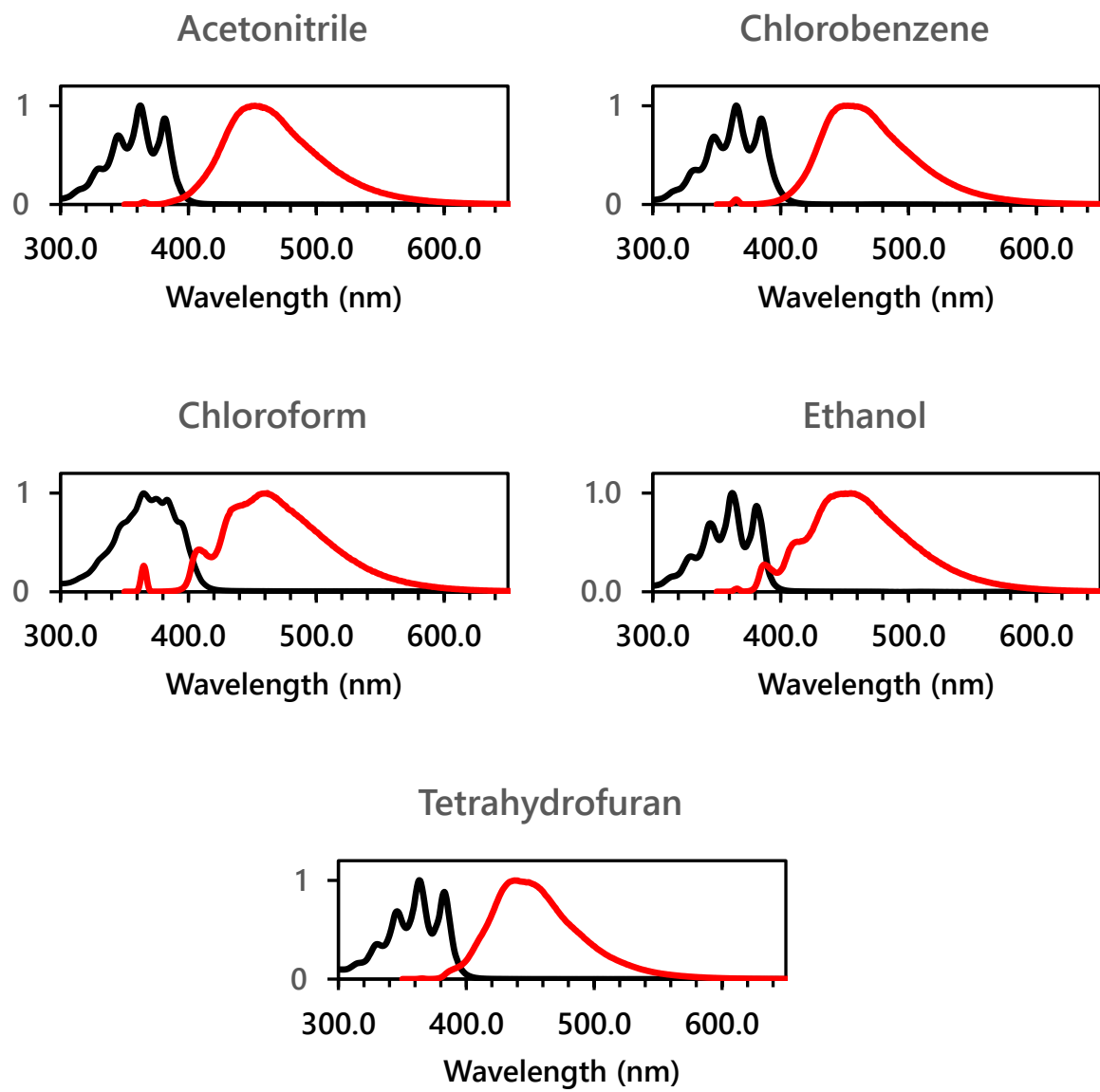


Figure 111 – Absorption and fluorescence overlap for 9-anthroic acid in various solvents. Excitation 365 nm.

## Concluding remarks

For further experimental trials, this study determines that chloroform has a slow solvation response to 9-anthroic acid. The remaining solvents show stability over a 24-hour period whilst remaining in solution. If performed quickly, trials comparing chloroform to the other peak broadening solvents may show variations in how solvent interacts with the outcome of energy transfer.

## FOLLOW-UP OF BASELINE PHOTOPHYSICS OF 9-ANTHROIC ACID IN SOLVENTS

### Preliminary

This trial is a follow-up to the previous baseline measurements to understand the solvent dependent photophysics of 9-anthroic acid. This set of data was collected using the same exact samples used in the first trial. The variable is the 24-hour time window between the measurements. Samples were stored in a cool dark place in interim.

### Results and Discussion

Figure 112 shows the normalized absorption and fluorescence of the 24-hour measurements. All fluorescent spectra were excited at 365 nm.

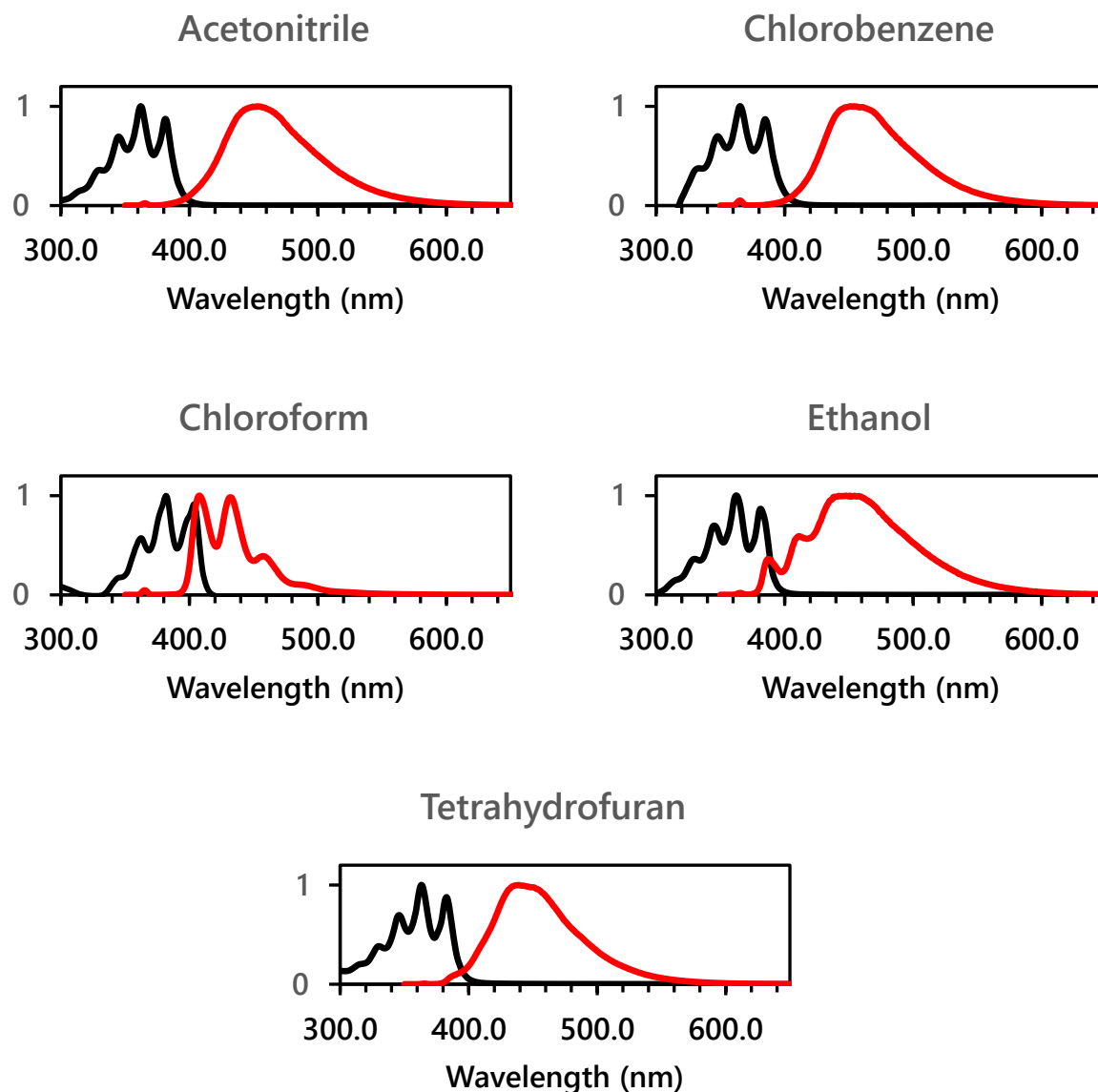


Figure 112 – Absorption and fluorescence overlap for 9-anthroic acid in various solvents. Excitation 365 nm.

Comparison between 0-hour and 24-hour begins with Figure 113. In cases for acetonitrile, chlorobenzene, ethanol, and tetrahydrofuran, very little spectral change for absorption is observed. Intensity and peak position are unchanged for acetonitrile, chlorobenzene ethanol and tetrahydrofuran. Chloroform, on the other hand, exhibits a significant change in spectral shape and appears to red-shift. A red shift of this magnitude could indicate the formation of j-aggregates, or

at least dimers, being formed after 24-hours in solution. Such change in spectral shape may only be observable for chloroform, yet be present with other solvents. The difference being rate of change. Chloroform as a solvent for 9-anthroic acid exhibits a slow enough solvating behavior that over a period of 24-hours spectral shift is observed. No other solvent in this trial exhibits this behavior.

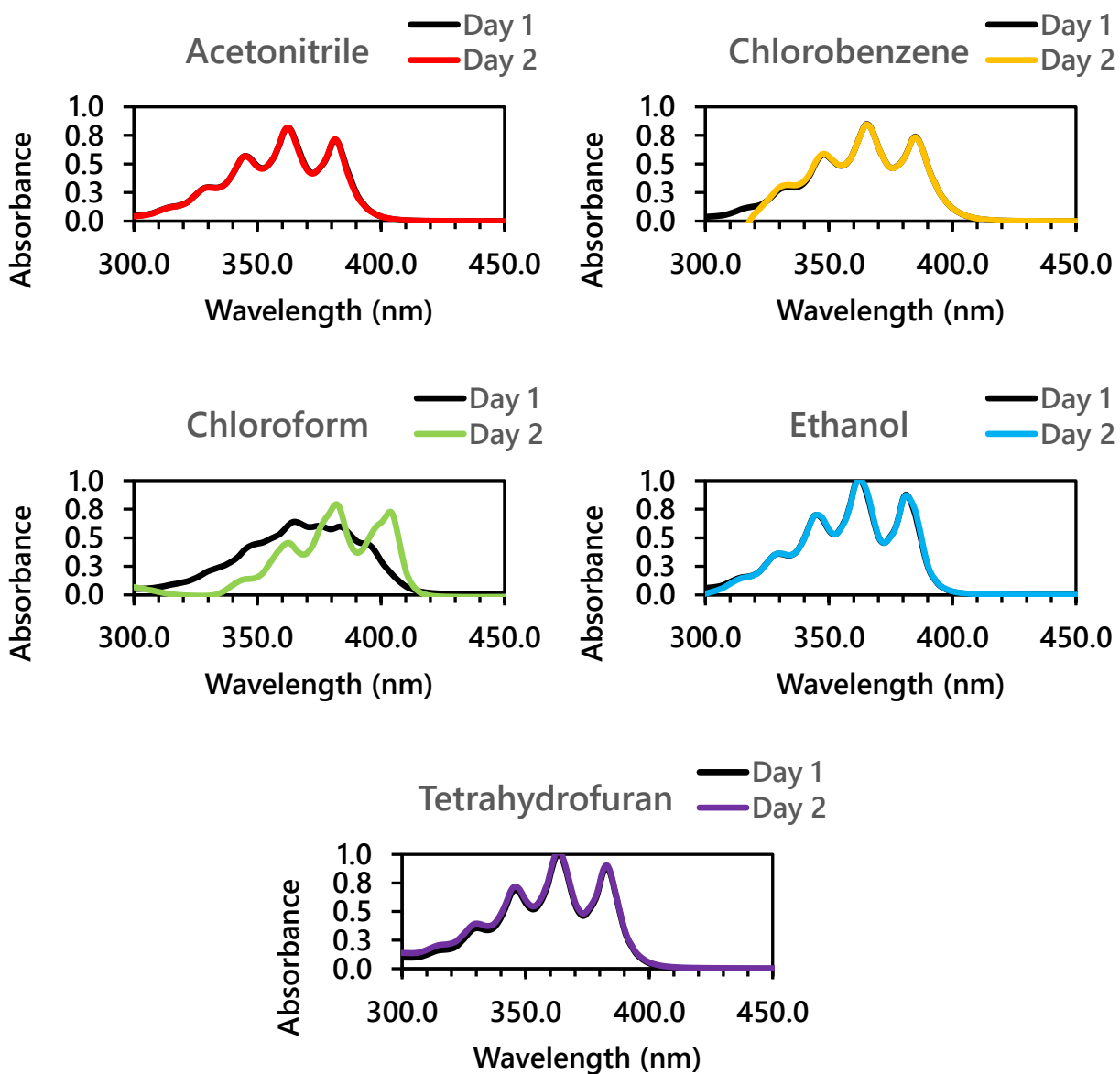


Figure 113 – Absorption comparison between 0-hour and 2- hour measurement of 9-anthric acid in various solvents

To further explore the solvent effects on 9-anthric acid, fluorescence measurements were repeated after 24 hours, also. Very little change to emission spectra for acetonitrile, chlorobenzene, ethanol, and tetrahydrofuran was observed. The magnitude and peak position remain very consistent. Again, chloroform stands out as the variable. The emission of 9-anthric acid in chloroform has increased in intensity considerably after remaining in solution for 24-hours. It is also the only

solvent to maintain the mirror rule with the vibronic peaks being clearly visible. It should also be noted after these experiments that ethanol provides the strongest emission intensity at the shortest wavelength. This is an indication of fluorescence from the higher energy excited states available to 9-anthroic acid: shortest wavelength peak at 395 nm. This is possibly true for chloroform also, having a primary peak around 410 nm. Other solvents have broad and strongly shifted bell-curve styled emission indicating the relaxation process in taking place from the lowest excited states available.

Furthermore, it is observed that photophysical stability remains for 9-anthroic acid after 24 hours in solution. A further trial may be needed to confirm that a steady state has been found for the chloroform sample.

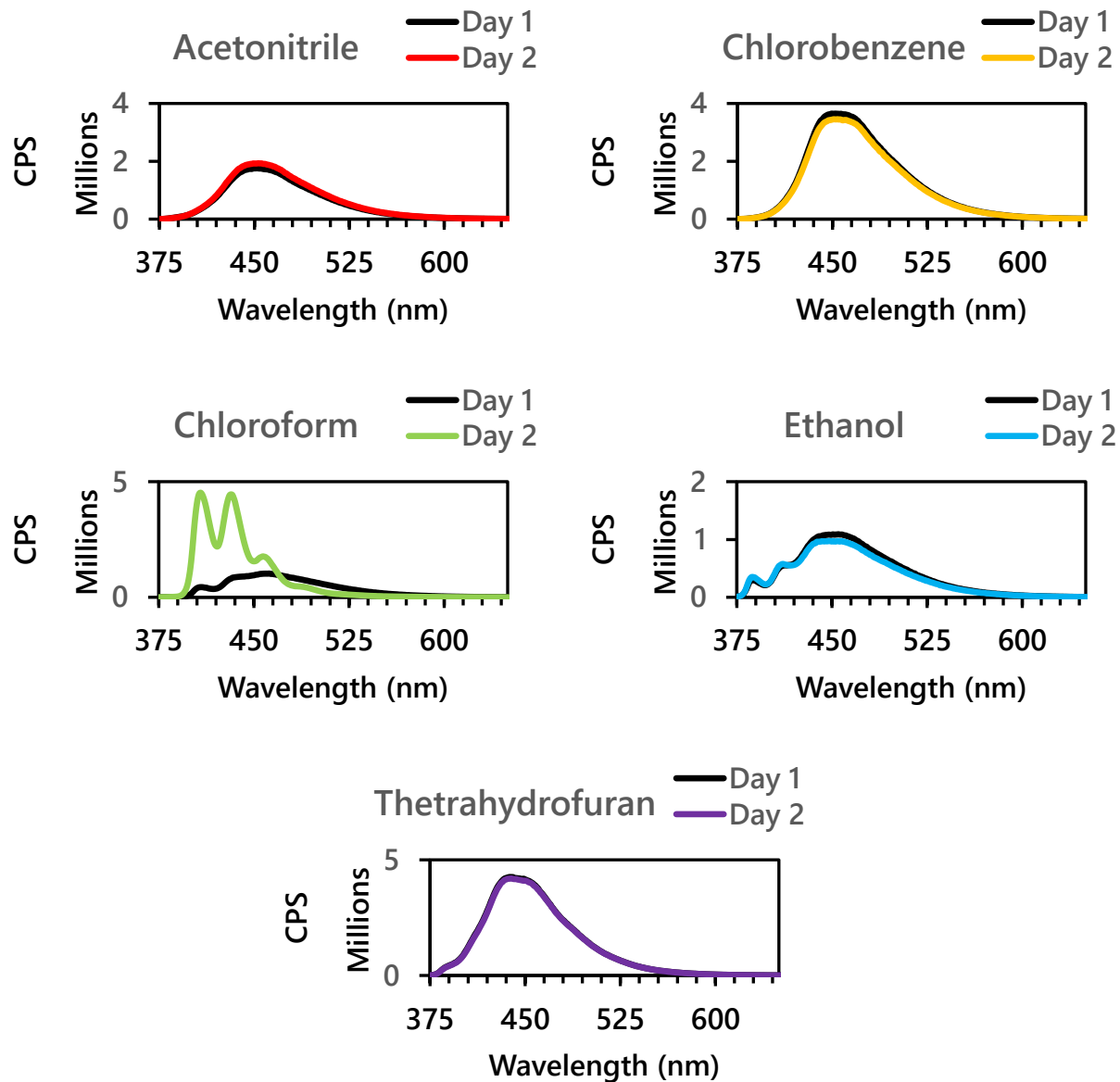


Figure 114 – Fluorescence comparison between 0-hour and 24-hour measurements of 9-anthracic acid in various solvents.

## Concluding remarks

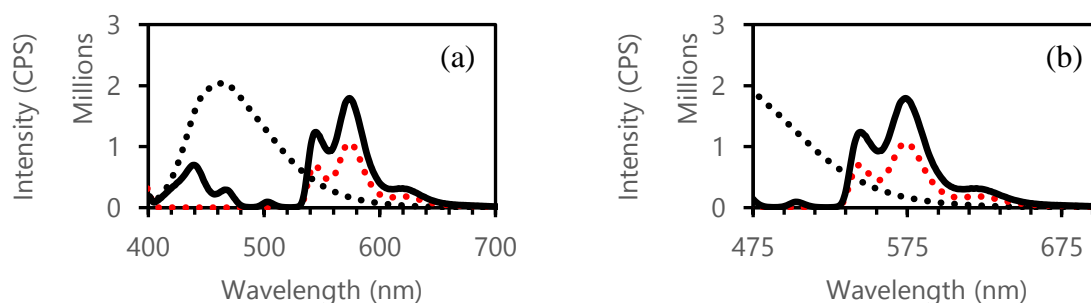
The follow-up analysis for solvated 9-anthracic acid showed consistent emission and absorption spectra for acetonitrile, chlorobenzene, ethanol, and tetrahydrofuran. Acetonitrile, chlorobenzene, and tetrahydrofuran exhibited the least resolved emission peak. Ethanol presented minor vibronic resolution yet remained comparably unchanged over the 24-hour period. Chloroform shows the most variation in the time provided. After 24-hours, it was the only solvent to present distinct vibronic peaks within a fluorescent emission spectra and maintain a mirror image.

## PRELIMINARY SOLVENT DEPENDENCE FOR DONOR/ACCEPTOR BLENDS

Blend trials with THF and acetonitrile were conducted to establish more reference data dependent upon solvent. These two solvents were used to produce a large contrast in polarity performance.

## Chloroform ( $\text{CHCl}_3$ )

Relative yield of 9-AA fluorescence is equivalent compared to PDI-silane in  $\text{CHCl}_3$ . Increase of blend emission is present with blended sample. Strong quenching of 9-AA emission is clear and present with blended sample. Magnified view of spectra shows 575 nm emission of PDI-silane to be the most enhanced region of emission spectra. Summation of PDI-silane reference and 9-AA reference was made to compare with blend spectra in order to emphasize contribution of resonance energy transfer over radiative emission. Blended emission still remained higher in magnitude over summation. This is strong evidence that FRET is contributing to enhanced emission.



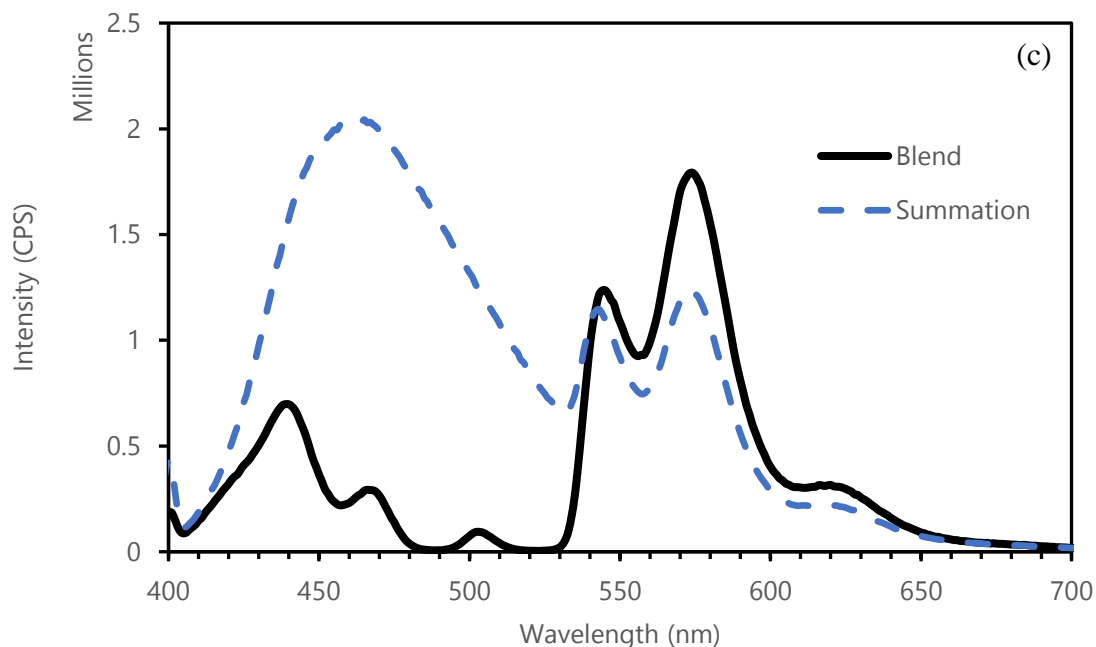


Figure 115 – (a and b) Fluorescence spectra for blend in  $\text{CHCl}_3$ . Black dot represents 9-AA reference sample, red dot represents PDI-s reference sample, and black line represents blended sample. Excitation at 365 nm. (c) Blend vs. summation of 9-AA reference and PDI-silane reference

FRET efficiencies were calculated for relative efficiency using corrective methods. After potential false emission contributions were subtracted from blend emission, relative FRET efficiency could be calculated to be 17.10%. Assuming no contribution to the blend emission spectra from 9-AA, relative FRET efficiency could be calculated to be as high as 25.90%.

<i>Method</i>	<i>Result</i>
<i>FRET Efficiency</i>	38.92% $\pm$ 9.44
<i>FRET Efficiency (Rad. Ex. Corr.)</i>	25.90% $\pm$ 8.13
<i>FRET Efficiency (Rad. Ex. Corr. + 9-AA Ex. Corr.)</i>	17.10% $\pm$ 6.34

Table 14 – Preliminary  $\text{CHCl}_3$  Relative FRET efficiency calculation results

### *Spectral Decomposition*

Gaussian fits were produced of the distinct emission peaks in the spectra of Figure 116. Three gaussians were used for an acceptably accurate fit with parameters provided in Table 15. The Gaussian is prepared with the following formula:

$$y = C e^{-\left(\frac{x-\mu}{\sigma}\right)^2} \quad (30)$$

No spectral overlap was accounted for in the blended spectra between acceptor and donor due to clear separation between the two spectral components.

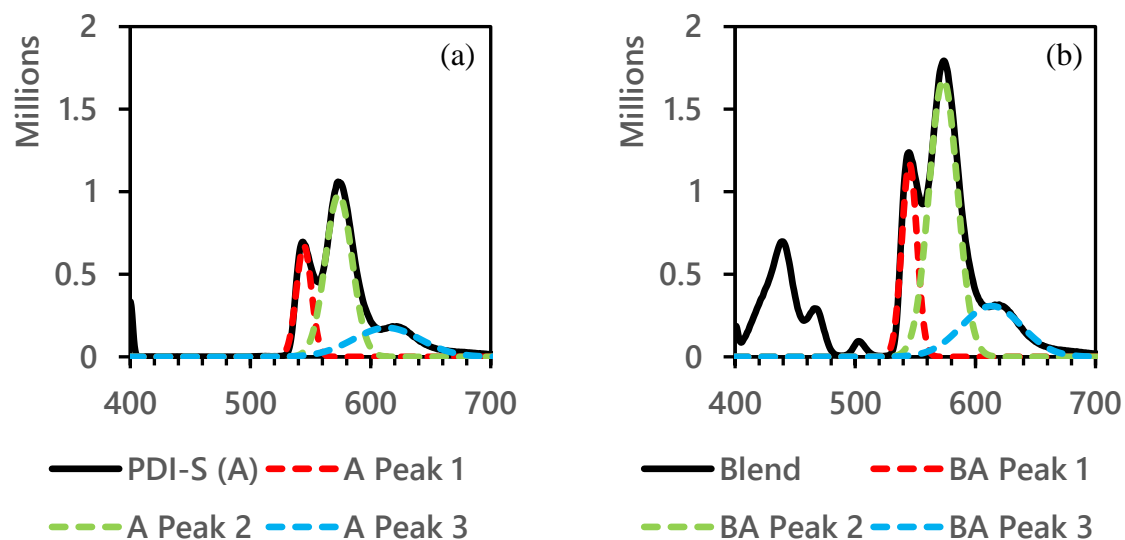


Figure 116 – Three gaussian spectral decomposition of THF solvated PDI-S reference solution and PDI-S blend component. (a) Reference PDI-S solution. (b) Blended PDI-S and 9AA solution.

	<i>Acceptor reference <math>S_1[0-0]</math></i>	<i>Acceptor reference <math>S_1[0-1]</math></i>	<i>Acceptor reference <math>S_1[0-2]</math></i>	<i>Acceptor blend <math>S_1[0-0]</math></i>	<i>Acceptor blend <math>S_1[0-1]</math></i>	<i>Acceptor blend <math>S_1[0-2]</math></i>
$\mu$	544.5	573.5	613.5	545.1	573.3	613.5
$\sigma$	8.87	15.65	39.38	8.959	16.74	35.43
$C$	6.71E+05	9.82E+05	1.76E+05	1.17E+06	1.68E+06	3.07E+05

Table 15 – Gaussian fit parameters for Figure 116

The growth of each emission peak from reference gaussian peak to blended gaussian peak is recorded in Table 16. The relative efficiency of energy transfer is implied to be much greater than calculations presented in Table 14.

	<i>Gaussian 1</i>	<i>Gaussian 2</i>	<i>Gaussian 3</i>
<i>Percent growth over reference</i>	76%	83%	57%

Table 16 – Growth of blended acceptor gaussian fits in comparison to reference acceptor peaks in chloroform.

#### Tetrahydrofuran (THF)

Relative yield of 9-AA fluorescence is strong compared to PDI-silane in THF. increase of blend emission is present with blended sample. Strong quenching of 9-AA emission is clear and present with blended sample. Residual emission of 9-AA occurs between 400-450 nm where PDI-silane absorption is weak. Magnified view of spectra shows 575 nm emission of PDI-silane to be the most enhanced region of emission spectra. Summation of PDI-silane reference and 9-AA reference was made to compare with blend spectra in order to emphasize contribution of resonance energy transfer over radiative emission. Blended emission still remained higher in magnitude over summation. this is strong evidence that FRET is contributing to enhanced emission.

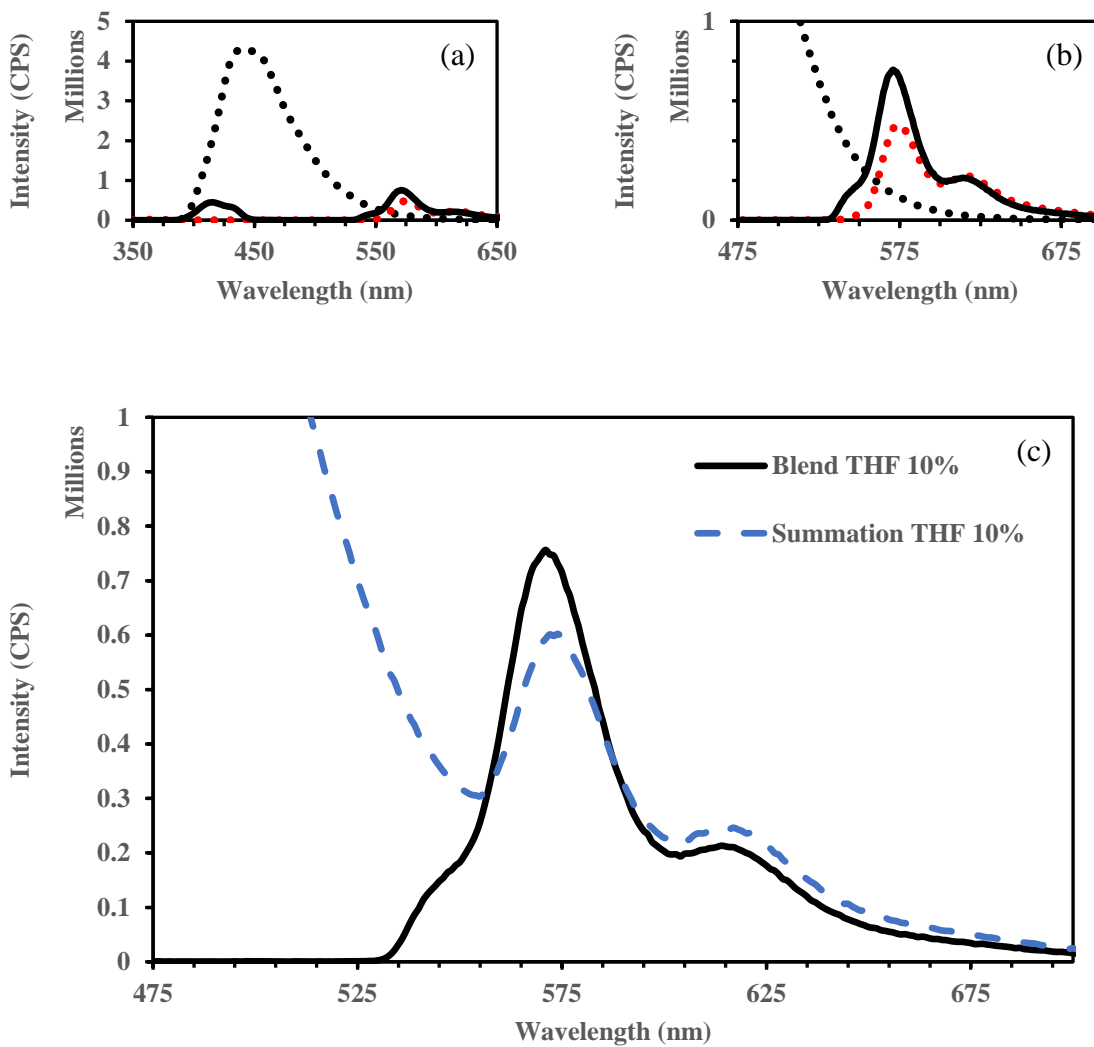


Figure 117 – (a and b) Fluorescence spectra for blend in THF. Black dot represents 9-AA reference sample, red dot represents PDI-s reference sample, and black line represents blended sample. Excitation at 365 nm. (c) Blend vs. summation of 9-AA reference and PDI-silane reference.

FRET efficiencies were calculated for relative efficiency using corrective methods. After potential false emission contributions were subtracted from blend emission, relative FRET efficiency could be calculated to be 3%. Assuming no contribution to the blend emission spectra from 9-AA, relative FRET efficiency could be calculated to be as high as 7%.

<i>Method</i>	<i>Result</i>
<i>FRET Efficiency</i>	12.77% $\pm$ 4.32
<i>FRET Efficiency (Rad. Ex. Corr.)</i>	6.70% $\pm$ 1.13
<i>FRET Efficiency (Rad. Ex. Corr. + 9-AA Ex. Corr.)</i>	2.62% $\pm$ 0.85

Table 17 – Preliminary THF Relative FRET efficiency calculation results

### *Spectral Decomposition*

Gaussian fits were produced of the distinct emission peaks in the spectra of Figure 118. Two gaussians were used for an acceptably accurate fit with parameters provided in Table 18.

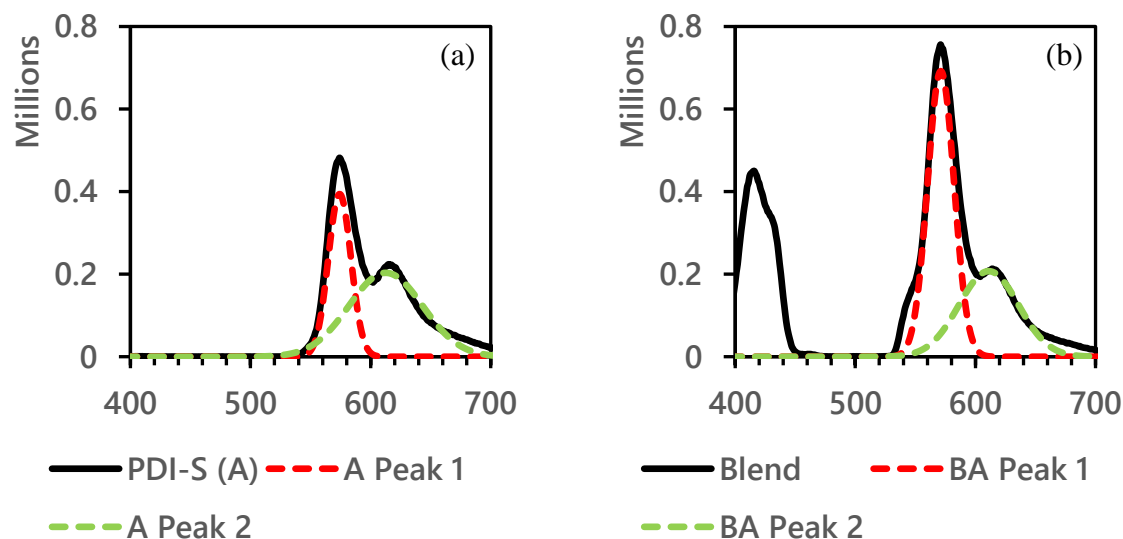


Figure 118 – Two gaussian spectral decomposition of chloroform solvated PDI-S reference solution and PDI-S blend component. (a) Reference PDI-S solution. (b) Blended PDI-S and 9AA solution.

No spectral overlap was accounted for in the blended spectra between acceptor and donor due to clear separation between the two spectral components.

	<i>Acceptor reference S<sub>1</sub> [0-1]</i>	<i>Acceptor reference S<sub>1</sub> [0-2]</i>	<i>Acceptor blend S<sub>1</sub> [0-1]</i>	<i>Acceptor blend S<sub>1</sub> [0-2]</i>
$\mu$	574.2	612.6	571.2	611.1
$\sigma$	13.34	43.4	15.65	35.03
$C$	3.94E+05	2.03E+05	6.92E+05	2.07E+05

Table 18 – Gaussian fit parameters for Figure 118

The growth of each emission peak from reference gaussian peak to blended gaussian peak is recorded in Table 19. The relative efficiency of energy transfer is implied to be much greater than calculations presented in Table 17.

	<i>Gaussian 1</i>	<i>Gaussian 2</i>
<i>Percent growth over reference</i>	106%	-18%

Table 19 – Growth of blended acceptor gaussian fits in comparison to reference acceptor peaks in THF

#### Acetonitrile (MeCN)

Acetonitrile shows lower yield for both 9-AA and PDI-silane when compared to THF. Blend sample shows poor quenching performance of 9-AA and little enhancement of PDI-silane emission over the 9-AA radiative emission profile. The summation spectral profile is consistently higher than the blend throughout the wavelengths. FRET efficiency calculations were not appropriate for this sample set due to no significant spectral contribution above the ‘noise’ of radiative emission.

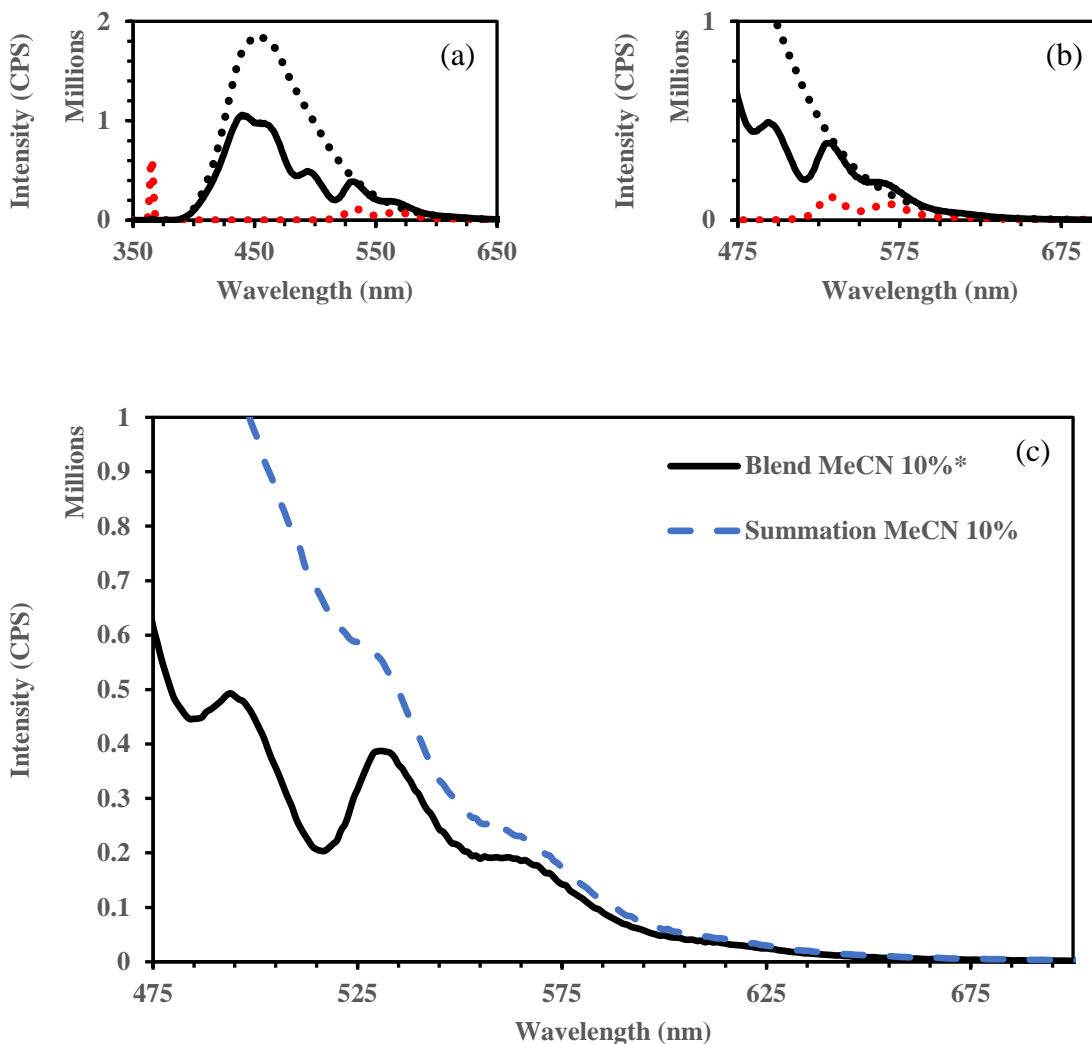


Figure 119 – (a and b) Fluorescence spectra for blend in acetonitrile. Black dot represents 9-AA reference sample, red dot represents PDI-s reference sample, and black line represents blended sample. Excitation at 365 nm. (c) Blend vs. summation of 9-AA reference and PDI-silane reference.

In an effort to improve quenching of 9-AA, concentration of the PDI-silane sample was increased 10x. At such concentration, solubility is poor, and it is unlikely sample was completely dissolved. fluorescent intensity increase indicates that the increase of material in solution was minimal due to marginal gains from emission intensity. Quenching of 9-AA could be seen to increase with comparison but did not significantly contribute to gained fluorescence from PDI-silane. It was

again not prudent to calculate FRET efficiency from such outcome due to overlapping radiative emission.

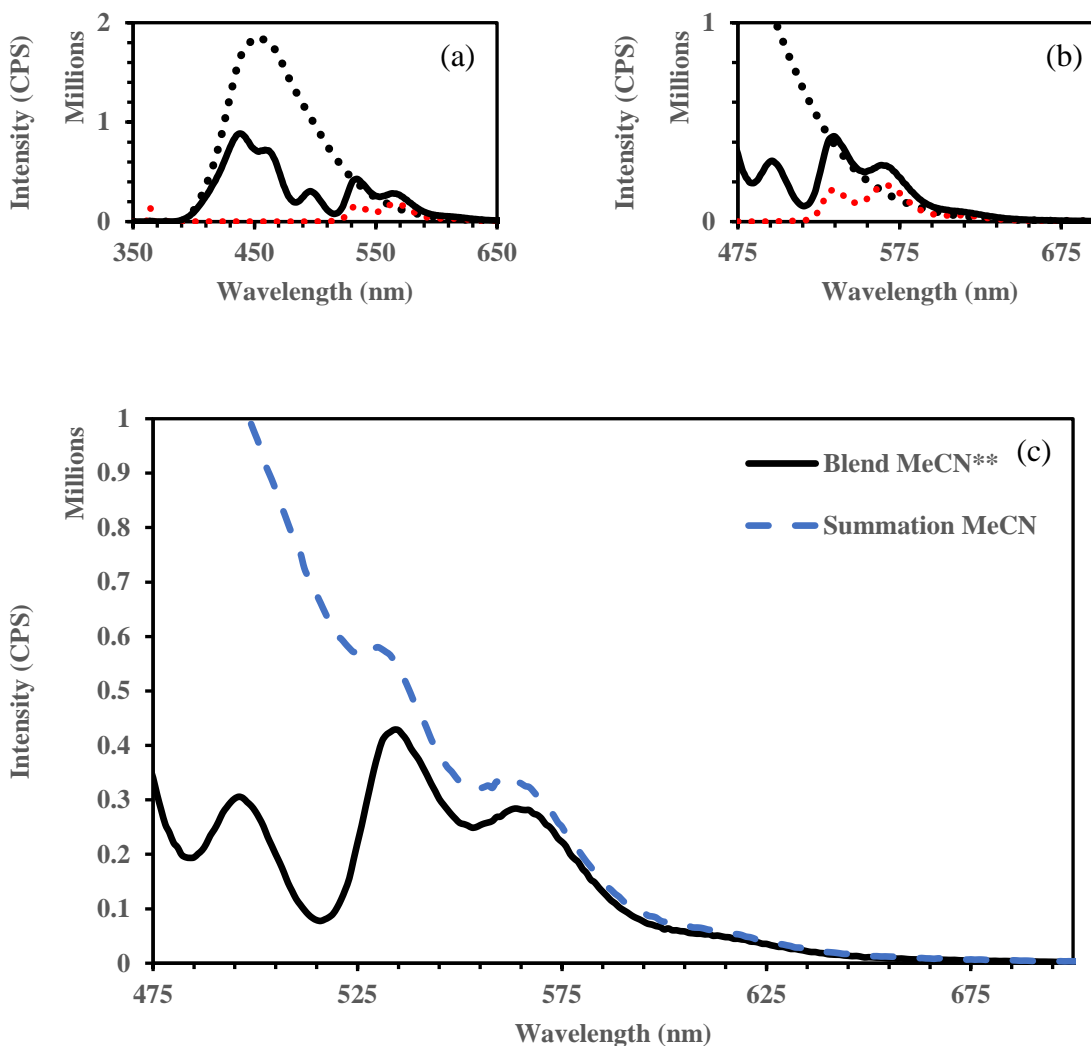


Figure 120 – Fluorescence spectra for blend in saturated acetonitrile. Black dot represents 9-AA reference sample, red dot represents PDI-s reference sample, and black line represents blended sample. Excitation at 365 nm. (c) Blend vs. summation of 9-AA reference and PDI-silane reference.

### *Spectral Decomposition*

Gaussian fits were produced of the distinct emission peaks in the spectra of Figure 121. Three gaussians were used for an acceptably accurate fit with parameters provided in Table 20.

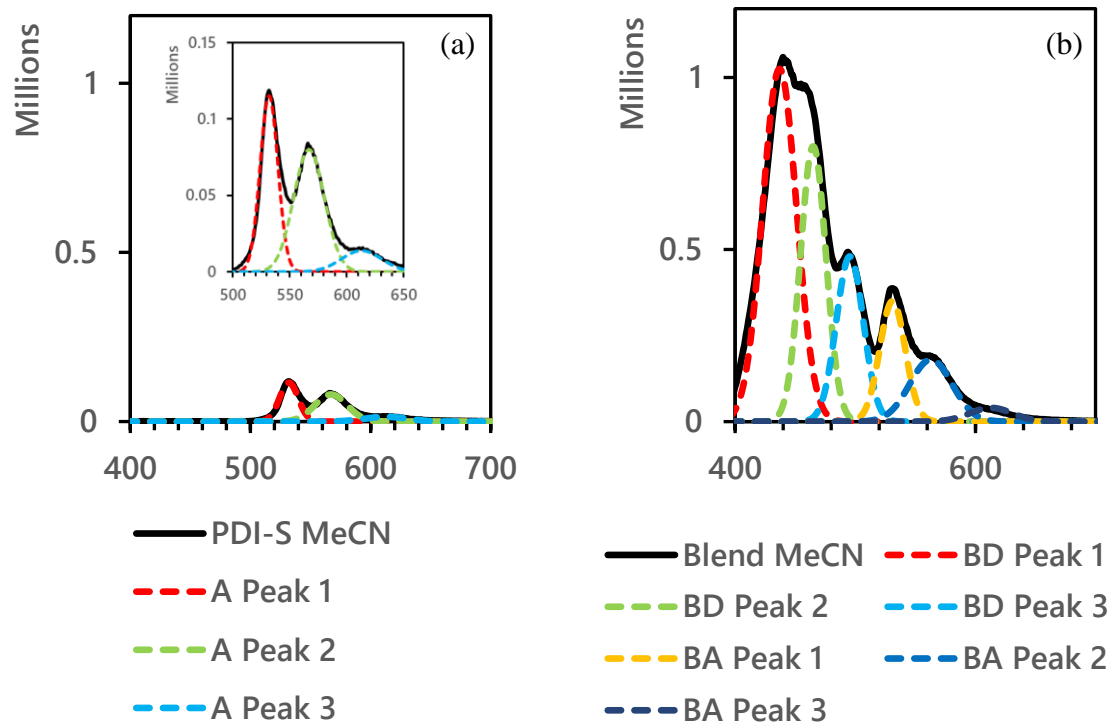


Figure 121 – Three gaussian spectral decomposition of acetonitrile solvated PDI-S reference solution and PDI-S blend component. (a) Reference PDI-S solution. (b) Blended PDI-S and 9AA solution

	<i>Acceptor reference S<sub>1</sub>[0-0]</i>	<i>Acceptor reference S<sub>1</sub> [0-1]</i>	<i>Acceptor reference S<sub>1</sub> [0-2]</i>	<i>Acceptor blend S<sub>1</sub> [0-0]</i>	<i>Acceptor blend S<sub>1</sub> [0-1]</i>	<i>Acceptor blend S<sub>1</sub> [0-2]</i>
$\mu$	532	567	613	531	563	613
$\sigma$	11	19	25	15	25	25
$C$	115000	80000	14000	350000	180000	40000

Table 20 – Gaussian fit parameters for Figure 121

The growth of each emission peak from reference gaussian peak to blended gaussian peak is recorded in Table 20. The relative efficiency of energy transfer is potentially present and perceivable unlike previous methods for calculations for interpreting energy transfer.

	<i>Gaussian 1</i>	<i>Gaussian 2</i>	<i>Gaussian 3</i>
<i>Percent growth over reference</i>	315%	196%	186%

Table 21 – Growth of blended acceptor gaussian fits in comparison to reference acceptor peaks in acetonitrile.

### Concluding Remarks

CHCl<sub>3</sub> provided the greatest FRET efficiency values using the current method with possible range between 17-26%. THF also proved to be a solvent capable of producing resonant energy transfer between PDI-silane and 9-AA. A potential efficiency between 3-7 % shows room for improvement through varying blend ratio and concentration. Acetonitrile acted as a poor solvent for this system and was not able to produce definitive results to suggest resonant energy transfer. overall, this trend of efficiencies matches with dielectric constant and viscosity trends found in comparable work<sup>82,83</sup>.

## QUANTUM YIELDS

### Molar Attenuation

Molar concentration and molar attenuation were calculated for PDMS-anthracene and PDI-silane based upon solution samples. These values were calculated using the following equations, respectively:

$$C = \frac{m}{M.W. \times V} \quad (31)$$

$$\varepsilon = \frac{A}{C \times L} \quad (32)$$

where  $m$  is the mass of material in solution,  $M.W.$  is the molecular weight of the material,  $V$  is the volume of solvent used,  $A$  is the absorbance, and  $L$  is the cuvette cell length.

<i>Material</i>	<i>Molar Concentration (C)</i>	<i>Molar Attenuation (<math>\varepsilon</math>)</i>
<i>PDMS-anthracene</i>	0.043 mol/m <sup>3</sup> (43 mol/L)	2160.23 m <sup>2</sup> /mol
<i>PDI-silane</i>	0.023 mol/m <sup>3</sup> (23 mol/L)	3886.53 m <sup>2</sup> /mol

Table 22 – Molar concentration and attenuation values for PDMS-anthracene and PDI-silane.

### Quantum Yield

Quantum yield has been calculated for PDMS-anthracene from comparative analysis to a standard of quinine sulphate. 1 mg (0.35 mmol) of PDMS-anthracene was added to 1 mL of CHCl<sub>3</sub> and sonicated for 5 minutes. Solution was diluted down to 10 µg/mL to reduce absorption to around 0.1. 2.72 mg (3.5 mmol) of quinine sulphate was then added to 1 mL of sulfuric acid (0.1M) and reduced to 2.72 µg/mL; to match molar concentration of the PDMS-anthracene solution. For further comparison and confirmation 9-anthroic acid was prepared in EtOH. 7.7 mg (35 mmol) was added to 1 mL of EtOH (200 proof) and reduced to 0.77 µg/mL; to match molar concentration of PDMS-anthracene. UV-vis and fluorescent spectra of all solutions was obtained and used for calculating quantum yield. Excitation wavelength for all samples was 365 nm.

UV-vis was completed of each sample to verify the peak position of maximum absorption around 365 nm and that the maxima were below 0.1 absorbance. Area under the fluorescence curve is used for quantum efficiency calculation. The following equation is used for such calculation <sup>84</sup>.

$$\phi_{fl,x} = \phi_{fl,ref} \left( \frac{A_{ref}(\lambda)}{A_x(\lambda)} \right) \left( \frac{\int E_x d\lambda}{\int E_{ref} d\lambda} \right) \left( \frac{n_x}{n_{ref}} \right)^2 \quad (33)$$

where,  $\phi_{fl}$  is the unknown fluorescence quantum yield of the sample,  $A$  is the absorbance of the solutions at the exciting wavelength  $\lambda$ ,  $\int E$  is the integrated and detector-corrected emission band area expressed in numbers of photons, and  $n$  is the refractive index of the solvent. Subscripts *ref* and *x* refer to the reference standard and to the unknown, respectively.

Quinine sulphate was used as the reference material due to its good emission spectrum overlap. From literature, the quantum yield of quinine sulphate is 0.54 between 400 – 600 nm <sup>85</sup>. As another comparative measure, 9-anthroic acid – one of the precursors to PDMS-anthracene – was experimentally evaluated and compared with literature. When an emission range of 400 – 600 nm was used, the quantum yield of 9-anthroic acid matched with literature value of 0.05 <sup>86</sup>. This provided good confidence for the accuracy of the experimental quantum yield for PDMS-anthracene. Computed within the same spectral range, PDMS-anthracene produces a quantum yield of 0.19,

	<b>Quinine sulphate</b>	<b>9-anthroic acid</b>	<b>PDMS-anthracene</b>
<i>Solvent</i>	Sulfuric acid (0.1M)	EtOH (200 proof)	CHCl <sub>3</sub> (anhydrous)
<i>Refractive Index</i>	1.33 (water)	1.365	1.45
<i>Excitation Wavelength</i>	365 nm	365 nm	365 nm
<i>Absorbance</i>	0.0094498	0.025581	0.10488
<i>Emission Range</i>	400 – 600 nm	400 – 600 nm	400 – 600 nm
<i>Emission Integral</i>	1.4508x10 <sup>8</sup>	3.748x10 <sup>7</sup>	4.6657x10 <sup>8</sup>
<i>Quantum Yield</i>	0.54	0.05	0.19

Table 23 – Quantum yield calculation data table for 400-600 nm emission range

As stated by a few sources, anthracene alone has a quantum yield of 0.27 between 360 – 480 nm. Because materials under investigation have resonant structure more like anthracene than quinine sulphate. The calculations were rerun with a narrower emission integral. The design of such was intended to cut off at the upper limit band of anthracenes accepted quantum efficiency. The reference still holds true to its quantum efficiency as calculations remain in the standardized range of measurement for quinine sulphate.

	<b>Quinine sulphate</b>	<b>9-anthroic acid</b>	<b>PDMS- anthracene</b>
<i>Solvent</i>	Sulfuric acid (0.1M)	EtOH (200 proof)	CHCl <sub>3</sub> (anhydrous)
<i>Refractive Index</i>	1.33 (water)	1.365	1.45
<i>Excitation Wavelength</i>	365 nm	365 nm	365 nm
<i>Absorbance</i>	0.0094498	0.025581	0.10488
<i>Emission Range</i>	400 – 480 nm	400 – 480 nm	400 – 480 nm
<i>Emission Integral</i>	1.0603x10 <sup>8</sup>	3.6265x10 <sup>7</sup>	2.898x10 <sup>8</sup>
<i>Quantum Yield</i>	0.54*	0.07	0.16

Table 24 – Quantum yield calculation data table for 400-480 nm emission range

#### Concluding Remarks

Quantum yield for PDMS-anthracene was calculated to be 0.16 in anhydrous chloroform between 400-480 nm when excited at 365 nm.

#### TRIAL ERRORS

The nature of the experiments conducted in this study provide multiple opportunities for procedure error to arise via minute differences in preparation conditions resulting in environmental variations. Such changes may very well alter the outcome of identically designed procedures therefore, this subsection intends to quantify likely variances in the succeeding work.

In order to construct a general guide of error, three independent sets of concentration blend trials were performed with identical formulation. The specific ratios are provided in Table 25. Stock solutions for both fluorophores were created at 10 mM/mL concentrations.

	<i>9AA 10% stock solution</i>	<i>PDI-S 10% stock solution</i>	<i>Chloroform</i>	<i>Molar Concentration</i>
<i>1:16 PDI-S reference</i>	0 $\mu\text{L}$	800 $\mu\text{L}$	200 $\mu\text{L}$	0 $\mu\text{M}$ D – 800 $\mu\text{M}$ A
<i>1:8 PDI-S reference</i>	0 $\mu\text{L}$	400 $\mu\text{L}$	600 $\mu\text{L}$	0 $\mu\text{M}$ D – 400 $\mu\text{M}$ A
<i>1:5 PDI-S reference</i>	0 $\mu\text{L}$	250 $\mu\text{L}$	750 $\mu\text{L}$	0 $\mu\text{M}$ D – 250 $\mu\text{M}$ A
<i>1:4 PDI-S reference</i>	0 $\mu\text{L}$	200 $\mu\text{L}$	800 $\mu\text{L}$	0 $\mu\text{M}$ D – 200 $\mu\text{M}$ A
<i>1:3 PDI-S reference</i>	0 $\mu\text{L}$	150 $\mu\text{L}$	850 $\mu\text{L}$	0 $\mu\text{M}$ D – 150 $\mu\text{M}$ A
<i>1:2 PDI-S reference</i>	0 $\mu\text{L}$	100 $\mu\text{L}$	900 $\mu\text{L}$	0 $\mu\text{M}$ D – 100 $\mu\text{M}$ A
<i>1:1 PDI-S reference</i>	0 $\mu\text{L}$	50 $\mu\text{L}$	950 $\mu\text{L}$	0 $\mu\text{M}$ D – 50 $\mu\text{M}$ A
<i>2:1 PDI-S reference</i>	0 $\mu\text{L}$	25 $\mu\text{L}$	975 $\mu\text{L}$	0 $\mu\text{M}$ D – 25 $\mu\text{M}$ A
<i>4:1 PDI-S reference</i>	0 $\mu\text{L}$	12.5 $\mu\text{L}$	987.5 $\mu\text{L}$	0 $\mu\text{M}$ D – 12.5 $\mu\text{M}$ A
<i>8:1 PDI-S reference</i>	0 $\mu\text{L}$	6.25 $\mu\text{L}$	993.75 $\mu\text{L}$	0 $\mu\text{M}$ D – 6.25 $\mu\text{M}$ A
<i>16:1 PDI-S reference</i>	0 $\mu\text{L}$	3.125 $\mu\text{L}$	996.875 $\mu\text{L}$	0 $\mu\text{M}$ D – 3.125 $\mu\text{M}$ A
<i>1:1 9AA reference</i>	50 $\mu\text{L}$	0 $\mu\text{L}$	950 $\mu\text{L}$	50 $\mu\text{M}$ D – 0 mM A
<i>1:16</i>	50 $\mu\text{L}$	800 $\mu\text{L}$	150 $\mu\text{L}$	50 $\mu\text{M}$ D – 800 $\mu\text{M}$ A
<i>1:8</i>	50 $\mu\text{L}$	400 $\mu\text{L}$	550 $\mu\text{L}$	50 $\mu\text{M}$ D – 400 $\mu\text{M}$ A
<i>1:5</i>	50 $\mu\text{L}$	250 $\mu\text{L}$	700 $\mu\text{L}$	50 $\mu\text{M}$ D – 250 $\mu\text{M}$ A
<i>1:4</i>	50 $\mu\text{L}$	200 $\mu\text{L}$	750 $\mu\text{L}$	50 $\mu\text{M}$ D – 200 $\mu\text{M}$ A
<i>1:3</i>	50 $\mu\text{L}$	150 $\mu\text{L}$	800 $\mu\text{L}$	50 $\mu\text{M}$ D – 150 $\mu\text{M}$ A
<i>1:2</i>	50 $\mu\text{L}$	100 $\mu\text{L}$	850 $\mu\text{L}$	50 $\mu\text{M}$ D – 100 $\mu\text{M}$ A
<i>1:1</i>	50 $\mu\text{L}$	50 $\mu\text{L}$	900 $\mu\text{L}$	50 $\mu\text{M}$ D – 50 $\mu\text{M}$ A
<i>2:1</i>	50 $\mu\text{L}$	25 $\mu\text{L}$	925 $\mu\text{L}$	50 $\mu\text{M}$ D – 25 $\mu\text{M}$ A
<i>4:1</i>	50 $\mu\text{L}$	12.5 $\mu\text{L}$	937.5 $\mu\text{L}$	50 $\mu\text{M}$ D – 12.5 $\mu\text{M}$ A
<i>8:1</i>	50 $\mu\text{L}$	~6.25 $\mu\text{L}$	~943.75 $\mu\text{L}$	50 $\mu\text{M}$ D – 6.25 $\mu\text{M}$ A
<i>16:1</i>	50 $\mu\text{L}$	~3.125 $\mu\text{L}$	~946.875 $\mu\text{L}$	50 $\mu\text{M}$ D – 3.125 $\mu\text{M}$ A

Table 25 – Sample concentration guide of error analysis

The average fluorescence intensity of 9-AAs emission in blend was taken for each ratio of D:A. The standard deviations of these averages were also calculated. These two sets of statistical values were used in conjunction with Stern-Volmer plots to confirm a bimodal quenching system and the confidence of such conclusion.

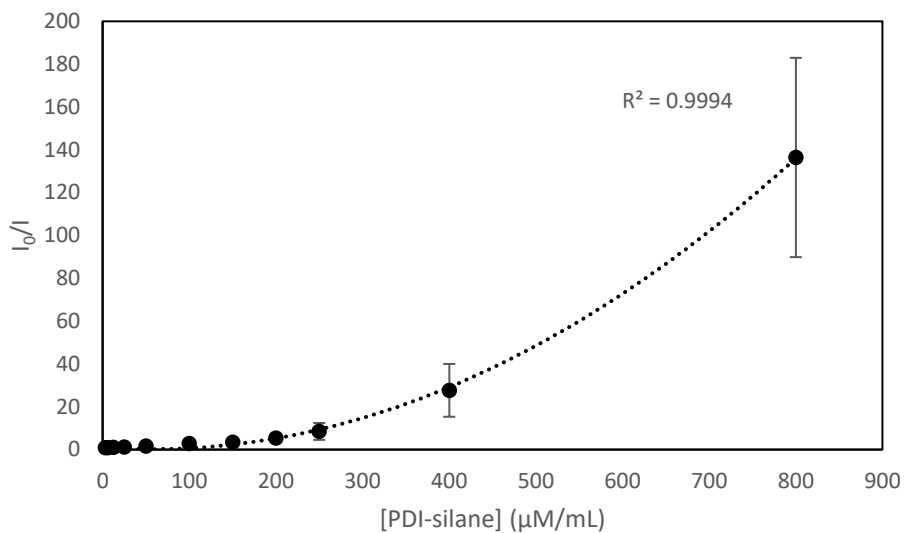


Figure 122 – Stern-Volmer plot of blended concentration error trials showing 2<sup>nd</sup> order quadratic fit and one standard deviation from the mean.

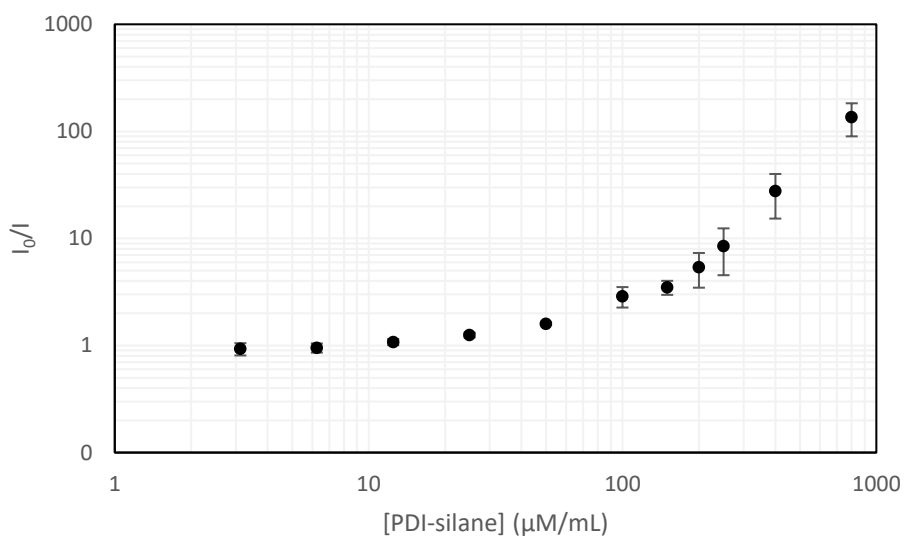


Figure 123 – Log base 10 scaled axes for Stern-Volmer plot of blended concentration error trials showing 2<sup>nd</sup> order quadratic fit and one standard deviation from the mean.

Figure 122 presents a highly confident second order quadratic fit to the quenching of 9-AA via PDI-silane. The logarithmic scale plot of Figure 123 provides visualization of the one standard deviation from the mean. To further explore the significance of error for each concentration blend

Figure 124 presents one standard deviation from the mean as CPS from the fluorometer and that same deviation as a percentage of the total fluorescent emission measured in CPS. This shows that the error of low concentrations of PDI-silane (<100  $\mu\text{M}/\text{mL}$ ) have minor variation relative to concentrations equal to and greater than 100  $\mu\text{M}/\text{mL}$ . Once concentrations reach 400  $\mu\text{M}/\text{mL}$  and above, remaining fluorescence is so minimal that standard deviation of such detection is large because the total CPS is so small. Most importantly, Figure 124 reveals that confidence with results using 200-250  $\mu\text{M}/\text{mL}$  concentrations of PDI-silane is most varied.

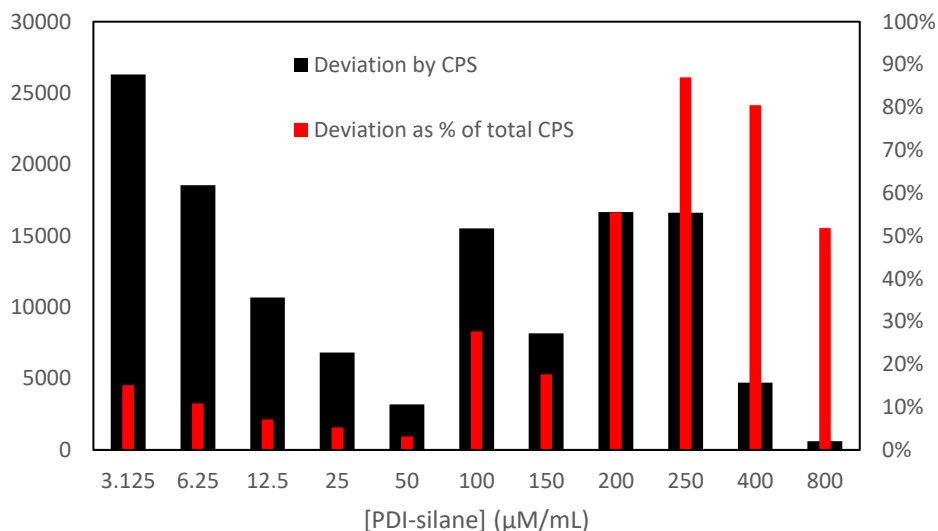


Figure 124 – Bar chart presenting the standard deviation in fluorescent emission CPS, and as a % of total CPS

For this work to be applied to future experiments, normalization is necessary. The best constant in this work is the reference fluorescence of 9-AA. Many subsequent studies use concentrations of 50  $\mu\text{M}/\text{mL}$ , or very near, and 9-AA should retain a linear dependence to concentration within one order of magnitude. Normalizing the trial set with respect to their independent reference 9-AA samples reveals very little variation in the Stern-Volmer analysis presented in Figure 125 and Figure 126. Taking the standard deviation of the normalized data provides a general error for each concentration case. Taking the average of these errors allows us to obtain a percentage of likely deviation like preceding normalized data may contain.

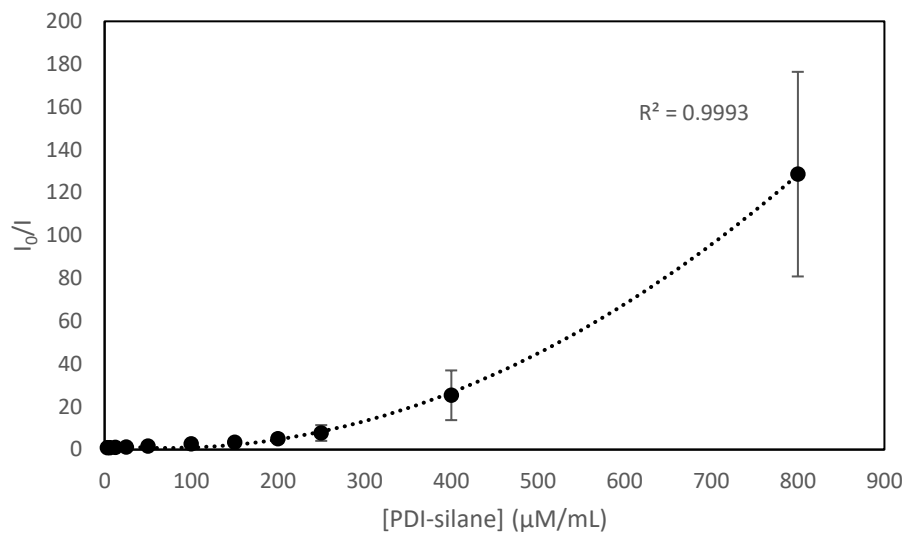


Figure 125 – Normalized 9-AA emission Stern-Volmer plot of blended concentration error trials showing 2<sup>nd</sup> order quadratic fit and one standard deviation from the mean.

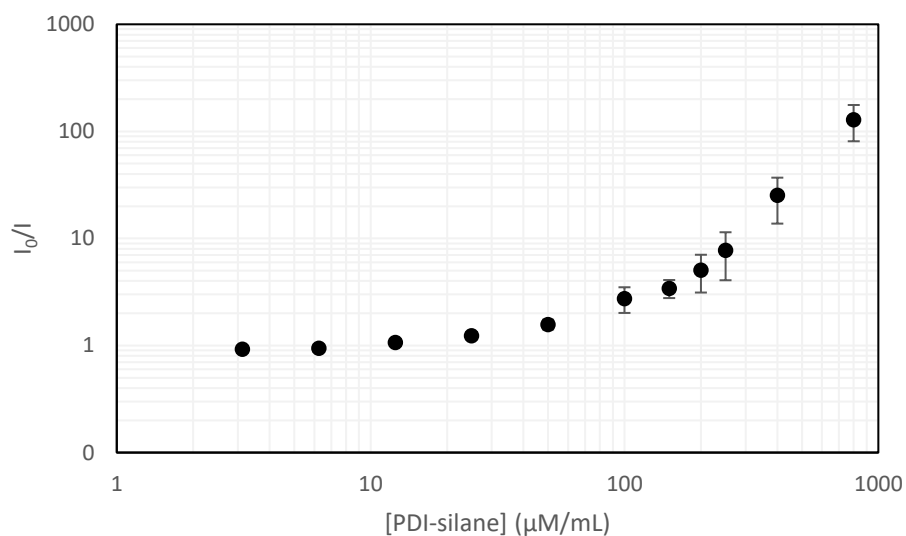


Figure 126 – Normalized 9-AA emission Log base 10 scaled axes for Stern-Volmer plot of blended concentration error trials showing 2<sup>nd</sup> order quadratic fit and one standard deviation from the mean.

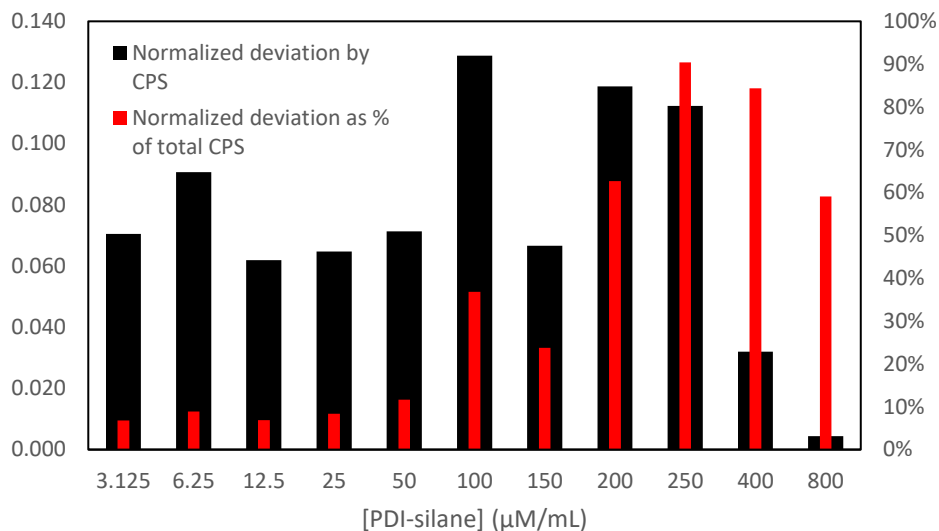


Figure 127 – Bar chart presenting the normalized 9-AA emission standard deviation in fluorescent emission CPS, and as a % of total CPS

The standard deviation of normalized spectra found in Table 26 will be used as an error window in further trials to prevent excessive duplicate trials. The standard deviation of normalized spectra as a percentage of maximum CPS can be used to obtain a quick error window by multiplying this value by the quenched 9-AA fluorescent peak maxima CPS.

<i>PDI-silane Concentration (<math>\mu\text{M}/\text{mL}</math>)</i>	<i>Standard Deviation of Normalized spectra</i>	<i>Standard Deviation of Normalized spectra as a percentage of maximum CPS</i>
3.125	0.071	7%
6.25	0.091	9%
12.5	0.062	7%
25	0.065	8%
50	0.071	12%
100	0.129	37%
150	0.067	24%
200	0.119	63%
250	0.112	90%
400	0.032	84%
800	0.004	59%
<i>Mean</i>	0.075	36%

Table 26 – Standard deviation of procedural error calculated for various PDI-silane concentrations blended with 50  $\mu\text{M}/\text{mL}$  9-AA.

As a final expansion of practicality of this error work, fitted equations were used to interpolate the likely error for concentrations not explicitly measured. two equations were created; one for reference data sets where only one species of fluorophores exists in solution, and another equations for the data from blended samples where two species exist in solution. It was important to separate these data sets as the data was not created with equal initial conditions. the logarithmic fit for the reference data provided a reasonable confidence for interpolation. regarding the blended fit, finding an ideal equation type was difficult. The final choice used a power type equation that provided the highest  $R^2$  value when compared to linear,  $n^{\text{th}}$  order polynomial, logarithmic, and exponential.

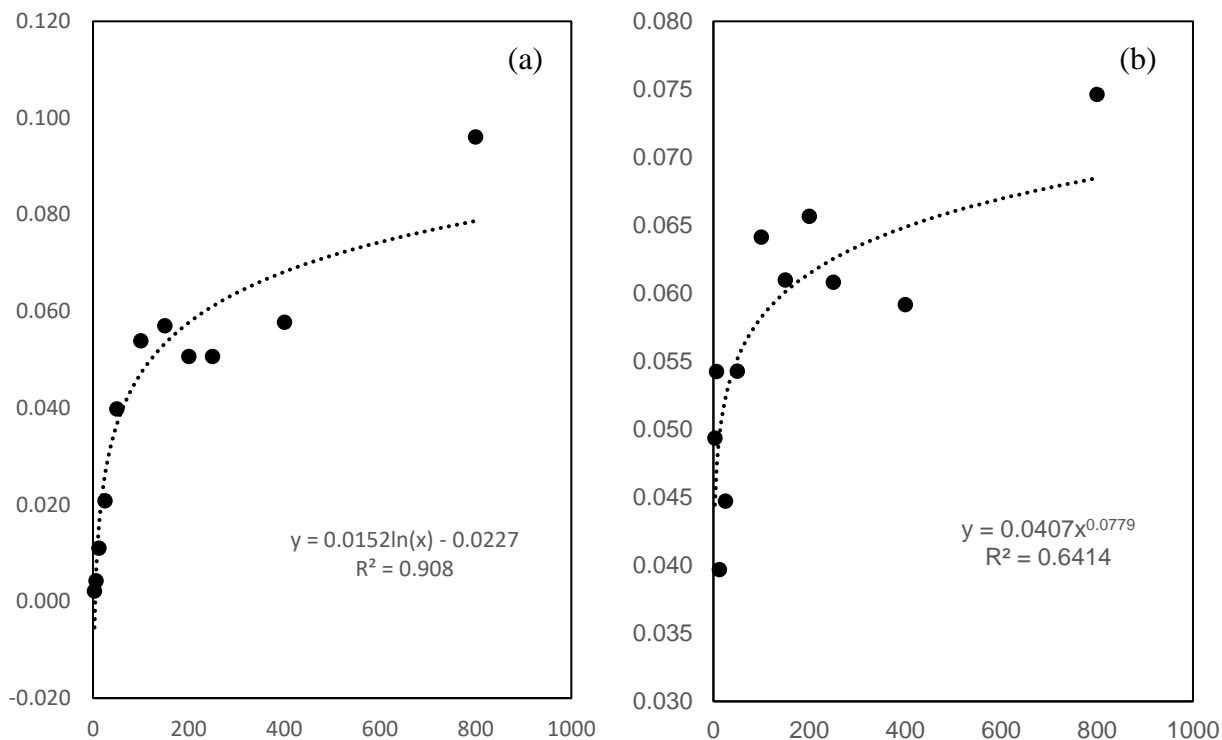


Figure 128 – (a) Fitting of standard deviation for reference spectra error. (b) Fitting of standard deviation for blended spectra error.

## THF PHOTOPHYSICAL BEHAVIOR

### Preliminary

Measuring high concentration samples with widely varying absorbances create a difficult scenario for data collection using a steady set of detector parameters. Fluorometer parameters were keyed in to provide a beam slit width of 2 nm and a detector slit width of 2 nm. These offered to ideal balance for detection intensity, illumination intensity and penetration through the sample, whilst not overloading the detector for any one sample blend/reference.

Table 27 provides information regarding each sample preparation for this experiment of high concentration blends using THF as the solvent. Blend ratios were doubled and halved twice from a center point of 1:1 blend ratio providing a wide catchment for observation of FRET.

Table 27 – Sample preparation conditions for blended and reference samples

	<b>9-AA</b>	<b>PDI-S</b>	<b>THF</b>	<b>Molar Concentration</b>
<i>1:4 PDI-S reference</i>	0 $\mu$ L	200 $\mu$ L	800 $\mu$ L	0 $\mu$ M : 200 $\mu$ M
<i>1:2 PDI-S reference</i>	0 $\mu$ L	100 $\mu$ L	900 $\mu$ L	0 $\mu$ M : 100 $\mu$ M
<i>1:1 PDI-S reference</i>	0 $\mu$ L	50 $\mu$ L	950 $\mu$ L	0 $\mu$ M : 50 $\mu$ M
<i>2:1 PDI-S reference</i>	0 $\mu$ L	25 $\mu$ L	975 $\mu$ L	0 $\mu$ M : 25 $\mu$ M
<i>4:1 PDI-S reference</i>	0 $\mu$ L	12.5 $\mu$ L	987.5 $\mu$ L	0 $\mu$ M : 12.5 $\mu$ M
<i>1:4</i>	50 $\mu$ L	200 $\mu$ L	700 $\mu$ L	50 $\mu$ M : 200 $\mu$ M
<i>1:2</i>	50 $\mu$ L	100 $\mu$ L	800 $\mu$ L	50 $\mu$ M : 100 $\mu$ M
<i>1:1</i>	50 $\mu$ L	50 $\mu$ L	850 $\mu$ L	50 $\mu$ M : 50 $\mu$ M
<i>2:1</i>	50 $\mu$ L	25 $\mu$ L	875 $\mu$ L	50 $\mu$ M : 25 $\mu$ M
<i>4:1</i>	50 $\mu$ L	12.5 $\mu$ L	887.5 $\mu$ L	50 $\mu$ M : 12.5 $\mu$ M
<i>9-AA reference</i>	50 $\mu$ L	0 $\mu$ L	950 $\mu$ L	50 $\mu$ M : 0 $\mu$ M

Excitation of each reference was taken prior to blended sample preparation to reduce the time with which the blended samples could settle.

## Results & Discussion

The reference spectra can be seen in Figure 129 as a compilation of each sample. Note that these are labeled with ratio characters but do not actually contain and Donor material. The ratio characters only are for matching with blend samples.

At these high concentrations, shifts in peak position and intensity are extremely prominent. At the lowest molar weight concentration (12.5  $\mu$ M), there is close to equality between peak maxima at 538 and 569 nm, with a very shallow third peak maximized around 615nm. Rising in concentration to 25  $\mu$ M, a near doubling of the second peaks intensity is observed and a slight shift in maxima to 570 nm. Its first peak maximum is almost unchanged in intensity but red shifted to 541 nm. The third peak presents with a substantial amplitude increase but a stable peak location at 615 nm.

Regarding the 50  $\mu\text{M}$  reference sample, a similar trend is observed. The second peak rises in amplitude and red shift slightly to 372 nm. The first peak loses a lot of definition as its amplitude sinks and its peak becomes more of a shoulder around 551 nm. The third peak has matured in this concentration with an increased maxima and slight red shift to 617 nm. By 100  $\mu\text{M}$ , there is no remanence of the first peak remaining. The second peak has reduced in amplitude and is further red-shifted to 575 nm. The third peak is still rising but has remained horizontally stably at 616nm. Finally, at 200  $\mu\text{M}$ , the second peak goes through an enormous reduction of peak amplitude and its position red-shifts all the way to 583 nm. The third peak retains amplitude and red-shifts slightly to 619 nm.

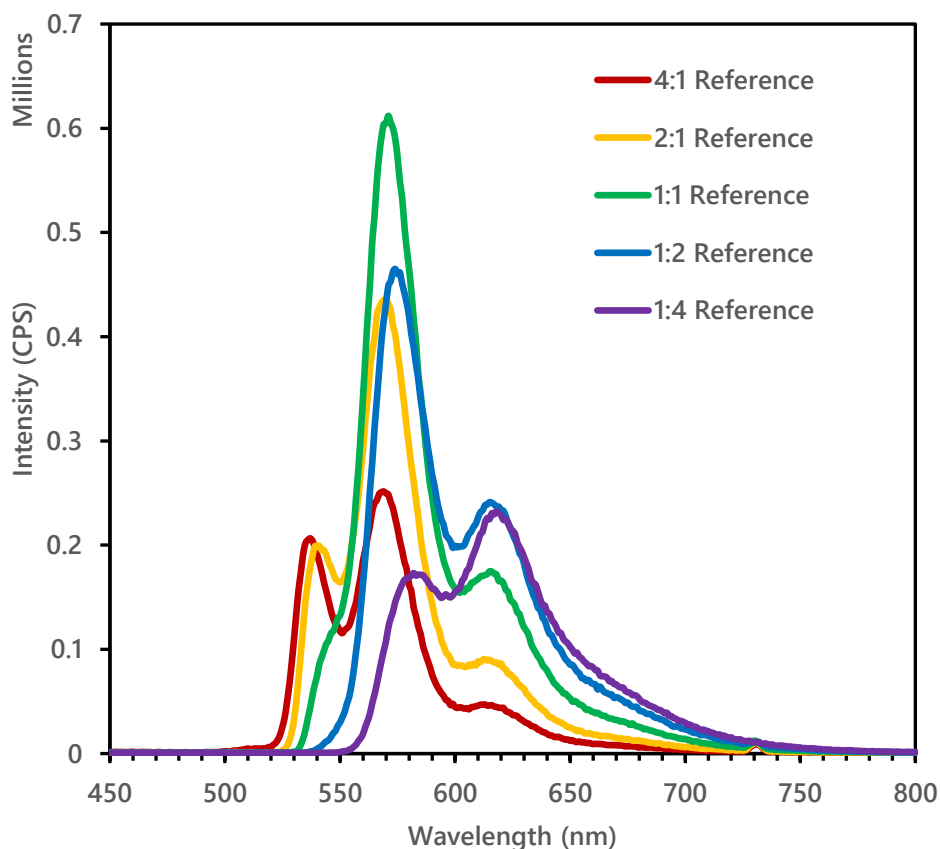


Figure 129 – Excitation spectra of reference solutions using 365 nm laser.

The mechanism for amplitude and peak position changes cannot be totally determined easily from Figure 129 alone. A very useful analysis is integration which can be used to determine a variant of total energy associated with the emission spectra. Figure 130 shows this integration and provides evidence the first three concentrations of 12.5, 25, and 50  $\mu\text{M}$  have behaved in a linear manor scaling the emission total energy appropriately with respect to molarity. At 100 and 200  $\mu\text{M}$  however, although the concentration continues to double, total area under the spectral curve does not continue an upwards trend. This indicates shelf quenching phenomena and will most likely cause performance issues with of the blended samples.

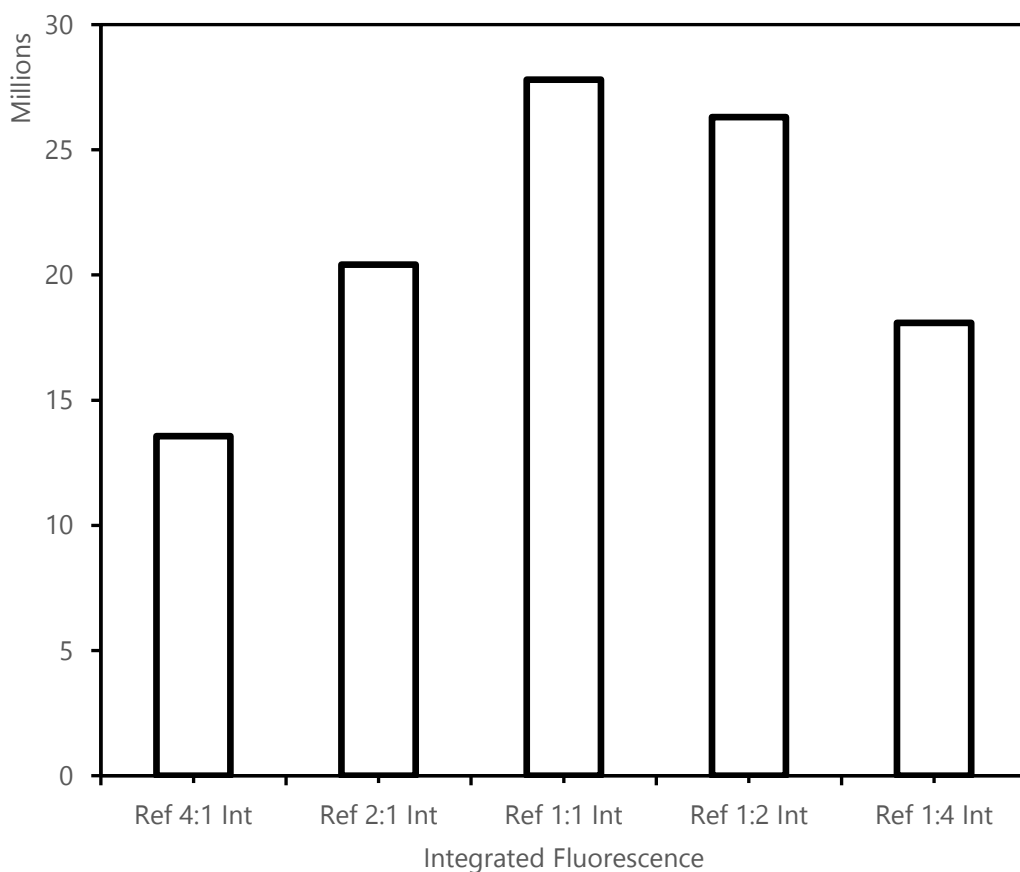


Figure 130 – Integration of each reference spectra from 350 – 800 nm.

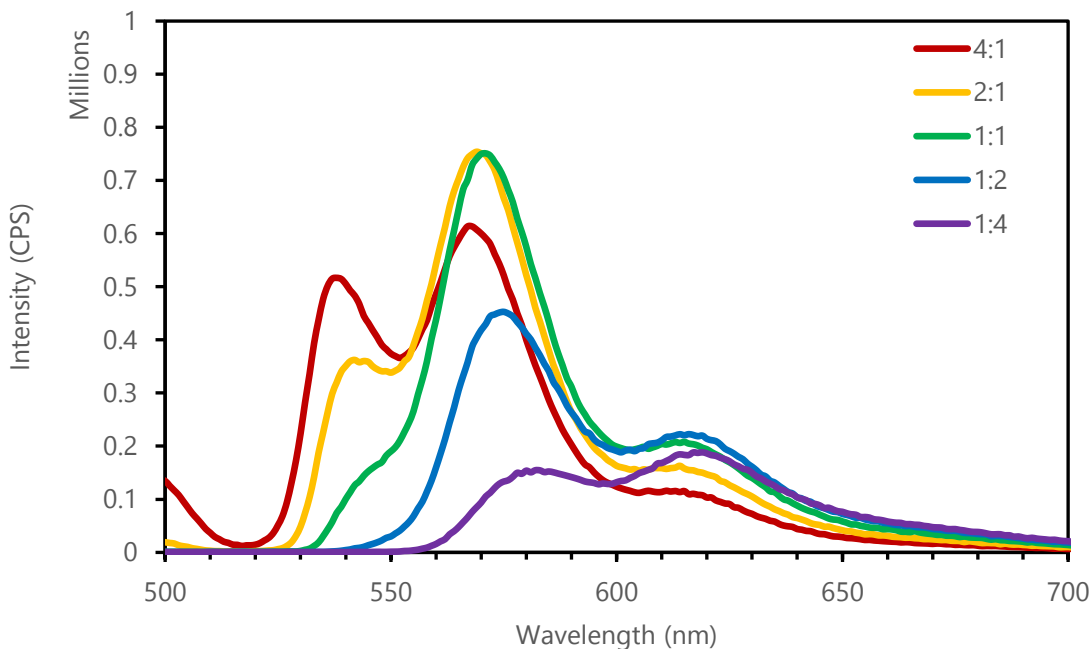


Figure 131 – excitation spectra blended solutions using 365 nm laser

For reference and summation comparison, Figure 132 a-e provide a clear case that increase ratio in favor of acceptor decreases FRET efficiency and even provides static quenching of the acceptor. Relative FRET efficiency calculations were taken from these data sets and presented in Figure 133 and Table 28. This presents the 4:1 ratio, where the acceptor is outnumbered by the donor, as the greatest efficiency for resonant energy transfer.

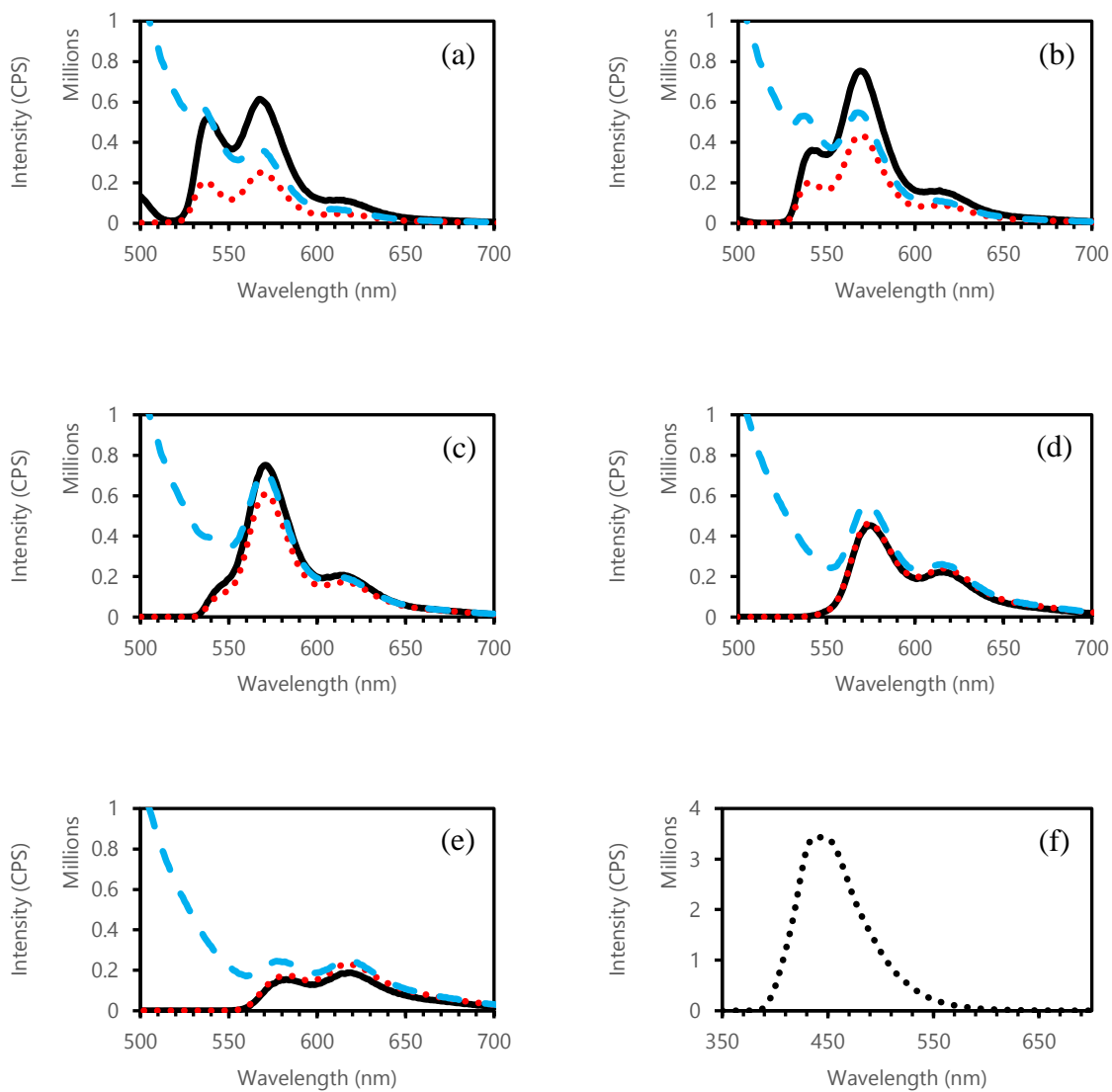


Figure 132 – (a-e) Reference, summation, and blend fluorescence spectra for ratio samples 4:1, 2:1, 1:1, 1:2, and 1:4, respectively. (f) Fluorescent spectrum for 9-AA excitation at 365 nm. Constant concentration of 50  $\mu$ M as donor for all trials.

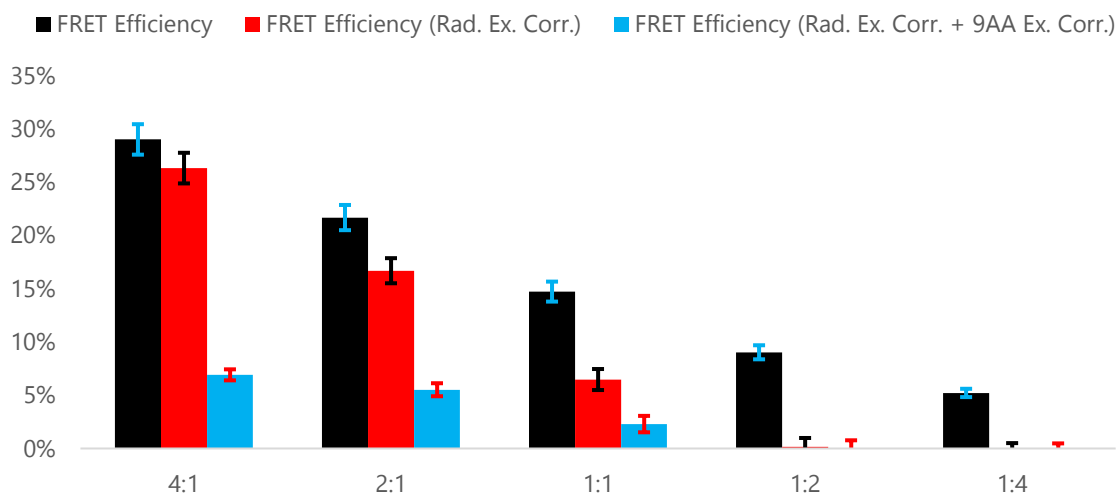


Figure 133 – Relative FRET efficiency calculation results for THF blend

	<i>Relative FRET Efficiency</i>	<i>Relative FRET Efficiency (Rad. Ex. Corr.)</i>	<i>FRET Efficiency (Rad. Ex. Corr. + 9AA Ex. Corr.)</i>
<i>4:1</i>	29% ±1.43	26% ±1.44	7% ±0.52
<i>2:1</i>	22% ±1.18	17% ±1.18	6% ±0.61
<i>1:1</i>	15% ±0.94	6% ±0.99	2% ±0.77
<i>1:2</i>	9% ±0.66	0% ±0.82	0% ±0.77
<i>1:4</i>	5% ±0.39	0% ±0.77	0% ±0.48

Table 28 – Relative FRET efficiency results for THF blend with error propagation

Stern-Volmer plots shown in Figure 134 provide evidence to a static and dynamically quenched system. At low concentrations, error in peak position remains small, however as quenching is almost complete variance increases as small differences contribute to a large percentage of the total fluorescence intensity. This fact makes it difficult to determine a confident quantifiable rate constant. Nevertheless, bimodal quenching remains present.

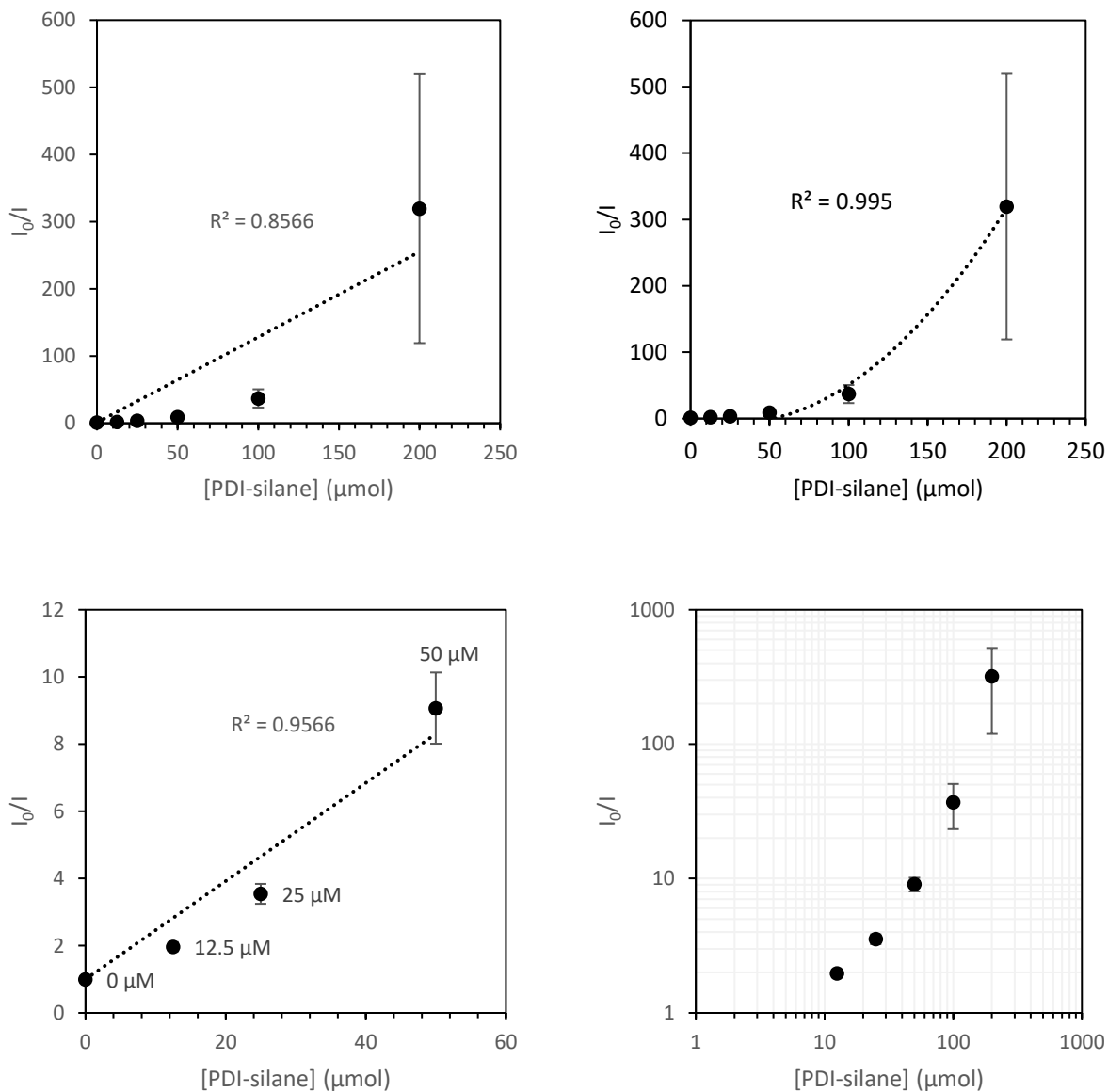


Figure 134 – Stern-Volmer plots for blended ratios in THF fitted with linear and quadratic curves.

### Concluding Remarks

THF is again shown to have properties conducive of resonant energy transfer between 9-AA and PDI-silane. With the unverified assumption of no 9-AA radiative emission contribution to the blended emission spectra, FRET efficiency showed results as high as 26 % for a 4:1 blend.

correcting for and 9-AA emission overlap, potential relative FRET efficiency was shown to be as high as 7% for the same ratio. Energy transfer efficiency was in consistent decline as ratio increased in favor of PDI-silane. This indicates that an excess of donor molecules at 4:1 is preferable for higher efficiency energy transfer.

#### CHLOROBENZENE PHOTOPHYSICAL BEHAVIOR

##### Preliminary

To investigate fluorescence quenching processes occurring in an environment of interaction between 9-anthracic acid and perylenediimide-silane two concentration studies were carried out. In this case, chlorobenzene is used as it has proven to be a great solvent for both moieties, allows strong fluorescent yields, and provides good characteristics for thin-film spin coating.

Concentrations of each sample are shown in Table 29 and Table 31. Samples were made immediately before measurement and blends were not formed until reference samples were measured. All spectra were gathered at 365 nm excitation.

<i>Sample</i>	<i>Concentrations</i> (Constant Volume)
<i>PDI-S #1</i>	250 $\mu\text{mol}$
<i>PDI-S #2</i>	375.5 $\mu\text{mol}$
<i>PDI-S #3</i>	500.6 $\mu\text{mol}$
<i>PDI-S #4</i>	625.8 $\mu\text{mol}$
<i>9-AA</i>	360 $\mu\text{mol}$
<i>Blend #1</i>	250 $\mu\text{mol}$ : 360 $\mu\text{mol}$
<i>Blend #2</i>	375.5 $\mu\text{mol}$ : 360 $\mu\text{mol}$
<i>Blend #3</i>	500.6 $\mu\text{mol}$ : 360 $\mu\text{mol}$
<i>Blend #4</i>	625.8 $\mu\text{mol}$ : 360 $\mu\text{mol}$

Table 29 – Sample concentration preparation guide

#### High (100s $\mu\text{M}$ ) Concentration Results & Discussion

Observed, is a clear limit to the fluorescent emission strength at high concentrations of PDI-Silane. Integration of the PDI-Silane emission reveals reduction in emission intensity, spectral-wide. This is caused by a self-quenching process known as an aggregation caused quenching, consequent of the intermolecular  $\pi$ - $\pi$  stacking between perylene cores. It is also worth noting that this same phenomenon is present for the Donor; chosen to be 9-anthroic acid. In this case, emission from 9-AA is reduced compared with the later experiment using a solution molarity 10x weaker.

When the blend samples are analyzed for fluorescent emission and extreme reduction in emission is observed for both Donor and Acceptor. This informs us that the excited state energy of the 9-AA is being consumed via an alternate path to radiative emission. The hope for this experiment was to observe FRET, this cannot be confirmed because the emission of the Acceptor has also been quenched considerably. It is important to note that the emission intensity hierarchy of PDI-Silane remains. The self-quenching mechanism is still present but by adding 9-AA, further, and almost complete quenching of the acceptor is seen.

The mechanism responsible for such an outcome must exist with a characteristic that excludes photon emission. The electron excitation experienced in these molecules is potentially exchanged via a singlet-singlet Dexter energy transfer instead. But this still doesn't explain the quenched Acceptors emission. Dexter energy transfer still leaves behind an excited state electron, just as FRET. The triplet-triplet Dexter energy transfer could only be observed with time dependent fluorescence spectroscopy. But again, provides no immediate conclusion as to how the energy of the excited state of the acceptor deactivates.

Another route to explain fluorescent quenching in this context can come from non-fluorescent complexes being formed at the ground state. These complexes absorb and return to ground state without the emission of photons. A complex of this type is known as static quenching. Resultant fluorescent intensity is proportional to the concentration of complexed and free fluorophore. In a solution containing both complexed and free fluorophores, the observations one can make are those from the still emitting free fluorophores. Fluorescent lifetime is unchanged and there is no interaction between complexed and free; and furthermore, there is no fluorescent lifetime to measure for the complexed material. Therefore, the only indication of static quenching is reduction of fluorescent intensity.

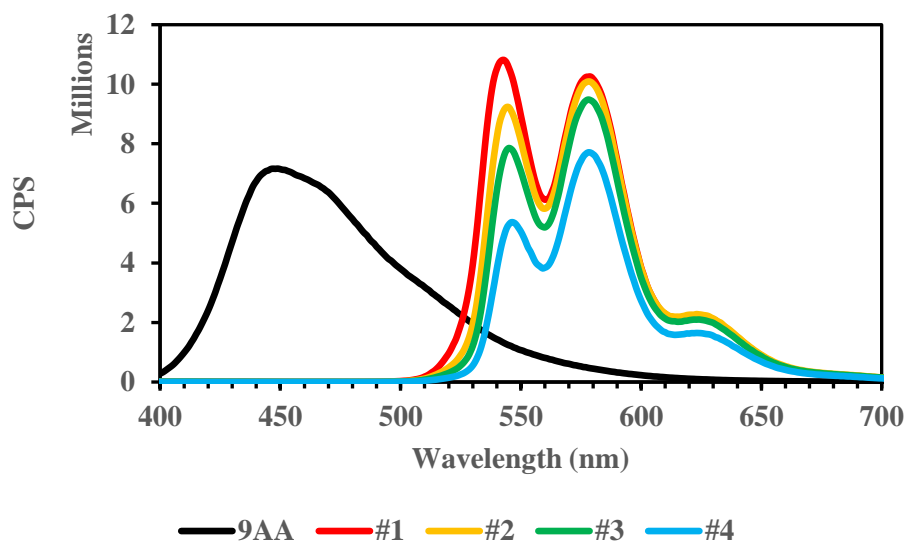


Figure 135 – Fluorescent spectra of 9-AA and PDI-S in chlorobenzene. 9-AA was dissolved at high concentration of 360  $\mu\text{mol/mL}$ . PDI-S #1-4 were dissolved at a ratio of 250  $\mu\text{mol/mL}$ , 376  $\mu\text{mol/mL}$ , 501  $\mu\text{mol/mL}$ , and 626  $\mu\text{mol/mL}$ , respectively.

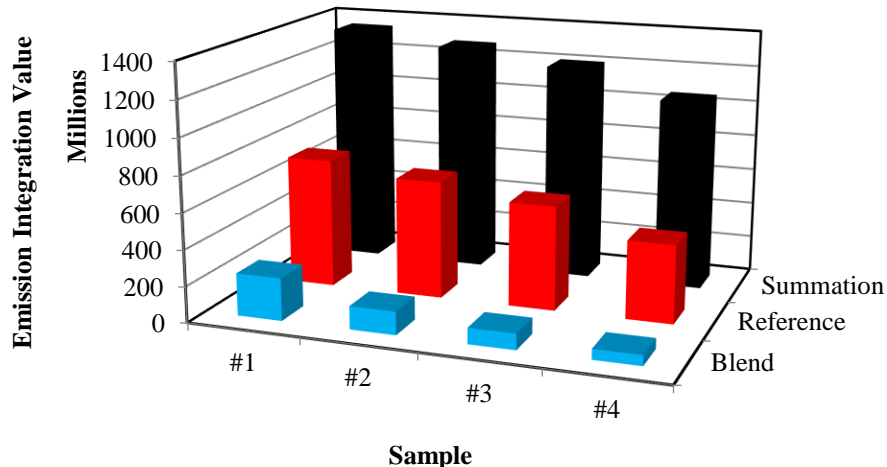


Figure 136 – Integration of spectra produced from high concentration blends in chlorobenzene. Data labelled ‘Summation’ consists of two cumulated components: firstly, and consistently, the integration of the reference 9-AA emission; secondly, to its corresponding number, the PDI-S reference spectral integration. Data marked as ‘Reference’ consists of just the PDI-S integrated spectra associated with its number. Finally, data marked as ‘Blend’ is the integration of the blended sample spectra where both moieties present.

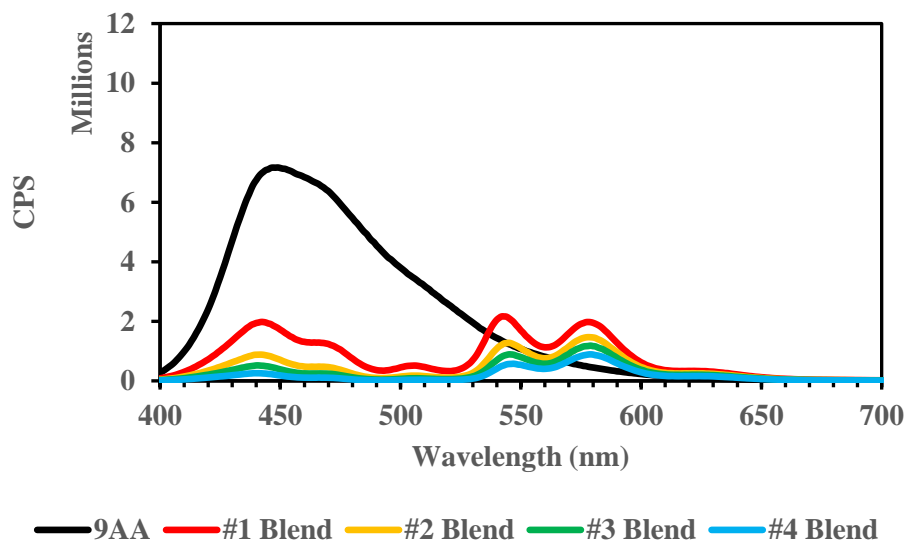


Figure 137 – Fluorescent spectra of 9-AA and PDI-S blended in chlorobenzene. 9-AA was dissolved at a high concentration of 360  $\mu\text{mol/mL}$ . Blends #1-4 contained 360  $\mu\text{mol/mL}$  of 9-AA and PDI-S at a molarity of 250  $\mu\text{mol/mL}$ , 376  $\mu\text{mol/mL}$ , 501  $\mu\text{mol/mL}$ , and 626  $\mu\text{mol/mL}$ , respectively.

Figure 138 helps to understand the inner workings of molecular interaction observed in the previous spectra. Typical Stern-Volmer plots produce linear fit in response the presence of a single form of quenching. A quadratic curve indicates both static and dynamic quenching is taking place in this blended system.

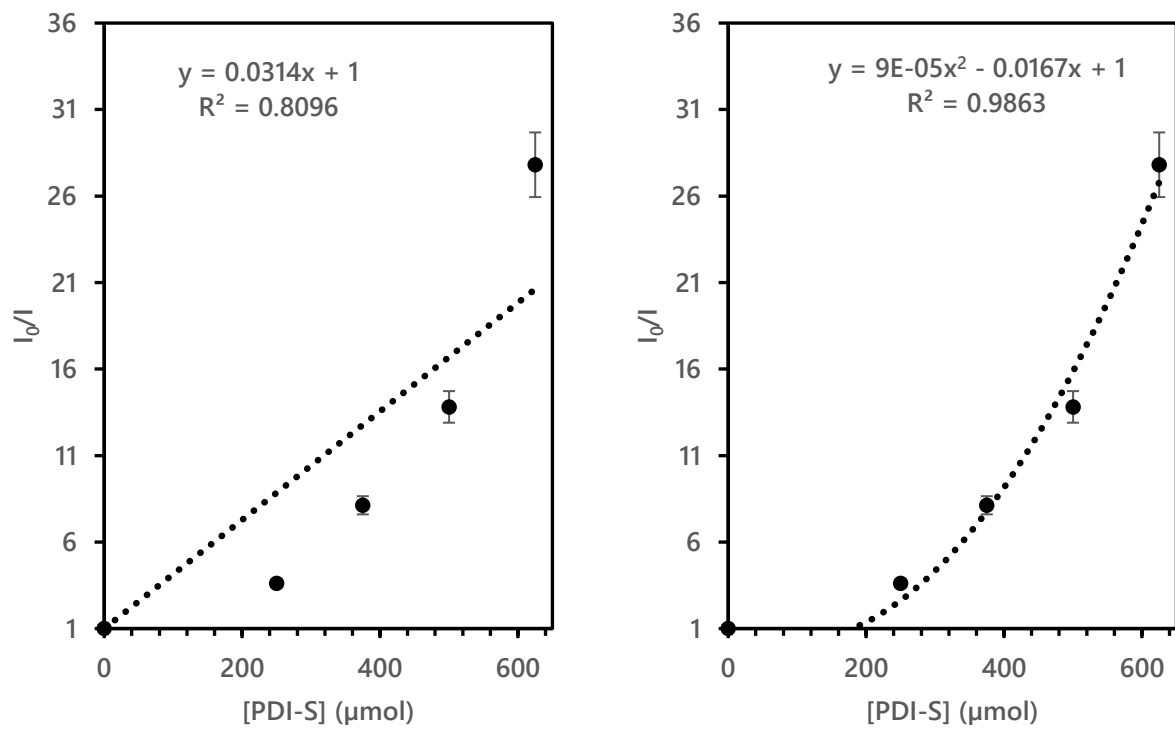


Figure 138 – Stern-Volmer plot produced from the high concentration blend study in chlorobenzene. The Fluorophore was represented by 9-AA, and the Quencher was PDI-S. Data fitted in linear equation (left) and quadratic (right).

#### Low (10s $\mu\text{M}$ ) Concentration Results & Discussion

Concentrations of each sample are shown in Table 30Table 32. Samples were made immediately before measurement and blends were not formed until reference samples were measured. All spectra were gathered at 365 nm excitation.

<i>Sample</i>	<i>Concentrations (Constant Volume)</i>
<i>PDI-S #1</i>	25 $\mu\text{mol}$
<i>PDI-S #2</i>	37.6 $\mu\text{mol}$
<i>PDI-S #3</i>	50 $\mu\text{mol}$
<i>PDI-S #4</i>	62.5 $\mu\text{mol}$
<i>9-AA</i>	36 $\mu\text{mol}$
<i>Blend #1</i>	25 $\mu\text{mol}$ : 36 $\mu\text{mol}$
<i>Blend #2</i>	37.5 $\mu\text{mol}$ : 36 $\mu\text{mol}$
<i>Blend #3</i>	50 $\mu\text{mol}$ : 36 $\mu\text{mol}$
<i>Blend #4</i>	62.5 $\mu\text{mol}$ : 36 $\mu\text{mol}$

Table 30 – Sample concentration preparation guide

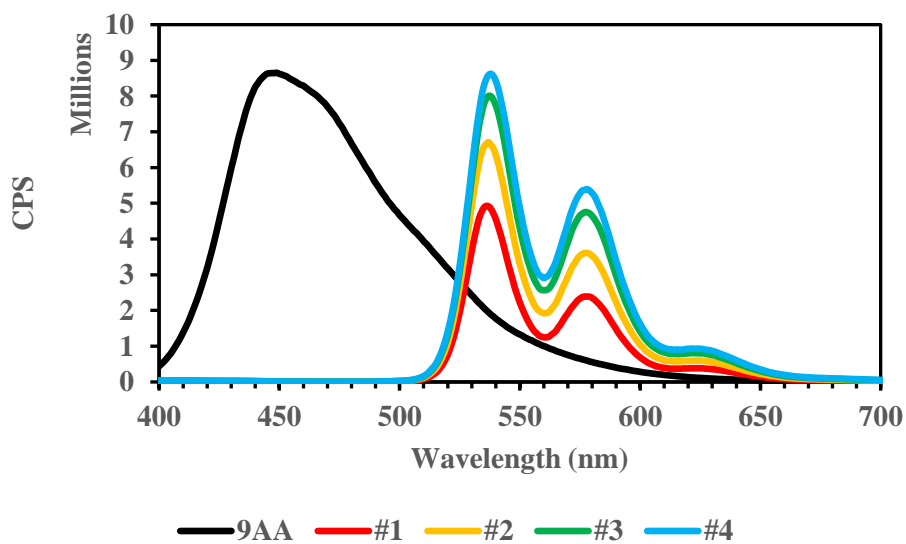


Figure 139 – Fluorescent spectra of 9-AA and PDI-S in chlorobenzene. 9-AA was dissolved at a concentration of 36  $\mu\text{mol/mL}$ . PDI-S #1-4 were dissolved at a ratio of 25  $\mu\text{mol/mL}$ , 38  $\mu\text{mol/mL}$ , 50  $\mu\text{mol/mL}$ , and 63  $\mu\text{mol/mL}$ , respectively.

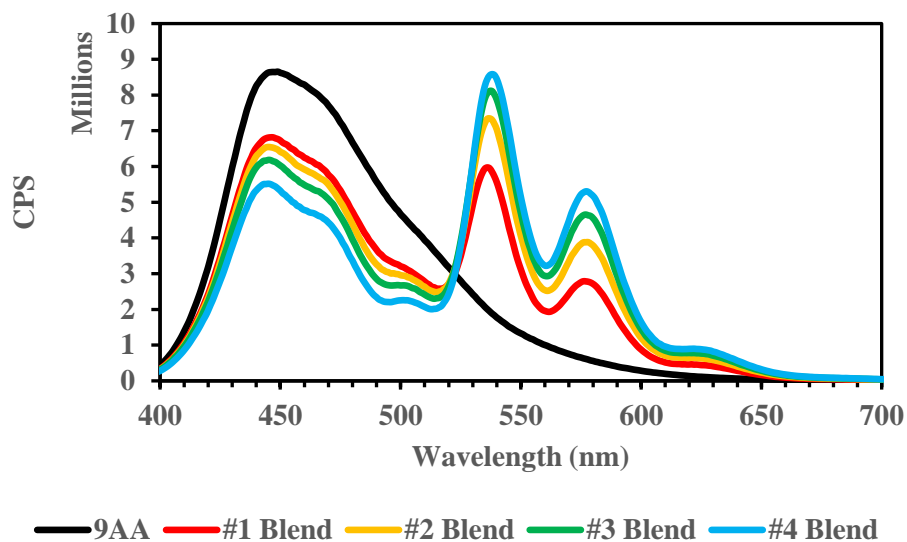


Figure 140 – Fluorescent spectra of 9-AA and PDI-S blended in chlorobenzene. 9-AA was dissolved at a concentration of  $36 \mu\text{mol/mL}$ . Blends #1-4 contained  $36 \mu\text{mol/mL}$  of 9-AA and PDI-S at a molarity of  $25 \mu\text{mol/mL}$ ,  $38 \mu\text{mol/mL}$ ,  $50 \mu\text{mol/mL}$ , and  $63 \mu\text{mol/mL}$ , respectively.

Figure 141 shows the interaction of molecules observed in the previous spectra. Typical Stern-Volmer plots produce linear fit in response the presence of a single form of quenching. This plot shows slight signs of quadratic shape but stays mainly true to the linear fit. This indicates that the quenching observed in Figure 140 is nearly exclusively either static or dynamic.

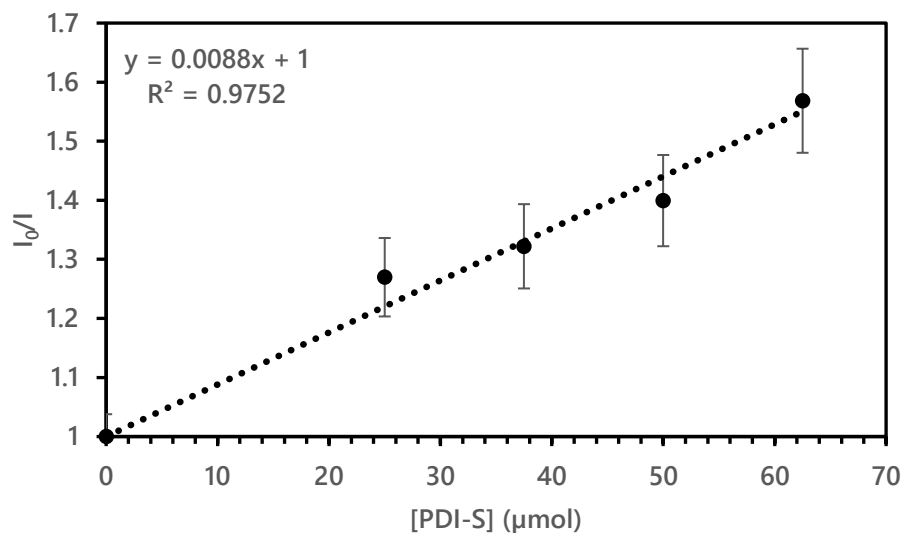


Figure 141 – Stern-Volmer plot produced from the low concentration blend study in chlorobenzene. The Fluorophore was represented by 9-AA, and the Quencher was PDI-S. Data fitted with a linear equation.

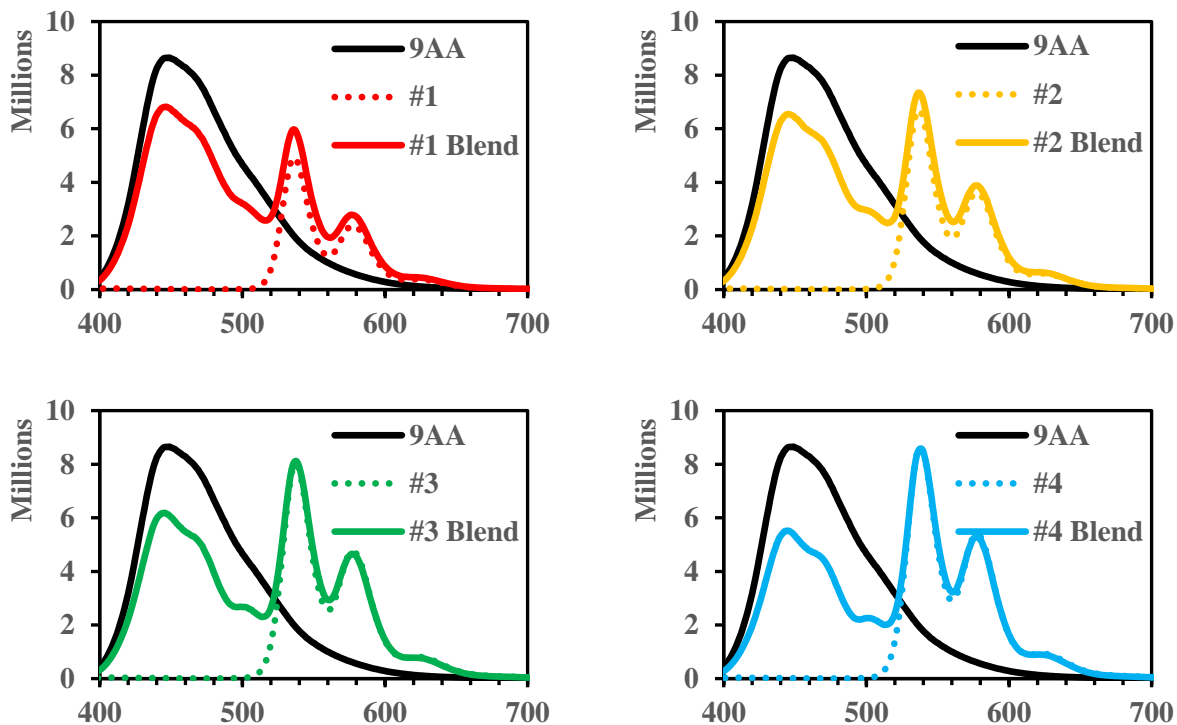


Figure 142 – Fluorescent spectra overlay comparing 9-AA, PDI-S and blends in chlorobenzene.

#### CHLOROFORM PHOTOPHYSICAL BEHAVIOR

##### Preliminary

To try and improve upon the chlorobenzene trial results, chloroform was used to repeat the experiment. Dried chloroform was used for this trial, meaning the ethanol stabilizer was removed using water and then magnesium sulfate was used to dehydrate the chloroform.

Past results have shown excellent FRET results when using chloroform and this experiment hoped to exceed the outcomes of the chlorobenzene trial.

## High (100s $\mu\text{M}$ ) Concentration Results & Discussion

Concentrations of each sample are shown in Table 31. Samples were made immediately before measurement and blends were not formed until reference samples were measured. All spectra were gathered at 365 nm excitation.

<i>Sample</i>	<i>Concentrations (Constant Volume)</i>
<i>PDI-S #1</i>	250 $\mu\text{mol}$
<i>PDI-S #2</i>	375.5 $\mu\text{mol}$
<i>PDI-S #3</i>	500.6 $\mu\text{mol}$
<i>PDI-S #4</i>	625.8 $\mu\text{mol}$
<i>9-AA</i>	360 $\mu\text{mol}$
<i>Blend #1</i>	250 $\mu\text{mol}$ : 360 $\mu\text{mol}$
<i>Blend #2</i>	375.5 $\mu\text{mol}$ : 360 $\mu\text{mol}$
<i>Blend #3</i>	500.6 $\mu\text{mol}$ : 360 $\mu\text{mol}$
<i>Blend #4</i>	625.8 $\mu\text{mol}$ : 360 $\mu\text{mol}$

Table 31 – Sample concentration preparation guide

At high concentration, in Figure 143, it can be seen that PDI-silane does not behave favorably for high yield of fluorescence. As concentration increases, the sample self-quenches. It forms into non-fluorescent complexes resulting in a consistent decrease in emission intensity.

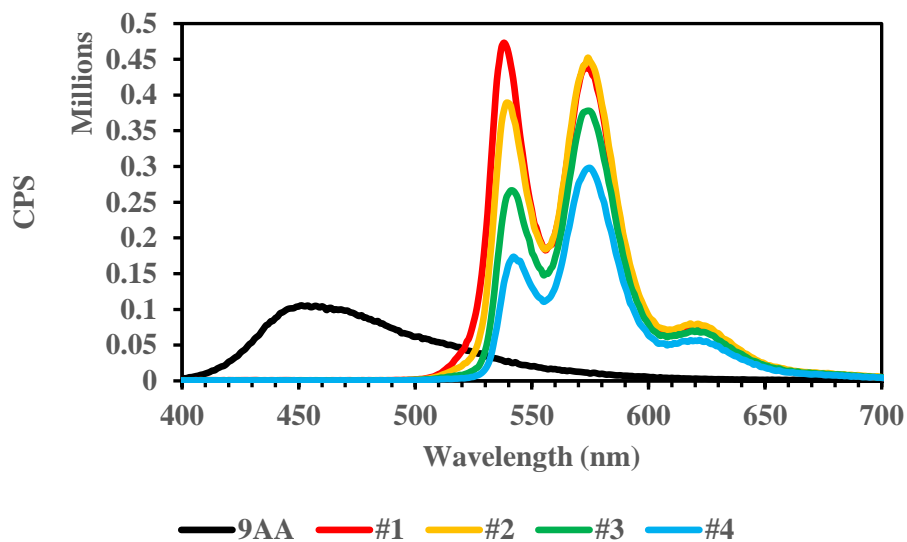


Figure 143 – Fluorescent spectra of 9-AA and PDI-S in chloroform. 9-AA was dissolved at a concentration of 360  $\mu\text{mol/mL}$ . PDI-S #1-4 were dissolved at a ratio of 250  $\mu\text{mol/mL}$ , 376  $\mu\text{mol/mL}$ , 501  $\mu\text{mol/mL}$ , and 626  $\mu\text{mol/mL}$ , respectively. Excitation 365 nm.

After Blending, for all samples, emission intensity is drastically reduced (Figure 144). Not only the region of the spectra associated with PDI-silane quenched, but also that of 9-anthroic acid. Initial hope for this experiment was that the emission of 9-anthroic acid would disappear, but not by sacrificing the PDI-silane emission. So far, it is possible to believe that non-radiative transfer has occurred between (-anthroic acid and PDI-silane. However, the total reduction of PDI-silane emission implies even stronger formation of non-fluorescent complexes. The question lies in whether new complexes were formed after the addition of 9-anthroic acid.

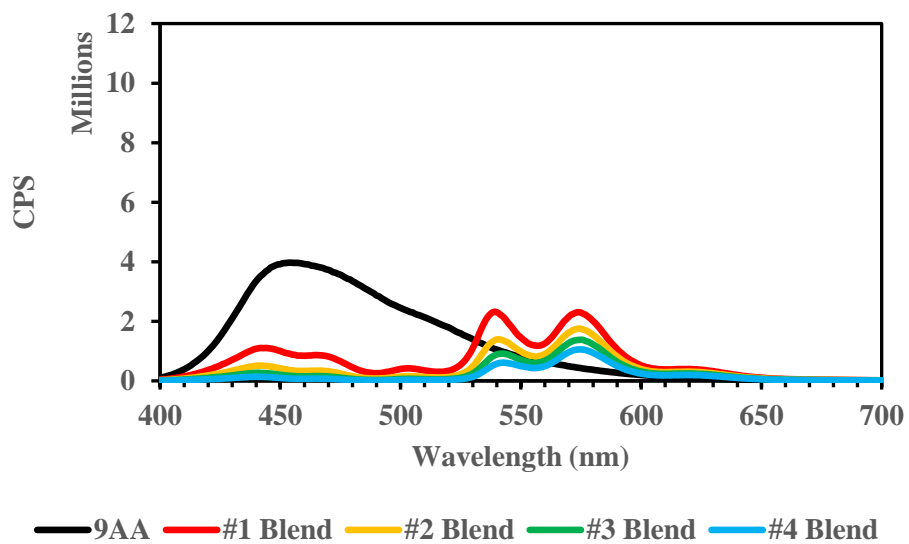


Figure 144 – Fluorescent spectra of 9-AA and PDI-S blended in chlorobenzene. 9-AA was dissolved at a high concentration of 360  $\mu\text{mol/mL}$ . Blends #1-4 contained 360  $\mu\text{mol/mL}$  of 9-AA and PDI-S at a molarity of 250  $\mu\text{mol/mL}$ , 376  $\mu\text{mol/mL}$ , 501  $\mu\text{mol/mL}$ , and 626  $\mu\text{mol/mL}$ , respectively. Excitation 365 nm.

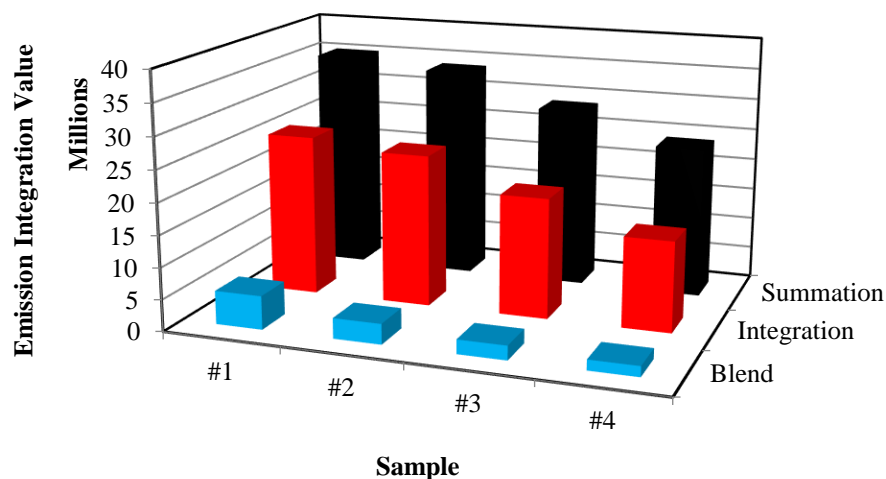


Figure 145 – Integration of spectra produced from high concentration blends in chloroform. Data labelled ‘Summation’ consists of two cumulated components: firstly and consistently, the integration of the reference 9-AA emission; secondly, to its corresponding number, the PDI-S reference spectral integration. Data marked as ‘Reference’ consists of just the PDI-S integrated spectra associated with its number. Finally, data marked as ‘Blend’ is the integration of the blended sample spectra where both moieties present.

As seen with the chlorobenzene trials, a high concentration blend of 9-anthroic acid and PDI-silane can result in a combination of static and dynamic quenching. The same can be said for when chloroform is used as the solvent. The Stern-Volmer plot in Figure 146 shows a convincing quadratic curve not suited to a linear fit. The implication of this data is that if both dynamics of quenching exist, then some molecules must still remain free in solution. It should be taken into consideration that Figure 147, later in this report, shows 9-anthroic acid’s low concentration reference emission intensity to be higher, by a margin, than that of the high concentration sample. It could be right to infer that at high concentrations, 9-anthroic acid also forms non-fluorescent complexes and self-quenches. This adds another variable in the equation to understand what happens in the high concentration blends. It is possible that both species are close to a critical mass for quenching and when blended, both are overrun.

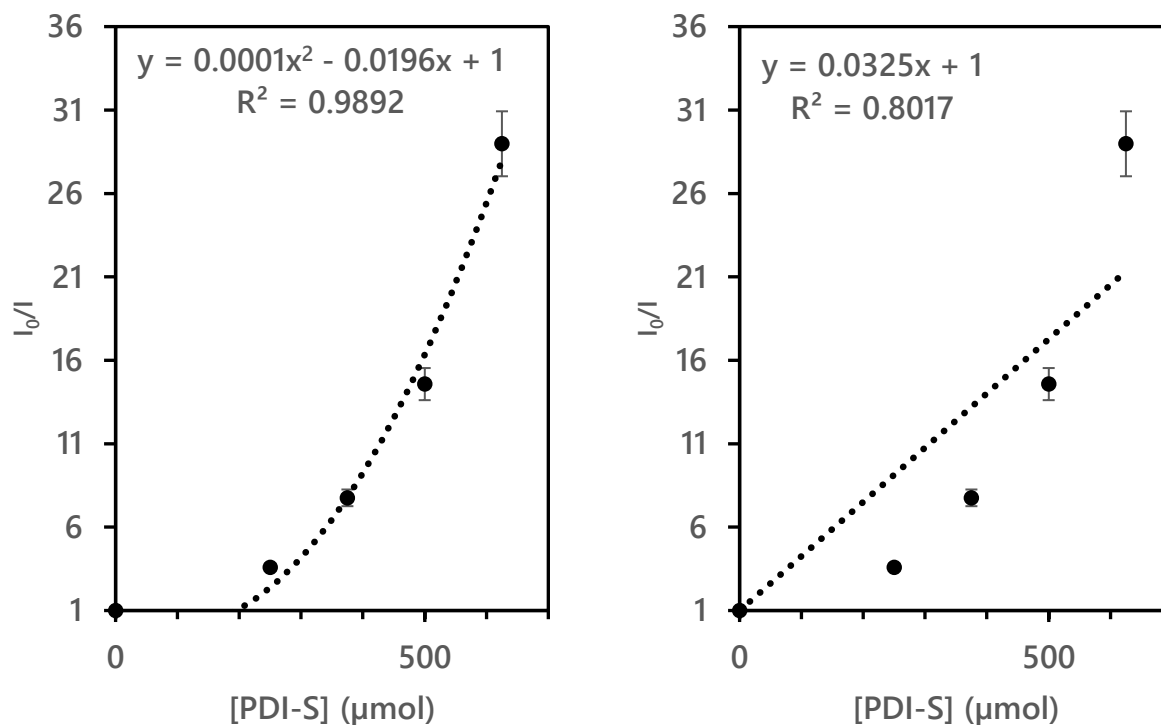


Figure 146 – Stern-Volmer plot produced from the high concentration blend study in chloroform. The Fluorophore was represented by 9-AA, and the Quencher was PDI-S. Data fitted in linear equation (left) and quadratic (right).

#### Low (10s $\mu\text{M}$ ) Concentration Results & Discussion

Concentrations of each sample are shown in Table 32. Samples were made immediately before measurement and blends were not formed until reference samples were measured. All spectra were gathered at 365 nm excitation.

<i>Sample</i>	<i>Concentrations (Constant Volume)</i>
<i>PDI-S #1</i>	25 $\mu\text{mol}$
<i>PDI-S #2</i>	37.6 $\mu\text{mol}$
<i>PDI-S #3</i>	50 $\mu\text{mol}$
<i>PDI-S #4</i>	62.5 $\mu\text{mol}$
<i>9-AA</i>	36 $\mu\text{mol}$
<i>Blend #1</i>	25 $\mu\text{mol}$ : 36 $\mu\text{mol}$
<i>Blend #2</i>	37.5 $\mu\text{mol}$ : 36 $\mu\text{mol}$
<i>Blend #3</i>	50 $\mu\text{mol}$ : 36 $\mu\text{mol}$
<i>Blend #4</i>	62.5 $\mu\text{mol}$ : 36 $\mu\text{mol}$

Table 32 – Sample concentration preparation guide

At low concentrations, PDI-silane reacts in a standard manner to increasing fluorescence intensity with increasing concentration. There is no indication that any non-fluorescent complexes have been formed at this point by ether moiety. Figure 147 shows the reference samples fluorescent emission.

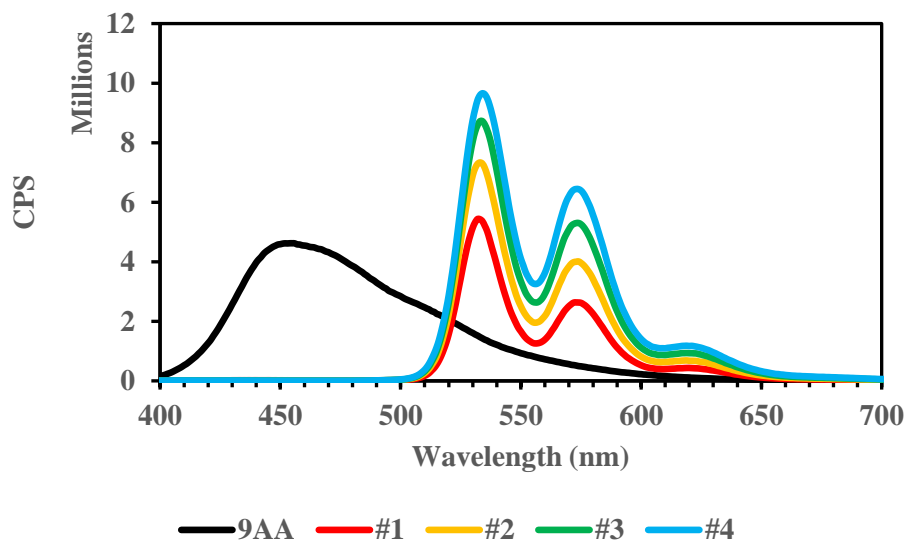


Figure 147 – Fluorescent spectra of 9-AA and PDI-S in chloroform. 9-AA was dissolved at a concentration of 36  $\mu\text{mol/mL}$ . PDI-S #1-4 were dissolved at a ratio of 25  $\mu\text{mol/mL}$ , 38  $\mu\text{mol/mL}$ , 50  $\mu\text{mol/mL}$ , and 63  $\mu\text{mol/mL}$ , respectively. Excitation 365 nm.

After blend (Figure 148) we can observe a slow yet significant reduction in the total emission in the 9-anthracic acid region of the spectrum. What is more difficult to see is any change in the magnitude of fluorescence emission from the PDI-silane. For that, Figure 150 is used to determine intensity increase by overlaying blend and reference emissions. Sample set #1 may imply a very small total increase in emission but, increasing concentration after that only equalizes or even decreases intensity. These concentrations seem to be the start of non-fluorescent complex formation.

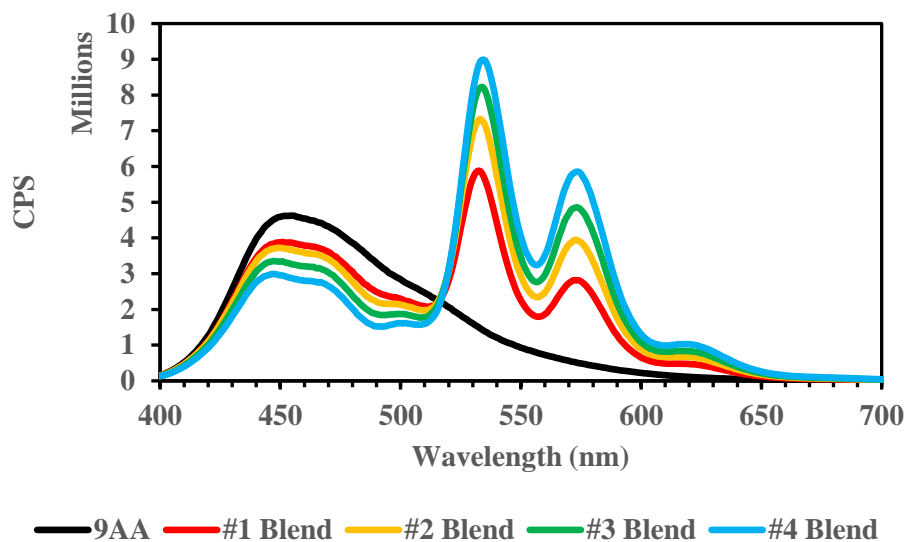


Figure 148 – Fluorescent spectra of 9-AA and PDI-S blended in chloroform. 9-AA was dissolved at a concentration of 36  $\mu\text{mol/mL}$ . Blends #1-4 contained 36  $\mu\text{mol/mL}$  of 9-AA and PDI-S at a molarity of 25  $\mu\text{mol/mL}$ , 38  $\mu\text{mol/mL}$ , 50  $\mu\text{mol/mL}$ , and 63  $\mu\text{mol/mL}$ , respectively.

The Stern-Volmer plot of Figure 149 shows an almost linear fit meaning that the quenching mechanism taking place is most dominantly only dynamic or static.

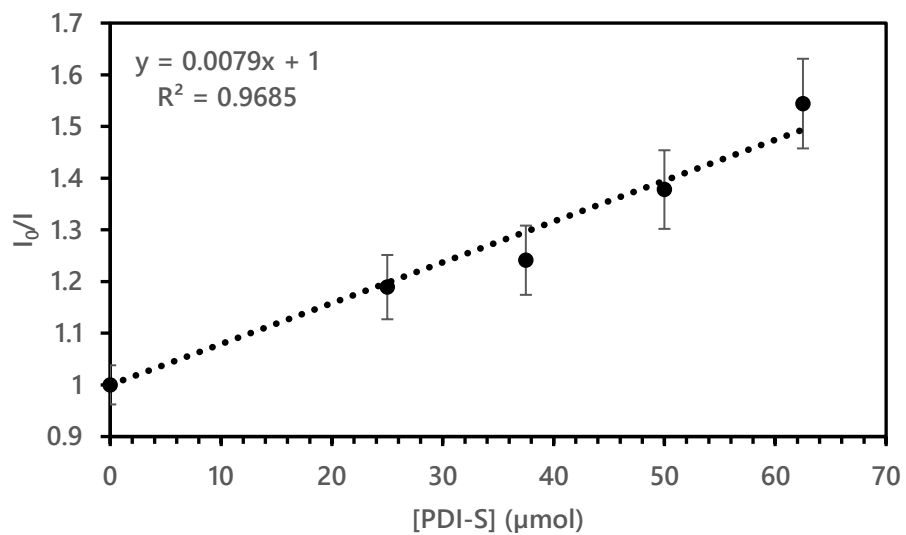


Figure 149 – Stern-Volmer plot produced from the low concentration blend study in chloroform. The Fluorophore was represented by 9-AA, and the Quencher was PDI-S. Data fitted with a linear equation.

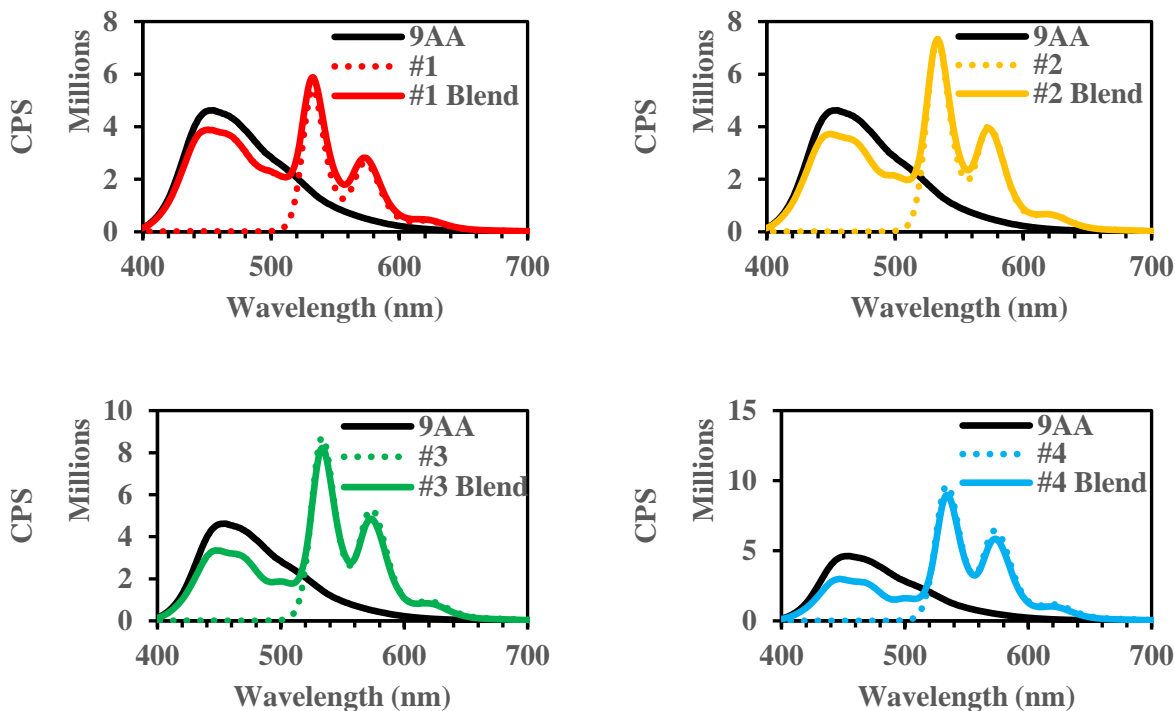


Figure 150 – Fluorescent spectra overlay comparing 9-AA, PDI-S and molar blends in chloroform.

#### TIME-DEPENDENT FLUORESCENCE

Time dependent fluorescence was produced to compare 5 mM and 50  $\mu$ M concentration samples of 9-AA, PDI-silane, and blend in both chloroform and THF. These two solvents have proved to be most reliable for inducing FRET and allow for a solvation of both moieties at 5 mM concentrations. Table 33 summarizes the lifetime measurements of all samples tested. At 5 mM concentrations in chloroform and THF, PDI-silane has two prominent fluorescent lifetimes fitting a double exponential decay. The majority of excited state lifetimes observed exist at  $5.01 \pm 0.05$  ns for chloroform and a slightly shorter lifetime in THF at  $4.87 \pm 0.02$  ns. These values are supported from literature that have confirmed similar perylene derivatives with singlet excited state lifetimes around 4 ns<sup>1</sup>. The second contributing portion of the lifetime measurements for PDI-silane comes from around 10% of the sample exhibiting a lifetime of  $22.74 \pm 2.7$  ns for chloroform and  $21.48 \pm 1.2$  ns for THF. This long lifetime suggests a complexed fluorescent structure. Work regarding excited state dimers of perylene (coined excimers) have shown the lifetime of such perylene excimers to

17.6 ns<sup>87</sup>. It is possible that this bifurcation of lifetimes is caused by a fraction of the 5 mM concentration PDI-silane sample forming aggregates or dimers in solution.

There is significant variation between the excited state lifetime of 9-anthracene comparing across both solvents. In chloroform, 9-AA exhibited fitting to a single exponential decay and a lifetime of  $6.25 \pm 0.02$  ns and for THF a lifetime of  $10.34 \pm 0.01$  ns. This presented as a consistent value for both 5 mM and 50  $\mu$ M concentrations tested. Concluding from this, the intermolecular and intramolecular interactions are not dependent upon concentration within the values tested here. An effect that is prominently observed for PDI-silane. The lifetimes reported here do appear high when compared to literature. Prior work has reported values of 2.0 ns for 9-AA at concentrations around 30  $\mu$ M<sup>88</sup>. This value was reported as a representation of infinite dilution for the monomer form of 9-AA. There were also statements that the concentration of such measurement was too low for measurement of excimer lifetime. With this work reporting consistent lifetimes comparing both 50  $\mu$ M and 5 mM concentrations, and measuring 3-5 times longer, it would be hard to argue the dominant existence of monomers in this reporting. There currently does not appear to be popular literature supporting 9-AA lifetimes in chloroform and THF matching values reported here. 9-acridinecarboxylic acid (9-ACA) and its methyl ester, 9-(methoxycarbonyl)acridine (9-MCA) have been measured at concentrations of 10  $\mu$ M<sup>89</sup>. 9-ACA exhibited lifetimes of 1.1 ns and 0.6 ns in THF and chloroform, respectively. 9-MCA exhibited lifetimes of 1.1 ns and 0.9 ns, respectively. This report did not measure 9-AA for their own comparison and did not appear to discuss lifetime variances between 9-AA and the alternate derivatives. 9-(N,N-Dimethylamino)anthracene (9-DMA) has excited state lifetimes reported in THF of 5.3 ns<sup>90</sup>. This work ruled out the formation of excimers in their experimentation. Finding literature to support excited state lifetime lengthening via excimer formation seems very rare for 9-AA. Work performed with pyrene finds monomer lifetimes of 680 ns and excimer lifetime of 90 ns<sup>91</sup>. This suggests that excimer formation should significantly reduce excited state lifetime. This is not supporting evidence for excimer formation of 9-AA in this study when using lifetime values as comparison from studies with 9-DMA, 9-ACA, and 9-MCA.

Under a 1:1 blended condition, lifetime measurements were biexponential for all four trials. In the 5 mM concentration study set, the count associated with PDI-silane was delayed by 0.7 ns. the

secondary decay was measured to be  $8.25 \pm 1.1$  ns. The primary decay of  $5.71 \pm 0.2$  ns can be linked to PDI-silane through the fluorescent emission spectrum taken of the blended sample (Figure 151). A majority of the counts recorded in that spectrum are from wavelengths belonging to PDI-silane. Considering that this work is pursuing identifying FRET care must be taken into attributing lifetime counts to certain origins. When considering Figure 151 and the lifetime measurements for the 5 mM concentration blended chloroform sample it would be brash to conclude FRET as a dominant quenching mechanism of the 9-AA. The lifetime measurements of the blend remain highly favorable to the primary exponential and emission magnitude is near half that of the PDI-silane reference sample. Quenching in this system is being sourced from non-fluorescent pathways. Furthermore, the secondary exponential from the PDI-silane does not appear in the blended sample. It is possible that the components responsible for the secondary PDI-silane lifetime are completely quenched by the introduction of 9-AA into the solvated system. This same statement could be proposed for chloroform and THF.

Further observation of the emission spectrum for 5 mM concentration samples in chloroform and THF reveal shoulders forming around 550 nm in association with the PDI-silane emission. This appearance indicates excitation of higher electronic and vibrational levels. These levels were not excited from direct photon absorption in the reference PDI-silane samples. Applying the mirror image rule, a 550 nm emission of PDI-silane has an absorption around 490 nm; this value also aligns well with strong emission from 9-AA. The this considered, PDI-silane emission around 550 nm appears to be a result of excitation from a non-radiative energy transfer. The counter argument to this observation is that fundamentally the donor lifetime should measurably decrease upon resonance energy transfer<sup>92</sup>. Observed here is a lengthening of the donor lifetime which is indication of trivial emission/reabsorption via a fluorescent photon from donor to acceptor. To then reevaluate the appearance of the PDI-silane shoulder around 550 nm it should be concluded that this region of the spectra has increased intensity via far-field radiative transfer.

	<i>PDI-silane</i>	<i>9-anthroic acid</i>	<i>Blend</i>
<i>Chloroform (5mM)</i>	5.01 ns (86.8%)	6.25 ns	5.71 ns (79.1%)
	22.74 ns (13.2%)		8.52 ns (20.9%)
<i>THF (5mM)</i>	4.87 ns (89.2%)	10.34 ns	6.54 ns (53.8%)
	21.48 ns (9.8%)		13.09 ns (46.2%)
<i>Chloroform (50μM)</i>	4.74 ns	6.42 ns	4.80 ns (73.5%)
			7.20 ns (26.5%)
<i>THF (50μM)</i>	4.35 ns	10.01 ns	4.24 ns (62.5%)
			11.13 ns (37.5%)

Table 33 – Fluorescent lifetime measurements for 5 mM and 50 μM concentration solutions mixed in THF and chloroform. Where applicable, contribution percentage is indicated.

	<i>PDI-silane</i>	<i>9-anthroic acid</i>	<i>Blend</i>
<i>Chloroform (5mM)</i>	2389	1098	26852
	364		7116
<i>THF (5mM)</i>	18805	16634	3245
	2273		2791
<i>Chloroform (50μM)</i>	3252	5249	3011
			1146
<i>THF (50μM)</i>	2006	1516	1431
			857

Table 34 – Fluorescent lifetime counts for 5 mM and 50 μM concentration solutions mixed in THF and chloroform.

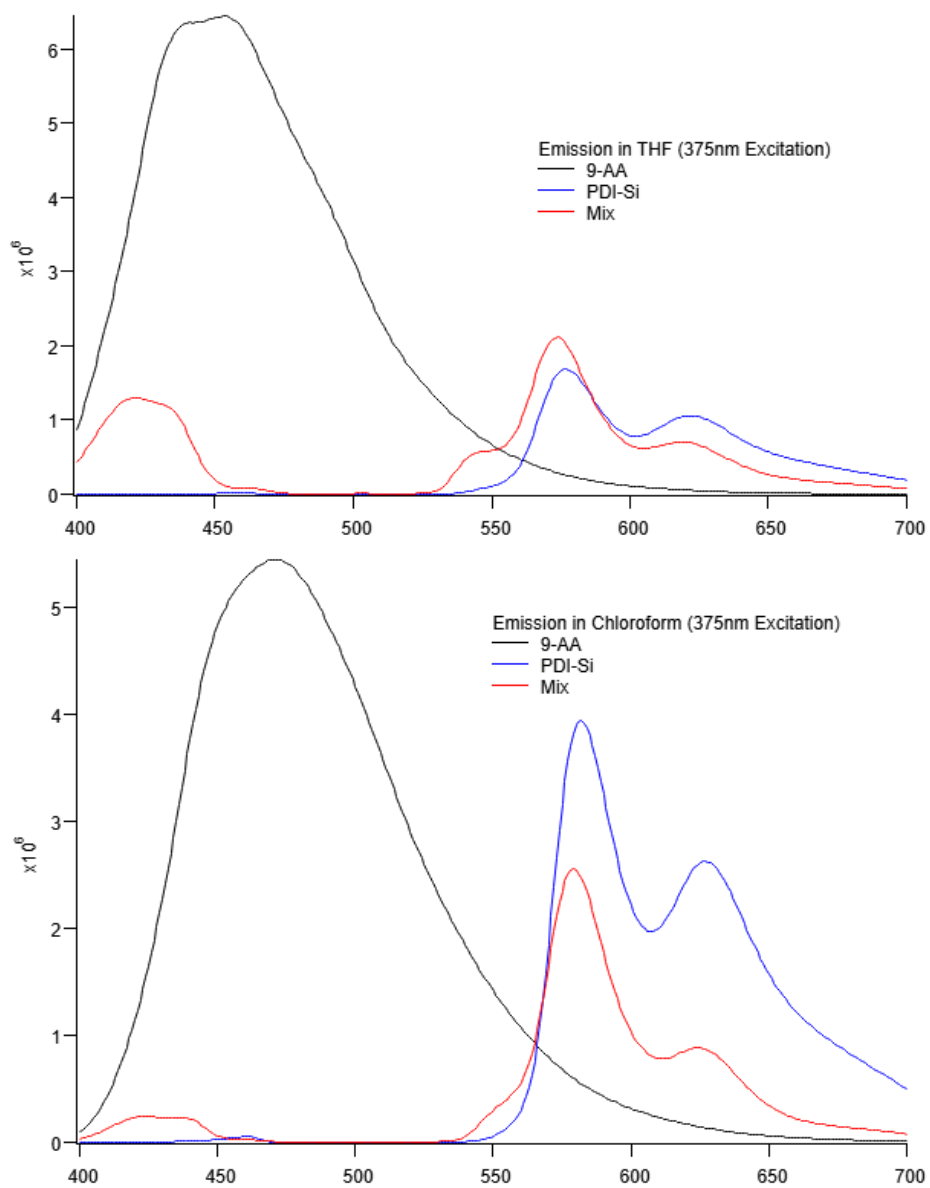


Figure 151 – Fluorescence emission spectra of 5 mM concentration samples used for excited state lifetime measurements.

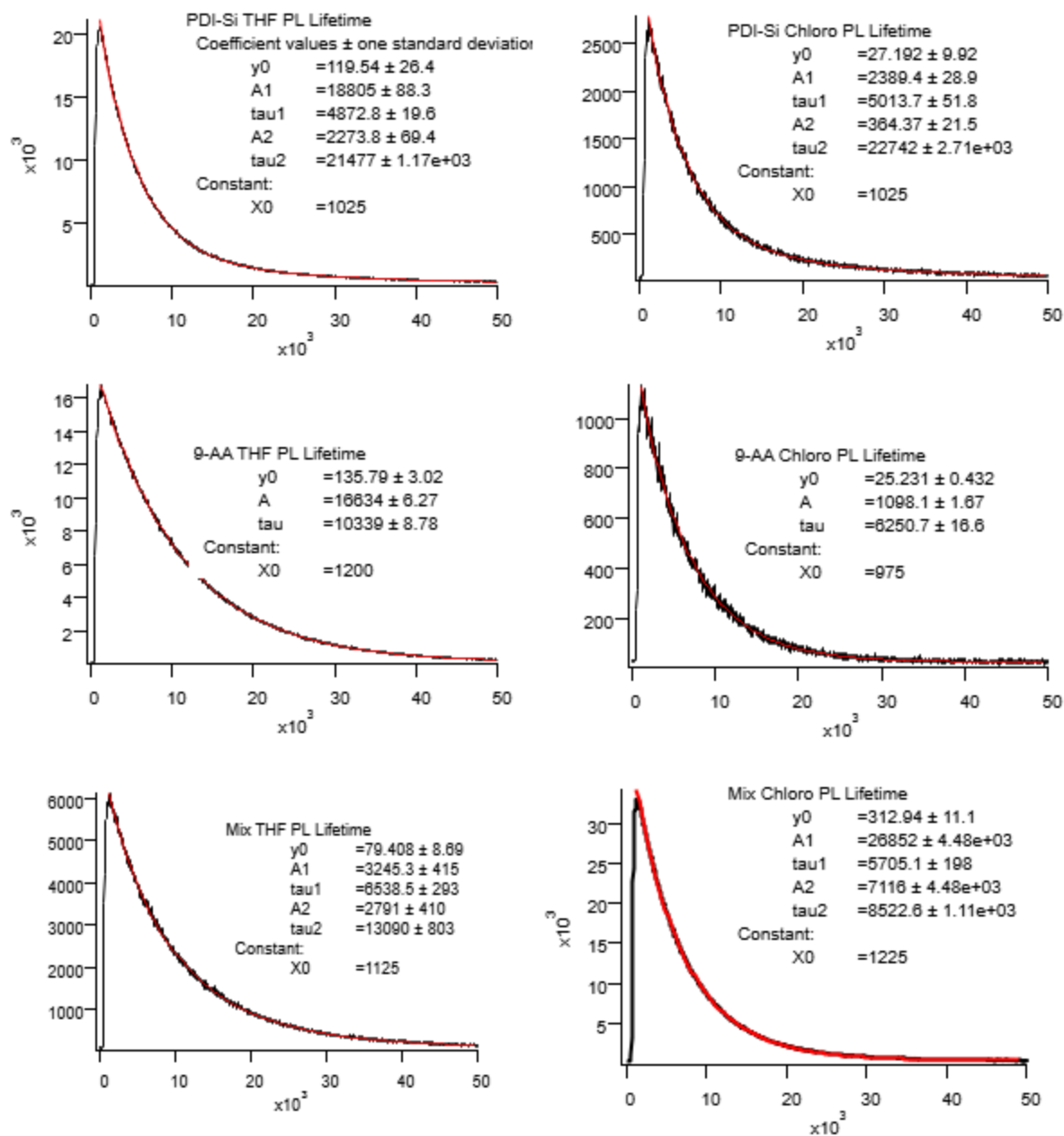


Figure 152 – Lifetime measurements of 5 mM concentrations THF and chloroform solvated samples of PDI-silane reference, 9-AA reference, and 1:1 blend.

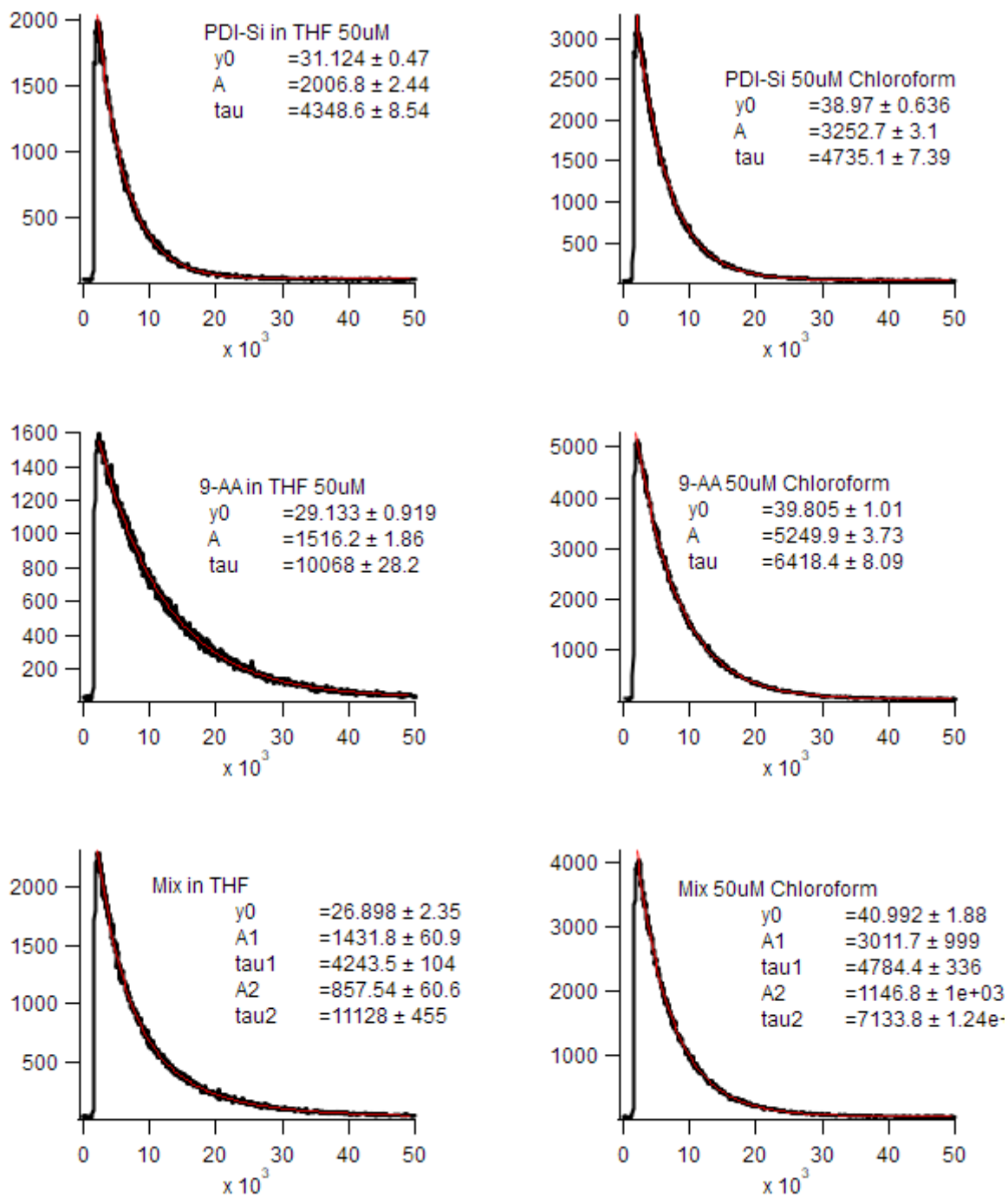


Figure 153 – Lifetime measurements of 50  $\mu\text{M}$  concentrations THF and chloroform solvated samples of PDI-silane reference, 9-AA reference, and 1:1 blend.

With respect to high concentration work (5 mM/mL) in THF the following observations can be made. Stern-Volmer plots showed that at high concentrations, THF presented static and dynamic quenching mechanisms. Such implies that ground state complexes have formed, and dynamic quenching is also present. Fluorescent spectra show an increase in PDI-silane emission with the addition of 9-AA. This points towards energy transfer as the dynamic quenching mechanism. 9-AA's emission was greatly reduced also which indicates an efficient quenching ability of PDI-silane and the possibility of dynamic and static quenching. From fluorescent lifetime measurements, a significant increase in the lifetime of PDI-silane was observed. This indicates a delayed energy absorption that may have been prolonged by energy absorption from a secondary source; further indicating 9-AA as a resonance donor. These points indicate that at very high concentrations, a radiative mechanism of energy transfer may outcompete FRET as seen when concentrations remain orders of magnitude lower.

High concentration work done with chloroform provides a Stern-Volmer plot indicating both static and dynamic quenching mechanisms. fluorescence spectra indicated that no dominating energy transfer existed due to a diminished PDI-silane fluorescence upon addition of donor. Fluorescent lifetimes of both the donor and acceptor increased which provides evidence to a radiative transfer mechanism; albeit a very weak one. Under these circumstances, it is fair to conclude that trivial energy transfer of emission and reabsorption is present to some magnitude and there is no conclusive evidence that FRET remains possible in this environment.

For low concentration work (50  $\mu$ M/mL) with THF, Stern-Volmer plots indicate a single quenching mechanism. Fluorescence and lifetime measurements indicate no resonant energy transfer present. with a minor increase in PDI-silane emission and a count split of 63:37 favoring the acceptor from the lifetime measurements there is a possibility of energy transfer from somewhere. the lifetime of 9-AA was measured just outside of error to increase upon quencher blend. these facts indicate a radiative energy transfer mechanism which is unusual for concentrations as low as 50  $\mu$ M/mL.

When considering the 50  $\mu$ M/mL samples in  $\text{CHCl}_3$ , the Stern-Volmer plots showed the presence of only one quenching mechanism. Fluorescence emission indicates that energy transfer is not

present. such conclusion is bolstered by the lifetime measurements of PDI-silane being unaffected by the addition of 9-AA. The lifetime of the donor also remained constant with and without the presence of the quencher. these points lead to a conclusion that at these very high concentrations, static quenching is entirely dominant in the chloroform system.

## CHAPTER VIII: OUTLOOK

### DONOR

This investigation was set to evaluate the efficacy of perylene and anthracene derivatives as a donor-acceptor pair used in Förster Resonance Energy Transfer. One objective for this work was completing synthesis of a novel polymer derived donor molecule that would aid in the preparation of thin-films whilst retaining fluorescent properties. The initial approach to this task used a polyimide known as poly[trimellitic anhydrous chloride-co-4, 4', methylenedianiline]. This was a chemically resilient polymer with the availability to functionalize end its groups. Direct attachment of 9-anthroic acid to the polyimide did not result in any meaningful success so a linker of 6-bromo-1-hexanol was used to act as an extension away from steric hindrances and a target for reaction with 9-anthroic acid. Although there was some success in attaching the linker to carboxylic acid, final production of the complete molecule did not produce any viable product for further analysis. A large yield was needed for solvent studies and its intended use a material for thin-film formation. With this drawback, attention was turn to a PDMS derivative as the backbone with the hope of greater synthesis success.

The use of PDMS allowed for a Steglich esterification reaction between the PDMS and 9-anthroic acid directly. This simplification of reaction scheme was in effort to improve yield. Multiple variations of this reaction were attempted by varying solvent type to improve access to the reactive sight, varying use of the reaction accelerant, and the number of intermediates that were able to form. Through these reactions, it was determined that the ideal synthesis approach was \*\*\*. From what material that did show promise of successful reaction some spectra were taken to show the persistence of absorption and fluorescence of the anthracene molecule whilst it terminated the PDMS chain. Furthermore, a quantum yield was obtained of 0.19 between the range of 400-600 nm whilst in chloroform after excitation at 365 nm. Given this small success, reaction remained poor, along with reliability of outcome. It was determined that this procedure was not a viable option in this instance for further development of an anthracene functionalized PDMS derivative as yield in volume was a necessity to continue work. For future studies into the approach of a

fluorescent polymer derivative it would be prudent to sample reaction schemes specifically designed and modified for long chain polymer reactants. Success in this field would allow for great ease of thin-film device creation that would accelerate iterative design of optoelectrical devices.

## ACCEPTOR

As a secondary to the task of material development perylene loaded nanoparticles were synthesized with for the purpose of photophysical characteristic comparison with the precursor PDI-silane. This work presents a modification to the synthesis procedure to enable smaller diameter particles to form. The leading synthesis reduced NP diameter by up to 32% creating particles measuring 25 nm on average. FRETs spatial dependence required particle size to drop in order to take advantage of as many fluorophores loaded into the siloxane particle. With a theoretical limiting FRET effective range of 10 nm and an instance of a 1 nm gap between donor and the acceptor NP, the reduction in diameter presented in this paper leaves only 2.2 % of the particles volume out of range. The 37 nm minimum average particle diameter of prior literature<sup>22</sup> would leave 43.3% of the particles volume inaccessible. By mass, this is valuable functional improvement providing potential utilization of almost the entire nanoparticle.

Considering the performance regarding thin-film formation of PDIB-NPs results appeared with fewer successes. It was determined that coatings from a drop-cast spin-coating technique could produce distribution of particles over a 1 inch<sup>2</sup> substrate. Topology, however, was far from ideal. PDIB-NPs remained in clusters non-homogeneously distributed across the substrate. Reasoning behind cluster formation appeared to be the higher affinity of the NPs to one another. Characterizing SEM imaging after synthesis of PDIB-NPs showed isolated particles were a natural occurrence however the spin-coating methods applied in this work do not provide the correct conditions. Under consideration is the surface roughness of the smaller particles relative to their size. It may allow for a greater contact area and attachment forces with neighbors. Future studies should be concerned about the relative strength of particle-particle attraction to the size. Smoother and more massive particles have an inherent ability to shear from one another with greater torque. This is potentially a valuable metric for monolayer film creation.

## PHOTOPHYSICS

An array of studies was conducted in order to understand the excited state interactions of PDI-silane and 9-anthroic acid. This work targeted the analysis of a FRET based quenching mechanism but also discovered the prevalence of alternate deexcitation pathways between these specific moieties. Data for setting a proof of viability early in this project presented a high FRET efficiency of 66% when the donor and acceptor were blended at a 1:1 ratio in chloroform. This data set a standard for guidance of concentration, solvent, component ratio, and preparation technique for following experimental procedure. Using the obtained experimental efficiency, the Förster distance was calculated to be 1.4 nm. This calculation prompted a quick average distance calculation between the monomer dyes in solution to provide further guidance with correct solution concentrations. This guidance concluded that concentrations to the order of 1 mg/mL would provide average distance between monomers larger than those calculated via the Förster distance calculations. This presented an inconsistency between the two methods and a bifurcation of the experimental approach. The work continued to use the concentrations proven to produce resonant energy transfer as the concentrations directed by the alternative would lead to aggregation and other quenching interactions that would interfere and obscure measurement of FRET.

To further explore the acceptor and donor in solution, experiments set to vary solvent and concentrations were performed. The variation of solvent was determined to change polarity hydrogen bonding effectiveness ultimately determining quality of donor and acceptor interactions. THF, chlorobenzene and acetonitrile were added to the experimental set as they could dissolve both moieties. Work with acetonitrile was limited as it could not reach high concentrations of solubility. It also proved to have poor results to determine if energy transfer had taken place. Acetonitrile was a fine solvent for 9-AA but too weak for PDI-silane. Although 9-AA was being quenched with the addition of PDI-silane, that quenching was not to equal magnitude of the performance of alternate solvents at equal concentrations. THF presented as a much better solvent for energy transfer and produced relative FRET efficiencies between 3-13 %, depending upon correction technique. The concentration set used for THF also presented great variation in the emission spectra for PDI-silane. as concentration increased, integration of the emission spectra presented a rise and fall. this meant that within the blended data set, the experiments covered both

sides of maximum radiative emission for PDI-silane (acceptor). Once concentrations increased to a point where the radiative emission decreased, no observation of enhanced emission via energy transfer could be observed. The dye appears to saturate as self-quenching prevents further excitation. The presence of PDI-silane's emission peak around 540 nm was an indicator for FRET when the donor was added to the solvated system.

The final experimental sets were designed to find similar performance turning points where acceptor concentration was a determining factor and further evaluate to cause of such quenching. Chlorobenzene and chloroform were used for these studies, and both presented strong emission peaks for 540 nm from PDI-silane through a large concentration set. Both solvents determined that the strong presence of the 540 nm peak was not a guaranteed marker for FRET at concentrations of 100s  $\mu\text{M}$ . In fact, both solvents showed drastic quenching of both moieties when blended at such concentrations. Stern-Volmer plots determined that there were two pathways of quenching present in these experiments suggesting a competing mechanism that would quench fluorescent emission of both types of fluorophores. This was true for both solvents. When concentrations were reduced to 10s  $\mu\text{M}$ , quenching of both fluorophores when blended was hindered and the Stern-Volmer plots presented a single mechanism of quenching.

Further understanding of these systems was greatly limited by the equipment being used so fluorescent lifetime measurements were performed for a more concise insight of the quenching mechanisms. THF and chloroform were used for this study along with concentrations of 5mM and 50  $\mu\text{M}$ . A characteristic FRET measurement of a donor/acceptor system would present via a lengthening of the acceptor fluorescent lifetime. However, lifetime measurements for 50  $\mu\text{M}$  sets presented the donor lifetime to lengthen with an unchanged acceptor lifetime. this is characteristic of trivial radiative emission and possible reabsorption. For 5 mM a lengthening of both donor and acceptor fluorescent lifetimes were observed indicating a competition between resonant energy transfer and radiative emission.

It is important to highlight that the move from THF to  $\text{CHCl}_3$  is an increase in solvent polarity but a decrease in solvent dipole moment and static dielectric constant. PDI-silane lengthens its excited state lifetime when solvated by  $\text{CHCl}_3$  as opposed to THF, regardless of concentration. the

opposite is true for 9-AA. It is well understood that 9-AA has strong dimer formation potential and the more polar a solvent is this less stable the dimer tends to be <sup>93</sup>. It is possible that 9-AA loses dimerization when CHCl<sub>3</sub> is used which is why THF presents with significantly higher lifetime measurements <sup>94</sup>. Such change in donor conformation could also explain the inconsistencies with FRET performance over a large range of concentrations when comparing these two solvents.

In total, this work presents the existence of a very narrow balance were these chosen fluorophores are capable and dominant at performing Förster resonant energy transfer. this balance is bound by aggregation induced self-quenching and trivial emission/reabsorption phenomenon allowed by the photophysical characteristics of 9-AA and PDI-silane.

## **OUTLOOK**

This project has explored multiple areas of interest in the field of energy transfer. The materials implemented are unique in their combination for the practice of FRET so far in literature. They present a promising possibility to further explore the potential of dye based resonant energy transfer. These materials still remain very complex in their nature of quenching pathways and currently an experimental approach is required to determine viability. Initial tests presented FRET as a dominating process given some consideration to right concentration and correct environmental parameters. Through experimentation this work concludes that such is not easily true. Conjugated molecules present diverse options of deexcitation which counter the intended use case. Further research into the hierarchy of mechanisms would be a valuable topic to explore with the consideration of controllability of each quenching mechanism in a practical application. In the future, a greater breadth of experimental work with fluorescent lifetime measurements would be of great value to further substantiate the findings of this work.

This concept overlaps the paralleling work presented here attempting to introduction a greater workability for fluorescent dyes. In doing so, it is clear that disruption to energy transfer mechanism must take place. This is work that must be taken to be considered of great importance in the future. For any reasonable application of FRET into devices there exists a compromise

between performance and practicality. This work has shown crudely that functional and workable materials could exist, but much work is needed to further the viability of such approaches.

Valuable future experimentation would be to create a liquid polymeric fluorophore with which curing through a cross-linker is feasible. Such a material would provide a gateway into using traditional thin-film and silicon chip manufacturing techniques for device creation. This would be a key step forward to closing the gap between some theoretical visions of FRET computers and the current practical limits of organic device fabrication.

Further avenues of exploration consist of the physical exclusion of transfer mechanisms via choice of structure. Nanoparticles, organic frameworks, and DNA present as interesting conformations able to restrain certain options of fluorophore interactions. These types of ‘cages’ may be a considered approach to controlling certain undesired quenching pathways that are problematic with organic fluorescent dyes.

## REFERENCES

- (1) Huang, C.; Barlow, S.; Marder, S. R. Perylene-3,4,9,10-Tetracarboxylic Acid Diimides: Synthesis, Physical Properties, and Use in Organic Electronics. *J. Org. Chem* **2011**, *76*, 2386–2407. <https://doi.org/10.1021/jo2001963>.
- (2) Frank Würthner. Perylene Bisimide Dyes as Versatile Building Blocks for Functional Supramolecular Architectures. *Chem. Commun.* **2004**, *0* (14), 1564–1579. <https://doi.org/10.1039/B401630K>.
- (3) Aaron, J.; Travis, K.; Harrison, N.; Sokolov, K. Dynamic Imaging of Molecular Assemblies in Live Cells Based on Nanoparticle Plasmon Resonance Coupling. *Nano Lett.* **2009**, *9* (10), 3612–3618. <https://doi.org/10.1021/NL9018275>.
- (4) Vaishnav, J. K.; Mukherjee, T. K. Long-Range Resonance Coupling-Induced Surface Energy Transfer from CdTe Quantum Dot to Plasmonic Nanoparticle. **2018**. <https://doi.org/10.1021/acs.jpcc.8b08757>.
- (5) Hong, F.; Tang, C.; Xue, Q.; Zhao, L.; Shi, H.; Hu, B.; Zhang, X. Simultaneously Enhanced Singlet Oxygen and Fluorescence Production of Nanoplatform by Surface Plasmon Resonance Coupling for Biomedical Applications. *Langmuir* **2019**, *35* (46), 14833–14839. <https://doi.org/10.1021/ACS.LANGMUIR.9B01727>.
- (6) Sokolov, K.; Rebecca Richards-Kortum, S.; Wolfgang Frey Ann Gillenwater Walter Hittelman, C.-S. Plasmon Resonance Coupling as a Tool for Detecting Epidermal Growth Factor Receptor Expression in Cancer Committee.
- (7) Lee, K. J.; Huang, T.; Nallathamby, P. D.; Xu, X.-H. N.; Xu, X. N. Wavelength Dependent Specific Plasmon Resonance Coupling of Single Silver Nanoparticles with EGFP.
- (8) Nafari, M.; Jornet, J. M. Modeling and Performance Analysis of Metallic Plasmonic Nano-Antennas for Wireless Optical Communication in Nanonetworks. *IEEE Access*

- 2017**, *5*, 6389–6398. <https://doi.org/10.1109/ACCESS.2017.2690990>.
- (9) Bidault, S.; Devilez, A.; Ghenuche, P.; Stout, B.; Bonod, N.; Wenger, J. Competition between Förster Resonance Energy Transfer and Donor Photodynamics in Plasmonic Dimer Nanoantennas. *ACS Photonics* **2016**, *3* (5), 895–903. <https://doi.org/10.1021/acsphotonics.6b00148>.
- (10) Zhang, X.; Marocico, C. A.; Lunz, M.; Gerard, V. A.; Gun'ko, Y. K.; Lesnyak, V.; Gaponik, N.; Susha, A. S.; Rogach, A. L.; Bradley, A. L. Experimental and Theoretical Investigation of the Distance Dependence of Localized Surface Plasmon Coupled Förster Resonance Energy Transfer. *ACS Nano* **2014**, *8* (2), 1273–1283. <https://doi.org/10.1021/nn406530m>.
- (11) Bricks, J. L.; Slominskii, Y. L.; Panas, I. D.; Demchenko, A. P. Fluorescent J-Aggregates of Cyanine Dyes: Basic Research and Applications Review. *Methods Appl. Fluoresc.* **2017**, *6* (1), 012001. <https://doi.org/10.1088/2050-6120/AA8D0D>.
- (12) Prevo, B.; Langmuir, O. V.-; 2004, undefined. Controlled, Rapid Deposition of Structured Coatings from Micro-and Nanoparticle Suspensions. *ACS Publ.* **2004**, *20* (6), 2099–2107. <https://doi.org/10.1021/la035295j>.
- (13) Klimov, V.; Sekatskii, S. K.; Dietler, G. Coherent Fluorescence Resonance Energy Transfer between Two Dipoles: Full Quantum Electrodynamics Approach. *J. Mod. Opt.* **2004**, *51* (13), 1919–1947. <https://doi.org/10.1080/09500340408232502>.
- (14) Li, J.; Yuan, S.; Qin, J.-S.; Huang, L.; Bose, R.; Pang, J.; Zhang, P.; Xiao, Z.; Tan, K.; Malko, A. V.; et al. Fluorescence Enhancement in the Solid State by Isolating Perylene Fluorophores in Metal–Organic Frameworks. *ACS Appl. Mater. Interfaces* **2020**, *12* (23), 26727–26732. <https://doi.org/10.1021/acsami.0c05512>.
- (15) Hummer, G.; Szabo, A. Dynamics of the Orientational Factor in Fluorescence Resonance Energy Transfer. *J. Phys. Chem. B* **2017**, *121* (15), 3331–3339. <https://doi.org/10.1021/acs.jpcc.6b08345>.

- (16) Takashima, Y.; Fukui, Y.; Otsubo, M.; Hamada, N.; Yamaguchi, H.; Yamamoto, H.; Harada, A. Emission Properties of Cyclodextrin Dimers Linked with Perylene Diimide—Effect of Cyclodextrin Tumbling. *Polym. J.* **2012**, *44* (3), 278–285. <https://doi.org/10.1038/pj.2011.128>.
- (17) Wahab, M. A.; Hussain, H.; He, C. Photoactive Perylenediimide-Bridged Silsesquioxane Functionalized Periodic Mesoporous Organosilica Thin Films (PMO-SBA15): Synthesis, Self-Assembly, and Photoluminescent and Enhanced Mechanical Properties. *Langmuir* **2009**, *25* (8), 4743–4750. <https://doi.org/10.1021/la900042g>.
- (18) Farag, A. A. M.; Osiris, W. G.; Yahia, I. S. Photovoltaic Performance Analysis of Organic Device Based on PTCDA/n-Si Heterojunction. *Synth. Met.* **2011**, *161* (17–18), 1805–1812. <https://doi.org/10.1016/J.SYNTHMET.2011.05.038>.
- (19) Gaudillat, P.; Wannebroucq, A.; Suisse, J. M.; Bouvet, M. Bias and Humidity Effects on the Ammonia Sensing of Perylene Derivative/Lutetium Bisphthalocyanine MSDI Heterojunctions. *Sensors Actuators B Chem.* **2016**, *222*, 910–917. <https://doi.org/10.1016/J.SNB.2015.09.015>.
- (20) Yongwei Huang; Ruijian Yuan; Shaomin Zhou. Gas Phase-Based Growth of Highly Sensitive Single-Crystal Rectangular Micro- and Nanotubes. *J. Mater. Chem.* **2011**, *22* (3), 883–888. <https://doi.org/10.1039/C1JM14238K>.
- (21) Türkmen, G.; Erten-Ela, S.; Icli, S. Highly Soluble Perylene Dyes: Synthesis, Photophysical and Electrochemical Characterizations. *Dye. Pigment.* **2009**, *83* (3), 297–303. <https://doi.org/10.1016/j.dyepig.2009.05.014>.
- (22) Rathnayake, H.; Binion, J.; McKee, A.; Scardino, D. J.; Hammer, N. I. Perylenediimide Functionalized Bridged-Siloxane Nanoparticles for Bulk Heterojunction Organic Photovoltaics. *Nanoscale* **2012**, *4* (15), 4631. <https://doi.org/10.1039/c2nr30538k>.
- (23) Solarczyk, K.; Wojcik, K.; Kulakowski, P. Nanocommunication via FRET with DyLight Dyes Using Multiple Donors and Acceptors. *IEEE Trans. Nanobioscience* **2016**, *15* (3),

- 275–283. <https://doi.org/10.1109/TNB.2016.2541462>.
- (24) Chan, K. L.; Sonar, P.; Sellinger, A. Cubic Silsesquioxanes for Use in Solution Processable Organic Light Emitting Diodes (OLED). *J. Mater. Chem.* **2009**, *19* (48), 9103. <https://doi.org/10.1039/b909234j>.
- (25) Förster, T. Experimentelle Und Theoretische Untersuchung Des Zwischenmolekularen Übergangs von Elektronenanregungsenergie. *Zeitschrift für Naturforsch. – Sect. A J. Phys. Sci.* **1949**. <https://doi.org/10.1515/zna-1949-0501>.
- (26) Roy, R.; Hohng, S.; Ha, T. A Practical Guide to Single-Molecule FRET. *Nat. Methods* **2008**, *5* (6), 507–516. <https://doi.org/10.1038/nmeth.1208>.
- (27) Kuscu, M.; Akan, O. B. The Internet of Molecular Things Based on FRET. *IEEE Internet Things J.* **2016**, *3* (1), 4–17. <https://doi.org/10.1109/JIOT.2015.2439045>.
- (28) Medintz, I. L.; Clapp, A. R.; Mattoussi, H.; Goldman, E. R.; Fisher, B.; Mauro, J. M. Self-Assembled Nanoscale Biosensors Based on Quantum Dot FRET Donors. *Nat. Mater.* **2003**, *2* (9), 630–638. <https://doi.org/10.1038/nmat961>.
- (29) Philipps, B.; Hennecke, J.; Glockshuber, R. FRET-Based in Vivo Screening for Protein Folding and Increased Protein Stability. *J. Mol. Biol.* **2003**. [https://doi.org/10.1016/S0022-2836\(03\)00077-9](https://doi.org/10.1016/S0022-2836(03)00077-9).
- (30) Schuler, B.; Eaton, W. A. Protein Folding Studied by Single-Molecule FRET. *Current Opinion in Structural Biology.* 2008. <https://doi.org/10.1016/j.sbi.2007.12.003>.
- (31) Sekar, R. B.; Periasamy, A. Fluorescence Resonance Energy Transfer (FRET) Microscopy Imaging of Live Cell Protein Localizations. *Journal of Cell Biology.* 2003. <https://doi.org/10.1083/jcb.200210140>.
- (32) Westphal, V.; Hell, S. W. Nanoscale Resolution in the Focal Plane of an Optical Microscope. *Phys. Rev. Lett.* **2005**, *94* (14), 143903. <https://doi.org/10.1103/PhysRevLett.94.143903>.

- (33) Raymo, F. M.; Giordani, S. Signal Processing at the Molecular Level. *J. Am. Chem. Soc.* **2001**, *123* (19), 4651–4652. <https://doi.org/10.1021/ja005699n>.
- (34) Ghenuche, P.; Mivelle, M.; de Torres, J.; Moparthi, S. B.; Rigneault, H.; Van Hulst, N. F.; García-Parajó, M. F.; Wenger, J. Matching Nanoantenna Field Confinement to FRET Distances Enhances Förster Energy Transfer Rates. *Nano Lett.* **2015**, *15* (9), 6193–6201. <https://doi.org/10.1021/acs.nanolett.5b02535>.
- (35) de Dood, M. J. A.; Knoester, J.; Tip, A.; Polman, A. Förster Transfer and the Local Optical Density of States in Erbium-Doped Silica. *Phys. Rev. B* **2005**, *71* (11), 115102. <https://doi.org/10.1103/PhysRevB.71.115102>.
- (36) Snoeks, E.; Lagendijk, A.; Polman, A. Measuring\_and\_modifying\_the\_spontaneous\_emission\_rate\_of\_erbium\_near\_a\_dielectric\_interface\_-\_Phys\_Rev\_Lett\_(1995).Pdf. 1995, pp 2459–2462.
- (37) Zhang, Q.; Cirpan, A.; Russell, T. P.; Emrick, T. Donor–Acceptor Poly(Thiophene-Block-Perylene Diimide) Copolymers: Synthesis and Solar Cell Fabrication. *Macromolecules* **2009**, *42* (4), 1079–1082. <https://doi.org/10.1021/MA801504E>.
- (38) Li, C.-Z.; Su, H. An Improved Perylene Sensitizer for Solar Cell Applications Cite This Paper Related Papers Rainbow Perylene Monoimides: Easy Control of Optical Properties Comparative Studies on Rigid  $\pi$  Linker-Based Organic Dyes: Structure-Property Relationships and Photo... <https://doi.org/10.1002/cssc.200800068>.
- (39) İçli, S.; İcil, H.; Gürol, I. High Rates of Fluorescence Quenching between Perylene Dodecyldiimide and Certain  $\pi$ -Electron Donors. *Turkish J. Chem.* **1997**.
- (40) Geng, T. M.; Li, D. K.; Zhu, Z. M.; Zhang, W. Y.; Ye, S. N.; Zhu, H.; Wang, Z. Q. Fluorescent Conjugated Microporous Polymer Based on Perylene Tetraanhydride Bisimide for Sensing O-Nitrophenol. *Anal. Chim. Acta* **2018**, *1011*, 77–85. <https://doi.org/10.1016/J.ACA.2018.01.002>.

- (41) Türkmen, G.; Erten-Ela, S.; Icli, S. Highly Soluble Perylene Dyes: Synthesis, Photophysical and Electrochemical Characterizations. *Dye. Pigment.* **2009**, *83* (3), 297–303. <https://doi.org/10.1016/J.DYEPIG.2009.05.014>.
- (42) Wang, B.; Yu, C. Fluorescence Turn-On Detection of a Protein through the Reduced Aggregation of a Perylene Probe. *Angew. Chemie* **2010**, *122* (8), 1527–1530. <https://doi.org/10.1002/ANGE.200905237>.
- (43) and, L. D. W.; Mattern\*, D. L. Donor– $\sigma$ –Acceptor Molecules Incorporating a Nonadecyl-Swallowtailed Perylenediimide Acceptor. *J. Org. Chem.* **2003**, *68* (26), 10058–10066. <https://doi.org/10.1021/JO035409W>.
- (44) Más-Montoya, M.; Janssen, R. A. J. The Effect of H- and J-Aggregation on the Photophysical and Photovoltaic Properties of Small Thiophene–Pyridine–DPP Molecules for Bulk-Heterojunction Solar Cells. *Adv. Funct. Mater.* **2017**, *27* (16), 1605779. <https://doi.org/10.1002/ADFM.201605779>.
- (45) Marfin, Y. S.; Banakova, E. A.; Merkushev, D. A.; Usoltsev, S. D.; Churakov, A. V. Effects of Concentration on Aggregation of BODIPY-Based Fluorescent Dyes Solution. <https://doi.org/10.1007/s10895-020-02622-y>/Published.
- (46) Baruah, M.; Qin, W.; Flors, C.; Hofkens, J.; Vallée, R. A. L.; Beljonne, D.; Van der Auweraer, M.; De Borggraeve, W. M.; Boens, N. Solvent and PH Dependent Fluorescent Properties of a Dimethylaminostyryl Borondipyrromethene Dye in Solution. *J. Phys. Chem. A* **2006**, *110* (18), 5998–6009. <https://doi.org/10.1021/jp054878u>.
- (47) Heutz, S.; Ferguson, A. .; Rumbles, G.; Jones, T. . Morphology, Structure and Photophysics of Thin Films of Perylene-3,4,9,10-Tetracarboxylic Dianhydride. *Org. Electron.* **2002**, *3* (3–4), 119–127. [https://doi.org/10.1016/S1566-1199\(02\)00049-6](https://doi.org/10.1016/S1566-1199(02)00049-6).
- (48) Zang, D. Y.; So, F. F.; Forrest, S. R. Giant Anisotropies in the Dielectric Properties of Quasi-Epitaxial Crystalline Organic Semiconductor Thin Films. *Appl. Phys. Lett.* **1991**, *59* (7), 823–825. <https://doi.org/10.1063/1.105274>.

- (49) Gangilenka, V. R.; Titova, L. V.; Smith, L. M.; Wagner, H. P.; Desilva, L. A. A.; Gisslén, L.; Scholz, R. Selective Excitation of Exciton Transitions in PTCDA Crystals and Films. *Phys. Rev. B – Condens. Matter Mater. Phys.* **2010**, *81* (15).  
<https://doi.org/10.1103/PHYSREVB.81.155208>.
- (50) Han, Y.; Ning, W.; Du, H.; Yang, J.; Wang, N.; Cao, L.; Li, F.; Zhang, F.; Xu, F.; Tian, M. Preparation, Optical and Electrical Properties of PTCDA Nanostructures. *Nanoscale* **2015**, *7* (40), 17116–17121. <https://doi.org/10.1039/C5NR04738B>.
- (51) Bachmann, L.; Zezell, D. M.; Ribeiro, A. da C.; Gomes, L.; Ito, A. S. Fluorescence Spectroscopy of Biological Tissues – A Review. *Applied Spectroscopy Reviews*. 2006.  
<https://doi.org/10.1080/05704920600929498>.
- (52) Carstea, E. M.; Bridgeman, J.; Baker, A.; Reynolds, D. M. Fluorescence Spectroscopy for Wastewater Monitoring: A Review. *Water Research*. 2016.  
<https://doi.org/10.1016/j.watres.2016.03.021>.
- (53) Valeur, B. *Molecular Fluorescence: Principles and Applications*; 2001.  
<https://doi.org/10.1002/3527600248>.
- (54) Bewersdorf, J.; Egner, A.; Hell, S. W. 4Pi-Confocal Microscopy Is Coming of Age. *Imaging Microsc.* **2004**.
- (55) Andrews, D. L.; Bradshaw, D. S. Virtual Photons, Dipole Fields and Energy Transfer: A Quantum Electrodynamical Approach. *Eur. J. Phys.* **2004**. <https://doi.org/10.1088/0143-0807/25/6/017>.
- (56) Schaufele, F.; Demacro, I.; Day, R. N. FRET Imaging in the Wide-Field Microscope. In *Molecular Imaging: FRET Microscopy and Spectroscopy*; Oxford University Press: Oxford, 2005; pp 72–94.
- (57) Gadella, T. W. J. Chapter 9 Total Internal Reflection Fluorescence Lifetime Imaging Microscopy. In *Laboratory Techniques in Biochemistry and Molecular Biology*; 2009; pp

- 395–412. [https://doi.org/10.1016/S0075-7535\(08\)00009-0](https://doi.org/10.1016/S0075-7535(08)00009-0).
- (58) Demchenko, A. P.; Demchenko, A. P. Fluorescence Detection Techniques. In *Introduction to Fluorescence Sensing*; 2015. [https://doi.org/10.1007/978-3-319-20780-3\\_3](https://doi.org/10.1007/978-3-319-20780-3_3).
- (59) Griffiths, D. J.; Inglefield, C. *Introduction to Electrodynamics. Am. J. Phys.* **2005**. <https://doi.org/10.1119/1.4766311>.
- (60) Serway, R. A.; Kirkpatrick, L. D. Physics for Scientists and Engineers with Modern Physics. *Phys. Teach.* **1988**. <https://doi.org/10.1119/1.2342517>.
- (61) Albani, J. R. *Structure and Dynamics of Macromolecules: Absorption and Fluorescence Studies*; 2004. <https://doi.org/10.1016/B978-0-444-51449-3.X5000-X>.
- (62) Reimers, J. The Appropriateness of Density-Functional Theory for the Calculation of Molecular Electronics Properties. <https://doi.org/10.1196/annals.1292.017>.
- (63) Godby, R. W.; Schlüter, M.; Sham, L. J. Self-Energy Operators and Exchange-Correlation Potentials in Semiconductors. *Phys. Rev. B* **1988**, *37* (17), 10159. <https://doi.org/10.1103/PhysRevB.37.10159>.
- (64) Levine, Z. H.; Allan, D. C. Linear Optical Response in Silicon and Germanium Including Self-Energy Effects. *Phys. Rev. Lett.* **1989**, *63* (16), 1719. <https://doi.org/10.1103/PhysRevLett.63.1719>.
- (65) Runge, E.; Gross, E. K. U. Density-Functional Theory for Time-Dependent Systems. *Phys. Rev. Lett.* **1984**, *52* (12), 997. <https://doi.org/10.1103/PhysRevLett.52.997>.
- (66) Conroy, E. M.; Li, J.; Kim, H.; Russ Algar, W. Self-Quenching, Dimerization, and Homo-FRET in Hetero-FRET Assemblies with Quantum Dot Donors and Multiple Dye Acceptors. *J. Phys. Chem. C* **2016**, 120–17817. <https://doi.org/10.1021/acs.jpcc.6b05886>.
- (67) Matej Bračič; Tamilselvan Mohan; Rupert Kargl; Thomas Griesser; Silvo Hribernik;

- Stefan Köstler; Karin Stana-Kleinschek; Lidija Fras-Zemljič. Preparation of PDMS Ultrathin Films and Patterned Surface Modification with Cellulose. *RSC Adv.* **2014**, *4* (23), 11955–11961. <https://doi.org/10.1039/C3RA47380E>.
- (68) Stöber, W.; Fink, A.; Bohn, E. Controlled Growth of Monodisperse Silica Spheres in the Micron Size Range. *J. Colloid Interface Sci.* **1968**, *26* (1), 62–69. [https://doi.org/10.1016/0021-9797\(68\)90272-5](https://doi.org/10.1016/0021-9797(68)90272-5).
- (69) Neises, B.; Steglich, W. Simple Method for the Esterification of Carboxylic Acids. *Angew. Chemie Int. Ed. English* **1978**, *17* (7), 522–524. <https://doi.org/10.1002/ANIE.197805221>.
- (70) Dimitrov, A. S.; Nagayama, K. Steady-State Unidirectional Convective Assembling of Fine Particles into Two-Dimensional Arrays. *Chem. Phys. Lett.* **1995**, *243* (5–6), 462–468.
- (71) Kobayashi, Y.; Miyauchi, H.; Gu, S.; ... D. N.-J. of chemical; 2004, undefined. Fabrication of Mono-and Multi-Layers of Submicron-Sized Spheres by a Dip-Coating Technique and Their Transmittance Property. *jstage.jst.go.jp*.
- (72) Lee, J. A.; Meng, L.; Norris, D. J.; Scriven, L. E.; Tsapatsis, M. Colloidal Crystal Layers of Hexagonal Nanoplates by Convective Assembly. *Langmuir* **2006**, *22* (12), 5217–5219. <https://doi.org/10.1021/LA0601206>.
- (73) Deckman, H. W. Macromolecular Self-Organized Assemblies. *J. Vac. Sci. Technol. B Microelectron. Nanom. Struct.* **1988**, *6* (1), 333. <https://doi.org/10.1116/1.583991>.
- (74) Szekeres, M.; Kamalin, O.; ... R. S.-J. of M.; 2002, undefined. Ordering and Optical Properties of Monolayers and Multilayers of Silica Spheres Deposited by the Langmuir–Blodgett Method. *pubs.rsc.org*. <https://doi.org/10.1039/b204687c>.
- (75) Reculosa, S.; materials, S. R.-C. of; 2003, undefined. Synthesis of Colloidal Crystals of Controllable Thickness through the Langmuir–Blodgett Technique. *ACS Publ.* **2003**, *15* (2), 598–605. <https://doi.org/10.1021/cm021242w>.

- (76) Ogi, T.; Modesto-Lopez, L. B.; Iskandar, F.; Okuyama, K. Fabrication of a Large Area Monolayer of Silica Particles on a Sapphire Substrate by a Spin Coating Method. *Colloids Surfaces A Physicochem. Eng. Asp.* **2007**, *297* (1–3), 71–78.  
<https://doi.org/10.1016/j.colsurfa.2006.10.027>.
- (77) physics, D. D.-T. journal of chemical; 1953, undefined. A Theory of Sensitized Luminescence in Solids. *aip.scitation.org* **1953**, *21* (5), 836.  
<https://doi.org/10.1063/1.1699044>.
- (78) Birks, J. B.; Georghiou, S.; Munro, I. H. Energy Transfer in Organic Systems V. Lifetime Studies of Anthracene-Perylene Transfer in Benzene Solutions. *J. Phys. B At. Mol. Phys.* **1968**, *1* (2), 266–273. <https://doi.org/10.1088/0022-3700/1/2/318>.
- (79) Geng, T. M.; Li, D. K.; Zhu, Z. M.; Zhang, W. Y.; Ye, S. N.; Zhu, H.; Wang, Z. Q. Fluorescent Conjugated Microporous Polymer Based on Perylene Tetraanhydride Bisimide for Sensing O-Nitrophenol. *Anal. Chim. Acta* **2018**, *1011*, 77–85.  
<https://doi.org/10.1016/j.aca.2018.01.002>.
- (80) Cheng, H.; Yang, L.; Zhang, S.; Rao, D.; Lu, X. Two-channel Near-infrared Fluorescence Ag + Ion Sensing of a New Star-shaped Dendrimer. *Luminescence* **2019**, *34* (6), 615–622.  
<https://doi.org/10.1002/bio.3647>.
- (81) Demmig, S.; Langhals, H. Leichtlösliche, Lichtechte Perylen-Fluoreszenzfarbstoffe. *Chem. Ber.* **1988**, *121* (2), 225–230. <https://doi.org/10.1002/CBER.19881210205>.
- (82) Silori, Y.; De, A. K. Tuning Effect of Local Environment to Control Mechanism of Fluorescence Depolarization: Rotational Diffusion and Resonance Energy Transfer within Homo-Aggregates of Xanthenes. *J. Photochem. Photobiol. A Chem.* **2019**, *377*, 198–206.  
<https://doi.org/10.1016/J.JPHOTOCHEM.2019.04.006>.
- (83) Bhavya, P.; Melavanki, R.; Kusanur, R.; Sharma, K.; Muttannavar, V. T.; Naik, L. R. Effect of Viscosity and Dielectric Constant Variation on Fractional Fluorescence Quenching Analysis of Coumarin Dye in Binary Solvent Mixtures. *Luminescence* **2018**,

- 33 (5), 933–940. <https://doi.org/10.1002/BIO.3492>.
- (84) Chen, Z.-K.; Huang, W.; Wang, L.-H.; Kang, E.-T.; Chen, B. J.; Lee, C. S.; Lee, S. T. A Family of Electroluminescent Silyl-Substituted Poly( p -Phenylenevinylene)s: Synthesis, Characterization, and Structure–Property Relationships. *Macromolecules* **2000**, *33* (24), 9015–9025. <https://doi.org/10.1021/ma0005670>.
- (85) Melhuish, W. H. QUANTUM EFFICIENCIES OF FLUORESCENCE OF ORGANIC SUBSTANCES: EFFECT OF SOLVENT AND CONCENTRATION OF THE FLUORESCENT SOLUTE 1. *J. Phys. Chem.* **1961**, *65* (2), 229–235. <https://doi.org/10.1021/j100820a009>.
- (86) Werner, T. C.; Hercules, D. M. Fluorescence of 9-Anthroic Acid and Its Esters. Environmental Effects on Excited-State Behavior. *J. Phys. Chem.* **1969**, *73* (6), 2005–2011. <https://doi.org/10.1021/j100726a060>.
- (87) Katoh, R.; Sinha, S.; Murata, S.; Tachiya, M. Origin of the Stabilization Energy of Perylene Excimer as Studied by Fluorescence and Near-IR Transient Absorption Spectroscopy. *J. Photochem. Photobiol. A Chem.* **2001**, *145* (1–2), 23–34. [https://doi.org/10.1016/S1010-6030\(01\)00562-7](https://doi.org/10.1016/S1010-6030(01)00562-7).
- (88) DYNAMICS OF PHOTODIMERIZATION OF 9-ANTHROIC ACID AND SODIUM 9-ANTHROATE – ProQuest <https://www.proquest.com/docview/302415465?pq-origsite=gscholar&fromopenview=true> (accessed Oct 2, 2021).
- (89) Joykrishna Dey; Judson L. Haynes III, and; Warner\*, I. M.; Chandra, A. K. Fluorescence Spectral Study of 9-Acridinecarboxylic Acid and Its Methyl Ester. Understanding the Unusual Fluorescence Behavior of 9-Anthroic Acid. *J. Phys. Chem. A* **1997**, *101* (12), 2271–2278. <https://doi.org/10.1021/JP963263H>.
- (90) Dey, J.; Warner, I. M. Dual Fluorescence of 9-(N,N-Dimethylamino)Anthracene: Effect of Solvent Polarity and Viscosity. **1997**.

- (91) 'Excimer' Fluorescence II. Lifetime Studies of Pyrene Solutions. *Proc. R. Soc. London. Ser. A. Math. Phys. Sci.* **1963**, 275 (1363), 575–588.  
<https://doi.org/10.1098/RSPA.1963.0187>.
- (92) Clegg, R. M. Fret and Flim Techniques. *Lab. Tech. Biochem. Mol. Biol.* **2009**, 33, 1–57.
- (93) Suzuki, S.; Fujii, T.; Yoshiike, N.; Komatsu, S.; Iida, T. Absorption and Fluorescence Spectra of Anthracenecarboxylic Acids. I. 9-Anthroic Acid and Formation of Excimer. *Bull. Chem. Soc. Jpn.* **1978**, 51 (9), 2460–2466. <https://doi.org/10.1246/bcsj.51.2460>.
- (94) Osaki, H.; Chou, C.-M.; Taki, M.; Welke, K.; Yokogawa, D.; Irle, S.; Sato, Y.; Higashiyama, T.; Saito, S.; Fukazawa, A.; et al. A Macrocyclic Fluorophore Dimer with Flexible Linkers: Bright Excimer Emission with a Long Fluorescence Lifetime. *Angew. Chemie* **2016**, 128 (25), 7247–7251. <https://doi.org/10.1002/ange.201602239>.

APPENDIX A: MOLECULAR ORBITAL SIMULATION

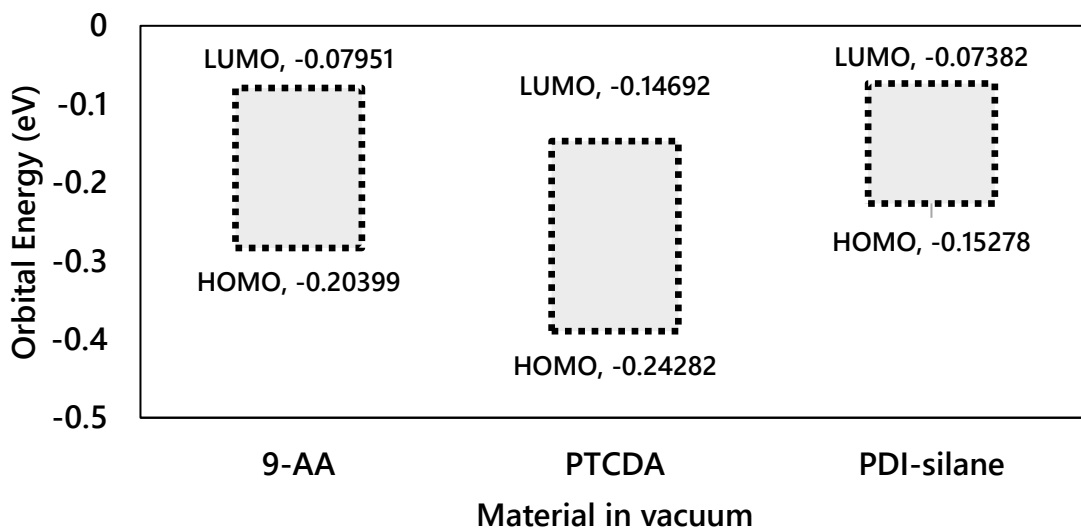


Figure 154 – Ground state HOMO-LUMO after geometry optimization simulation via DFT for 9-AA, PTCDA, and PDI-silane.

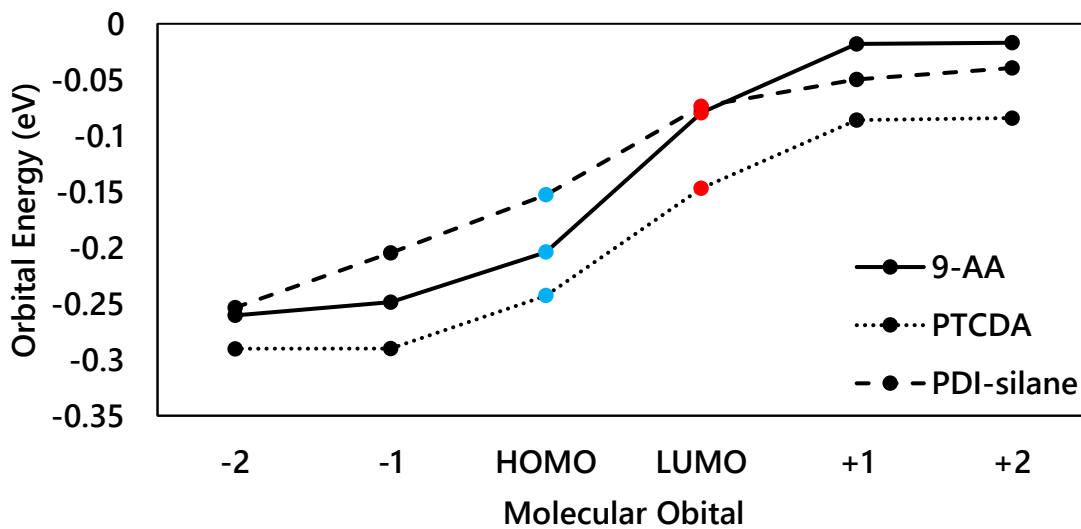


Figure 155 – Ground state molecular orbitals after geometry optimization via DFT for 9-AA, PTCDA, and PDI-silane.

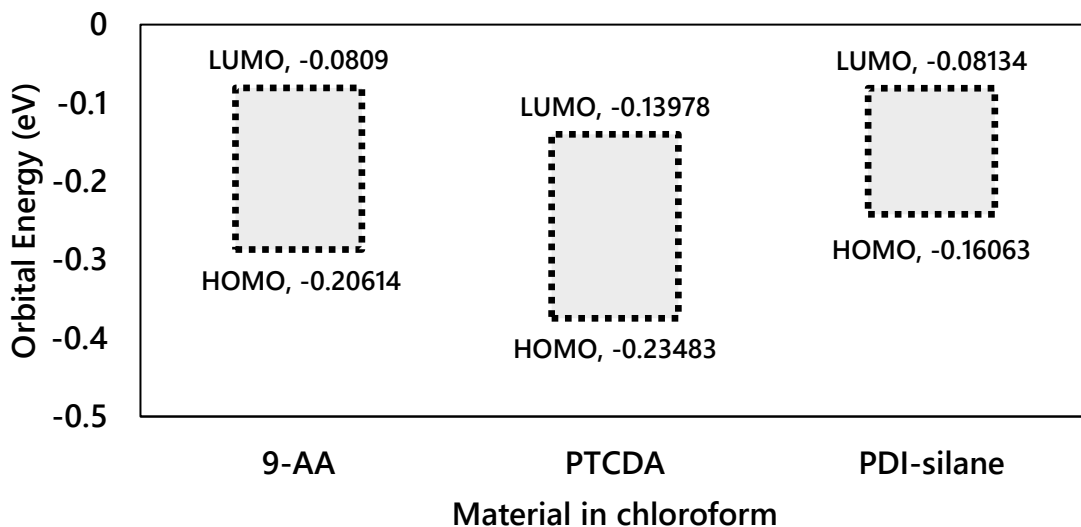


Figure 156 – Ground state HOMO-LUMO after geometry optimization simulation via DFT in chloroform for 9-AA, PTCDA, and PDI-silane.

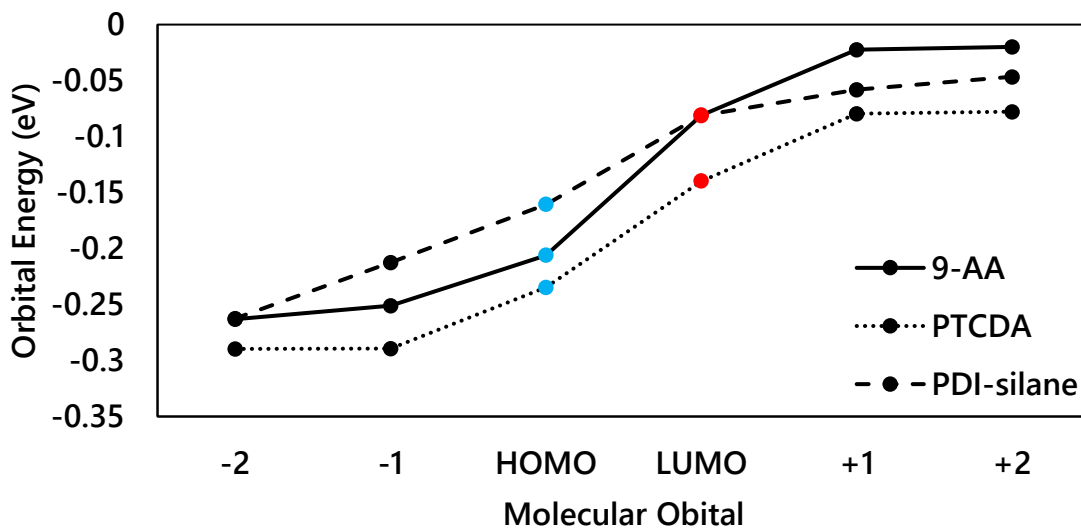


Figure 157 – Ground state molecular orbitals after geometry optimization via DFT in chloroform for 9-AA, PTCDA, and PDI-silane.

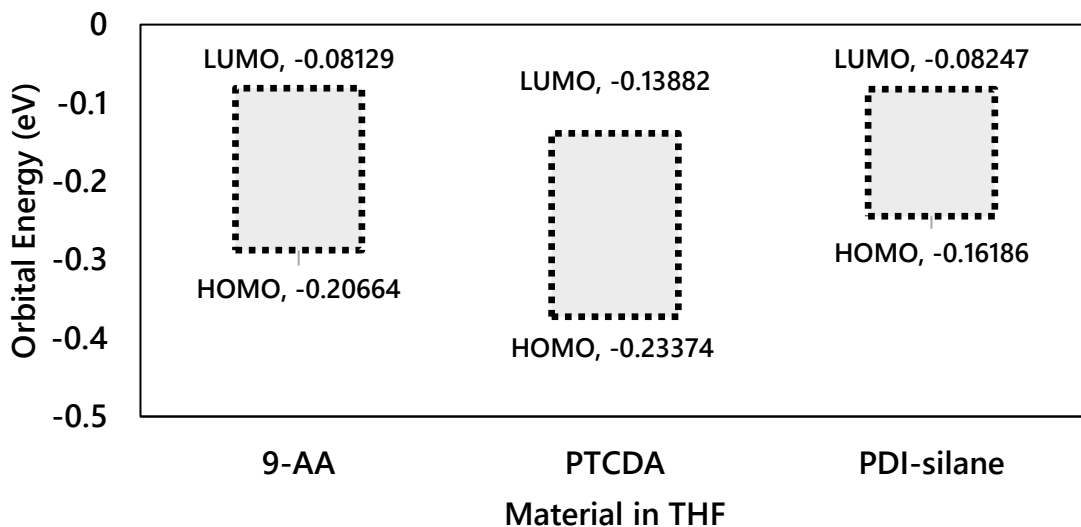


Figure 158 – Ground state HOMO-LUMO after geometry optimization simulation via DFT in THF for 9-AA, PTCDA, and PDI-silane.

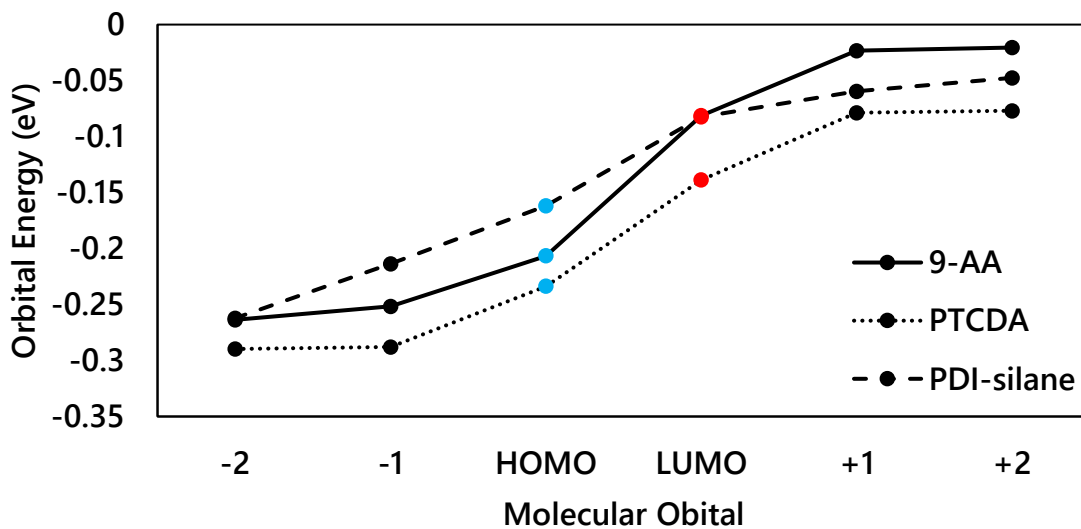


Figure 159 – Ground state molecular orbitals after geometry optimization via DFT in THF for 9-AA, PTCDA, and PDI-silane.

<i>Orbital</i>	<i>9-AA</i>				<i>PTCDA</i>				<i>PDI-silane</i>			
	Alpha MOs	Vacuum	CHCL3	THF	Alpha MOs	Vacuum	CHCl3	THF	Alpha MOs	Vacuum	CHCl3	THF
+2	61	-0.01692	-0.01992	-0.0205	103	-0.08414	-0.07773	-0.0769	216	-0.03948	-0.04657	-0.04757
+1	60	-0.01794	-0.02248	-0.02333	102	-0.08591	-0.07964	-0.07882	215	-0.04975	-0.05821	-0.0595
<i>LUMO</i>	59	-0.07951	-0.0809	-0.08129	101	-0.14692	-0.13978	-0.13882	214	-0.07382	-0.08134	-0.08247
<i>HOMO</i>	58	-0.20399	-0.20614	-0.20664	100	-0.24282	-0.23483	-0.23374	213	-0.15278	-0.16063	-0.16186
-1	57	-0.24846	-0.2509	-0.25146	99	-0.28998	-0.28925	-0.28792	212	-0.20464	-0.21246	-0.21371
-2	56	-0.26042	-0.26308	-0.26365	98	-0.29018	-0.28961	-0.28969	211	-0.25346	-0.26244	-0.26216

Table 35 – Ground state molecular orbitals after geometry optimization via DFT for 9-AA, PTCDA, and PDI-silane